An Experimental and Computational Investigation of Bone Cement Residual Stresses

By

John A. Hingston, B.Eng.

This thesis is submitted to Dublin City University as the fulfillment of the requirement for the award of the degree of

Doctor of Philosophy

Supervisors:

Dr. Garrett McGuinness

Dr. Lisa Looney

External Advisor:

Dr. Nicholas Dunne

(The Queen's University of Belfast)

School of Mechanical and Manufacturing Engineering

Dublin City University

September 2006

Declaration

I hereby certify that this material, which I now submit for assessment on the programme of study leading to the award of Doctor of Philosophy, is entirely my own work and has not been taken from the work of others save and to the extent that such work has been cited and acknowledged within the text of my work.

Signed: 
John Allen Hingston

ID No.: 98047884

Date: 08/09/2006

Acknowledgements

I would like to acknowledge and extend my gratitude to the numerous individuals that have contributed to this work, both directly and indirectly. Firstly I would like to express my sincere gratitude to my supervisor Dr. Garrett McGuinness, to whom I am indebted for his help, guidance, advice and friendship throughout this project. His availability to discuss issues and willingness to give of his knowledge were instrumental to the completion of this work. I would also like to extend my sincere gratitude to Dr. Nicholas Dunne for facilitating my entrance into the field of Bioengineering and his continued advice and support throughout this work.

I wish to acknowledge and thank all the staff of the School of Mechanical and Manufacturing Engineering, Dublin City University, who helped me over the course of this work. I am particularly grateful too and would like to sincerely thank Alan Meehan and Liam Domican for their interest in my research and extending their help and advice. I wish to give special mention to my colleagues David Mathews, Declan Noone and Anthony Comer for the many light-hearted and energising conversations. I would also like to sincerely thank Wayne Young of PEI Ltd. for his technical advice with respect to bone cement preparation and Thomas Smyth for his invaluable IT support.

I wish to acknowledge the Irish Research Council for Science Engineering and Technology (IRCSET) who provided financial support for this research over the first three years.

I would like to convey my sincere thanks to my parents Billy and Betty for their continued and unwavering support that allowed me to pursue my education to the highest level, for which I am entirely grateful. Last but by no means least, I would like to sincerely thank my fiancée Renata Filippo, for her continued support, encouragement and confidence in my ability and who continually uplifted my spirit.

Publications and Presentations

Conference Oral Presentations:

Hingston, J., McGuinness, G.B. and Dunne N.J., Comparison between CMW® 1 and SmartSet® bone cements with respect to residual stresses, 12th Annual Bioengineering In Ireland Conference, Galway, Ireland, January 2006, 38

Hingston, J.A., McGuinness, G.B., Looney, L.L., Dunne, N.J. and Orr, J.F., Computational analysis of shrinkage stresses in acrylic bone cement, The Institute of Materials Minerals and Mining: Materials Congress 2004, London, England, March 2004, 34

Hingston, J.A., McGuinness, G.B., Looney L.L. and Dunne N.J., Computational investigation of bone cement thermal shrinkage about the stem/cement interface, 10th Annual Bioengineering In Ireland Conference, Co. Limerick, Ireland, January 2004, 79

Conferences Poster Presentations:

Hingston, J., McGuinness, G., Looney, L. and Dunne, N., A computational and experimental investigation of the dimensional changes in self-curing acrylic bone cement, 3rd Symposium of the Irish Research Council for Science, Engineering and Technology, Dublin, Ireland, November 2005, 205

Hingston, J.A., McGuinness, G.B., Looney, L.L. and Dunne, N.J., Anatomically representative computational modelling of residual stresses in self curing acrylic bone cement, 19th European Conference on Biomaterials, Sorrento, Italy, September 2005

Hingston, J.A., McGuinness, G.B., Looney, L.L. and Dunne, N.J., Acrylic bone cement residual stresses around a femoral implant, 25th Northern Ireland Biomedial Engineering Society, Belfast, Northern Ireland, April 2005, 44

Hingston, J., McGuinness, G., Looney, L. and Dunne, N., A computational and experimental investigation of the dimensional changes in self-curing acrylic bone cement, 2nd Symposium of the Irish Research Council for Science, Engineering and Technology, Dublin, Ireland, November 2004, 160

Hingston, J.A., McGuinness, G.B., Looney, L., Dunne N.J. and Orr, J.F., Computational analysis of bone cement thermal shrinkage about the stem/cement interface, 7th World Biomaterials Congress, Sydney, Australia, May 2004, 1466

Hingston, J., McGuinness, G., Looney, L. and Dunne, N., A computational and experimental investigation of the dimensional changes in self-curing acrylic bone cement, 1st Symposium of the Irish Research Council for Science, Engineering and Technology, Dublin, Ireland, November 2003, 155

Hingston, J.A., McGuinness, G.B., Looney, L., Dunne, N.J. and Orr, J.F., Computational analysis of acrylic bone cement thermal shrinkage stresses, 18th European Conference on Biomaterials, Stuttgart, Germany, October 2003, LMP040

Refereed Conference Proceedings

Orr, J.F., Dunne, N.J., Hingston, J., McGuinness, G., Mitchell, J.B. and Cabrera, N.O., The effect of shrinkage on stresses in a mantle of curing acrylic bone cement, 7th World Biomaterials Congress, Sydney, Australia, May 2004, 525

Table of Contents

Declaration ii

Acknowledgements iii

Publications and Presentations iv

Table of Contents vi

List of Figures x

List of Tables xx

Abbreviations xxiii

Nomenclature xxiv

Abstract xxvi

Chapter 1: Introduction 1

1.1 TOTAL HIP ARTHROPLASTY 2

1.1.1 Historical Perspective 2

1.1.2 Femoral Prosthesis 3

1.1.3 Polymethyl Methacrylate 5

1.2 PRE-OPERATIVE MOTIVATION 6

1.3 OPERATIVE PROCEDURE 8

1.4 ARTHROPLASTY FAILURE 11

1.4.1 Aseptic Loosening 12

1.5 RESEARCH OBJECTIVES AND METHODOLOGIES 13

Chapter 2: Literature Survey 19

2.1 INTRODUCTION 19

2.2 ACRYLIC BONE CEMENT 19

2.2.1 Chemical Composition 20

2.2.2 Polymerisation Characteristics 21

2.2.3 The Exothermic Reaction 23

2.2.4 Cement Mixing Systems 29

2.2.5 Cement Pressurisation 30

2.2.6 Mechanical Properties 31

2.3 Residual Stress Development 39
2.3.1 *Volume Alteration Mechanisms* 40
2.3.2 *Stress-Locking* 46
2.3.3 *Transient Net Volume Alteration* 47
2.4 Residual Stress Studies 49
2.4.1 *Mathematical Studies* 49
2.4.2 *Finite Element Studies* 52
2.4.3 *Experimental Studies* 57
2.5 Residual Stress Under Load Conditions 61
2.6 Concluding Remarks 64

Chapter 3: Experimental Investigation Of Bone Cement Residual Stresses 66

3.1 Introduction 66
3.2 Materials And Methods 66
3.2.1 *Materials* 67
3.2.2 *Strain Measurement* 70
3.2.3 *Temperature Measurement* 75
3.2.4 *Data Acquisition* 76
3.2.5 *Experimental Procedure* 77
3.2.6 *Validation* 79
3.3 Results 84
3.3.1 *Thermal Results* 86
3.3.2 *Strain Results* 96
3.4 Discussion 105
3.5 Chapter Summary 111

Chapter 4: Finite Element Analysis Of *In Vitro* Residual Stresses 113

4.1 Introduction 113
4.2 Preliminary Finite Element Analysis: Morse Taper Experiments 115
4.2.1 *Model Definition* 115
4.2.2 *Material Properties* 119
4.2.3 *Boundary Conditions And Loading* 119
4.2.4 *Results* 120

4.2.5 Validation *122*
4.3 FINITE ELEMENT ANALYSIS OF EXPERIMENTAL WORK 123
4.4 MODEL DEFINITION 123
4.5 MATERIAL PROPERTIES 127
4.5.1 Dilatometer Measurements *127*
4.5.2 316L Stainless Steel Material Properties *131*
4.5.3 Acrylic Bone Cement Material Properties *131*
4.5.4 E-glass/epoxy Material Properties *132*
4.6 BOUNDARY CONDITIONS AND LOADS 134
4.6.1 Transient Thermal Analysis *135*
4.6.2 Mechanical Analysis *141*
4.7 FINITE ELEMENT ANALYSIS RESULTS 143
4.7.1 Transient Thermal Results *143*
4.7.2 Residual Stress Results *148*
4.8 DISCUSSION 151
4.9 CHAPTER SUMMARY 156

Chapter 5: Finite Element Analysis Of *In Vivo* Residual Stresses 157

5.1 INTRODUCTION 157
5.2 MODEL DEFINITION 159
5.2.1 Femoral Prosthesis Geometry *159*
5.2.2 Bone Cement Mantle Geometry *160*
5.2.3 Femur Geometry *163*
5.2.4 Model Assembly *165*
5.3 MATERIAL PROPERTIES 167
5.3.1 Femoral Prosthesis Material Properties *167*
5.3.2 Bone Cement Material Properties *169*
5.3.3 Femoral Bone Material Properties *169*
5.4 BOUNDARY CONDITIONS AND LOADING 171
5.4.1 Transient Thermal Analysis *172*
5.4.2 Residual Stress Analysis *174*
5.4.3 Physiological Load Analysis *175*
5.4.4 Rehabilitation Analysis *178*
5.5 RESULTS 178

5.5.1 Transient Thermal Results *178*
5.5.2 Residual Stress Results *181*
5.5.3 Physiological Load Results *186*
5.5.4 Rehabilitation Stress Results *189*
5.6 DISCUSSION 196
5.7 CHAPTER SUMMARY 204

Chapter 6: Conclusions And Future Work **206**

6.1 THESIS CONTRIBUTION 206
6.2 CONCLUSIONS 207
6.3 FUTURE WORK 210

References **212**

Appendix A: Hip Anatomy **229**

Appendix B: Anatomical Directional Terminology **232**

Appendix C: Electrical Resistance Strain Gauge Principles **234**

Appendix D: Data Acquisition **237**

Appendix E: CMW® 1 Gentamicin Transient Thermal Results **241**

Appendix F: SmartSet® Gentamicin Transient Thermal Results **244**

Appendix G: Instrumented Femur Transient Strain Results **246**

Appendix H: Instrumented Stem Transient Strain Results **249**

Appendix I: Theoretical Model **252**

Appendix J: Coefficient Of Thermal Convection **261**

Appendix K: Anatomical Model Mesh **263**

Appendix L: Anatomical Model Principal Stress Results **266**

Appendix M: Residual Stress Relaxation **268**

List of Figures

Figure 1.1: Schematic of a cemented artificial hip replacement. Adapted from Huiskes [8]. 4
Figure 1.2: Line diagrams of popular stems. Adapted from Brockhurst and Svensson [9]. 5
Figure 1.3: Femoral taper reamer 9
Figure 1.4: Cement pressurisation. Adapted from Colwell and Ritter [17]. 10
Figure 1.5: Flow chart of research objectives and methodologies 18
Figure 2.1: Monomer ampoule (left) and polymer packet (right) of CMW® 1 Gentamicin bone cement 20
Figure 2.2: Typical temperature versus time trace for polymerising bone cement 21
Figure 2.3: Description of polymerisation process in which MMA molecules are connected to form polymer chains [8] 23
Figure 2.4: Heat generation rate for Simplex® P bone cement at various isothermal temperatures. Adapted from Baliga et al [55]. 25
Figure 2.5: Typical curve logging percentage residual monomer versus time. Adapted from Kuhn [10]. 28
Figure 2.6: Zimmer Osteobond™ vacuum mixing system, (A) Bowl system (B) Cartridge system. Reprinted with permission [45]. 30
Figure 2.7: Typical S-N curves for hand mixed and vacuum mixed cement [89] 35
Figure 2.8: Percentage creep versus number of cycles, at a stress of 10.6 MPa, frequency of 1 Hz, at 37°C [94] 37
Figure 2.9: Stress relaxation of Palacos® R bone cement over a 48 hour period, based on 7 day old samples in saline solution at 37°C. Adapted from Lee et al [93]. 38
Figure 2.10: Linear coefficient of thermal expansion, both experimental and theoretical findings. Adapted from Ahmed et al [65]. 39
Figure 2.11: Percentage shrinkage versus percentage MMA [98]. Dashed line represents theoretical shrinkage, solid line represents experiment findings. 41

Figure 2.12: A scanning electron micrograph of a typical acrylic bone cement sample, identifying micropores and macropores 42
Figure 2.13: Typical sample of non-vacuum mixed bone cement. Reprinted with permission [45]..... 44
Figure 2.14: Typical sample of vacuumed mixed cement. Reprinted with permission [45]..... 45
Figure 2.15: Strain (left axis) and temperature (right axis) trace versus time for polymerising CMW® 1 bone cement. Adapted from Roques et al [34]. 48
Figure 2.16: A typical plot relating polymerisation fraction and polymerisation temperature with time. Adapted from Lennon et al [107]. 49
Figure 2.17: Circumferential residual stresses (MPa) versus temperature (°C) [33]. Solid line represents non-vacuumed cement. Dashed line represents vacuumed cement. 52
Figure 2.18: Typical change in temperature distribution assumed by Huiskes and De Wijn [109] 53
Figure 2.19: Typical residual stress result by Huiskes and De Wijn [109] 54
Figure 2.20: Schematic of FE model employed by Lennon and Prendergast [32] to compute residual stresses. Image adapted from Lennon and Prendergast [32]. 55
Figure 2.21: No.2 Morse taper mandrel with an acrylic bone cement ring assembled. Reprinted with permission of Orr et al [33]..... 58
Figure 2.22: Typical crack found by Orr et al [33] due to thermal cooling. Reprinted with permission. 59
Figure 2.23: Finite element model employed by Nuno and Amabili [38] and Nuno and Avanzolini [112] to investigate the impact of residual stress on a loaded artificial hip joint (units in mm's). Image adapted from Nuno and Avanzolini [112]. 63
Figure 3.1: 316L stainless steel tube used to represent the femoral prosthesis in the experimental model..... 67
Figure 3.2: E-glass/epoxy cylinders; (Left) Unedited cylinder; (Right) Modified cylinder used to represent the femur in the experimental model 68
Figure 3.3: CAD cross-section isometric view of experimental rig, with the assembly of the representative stem and femur included 70

Figure 3.4: Tee rosette strain gauge before application to the representative stem 73
Figure 3.5: Quarter bridge circuit schematic with dummy strain gauge temperature compensation 73
Figure 3.6: Dummy strain gauge assembly applied the exterior of the representative femur. Note the strain gauge is bonded to the thin detached piece of e-glass/epoxy which in turn is applied to the representative femur with thermal paste. 74
Figure 3.7: Oven and data acquisition system 77
Figure 3.8: CEMVAC® disposable vacuum tube mixing system 78
Figure 3.9: Representative femoral construct at breakdown. Note cement ingress into the representative cancellous bone structure and guide fins at base of cement mantle used to ensure an even cement mantle. 79
Figure 3.10: Representative femoral construct after pressurisation. Note cement extrusion from representative cancellous bone structure and pressuriser on top of cement mantle 80
Figure 3.11: Apparent strain levels for instrumented stem under simulated experimental conditions 82
Figure 3.12: Apparent strain versus temperature for the instrumented femur 83
Figure: 3.13: Scanning electron microscope image of e-glass/epoxy composite taken approximately transverse to the axial direction 85
Figure 3.14: Transient thermal result for polymerising CMW® 1 Gentamicin bone cement over the first 600 seconds (10 minutes). Note thermocouple locations are indicated on CAD solid model image. 86
Figure 3.15: Typical thermal history for polymerising CMW® 1 Gentamicin bone cement over the first 5,400 seconds (1.5 hours). Note thermocouple locations are indicated on CAD solid model image. 88
Figure 3.16: Typical thermal history for polymerising SmartSet® HV Gentamicin bone cement over the first 800 seconds (13.3 minutes). Note thermocouple locations are indicated on CAD solid model image. 89
Figure 3.17: Solid representative stem transient thermal history, taken from experiment number 29. Note thermocouple locations are indicated on top of image. 95

Figure 3.18: Instrumented femur transient strains with associated temperatures over the first 600 seconds (10 minutes). Data taken from experiment number 1 (CMW® 1 Gentamicin, non-vacuumed, non-pressurised).97
Figure 3.19: Typical instrumented femur strain result with associated temperatures over the first 10,800 seconds (3 hours). Data taken from experiment number 1 (CMW® 1 Gentamicin, non-vacuumed, non-pressurised). 98
Figure 3.20: Instrumented stem results with associated temperatures over the first 600 seconds (10 minutes). Data taken from experiment number 1 (CMW® 1 Gentamicin, non-vacuumed, non-pressurised). 99
Figure 3.21: Typical instrumented stem strain result with associated temperatures over the first 10,800 seconds (3 hours). Data taken from experiment number 1 (CMW® 1 Gentamicin, non-vacuumed, non-pressurised). 100
Figure 4.1: Flow chart of model development and the fulfillment of thesis objectives 114
Figure 4.2: Line diagram of SOLID92 element. Adapted from ANSYS [130]. 117
Figure 4.3: 3-D meshed model of Morse taper with cement ring assembled 118
Figure 4.4: Cross sectional view of von Mises stresses (MPa) induced from an assembly temperature of 100°C. Note displacements were magnified by a factor of 10. 121
Figure 4.5: Peak residual stresses versus assembly temperature, predicted by finite element model 121
Figure 4.6: Flow chart of finite element methodology for the quantification of residual stress 124
Figure 4.7: 3-D CAD model of experimental construct 125
Figure 4.8: Geometry of SOLID87 element. Adapted from ANSYS help [130] 125
Figure 4.9: 3-D experimental model after meshing with element SOLID87.....126
Figure 4.10: Bone cement sample within dilatometer 127
Figure 4.11: DSC exotherm result for CMW® 1 Gentamicin from the DSC thermal history of 30°C for the first 90 seconds (until approximately 200s from start of mixing) and 10°C/min for the remainder of the experiment....138

Figure 4.12: Exotherm profile applied to FE model 138
Figure 4.13: FEA transient thermal result over first 600 seconds 143
Figure 4.14: Cross sectional view of finite element result at 327 seconds after initiation of mixing. Units are in degrees Celsius. 144
Figure 4.15: Thermal distribution at 320 seconds, the moment of assumed stress locking; (Top) Solid model thermal distribution; (Bottom) Temperature profile along path 25 mm from the base as indicated on solid model result 146
Figure 4.16: Comparison between experimental result (top) and FEA result (bottom) over the first 3,600 seconds (1 hour) after initiation of mixing 147
Figure 4.17: (Top) Experimental solid model (Q-slice) residual radial stress (MPa) result; (Bottom) Approximate principal stress distribution for path defined on the solid model 149
Figure 4.18: Experimental solid model (Q-slice) residual stress (MPa) distribution in the Z direction (assumed longitudinal stresses) 150
Figure 4.19: Experimental solid model (Q-slice) residual stress (MPa) distribution in the X direction (assumed hoop stresses) 151
Figure 4.20: Experimental solid model (Q-slice) von Mises stress (MPa) distribution 152
Figure 5.1: 3-D CAD solid model of No.2 44 mm Exeter™ V40™ stem prosthesis with a 26 mm diameter head (Left) Elevation view (Middle) End-view (Right) Auxiliary view 160
Figure 5.2: Longitudinally sectioned femoral artificial hip joints in cadaver femora. Adapted from Bishop et al [148] 161
Figure 5.3: 3-D solid model of cement mantle (a) Solid cement mantle before Exeter™ stem volume cut-out (b) Bone cement mantle after Exeter™ volume cut out (c) Auxiliary view of sectioned bone cement mantle 162
Figure 5.4: Standardised Femur obtained from SFP web depository [149] (a) Anterior-posterior view (b) Medial-lateral view 163
Figure 5.5: Standardised femur with femoral head removed 164
Figure 5.6: Assembly of Exeter™ stem with femur (a) Assembly with original standardised femur, note shaft misalignment (b) Assembly with

reduced femur. Note alignment with both shaft centre-lines and head pivot points.....166
Figure 5.7: 3-D CAD anatomical model (a) Sectioned anterior-posterior view (b) Medial-lateral view (c) Auxiliary view 167
Figure 5.8: Anatomical model post meshing (a) Elevation view of meshed anatomical model (b) Elevation view of sectioned anatomical model to reveal internal mesh (c) Auxiliary view of anatomical model....168
Figure 5.9: Young's modulus versus femoral cortical bone density. Adapted from Wirtz et al [152]. 170
Figure 5.10: Comparison of the complex model (a) and most simplified model (b) of the hip musculature developed by Heller et al [84]. Image adapted from Heller et al [84]. 176
Figure 5.11: Posterior-anterior view of anatomical model with loads applied. Note triad at bottom right denoting X, Y, and Z directions; (Left) Complete model with loads applied. Note loads were applied over 2 to 3 nodes; (Right) Nodal view of proximal portion of construct with loads applied 178
Figure 5.12: Anatomical model transient thermal result over first 600 seconds (10 minutes) 179
Figure 5.13: Thermal distribution (°C) at 315 seconds after initiation of bone cement mixing. This thermal distribution represents the moment of peak temperature for the majority of the cement mantle. 180
Figure 5.14: Thermal distribution (°C) at 308 seconds after initiation of cement mixing. This thermal distribution represents the moment of assumed bone cement stress-locking. 181
Figure 5.15: Temperature profile (°C) along the path as indicated on left solid model at the moment of assumed stress-locking.....182
Figure 5.16: Peak bone cement mantle von Mises residual stress distribution (MPa) 183
Figure 5.17: Bone cement mantle residual stress distribution over a stress range of 0 to 14 MPa.....183
Figure 5.18: Bone cement mantle von Mises residual stress (MPa), with regions of the mantle under highest stress indicated by grey.....184

Figure 5.19: Approximate principal residual stresses for the path defined on solid model 185
Figure 5.20: Von Mises stress (MPa) distribution for the artificial hip construct due to the peak physiological load from walking 186
Figure 5.21: Von Mises stress (MPa) distribution for the bone cement mantle due to the peak physiological load from walking 187
Figure 5.22: Bone cement mantle stress percentage volume distribution over a von Mises stress range of 0 to 12 MPa, due to the peak load from walking 188
Figure 5.23: Von Mises stress (MPa) due to peak walking load, with regions of the mantle under highest stress indicated by grey 189
Figure 5.24: Approximate longitudinal, hoop and radial stresses due to the peak load from walking; (Top) Path location and principal stresses along defined path; (Bottom) Magnified view of defined path principal stresses 190
Figure 5.25: Von Mises stress (MPa) for the rehabilitation activity of walking on the artificial hip construct 191
Figure 5.26: Peak bone cement mantle von Mises stress (MPa) for the rehabilitation activity of walking 192
Figure 5.27: Bone cement mantle stress percentage volume distribution over a von Mises stress range of 0 to 14 MPa for the rehabilitation activity of walking 192
Figure 5.28: Bone cement von Mises stress (MPa) for the rehabilitation activity of walking, with regions of the mantle under highest stress indicated by grey 193
Figure 5.29: Bone cement von Mises stresses (MPa) for the rehabilitation activity of walking, with regions of the mantle with a von Mises stress greater than 24 MPa indicated by grey 194
Figure 5.30: Approximate longitudinal, hoop and radial stresses for the rehabilitation activity of walking; (Top) Path location and principal stresses along defined path; (Bottom) Magnified view of principal stresses 195
Figure A.1: The hip joint. Adapted from Tortora and Grabowski [15]. 229
Figure A.2: Pelvic girdle and femur. Adapted from Hall [166]. 230

Figure A.3: Anatomy of the femur. Adapted from Seeley et al [1].....231
Figure B.1: Directional terminology with respect to a left femur with an artificial hip implanted.....232
Figure B.2: Directional terminology with respect to a left femur with an artificial hip implanted.....233
Figure C.1: Schematic of Wheatstone bridge circuit.....235
Figure D.1: Graphical user interface of adapted Labview programme used for the acquisition and logging of thermocouple and strain gauge data.....237
Figure D.2: Temperature measurement subroutine.....238
Figure D.3: Strain gauge measurement subroutine.....238
Figure D.4: Temperature measurement subroutine code.....239
Figure D.5: Strain gauge measurement subroutine code.....240
Figure E.1: Thermal history for polymerising CMW® 1 Gentamicin bone cement over the first 1.5 hours. Data taken from experiment number 3 (CMW® 1 Gentamicin, non-vacuumed, non-pressurised).....241
Figure E.2: Thermal history for polymerising CMW® 1 Gentamicin bone cement over the first 1.5 hours. Data taken from experiment number 19 (CMW® 1 Gentamicin, non-vacuumed, pressurised).....242
Figure E.3: Thermal history for polymerising CMW® 1 Gentamicin bone cement over the first 1.5 hours. Data taken from experiment number 20 (CMW® 1 Gentamicin, non-vacuumed, pressurised).....242
Figure E.4: Thermal history for polymerising CMW® 1 Gentamicin bone cement over the first 1.5 hours. Data taken from experiment number 22 (CMW® 1 Gentamicin, vacuumed, non-pressurised).....243
Figure E.5: Thermal history for polymerising CMW® 1 Gentamicin bone cement over the first 1.5 hours. Data taken from experiment number 27 (CMW® 1 Gentamicin, vacuumed, pressurised).....243
Figure F.1: Thermal history for polymerising SmartSet® Gentamicin bone cement over the first 800 seconds. Data taken from experiment number 7 (SmartSet® Gentamicin, non-vacuumed, non-pressurised).....244
Figure F.2: Thermal history for polymerising SmartSet® Gentamicin bone cement over the first 800 seconds. Data taken from experiment

number 8 (SmartSet® Gentamicin, non-vacuumed, non-pressurised). 245
Figure F.3: Thermal history for polymerising SmartSet® Gentamicin bone cement over the first 800 seconds. Data taken from experiment number 10 (SmartSet® Gentamicin, non-vacuumed, non-pressurised). 245
Figure G.1: Instrumented femur strain result with associated temperatures over the first 10,800 seconds (3 hours). Data taken from experiment number 1 (CMW® 1 Gentamicin, non-vacuumed, non-pressurised). 246
Figure G.2: Instrumented femur strain result with associated temperatures over the first 10,800 seconds (3 hours). Data taken from experiment number 3 (CMW® 1 Gentamicin, non-vacuumed, non-pressurised). 247
Figure G.3: Instrumented femur strain result with associated temperatures over the first 10,800 seconds (3 hours). Data taken from experiment number 15 (CMW® 1 Gentamicin, non-vacuumed, pressurised). ..247
Figure G.4: Instrumented femur strain result with associated temperatures over the first 10,800 seconds (3 hours). Data taken from experiment number 23 (CMW® 1 Gentamicin, vacuumed, non-pressurised). ..248
Figure H.1: Instrumented stem strain result with associated temperatures over the first 10,800 seconds (3 hours). Data taken from experiment number 1 (CMW® 1 Gentamicin, non-vacuumed, non-pressurised).....249
Figure H.2: Instrumented stem strain result with associated temperatures over the first 10,800 seconds (3 hours). Data taken from experiment number 3 (CMW® 1 Gentamicin, non-vacuumed, non-pressurised).....250
Figure H.3: Instrumented stem strain result with associated temperatures over the first 10,800 seconds (3 hours). Data taken from experiment number 15 (CMW® 1 Gentamicin, non-vacuumed, pressurised).....250
Figure H.5: Instrumented stem strain result with associated temperatures over the first 10,800 seconds (3 hours). Data taken from experiment number 26 (CMW® 1 Gentamicin, vacuumed, pressurised). 251
Figure I.1: Compound cylinder 252
Figure I.2: Graphical description of interference 254

Figure I.3: Von Mises, hoop and radial stress distributions within Morse taper and bone cement ring, based on cement assembly temperature of 100 °C 259
Figure I.4: Residual stresses versus peak cement temperature, calculated by theoretical model 260
Figure K.1: (Left) Elevation view of meshed Exeter™ stem; (Middle) Elevation view of sectioned Exeter™ stem to reveal internal mesh; (Right) Auxiliary view of meshed Exeter™ stem 263
Figure K.2: (Left) Elevation view of meshed cement mantle; (Middle) Elevation view of sectioned cement mantle to reveal internal mesh; (Right) Auxiliary view of meshed bone cement mantle 264
Figure K.3: (Left) Elevation view of meshed femur; (Middle) Elevation view of sectioned femur to reveal internal mesh; (Right) Auxiliary view of meshed femur 265
Figure L.1: Anatomical model principal residual stresses for path defined 266
Figure L.2: Principal stresses due to the peak load from walking for path defined on solid model 267
Figure L.3: Principal stresses for the rehabilitation scenario for the path defined on solid model 267
Figure M.1: CMW® 1 Gentamicin residual stress relaxation over 5.1 days. Data taken from a vacuum mixed non-pressurised experiment 268

List of Tables

Table 1.1: Ten of the most popular cemented stems used in England and Wales in 2004 [4] 4
Table 1.2: Most popular bone cement brands used in Australia from September 1999 until December 2003 for a femoral primary hip replacement [5] 6
Table 1.3: Pre-operative motivations for cemented primary THA [4] 7
Table 1.4: Indications for revision surgery according to the NJR for England and Wales [4]. More than one indication may be selected for a single procedure 12
Table 2.1: Summary of Yang et al [59, 60] DSC experimental results 25
Table 2.2: Relationship between cement mixing systems and resultant mean porosity ($\bar{x}$) with standard deviation (σ) 31
Table 2.3: Mean uniaxial static compressive properties of bone cement, as cited by Lewis [48] 32
Table 2.4: Uniaxial static tensile properties of popular bone cement brands 33
Table 2.5: Palacos® R flexural modulus and Poisson's ratio with respect to bone cement vacuum level [33] 34
Table 2.6: Tension-tension (2 Hz, 0.3-22 MPa) fatigue results for non-vacuum mixed commercial bone cements [47] 35
Table 2.7: Summary of bone cement shrinkage data from published literature ..43
Table 2.8: Relationship between vacuum level and mean shrinkage based on Palacos® R bone cement [33] 44
Table 2.9: Calculated residual hoop stresses based on Equation 2.2, developed by Stachiewicz et al [106] 50
Table 2.10: Summary of residual stress studies in the published literature 62
Table 3.1: Summary of experiments performed 85
Table 3.2: CMW® 1 Gentamicin thermal results for non-vacuum mixed, non-pressurised experiments 89
Table 3.3: SmartSet® HV Gentamicin thermal results for non-vacuum mixed, non-pressurised experiments 90

Table 3.4: CMW® 1 Gentamicin thermal results for non-vacuum mixed, pressurised experiments 91
Table 3.5: CMW® 1 Gentamicin thermal results for vacuum-mixed, non-pressurised experiments 92
Table 3.6: CMW® 1 Gentamicin thermal results for vacuum-mixed, pressurised experiments 93
Table 3.7: Thermal results for solid representative stem experiments 94
Table 3.8: Summary of mean experimental thermal results 96
Table 3.9: CMW® 1 Gentamicin residual strain results for non-vacuumed, non-pressurised experiments 100
Table 3.10: SmartSet® HV Gentamicin residual strain results for non-vacuumed, non-pressurised experiments 101
Table 3.11: CMW® 1 Gentamicin residual strain results for non-vacuumed, pressurised experiments 102
Table 3.12: CMW® 1 Gentamicin residual strain results for vacuum-mixed, non-pressurised experiments 103
Table 3.13: CMW® 1 Gentamicin residual strain results for vacuum mixed, pressurised experiments 103
Table 3.14: Residual strain results for solid stem experiments (CMW® 1 Gentamicin, non-vacuumed, non-pressurised) 104
Table 3.15: Residual strain results for debonded interface experiments 105
Table 3.16: Summary of mean residual strain results 106
Table 4.1: Material properties assumed for Morse taper and bone cement ring 119
Table 4.2: Comparison between finite element model results and mathematical model results 122
Table 4.3: Dilatometer experimental results for CMW® 1 Gentamicin bone cement 128
Table 4.4: Dilatometer experimental results for SmartSet® HV Gentamicin bone cement 129
Table 4.5: Dilatometer experimental results for e-glass/epoxy in the longitudinal direction 130
Table 4.6: 316L stainless steel tube mechanical and thermal properties 131
Table 4.7: Bone cement assumed mechanical and thermal properties 132
Table 4.8: E-glass/epoxy assumed mechanical and thermal properties 132

Table 4.9: Differential scanning calorimetry programmed thermal profiles and the measured exotherm results based on CMW® 1 Gentamicin bone cement....136
Table 4.10: Comparison of peak temperatures attained and time of occurrence between mean experimental results (all CMW® 1 Gentamicin experiments performed with instrumented stem) and FEA results.145
Table 4.11: Comparison between mean experimental temperatures and FEA result, both at 7 seconds before the attainment of peak temperature 145
Table 4.12: Comparison between mean experimental (all experiments performed with the instrumented stem that were non-pressurised) residual strain results versus the residual strains calculated by the finite element model 148
Table 5.1: Mechanical and thermal properties applied to Exeter™ prosthesis...168
Table 5.2: Mechanical and thermal properties applied to bone cement mantle.169
Table 5.3: Summary of femur mechanical properties as reported by Couteau et al [156] and Taylor et al [155] 170
Table 5.4: Mechanical and thermal properties assumed for the femoral bone ..171
Table 5.5: Forces applied to the anatomical finite element model, representative of peak load from walking 177
Table B.1: Definitions of anatomical directional terms....233
Table M.1: Measured residual strain levels for the representative femur in the axial direction....269
Table M.2: Measured residual strain levels for the representative stem in the axial direction....270
Table M.3: Measured residual strain levels for the representative stem in the hoop direction....270

Abbreviations

2-D	Two dimensional
3-D	Three dimensional
CAD	Computer aided design
CT	Computer tomography
DSC	Differential scanning calorimetry
FEA	Finite element analysis
GF	Gauge factor
HGEN	Heat generation
MMA	Methyl methacrylate
MRI	Magnetic resonance imaging
NJR	National joint registry
PMMA	Polymethyl methacrylate
SEM	Scanning electron microscope
SF	Standardised femur
SFP	Standardised femur project
STC	Self temperature compensation
Std. Dev	Standard deviation
THA	Total hip arthroplasty
THR	Total hip replacement
UHMWPE	Ultra-high-molecular-weight-polyethylene

Nomenclature

Symbol	Definition	Unit
h	Coefficient of thermal convection	$W/m^{2o}C$
l_o	Original length	m
r	Radius	m
r_i	Inner radius of Morse taper	m
r_m	Radius of mating surfaces	m
r_o	Outer radius of bone cement ring	m
v_m	Volume fraction of polymerising monomer	-
A	Area	m^2
D_o	Outer diameter	m
D_i	Inner diameter	m
E	Young's modulus	Pa
L	Length	m
P	Degree of polymerisation	%
Q	Heat generated per unit volume of acrylic cement	J/m^3
Q_t	Heat generated per unit mass of monomer	J/kg
Q_{totat}	Total amount of heat liberated	J
R	Electrical resistance	Ω
S	Percent volumetric shrinkage	%
S_p	Instantaneous amount of heat generated by the bone cement during its polymerisation	J
T	Temperature	°C
T_f	Final temperature	°C
T_i	Initial temperature	°C
V	Voltage	V
α	Linear coefficient of thermal expansion	$°C^{-1}$
β	Degree of polymerisation	%
δ	Radial interference	m
δl	Change in length	m
ε	Strain	-

ρ	Resistivity	Ωm
ρ_m	Density of monomer	kg/m^3
σ_r	Radial stress	Pa
σ_θ	Hoop/circumferential stress	Pa
ν	Poisson's ratio	-
Δ	Radial interference	m

An Experimental and Computational Investigation of Bone Cement Residual Stresses

By

John Allen Hingston

Abstract

Hip arthroplasty is a common orthopaedic procedure with considerable success in alleviating hip joint pain and disability. To transfer loads from the prosthesis to the contiguous bone, self-curing polymethyl methacrylate, often referred to as *bone cement*, is routinely used. Residual stresses due to shrinkage of the bone cement during and after polymerisation have been implicated in the formation of cement mantle cracks before any functional loading.

Contemporary cemented hip arthroplasties involve mixing the bone cement under vacuum and applying bone cement pressurisation *in situ*. However vacuum-mixed bone cement has been linked with increased cement shrinkage and theoretically linked with greater residual stress. In this thesis, experimental work was performed to investigate the effect of vacuum mixing and pressurisation with respect to bone cement residual stress. Also, two commercial brands of bone cement were compared against each other. Results revealed that vacuum mixing did not appreciably alter the residual stress levels compared with cement mixed under atmospheric conditions. Likewise, negligible residual stress difference was measured between CMW® 1 Gentamicin and SmartSet® HV Gentamicin bone cements. However, pressurisation of the curing bone cement mass had a significant effect on the residual stress magnitudes.

Finite element analysis was implemented to quantify the bone cement residual stresses for the experimental construct. Differential scanning calorimetry and dilatometry experimentation was performed to quantify the bone cement's exotherm and linear coefficient of thermal expansion properties respectively. Both the transient thermal and residual stress predictions were directly comparable with the experimental measurements. Utilising the same finite element methodology, the transient thermal and residual stresses were predicted for a representative *in vivo* scenario. The representative *in vivo* stresses for the rehabilitation activity of walking was also predicted. Predictions revealed the residual stresses were significant and should be included to establish the cement mantle stress magnitude and distribution for the early portion of the artificial hip replacement lifetime.

Chapter 1

Introduction

Joint disorders are common, affecting approximately 10% of the world's population [1]. They are a leading cause of pain and disability, second only to heart disease [2]. The hip joint is the joint most commonly affected by injury or disease and where loss of functionality causes the severest handicap [3]. An increasing number of people require and receive hip arthroplasty to relieve hip joint pain and loss of mobility [4, 5].

Hip arthroplasty is a common orthopaedic procedure with considerable success in alleviating pain and disability. It has been estimated that approximately one million Total Hip Arthroplasty (THA) procedures are performed each year in developed countries [6]. For cemented THA, polymethyl methacrylate (PMMA) is used to mechanically lock the prosthesis to the contiguous bone. Polymethyl methacrylate is often referred to as *acrylic bone cement* or *bone cement*. According to the National Joint Registry (NJR) for England and Wales in the 2004 annual report, 77% of femoral procedures utilised bone cement, while 56% of acetabular procedures utilised bone cement [4]. Hip anatomy terminology is described in Appendix A. The outcome of these operations in the majority of cases are successful, offering significant relief from pain and improved mobility. According to the NJR for England and Wales in the 2004 annual report, only 3.5% of patients were unsatisfied with their hip replacement [4].

The longevity or lifespan of the replacement is of concern. Due to the success of cemented hip replacements, it is increasingly performed on younger individuals [5]. This combined with an ageing population has resulted in an increase in the number of revision operations. Revision surgery is associated with increased morbidity and mortality and has a far less successful outcome than primary hip replacement. Thus increasing the longevity of the primary hip replacement is highly beneficial.

1.1 Total Hip Arthroplasty

A number of hip arthroplasty procedures exist. The most popular is the cemented THA [4]. Cemented THA involves the surgical removal of the damaged hip joint, both the femoral head and the acetabulum, and the replacement with an artificial device to replicate the original hip function. Bone cement is utilised to mechanically lock the prosthesis to the contiguous bone.

An uncemented THA is similar to a cemented THA, but the prosthesis is held in place without the use of bone cement. Two popular ways to achieve fixation are by mechanical fixation or biological fixation. Mechanical fixation may involve the use of screws, bolts, nuts, wires and/or an interference fit. Biological fixation involves the growth of the contiguous bone onto or into the biocompatible porous surface of the prosthesis.

A hybrid THA involves a cemented femoral prosthesis and an uncemented acetabular prosthesis. For a reverse hybrid, the acetabular prosthesis is cemented while the femoral prosthesis is uncemented. Finally a partial hip arthroplasty involves the replacement of either the femoral or acetabulur part of the hip joint with a prosthesis.

1.1.1 Historical Perspective

The first recorded THA technique was recorded by Mr. Tomas Gluck from Germany in the early 1890's [7]. Mr. Gluck recommended the ball and socket be

made from ivory and that the replacement be fixed to the skeleton via nickel-plated steel screws [3]. Over the years a large number of improvements were made, including the first metallic Total Hip Replacement (THR) in 1938 by Dr. Philip Wiles (Middlesex, UK) and the first use of acrylic bone cement for the fixation of prosthesis in 1951 by Dr. Haboush (New York, USA). By the mid 1950's a large number of different prosthesis were commercially available.

In 1958 Sir John Charnley (England) used a low friction combination of polytetrafluorethylene (PTFE) for the acetabular socket and stainless steel for the femoral stem. This was the first THR prosthesis to use different materials for the acetabular socket and femoral stem. Charnley further improved the THR design by using high-density polyethylene (HDPE), a more wear resistant plastic, for the acetabular socket. This THR design combined low friction with high wear resistance and significantly increased the longevity of the implant. Charnley further increased the longevity of a THR in 1960 by introducing significant amounts of acrylic bone cement to mechanically lock the prosthesis to the contiguous bone [3]. Over 4 decades later this is still considered to be the standard method for a primary THA.

Present day femoral prostheses are made from a number of materials, primarily 316L stainless steel, cobalt-chromium molybdenum alloy or titanium alloy (Ti-6Al-4V) [7]. For the acetabular cup ultra-high-molecular-weight-polyethylene (UHMWPE) is used over high density polyethylene due to its superior properties. Figure 1.1 illustrates a typical cemented THR.

1.1.2 Femoral Prosthesis

The main design objective of a total hip prosthesis is to restore normal joint functionality in a pain free manner while maximising the implant longevity. A large number of hip prosthesis designs exist on the market. For example, in 2004 101 different brands of femoral stems were utilised in England and Wales alone [4]. Despite the large number of hip prostheses on the market, a small number of brands dominate. Table 1.1 outlines 10 of the most popular cemented stems used in 2004 for England and Wales.

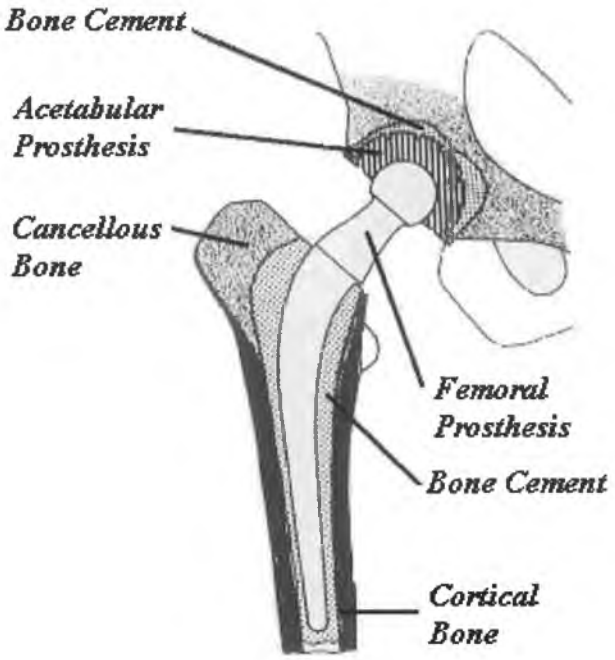

Figure 1.1: Schematic of a cemented artificial hip replacement. Adapted from Huiskes [8].

Implant Brand (Manufacturer)	Percentage Of Market	Quantity
Exeter (Stryker Howmedica Osteonics)	44.9	13,808
Charnley (DePuy)	17.1	5,248
C Stem (DePuy)	9.2	2,826
CPT (Zimmer)	6.5	2,000
Stanmore (Biomet)	4.0	1,232
Elite Plus (DePuy)	2.8	866
Furlong Modular (Joint Replacement Instrumentation Ltd)	2.1	633
SPII (Waldemar Link)	1.9	580
Omnifit Cemented (Stryker Howmedica Osteonics)	1.7	533
Muller Modular (Centerpulse)	1.6	489

Table 1.1: Ten of the most popular cemented stems used in England and Wales in 2004 [4]

Figure 1.2 illustrates some of the more popular femoral stems utilised.

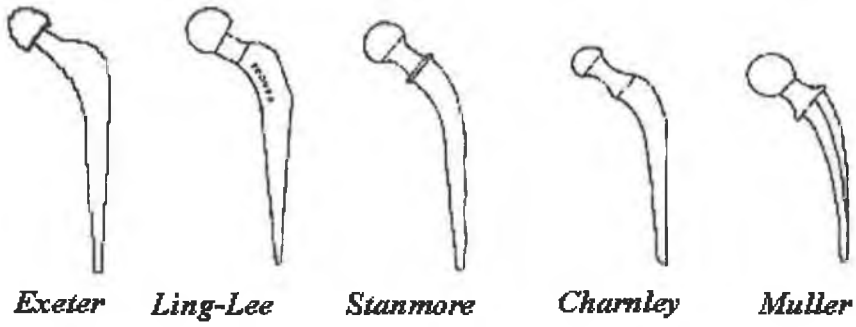

Figure 1.2: Line diagrams of popular stems. Adapted from Brockhurst and Svensson [9].

1.1.3 Polymethyl Methacrylate

In the early 1890's, Thomas Gluck first conceived the idea of using an adhesive to anchor a prosthesis *in situ* [3]. Mr. Gluck tried to create an adhesive composed of colophony, pumice power and plaster, but was unsuccessful. Dr. Hasboush in 1951 became the first person to use acrylic bone cement for a hip arthroplasty. However, considering it to be an adhesive, Dr. Hasboush used small amounts. This arthroplasty methodology proved unsuccessful. Sir John Charnley realised in the late 1950's that bone cement did not have sufficient adhesive characteristics for a hip arthroplasty. Mr. Charnley applied ample amounts of bone cement to the artificial replacement, utilising it as a grout to mechanically lock the artificial prosthesis to the contiguous bone. Over 4 decades later, bone cement remains the only material used for the mechanical anchoring of the prosthesis to the contiguous bone.

Cemented THA is one of the most frequently performed orthopaedic procedures in the world [10]. Commercially, there exist approximately 70 different brands of acrylic bone cements. However, they are all derived from the same chemical substance, methyl methacrylate (MMA). Some bone cements also contain antibiotics to reduce infection risks. For England and Wales in 2004, antibiotic loaded bone cements accounted for 85.4% of all cemented hip procedures, with a

further 3.7% of procedures using a mixture of antibiotic loaded and non-antibiotic loaded bone cements. Some bone cements contain radiopacifiers to achieve x-ray opacity. Some cements are designed to have a low viscosity, while others are designed to have a high viscosity. The cements viscosity affects the mixing behaviour, the cements penetration into the cancellous bone structure, the cements resistance to bleeding and the ease of implant insertion [11].

Despite the large number of cement brands, a relatively small number dominate the market. Table 1.2 outlines the more popular bone cement brands used in Australia from September 1999 until December 2003.

Cement Brand	Percentage Of Market	Number
Simplex®-P	33.1	10,441
Antibiotic Simplex®	19.5	6,139
Simplex® Tobra	11.4	3,609
Palacos® R	8.5	2,675
CMW® 1	8.1	2,558
CMW® 1 Antibiotic	4.7	1,497
Palacos® E	3.6	1,120
CMW® 3 Antibiotic	2.4	755
Other	5.4	2,738

Table 1.2: Most popular bone cement brands used in Australia from September 1999 until December 2003 for a femoral primary hip replacement [5]

1.2 Pre-operative Motivation

Table 1.3 outlines the principal diagnosis for a cemented primary total hip replacement, based on the 2004 NJR for England and Wales [4]. From Table 1.3 it is evident that osteoarthritis is the principal motivation for a cemented THA. There are more than 100 different types of arthritis [1]. In Ireland, arthritis affects approximately half a million people or 13% of the population [12].

Preoperative Motivation	Percentage	Number
Osteoarthritis	94.0	22,548
Avascular necrosis	3.2	774
Fractured neck of femur	1.4	344
Rheumatoid arthritis	1.0	243
Failed internal fixation	0.8	190
Dysplasia of the hip	0.8	181
Other	2.5	613

Table 1.3: Pre-operative motivations for cemented primary THA [4]

1.2.1 Osteoarthritis

Osteoarthritis (sometimes called degenerative joint disease) is the most common form of arthritis, affecting 10% of the United States population [1]. Of those affected, 85% are over 70 years old. Osteoarthritis is a progressive joint disorder where the articular cartilage of the joint slowly degenerates. This degeneration causes an increase in the coefficient of friction between the two articulating surfaces. When this happens the individual may experience pain, stiffness, swelling and functional disability. In severe cases, most of the articular cartilage is worn away and bone articulates on bone. Contributing factors towards the development of osteoarthritis appear to include long-term strenuous physical activity, obesity, heredity or genetic factors and increasing age. THA is performed in severe cases to alleviate pain and increase functionality.

1.2.2 Avascular Necrosis

Avascular necrosis is a disease that can result from temporary or permanent loss of blood supply to the bones [13]. Without blood the bone structure weakens and eventually dies. Over time the bone may fail structurally. Avascular necrosis has been linked to excessive alcohol use, long-term cortisone usage and trauma [14]. Avascular necrosis primarily affects adults between 30 and 50 years old. With respect to the hip joint, without treatment, most clinically diagnosed cases of

avascular necrosis lead to collapse of the femoral head. THA is the treatment with the highest likelihood of providing symptom free relief and good functional outcome. However the longevity of the THR is of concern, as this disease affects relatively young active patients.

1.2.3 Rheumatoid Arthritis

Rheumatoid arthritis is the second most common form of arthritis [1]. It affects approximately 3% of all women and 1% of all men in the United States. Rheumatoid arthritis is an autoimmune disorder in which the immune system attacks healthy tissue, most notably cartilage and joint linings [15]. The result is a joint that is stiff, inflamed and deformed. The joint is also often warm, swollen and painful. In common with osteoarthritis, THA is performed to alleviate pain and increase functionality in severe cases.

1.3 Operative Procedure

A number of THA surgical procedures exist. The more popular methods include the *lateral approach*, the *Smith-Peterson anterior approach* and the *Harding anterior approach* [16]. Appendix B contains explanations of anatomical directional terminology.

For the lateral approach procedure, the patient is laid on his/her side with the hip to be operated upon being uppermost [7]. To expose the hip, an incision towards the posterior is made. The joint is dislocated and the femoral neck is sectioned. The position and angle of the section is not critical. The acetabulum is deepened medially, often with the aid of power tools by drilling and wearing/grinding the socket. Cancellous bone is exposed wherever possible. Finally, reaming is performed. The size of the prepared socket may be checked from time to time with a trial cup. Once the socket is the desired size, cleaning is performed. Any bone marrow or bone debris within the cancellous bone is removed. This may be achieved by applying high pressure solution with brushings [17]. Once cleaned,

the socket may be packed with a cloth soaked with an agent to reduce bleeding e.g. neosynephrine or hydrogen peroxide. When ready, the acrylic bone cement is placed into the socket and pressure applied. Pressurisation may be achieved with the aid of a pressurisation device. Pressure is applied to extrude the viscous cement into the cancellous bone structure and to reduce blood contamination of the cement mantle. After a short period of time, the prosthesis cup is added to the system and embedded into the cement. Once in place and stable, the cement is given time to set.

After the acetabular cement mantle has hardened, the femur is prepared. By using a broach and curette, space at the upper medullary cavity is created for the lateral part of the stem [7]. The medullary canal is then reamed with a number of femoral taper reamers, (Figure 1.3) to create space and the desired shape for the stem and cement mantle. Cancellous bone is exposed where possible. A test prosthesis may be used from time to time to check if the modified medullary cavity is large enough for the prosthesis and the cement mantle.

Figure 1.3: Femoral taper reamer

Modern cementing techniques employ bone cement pressurisation [17, 18]. For this technique, after the medullary cavity has been reamed to the correct size an

intramedullary plug (sometimes called an *intramedullary cement restrictor*) is placed at the distal end of the medullary cavity [17]. The intramedullary plug is applied to prevent cement distal movement during cement pressurisation. The intramedullary plug is placed such that approximately 2 to 3 cm clearance exists between the plug and the most distal tip of the stem. After the intramedullary plug has been applied, the medullary canal is cleaned with pulsatile lavage and brushed to remove debris, bone marrow, blood etc. Similar to that of the acetabular socket, once cleaned, the canal may be packed with an agent to reduce bleeding. After the bone cement has been prepared, the bone cement is injected into the medullary cavity in a retrograde fashion with a cement gun until the canal has been filled with cement. Once complete, the bone cement may be pressurised. Cement pressurisation is associated with reduced blood contamination of the cement mantle due to reduced medullary canal bleeding [19, 20] and an improved cement-bone mechanical lock due to greater cement interdigitation into the cancellous bone structure [21-24]. Cement pressurisation may be implemented manually or by a mechanical device called a pressuriser, (Figure 1.4).

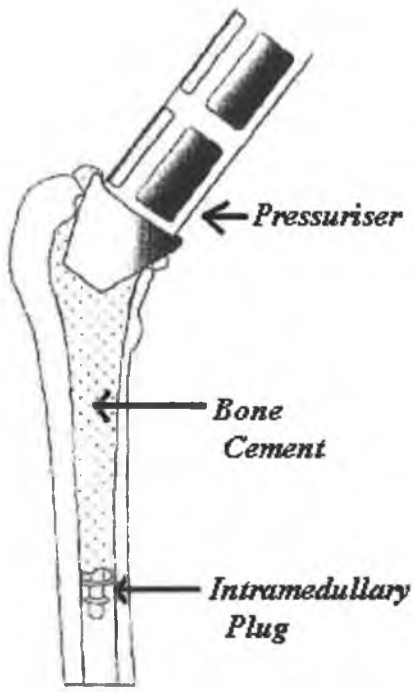

Figure 1.4: Cement pressurisation. Adapted from Colwell and Ritter [17].

After pressurisation, a centraliser may be fitted to the distal end of the stem prosthesis and the stem-centraliser assembly forced down into the cement filled medullary canal. The stem centraliser is utilised to ensure the distal end of the stem is centred, thus creating an even cement mantle. Cement mantle pressure is maintained by the physical insertion of the stem. A proximal seal may be utilised during stem insertion to help maintain cement pressure. After the stem has been inserted and is in its final position, finger packing is normally performed to ensure adequate fill of cement proximally about the stem and to maintain cement pressure as the cement polymerises.

Once hardened, both articulating surfaces of the stem and socket are inspected for debris and cleaned if necessary [7]. If not removed, any debris may accelerate the wear of the articulating surfaces considerably. A specialised tool is often used to ensure neither articulating surfaces becomes scratched or contaminated while being fitted together. Finally, any remaining debris is removed and the incision is stitched up. Typically the patient begins rehabilitation 1 to 2 days after the surgery [25, 26]. This normally involves teaching the patient to walk, climb stairs with the aid of a walker or crutches, get into and out-of bed, and to perform exercises to improve the range of motion and strength of the hip joint. If the patient shows no sign of infection and is in good health, the patient is normally discharged approximately 4 to 6 days post surgery.

1.4 Arthroplasty Failure

The outcome of hip arthroplasty in the majority of cases is satisfactory, offering significant relief from pain and improved mobility for the patient. This usually results in a return to normal activities for the patient. However some failures do occur. According to the NJR for England and Wales, of the 48,987 recorded hip arthroplasties performed in 2004, 9.2% (4,516) were revision surgeries [4]. Unfortunately revision surgery is more complicated. Revision surgery is associated with greater morbidity and mortality. It also has a far less successful outcome when compared to primary THR. Table 1.4 summarises the preoperative motivation for a revision surgery.

Revision Surgery Motivation	Percentage (%)
Aseptic loosening	78.8
Lysis	24.6
Pain	16.1
Dislocation/subluxation	12.6
Periprosthetic fracture	7.0
Infection	6.9
Malalignment	6.0
Other	23.6

Table 1.4: Indications for revision surgery according to the NJR for England and Wales [4]. More than one indication may be selected for a single procedure.

1.4.1 Aseptic Loosening

As is evident from Table 1.4, aseptic loosening is the primary reason for revision surgery. Aseptic loosening is the occurrence of loosening with respect to the mechanical bond between the bone and the implant by a cause other than infection [8]. Typically the patient feels pain on load bearing activities. There are a large number of hypotheses to explain aseptic loosening. However the most popular hypothesis is the *accumulated damage scenario,* sometimes called *fatigue failure scenario* [27-29].

Accumulated Damage Scenario

A typical patient with an artificial hip joint performs 1.1 million hip joint cycles (loading-unloading cycles) per year [30]. According to the accumulated damage scenario, complete cracks are formed across the cement mantle as a result of fatigue. The complete cracks eventually degenerate the mechanical bond between the bone cement and the contiguous bone resulting in relative motion between the cement mantle and the bone [31]. This relative motion causes an inflammatory reaction, depositing fibrous tissue between the cement and bone

over time. Slowly the contiguous bone about the implant becomes absorbed leading to aseptic loosening and the eventual failure of the hip replacement.

Residual Stress And Accumulated Damage Scenario

It has been hypothesised in the literature that residual stresses resultant from the bone cement polymerisation process may play two roles to exacerbate the accumulated damage scenario. Firstly, it has been hypothesised by numerous authors [29, 32, 33] that the residual stresses in the bone cement, coupled with stress concentrators such as pores, voids or contaminants, may create microcracks in the bone cement mantle before any functional loading of the artificial hip joint. Laboratory work and post-mortem evidence provide support for this hypothesis [29, 32-36]. From fatigue theory, the initial inclusion of microcracks significantly reduces the fatigue lifetime of the material, compared to the same material without initial microcracks [37].

Secondly, it has been hypothesised that after polymerisation, a tensile residual stress exists at the cement-bone interface, due to shrinkage of the cement mantle during polymerisation [32]. This tensile residual stress on the bond between the bone cement mantle and the contiguous bone may accelerate the debonding of the cement-bone interface, which in turn leads to relative motion between the bone cement mantle and the contiguous bone and eventual replacement failure. Numerous sources in the literature provide evidence of bone cement shrinkage due to polymerisation [34, 38-41].

1.5 Research Objectives And Methodologies

Objective No. 1

Acrylic bone cement has not changed substantially since it was first introduced over 45 years ago [42]. However the method of mixing and delivering the cement has evolved greatly. Modern cementing techniques mix the bone cement under the application of vacuum to improve the cements mechanical properties.

However, vacuum mixing bone cement has been linked with increased cement shrinkage [33]. From this observation, Orr *et al* [33] hypothesised that vacuum mixed bone cement may produce greater residual stress levels compared with non-vacuum mixed bone cement. From a search of the published literature, no experimental work has previously been performed to investigate this hypothesis put forward by Orr *et al* [33].

The first objective of this research is to experimentally investigate if vacuum mixing bone cement increases residual stresses, as hypothesised by Orr *et al* [33]. This objective was approached by comparing the residual strain levels developed between cement mantles prepared under atmospheric conditions and cement mantles prepared under vacuum conditions, based on a representative artificial femoral construct. The representative artificial femoral construct consisted of a stainless steel cylinder representative of a stem and an e-glass/epoxy composite cylinder representative of a femur. Between these cylinders bone cement was applied and allowed to polymerise. Strain gauges were applied to the representative stem and femur to measure the transient residual strains during and after bone cement polymerisation. Thermocouples were applied to the representative stem, cement mantle and femur, to measure the transient temperatures during and after bone cement polymerisation.

Objective No. 2

As mentioned in Section 1.3, modern cementing techniques employ cement pressurisation to reduce medullary canal bleeding [19, 20] and to increase the strength of the cement-bone mechanical lock by greater cement interdigitation into the cancellous bone structure [21-24].

The hypothesis is proposed in this thesis that pressurisation of the bone cement mantle during polymerisation would have an effect on the residual stress levels. The second objective of this research is to investigate this hypothesis. From a search of the published literature, neither the proposed hypothesis has been previously documented nor any investigation related to the proposed hypothesis.

The second objective was approached by experimentally comparing the residual strain levels developed between cement mantles that were pressurised against cement mantles that were not pressurised, based on the same instrumented representative femoral construct employed to investigate the effects of vacuum mixing (Objective No. 1).

Objective No. 3

As mentioned in Section 1.1.3, approximately 70 different brands of acrylic bone cement exist on the commercial market [10]. During bone cement polymerisation, a significant amount of thermal energy is released. It has been established that significant differences exist in transient temperature profiles [43-46] and mechanical properties [47, 48] between different bone cement brands.

The hypothesis is proposed in this thesis that different brands of bone cement may produce significantly different residual stress levels as a consequence of the different exotherms and/or mechanical properties between bone cement brands. The third objective of this research is to investigate this hypothesis. From a search of the published literature, neither the proposed hypothesis has been previously documented, nor any investigation related to the proposed hypothesis been previously performed.

The third objective was approached by experimentally comparing the residual strain levels developed between two commercially available brands of bone cement with previously established different polymerisation rates. In line with the first and second objective, this investigation was performed on the instrumented representative femoral construct, as described in Objective No. 1.

Objective No. 4

The instrumented representative femoral construct employed to realise objectives one, two and three, measured the residual strains induced in the representative stem and representative femur. The fourth objective of this research is to predict

the bone cement mantle residual stresses for the instrumented representative femoral construct.

To implement this objective, finite element methods were employed. Differential scanning calorimetry and dilatometry experimentation was performed to quantify the bone cements exotherm and linear coefficient of thermal expansion respectively. Results from the finite element model were compared with the experimental results to validate the finite element methodology and model.

Objective No. 5

The residual stresses calculated for the instrumented representative femoral construct will not be the same as the residual stresses *in vivo,* due to different geometries, material properties and initial conditions. From a search of the published literature, all previous residual stress investigations, both experimental and theoretical, have been based on concentric cylinders or models representative of *in vitro* work. Thus, no research has previously been performed that attempted to quantify the residual stresses *in vivo* based on a 3-D finite element model of the anatomical construct.

The fifth objective of this research is to predict the residual stresses for the *in vivo* scenario based on a 3-D finite element model of the anatomical construct. The 3-D anatomical model was developed about on the Exeter™ V40™ 44 mm No. 2 femoral prosthesis by Stryker®-Howmedica-Osteonics (Stryker Corporation, Kalamazoo, MI, USA). The same finite element methodology utilised to model the instrumented representative femoral construct was applied to the 3-D anatomical model.

Objective No. 6

As mentioned previously (Section 1.3), the patient typically begins rehabilitation 1 to 2 days after arthroplasty [25, 26]. A typical rehabilitation activity is teaching the patient to walk with their new artificial hip. The residual stresses from bone cement polymerisation reduce over time due to the viscoelastic nature of bone

cement [8, 34, 41]. However relatively recent research by Roques [41] has reported that the stress relieving mechanisms from residual stresses take place at a relatively slow rate. From this result, Roques [41] postulated that when the artificial hip is loaded for the first time by the patient, the residual stresses would be only partially relieved. As a consequence, Roques [41] recommended that residual stresses be included in the calculation of artificial hip construct stresses, for the early portion of the replacement lifetime. From a search of the published literature, no such research has previously been performed.

The sixth and final objective of this research is to predict the artificial femoral construct stresses for the early portion of the implant lifetime, and to investigate the significance of residual stresses. To implement this, the stresses of the artificial femoral construct *in vivo* for the rehabilitation activity of walking (peak stress due to walking in conjunction with residual stress due to polymerisation) were predicted. To investigate the significance of residual stresses, the rehabilitation prediction was compared with the peak walking stress prediction and with the residual stress prediction.

Research Objectives And Methodologies Flow Chart

Figure 1.5 summarises the thesis research objectives and methodologies employed.

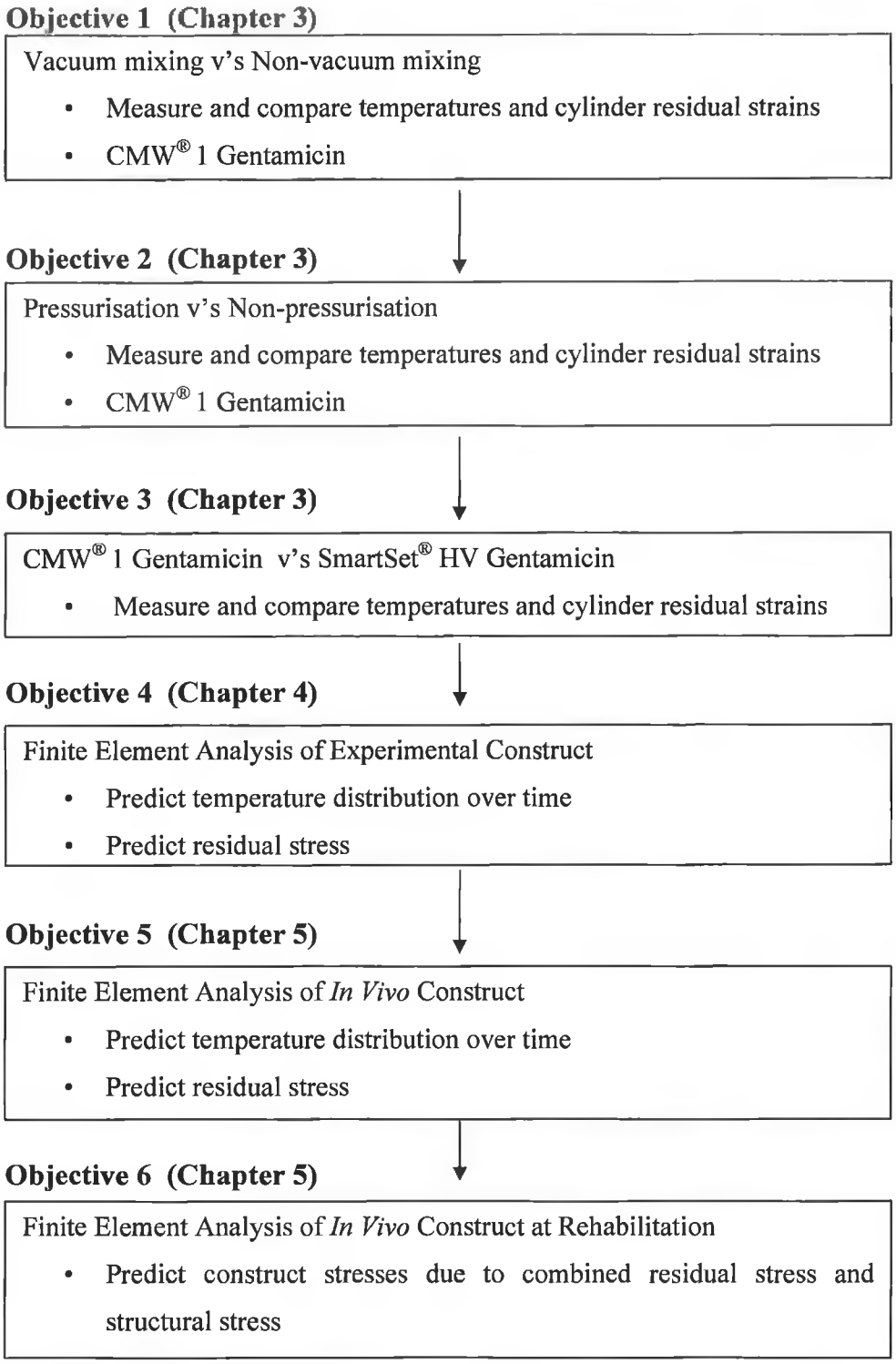

Figure 1.5: Flow chart of research objectives and methodologies

Chapter 2

Literature Survey

2.1 Introduction

Since bone cement was first introduced by Sir John Charnley over 45 years ago, an enormous amount of research has been performed on the material, and possible consequences of its use. Significant research is still undertaken, as bone cement remains the only material used to mechanically lock the prosthesis to the contiguous bone, be it for a hip arthroplasty, knee arthroplasty or shoulder arthroplasty.

Despite bone cements extensive history, certain aspects of its mechanical behaviour are not fully understood. One such aspect is the quantification of bone cement residual stresses and their impact on clinical outcomes. In this chapter the relevant properties of bone cement and modern cementing techniques are reviewed. Finally a comprehensive review of the published literature related to bone cement residual stresses is presented.

2.2 Acrylic Bone Cement

Acrylic bone cements are commercially supplied as separate polymer powder and liquid monomer, (Figure 2.1). Bone cement is formed by mixing the polymer powder with the liquid monomer for approximately 60 seconds.

Figure 2.1: Monomer ampoule (left) and polymer packet (right) of CMW® 1 Gentamicin bone cement

2.2.1 Chemical Composition

The powder component contains approximately 95% [49] prepolymerised beads or spheres of polymethyl methacrylate, 1 to 125 microns in diameter [10]. The prepolymerised PMMA significantly reduces the amount of heat energy released, volumetric shrinkage and cure time during polymerisation. To help initiate polymerisation dibenzoyl peroxide (BPO), an initiator, is added to the polymer powder. Some surgeons like to monitor the artificial joint after arthroplasty. To increase X-ray opacity radiopacifiers such as barium sulphate ($BaSO_4$) or zirconium dioxide (ZrO_2) are added, ranging from 8% to 15% by weight [50]. Some bone cements also contain antibiotics such as gentamicin to help prevent infection.

The liquid monomer component contains approximately 97% methyl methacrylate (MMA) [49]. To launch and control the polymerisation process an activator and inhibitor are added to the liquid monomer. The activator consists of N,N-dimethyl-*p*-toluidine (DmpT) while trace amounts of inhibitor are added to

prevent self-polymerisation, which may occur under the exposure of ultraviolet radiation.

2.2.2 Polymerisation Characteristics

To form bone cement, the liquid monomer is mixed with the powder polymer. During the polymerisation, the cements temperature and handling characteristics change. To quantify the handling characteristics during polymerisation, the entire curing cycle of the cement is divided up into 4 phases, namely the *mixing phase*, *waiting phase*, *working phase* and *setting phase*. Figure 2.2 illustrates a typical temperature versus time trace for polymerising bone cement, with the curing phases indicated.

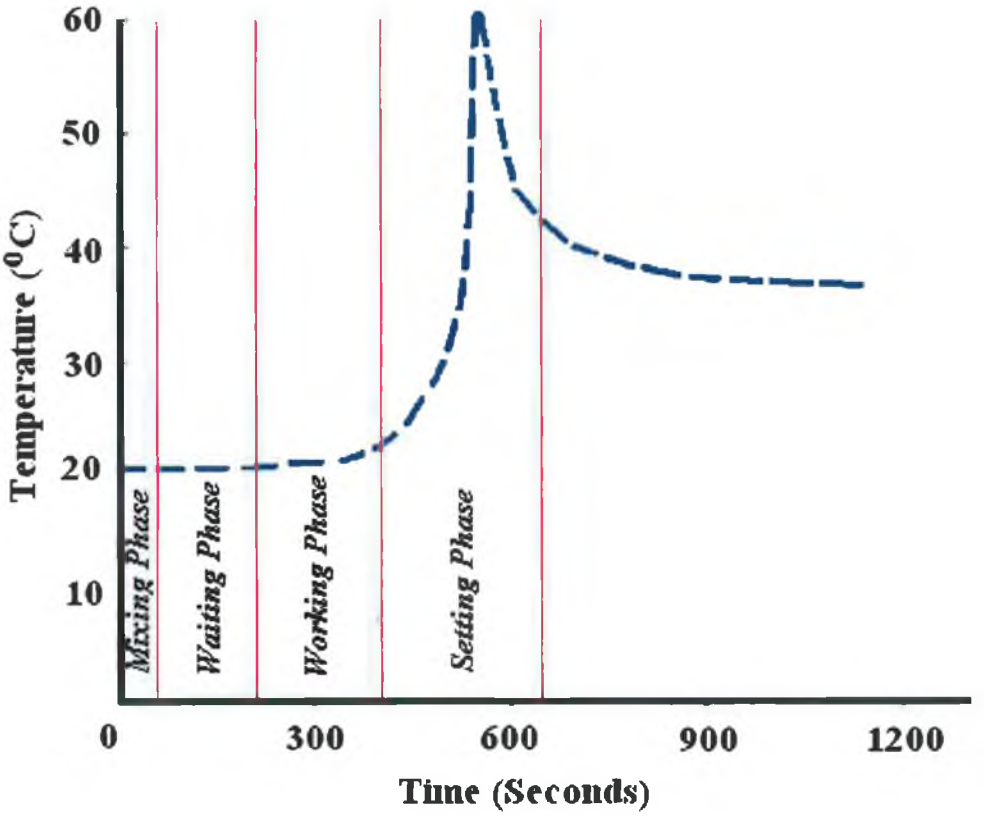

Figure 2.2: Typical temperature versus time trace for polymerising bone cement

Mixing Phase

The mixing phase involves continuously mixing together the liquid monomer and powder polymer to form a low-viscosity mass [10]. During the mixing phase BPO from the polymer and DmpT from the monomer produce free radicals, enabling the bone cement to self-polymerise at room temperature. To ensure a homogeneous paste, the mixing phase normally lasts approximately 60 seconds.

Waiting Phase (Dough Phase)

After the mixing phase, the bone cement is in a highly fluid state and adhesive to surgical gloves [10, 49]. The waiting phase allows time for the bone cement to become more cohesive and less adhesive. The waiting phase normally lasts approximately 160 seconds and spans from 60 to 220 seconds. The waiting phase is considered over, when the bone cement no longer adheres to a surgical glove.

Working Phase (Handling Phase)

The working phase is considered the ideal time for the surgeon to utilise the bone cement [10, 49]. The bone cement is readily workable neither being excessively fluid or excessively set. The working phase normally lasts for 180 seconds and typically spans from 220 to 400 seconds.

Setting Phase

The setting phase is the final phase of polymerisation [10, 49]. The setting phase is the time allowed for the bone cement mantle to become a complete solid, thereby securing the prosthesis *in situ*. During this time the prosthesis must not be disturbed, or gaps may be formed between the prosthesis and the bone cement mantle. The setting phase normally takes 240 seconds and typically spans from 400 to 640 seconds.

2.2.3 The Exothermic Reaction

The amount of time taken for the bone cement to completely cure and the peak temperature attained during polymerisation is dependent on a number of variables. The more significant of these variables include [8, 10, 44, 51-53];

- Polymer and monomer initial temperature
- Prosthesis initial temperature
- Quantity of cement applied
- Composition of bone cement
- Mixing method/system
- Environment

Heat Liberation

The exothermic polymerisation of high-energy unstable monomer to low energy stable polymer releases significant amounts of thermal energy [10, 51, 52, 54, 55]. Peak polymerisation temperatures typically range from 50 to 100°C. The thermal energy generated by the bone cement is directly related to the breakage of the double bond in the MMA molecules during polymerisation. During this process, MMA molecules form polymer chains liberating heat as described by Figure 2.3.

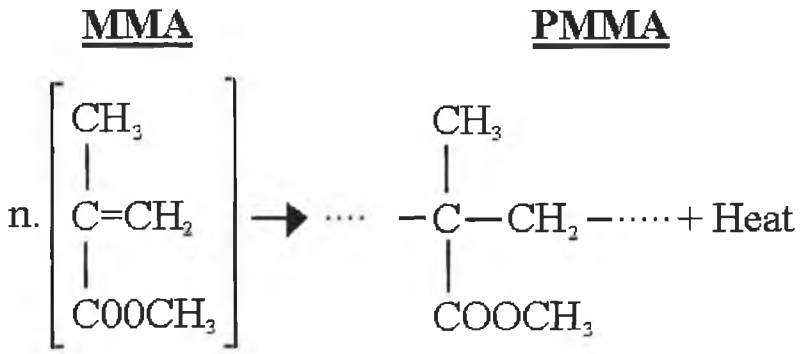

Figure 2.3: Description of polymerisation process in which MMA molecules are connected to form polymer chains [8]

Huiskes [8] proposed that the quantity of heat generated per unit volume of bone cement (Q) is dependent on the volume fraction of polymerised monomer (v_m),

density of monomer (ρ_m) and on the total amount of heat liberated by the monomer per unit mass (Q_t), as described by Equation 2.1.

$$Q = v_m \rho_m Q_t \tag{2.1}$$

Meyer *et al* [52] reported a liberation of 130 calories (544 Joules) of thermal energy per gram of monomer. Assuming a typical ratio of two parts polymer to one part monomer, the total heat liberated was 214.1 MJ/m^3. Swenson *et al* [56] used 36 cal/cm^3 (150.7 MJ/m^3) based on Simplex® P bone cement for their finite element model. Baliga *et al* [55] reported a total heat liberation of 155 MJ/m^3 and 180 MJ/m^3 derived from FEA (Finite Element Analysis) results that best matched the experimental findings. Huiskes [8] used a total heat liberation of 170 MJ/m^3 for analytical work that best matched experimental findings. Mazzullo *et al* [57] and Baliga *et al* [55] reported the effect of different isothermal temperatures on the polymerisation characteristics of bone cement, based on Differential Scanning Calorimetry (DSC) experiments. Both authors reported significantly different polymerisation rates for different DSC isothermal temperatures. Figure 2.4 illustrates the reported findings by Baliga *et al* [55] for Surgical Simplex® P bone cement.

Nzihou *et al* [58] performed a number of DSC experiments based on isothermal conditions of 25°C. Utilising laboratory made bone cement, the average measured thermal energy output was 179.5 MJ/m^3. Yang *et al* [59, 60] conducted numerous DSC experiments utilising Simplex® P bone cement. Table 2.1 summarises the heating rate applied to the DSC and the measured exotherm.

Thermal Distribution And Peak Temperature

As mentioned previously, the total amount of time taken for the bone cement to completely polymerise and the peak temperature attained are dependent on a large number of variables. As a result, there exists significant variance in the literature with respect to thermal distribution and peak temperature attained. The literature can be divided into three categories, clinical studies, experimental studies and analytical studies.

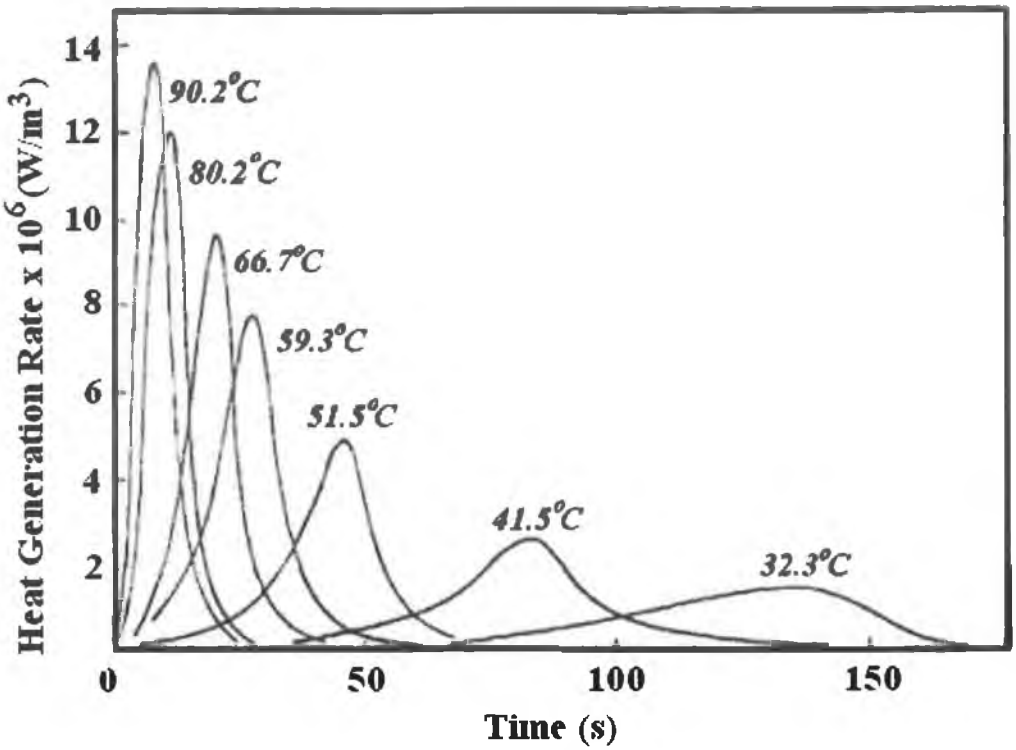

Figure 2.4: Heat generation rate for Simplex® P bone cement at various isothermal temperatures. Adapted from Baliga et al [55].

Heating Rate (°C/min)	Measured Exotherm (MJ/m^3)
0	86.1
5	118.2
10	129.4
20	145.0

Table 2.1: Summary of Yang et al [59, 60] DSC experimental results

Clinical Studies

Toksvig-Larsen *et al* [61] measured the cement-femur interface temperature *in vivo* during 41 arthroplasties that utilised Palacos® R bone cement. The average cement-femur interface temperature was 40°C, ranging between 29 to 56°C with a standard deviation of 6°C. Meyer *et al* [52] monitored the temperature for 10 THA procedures where Simplex® P bone cement was utilised. The authors reported a peak temperature of 70°C at the cement-bone interface. Huiskes [8]

cited *in vivo* studies by Labitzke *et al* [62] and Biehl *et al* [63] that reported the *in vivo* femur-cement interface to be 45°C and 47°C respectively.

Experimental Studies

A large volume of experimental studies exist in the published literature which reports the measurement of transient and peak temperatures for polymerising bone cement. Some of these studies are reviewed here.

Swenson *et al* [56] cited *in vitro* work by Ohnsorge and Goebel [64]. Ohnsorge and Goebel constructed an *in vitro* model utilising a fresh, moist, femoral bone warmed to 37°C in physiological saline solution, Palacos® R bone cement and a Thompson femoral prosthesis. The bone cement mantle was 9 mm thick proximally and 5 mm thick distally. The authors recorded a peak proximal cement-bone interface temperature of 58°C and a maximum stem temperature of 55°C. Ahmed *et al* [65] utilised a stainless steel tube of 19 mm inside diameter of 1.2 mm thickness to represent a stem, and a cardboard outer tube to represent a femur, to form an 8 mm thick cement mantle. The authors measured a peak temperature of 110°C at the centre of the cement mantle and approximately 90°C at both interfaces. Baliga *et al* [55] conducted a similar experiment, but for a 5 mm thick cement mantle created between two copper tubes. The inner tube had an interior diameter of 22 mm and a wall thickness of 1.6 mm. A peak temperature of 65°C was reported. Roques *et al* [34] performed a number of experiments curing CMW® 1 bone cement between a 1 mm thick stainless steel tube of 12 mm external diameter and a composite femur (Sawbones Europe AB, Sweden) of 16 mm internal diameter. From 5 experiments the average peak cement was 58.5°C with a standard deviation of 3.5°C.

Jefferiss *et al* [51] conducted a number of experiments to establish any relationship between sample size, (solid bone cement cylinders ranging in diameter from 2.5 to 30 mm, with a constant length to diameter ratio of 3 to 1) mould material (teflon or aluminium) and peak temperature. The peak temperatures recorded varied from 35 to 122°C at the centre of the cement cylinders and from 25 to 58°C at the edge of the cement cylinders. The authors noted a distinct relationship existed between peak polymerisation temperature

and both the mould material used and diameter of the mould. Meyer *et al* [52] investigated the effect of varying the thermocouple position within setting cement. The authors reported a temperature differential of approximately 40°C (between 70 to 110°C). DiPisa *et al* [53] investigated the effect of pre-cooling the acetabular prosthesis. By pre-cooling the prosthesis to –84°C, the average peak temperature reduced from 70.4°C without pre-cooling to 49.2°C. The authors also noted a 5 minute increase in the cements setting time as a consequence of the pre-cooling. Dunne and Orr [42-45] reported that different brands of cement and cement mixing systems had a notable effect on the temperature curve and on the peak cement temperature attained during polymerisation. Based on an *in vitro* model, peak cement temperatures typically varied from 40 to 60°C, for the different cements and mixing systems considered.

Theoretical Studies

Similar to the experimental studies, a large volume of theoretical studies exist in the published literature for the quantification of cement transient and peak temperatures. Some of these studies are reviewed here. Swenson *et al* [56] modelled a cemented femoral arthroplasty using FE techniques. Three axisymmetric models were developed with different cement mantle thickness to investigate this variable. Using a predefined exotherm with a total thermal liberation of 150.7 MJ/m^3 the authors predicted a peak cement temperature of 80.2°C, 97.7°C and 88.6°C for a 5 mm, 10 mm and 5 to 10 mm tapered cement mantle respectively. The authors predicted temperatures of 53.7°C, 66.3°C, 57.1°C at the cement-bone interface respectively.

Starke *et al* [66] utilised finite element techniques to investigate cement temperatures for a 1.5 mm and 2.5 mm thick cement mantle, based on a plane strain model. Founded on research by Baliga *et al* [55], the heat produced by the cement was represented as a function of cement polymerisation and temperature. Results predicted the thicker cement mantle may produce localised regions where the cement exceeds 80°C. Overall, the 1.5 mm thick cement mantle produced temperatures 10 to 15°C lower than the 2.5 mm thick cement mantle. Similar to Starke *et al* [66], Li *et al* [67] conducted FEA based on the polymerisation method described by Baliga *et al* [55]. The axisymmetric model was based on

cylindrical representative geometries, consisting of a solid stem (diameter 16 mm), surrounded by a 5 mm thick cement mantle, which in turn was surrounded by an 8 mm thick cylinder, representative of the femur. A peak temperature of 80°C was predicted to occur at approximately the centre of the cement mantle after 847 seconds (14.1 minutes) from mixing. The peak predicted temperature at the bone-cement interface was approximately 53°C, while the peak predicted temperature at the stem-cement interface was approximately 50°C. The authors suggested that polymerisation occurred at a faster rate at the bone-cement interface and was the first region of the cement mantle to solidify, based on a stem initially at room temperature.

Residual Monomer Release

Not all the monomer is converted to polymer during polymerisation. Approximately 2 to 6% of the monomer eludes polymerisation [10]. Kuhn [10] cited research by Scheuermann [68] who reported that the proportion of residual monomer decreases to approximately 0.5% within 2 to 3 weeks from mixing, due to a slowly progressing continuous polymerisation post arthroplasty, (Figure 2.5). Others speculate that a percentage of this residual monomer leaches from the cement mantle causing chemical tissue necrosis [48, 51].

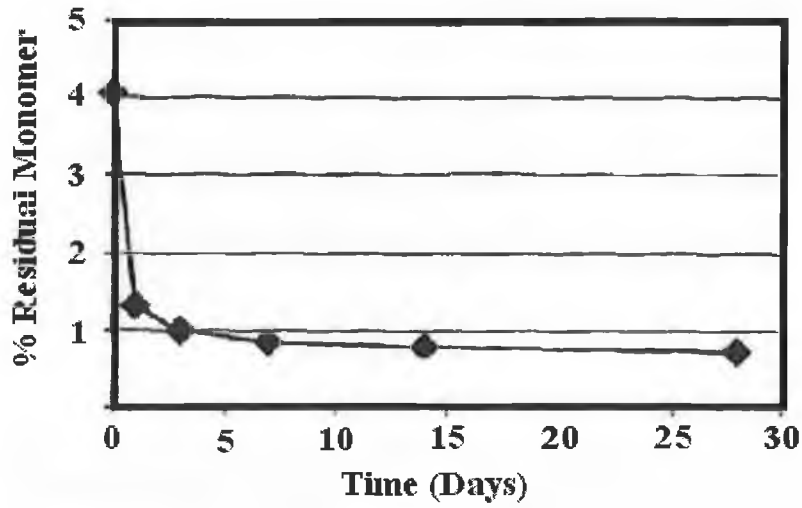

Figure 2.5: Typical curve logging percentage residual monomer versus time. Adapted from Kuhn [10].

2.2.4 Cement Mixing Systems

As mentioned in Section 1.5, the method of mixing and delivering cement has evolved greatly since bone cement was first introduced. Initially, bone cement was mixed using a bowl and spatula with no accessories. These mixers became known as the *first generation* of cementing devices. Unfortunately this method exposed the operative mixing the cement to a high level of methyl methacrylate vapour, which is noxious. To improve the cement quality and safety aspects, a new generation of mixers where developed. The *second generation* of cementing devices was similar to the first generation, but had the modification of a filter attached to the bowl to purify the noxious methyl methacrylate fumes [45].

From mechanical tests, it became apparent that pores in the cement mantle acted as stress concentrators and that fatigue failure almost exclusively occurred through these pore sites [69]. In an attempt to reduce the porosity level and hence improve its mechanical properties, a number of devices were developed. These devices included a hand-mixing device with vibration, post mixing centrifugal device, mixing under pressure and in 1983 mixing under vacuum [70, 71]. Centrifugal and vacuum mixed devices produced the least porous cement and became popular. However, there were concerns about the centrifugal device producing inhomogeneous cement, as the heavier elements may be forced to one end and the lighter elements to the other [31]. Partially due to this, contemporary third-generation mixing devices use vacuum to reduce porosity. In common with the second generation devices, the monomer fumes are either filtered or extracted from the operating theatre atmosphere [42]. Some third generation cement mixing devices mix the cement in a cartridge/syringe, which later forms part of a gun used to inject the cement onto the cancellous bone, (Figure 2.6).

According to the NJR for England and Wales for 2004, 94.5% of cemented hip arthroplasties utilised vacuum mixing or fume extraction for the preparation of bone cement [4]. Table 2.2 summarises research that related cement mixing method with resultant cement porosity.

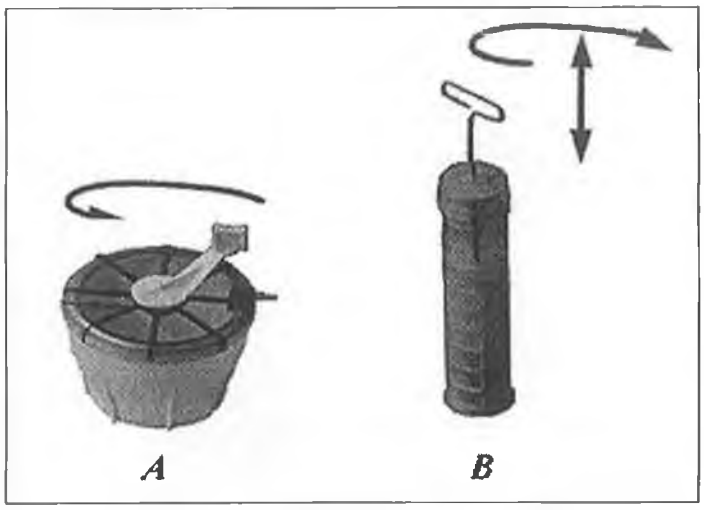

Figure 2.6: Zimmer Osteobond™ vacuum mixing system, (A) Bowl system (B) Cartridge system. Reprinted with permission [45].

2.2.5 Cement Pressurisation

As mentioned in Section 1.3, modern cementing techniques employ cement pressurisation. Cement pressurisation has been credited with reduced blood contamination of the cement mantle and greater cement interdigitation into the cancellous bone structure. Significant variance exists in the literature with respect to the magnitude of pressure achieved. McCaskie *et al* [72] performed clinical studies to compare traditional finger packed pressurisation techniques with a modern mechanical cement pressuriser. For finger pressurised cement, based on a sample number of 15 patients, the average cement-bone pressure was 17 ± 9 kPa with peak values of 81 ± 52 kPa. For the mechanical pressuriser, based on a sample number of 16 patients, the average pressure was 43 ± 30 kPa with peak values of 157 ± 83 kPa. *In vitro* work by Bourne *et al* [73] reported pressure measurements up to 970 kPa at the distal region during stem insertion and proximal pressures of approximately 100 kPa, for a plugged medullary cavity. *In vitro* work by Dunne *et al* [18] reported pressure measurements ranging from approximately 10 kPa to approximately 600 kPa, dependent on pressurisation method, location of pressure gauge and stem utilised.

Cement Mixing Method/System	Vacuum Level (kPa)	Bone Cement Brand	Porosity (%)		Reference
			$\bar{x}$	σ	
Stryker® Howmedica-Osteonics Mix Kit I	0	Palacos® R	16.4	0.78	[42] Dunne and Orr, 2001
Zimmer Osteobond™	39	Palacos® R	10.3	0.81	
Summit® LoVac Bowl	39	Palacos® R	9.86	1.24	
Cemvac®	69	Palacos® R	4.37	1.55	
Summit® HiVac Syringe	72	Palacos® R	3.17	1.54	
Summit® HiVac Syringe	86	Palacos® R	1.70	0.76	
Mitab Optivac®	86	Palacos® R	1.44	0.24	
Hand Mixed	-	Simplex® P	7.2	-	[71] Wixson *et al,* 1987
Centrifuged	-	Simplex® P	4.8	-	
Vacuum	-	Simplex® P	0.8	-	
Hand Mixed	0	-	5.3	-	[74] Hamilton *et al,* 1988

Table 2.2: Relationship between cement mixing systems and resultant mean porosity ($\bar{x}$) with standard deviation (σ)

2.2.6 Mechanical Properties

The relatively poor mechanical properties of bone cement in comparison to the prosthesis and femoral bone make it the weakest link in the artificial hip construct. This section considers the mechanical properties of bone cement.

The mechanical properties of bone cement reported in the literature vary over a wide range [48]. This is due to the large number of variables that affect the

cements mechanical properties. Possibly the most influential variable is porosity, a function of mixing method.

Static Properties

Table 2.3 summarises the mean uniaxial compressive properties for popular bone cement brands and the mixing method utilised.

Bone Cement Compressive Properties				
Cement Brand	**Mixing Method**	**Young's Modulus (MPa)**	**Ultimate Compressive Strength (MPa)**	**Reference**
Palacos® R	Vacuum (20 kPa)	1,940	97	[75] Vaughan, 1995
Simplex® P	Bowl & spatula	2,672	102.5	[76] Trieu *et al*, 1994
Simplex® P	Vacuum (31 kPa)	3,000	114.3	
Simplex® P	Centrifuged @ 2950rpm	2,623	101.4	
CMW® 3	Vacuum (13 kPa)	1,950	81.4	[77] Lewis and Austin, 1994
CMW® 1	Bowl & spatula	1,990	110	[78] Tanzi *et al*, 1991
Simplex® P	Bowl & spatula	2,830	104.7	[79] Krause and Hofmann, 1989
Zimmer® LVC	Bowl & spatula	2,200	102.6	

Table 2.3: Mean uniaxial static compressive properties of bone cement, as cited by Lewis [48]

Table 2.4 summarises the mean uniaxial tensile properties for popular bone cement brands and the mixing method utilised.

Bone Cement Tensile Properties				
Cement Brand	**Mixing Method**	**Young's Modulus (MPa)**	**Ultimate Tensile Strength (MPa)**	**Reference**
Palacos® R	Bowl & spatula	3,210	51.4	[47] Haper and Bonfield, 2000
Sulfix® 60	Bowl & spatula	3,260	50.7	
Simplex®	Bowl & spatula	3,430	50.1	
CMW® 3	Bowl & spatula	3,530	44.7	
CMW® 1	Bowl & spatula	2,960	39.1	
Osteobond™	Bowl & spatula	3,380	38.2	
Endurance®	Bowl & spatula	2,990	37.1	
Zimmer®	Bowl & spatula	2,790	31.7	
Palacos® R	Bowl & spatula	-	33	[80] Kindt-Larsen *et al*, 1995
Palacos® R	Vacuum (20 kPa)	-	40	
CMW® 1	Vacuum (20 kPa)	-	47.0	
Simplex® P	Bowl & spatula	3,080	44.4	[81] Krause *et al*, 1988
Simplex® P	Bowl & spatula	2,530	36.2	[82] Davies *et al*, 1987
Zimmer® LVC	Bowl & spatula	3,070	39.8	
Zimmer® LVC	Centrifugation	2,950	49.2	

Table 2.4: Uniaxial static tensile properties of popular bone cement brands

Orr *et al* [33] related Palacos® R bone cement flexural modulus and Poisson's ratio with vacuum level. Table 2.5 summarises the reported findings.

Lewis [48] published a literature review of bone cement mechanical properties in 1997. Reported values for ultimate tensile strength ranged from 24 to 49 MPa, ultimate compressive strength from 73 to 117 MPa, flexural strength from 50 to 125 MPa and shear strength from 32 to 69 MPa.

Vacuum Level (kPa)	Flexural Modulus (GPa)	Poisson's Ratio
0	2.11	0.45
39	2.65	0.32
72	2.60	0.39
86	2.54	0.48

Table 2.5: Palacos® R flexural modulus and Poisson's ratio with respect to bone cement vacuum level [33]

Fatigue Properties

From gait analysis, it has been noted that typically 2 to 4 times body weight is experienced by the hip joint during walking [83-86]. This combined with approximately 16.5 million cycles over 15 years reveals the importance of bone cement fatigue properties [30]. It is widely accepted that bone cement mechanical failure due to fatigue plays a central role in aseptic loosening and the eventual failure of the artificial hip joint [27-29, 31, 87].

A great deal of research has been carried out to determine the bone cements fatigue properties. However due to the porous brittle nature of bone cement and the large number of variables that affect its mechanical properties, the reported fatigue properties vary significantly for identical tests. Table 2.6 summarises fatigue test results (tension-tension, 2 Hz, 0.3 to 22 MPa) by Harper and Bonfield [47] on popular brands of bone cement.

Most fatigue studies conclude that a significant increase in fatigue lifetime is achieved by vacuum mixing [71, 88, 89]. Figure 2.7 illustrates a typical S-N fatigue curve comparing vacuum mixed and non-vacuum mixed cement.

Viscoelastic Properties

The viscoelastic properties of bone cement have been associated with stem subsidence [48, 90] and residual stress relaxation [8, 41]. Bone cement mantles have revealed signs of gross plastic deformation [91, 92]. Consequently, the

Cement Brand	Cycles To Failure	
	Range	Weibull Medium
Simplex® P	8,933 - 93,345	36,677
Palacos® R	18,362 - 49,285	27,892
CMW® 3	5,996 - 38,262	16,441
Osteobond™	5,527 - 25,825	16,162
Sulfix®-60	2,902 - 29,275	9,816
CMW® 1	3,042 - 8,835	4,407
Endurance®	1,663 - 12,947	4,355
Zimmer®	153 - 3,978	781
Boneloc®	4-647	164

Table 2.6: Tension-tension (2 Hz, 0.3-22 MPa) fatigue results for non-vacuum mixed commercial bone cements [47]

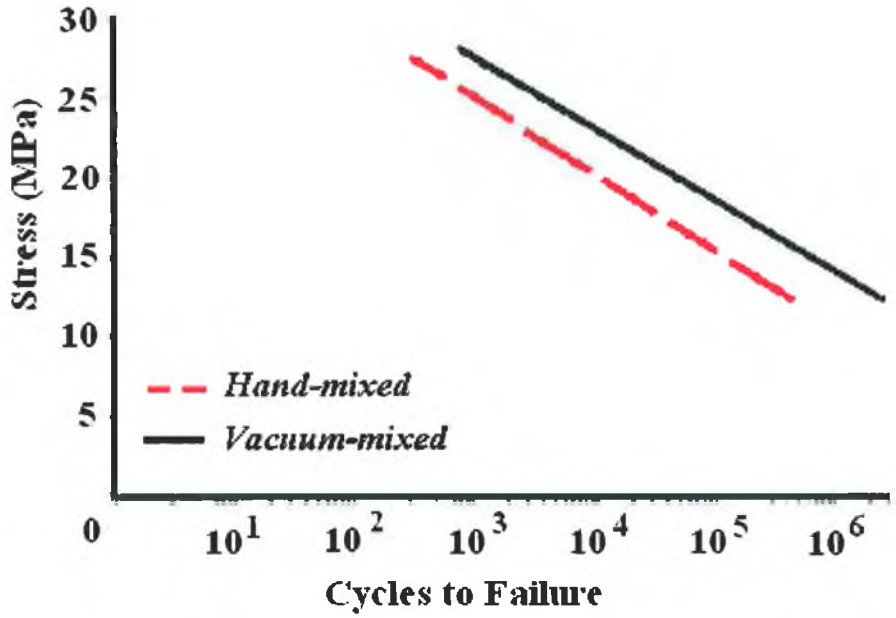

Figure 2.7: Typical S-N curves for hand mixed and vacuum mixed cement [89]

viscoelastic properties of bone cement have been hypothesised to contribute to implant loosening and eventual failure. Research studies investigating the viscoelastic properties of bone cement may be divided into three main categories;

static viscoelastic research, dynamic viscoelastic research and stress relaxation research. In line with previous mechanical properties, significant variance exists in the literature, with little consensus.

Static Viscoelastic Research

Chwirut [92] performed compressive creep tests on 5 commercially available bone cements brands over a 1,000 hour (41.5 day) period. From this the author reported significant differences between the different cement brands, and proposed a mathematical model to predict creep strains.

Norman *et al* [91] investigated the creep rates for different stress levels and preparation methods. Results revealed higher creep strains for the hand-mixed cement versus vacuum mixed cement. Results also revealed significantly different creep rates between different stress levels. For example, an average creep strain of 0.11% was measured after 6 hours at 10.5 MPa, while at 50 MPa over the same time period the average creep strain was 9.9%.

Lee *et al* [93] investigated the effect of;

- Different cement brand
- Room temperature versus body temperature
- Dry samples versus hydrated samples
- Different bone cement sample ages

The authors tested the samples under tension, compression and 4 point bending conditions, typically over an 80 hour period. Results revealed that the creep rates were dependent on all variables. Some variables had a greater influence than others. The creep rate differences between the different bone cement brands were minor in comparison with specimen age, hydration and temperature.

Dynamic Viscoelastic Research

Liu *et al* [94, 95] postulated that the viscoelastic response due to a cyclic load would be more representative of *in vivo* conditions compared with static creep tests. Liu *et al* [94] compared the dynamic creep rates between CMW® 1 and

Palacos® R-40 bone cements. The authors measured significant differences between both brands, with the Palacos® R-40 brand reported to have a greater creep resistance compared to CMW® 1, (Figure 2.8).

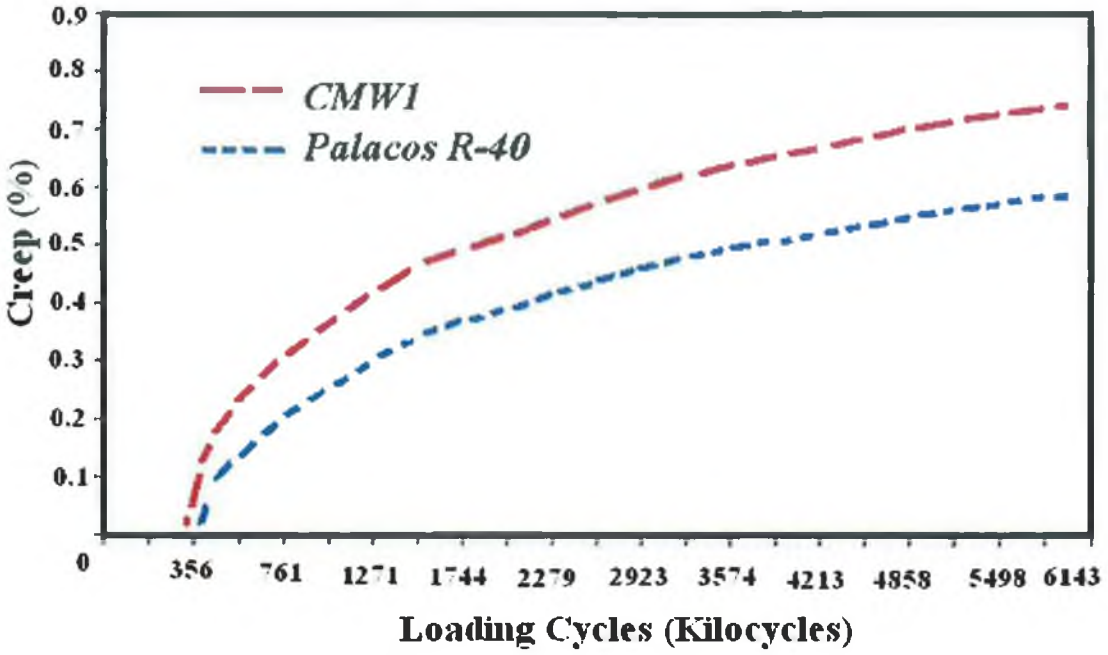

Figure 2.8: Percentage creep versus number of cycles, at a stress of 10.6 MPa, frequency of 1 Hz, at 37°C [94]

Stress Relaxation Research

Eden *et al* [90] investigated the effect of bone cement specimen age on stress relaxation. Based on Simplex® P bone cement, the authors noted that the older the bone cement sample, the more resistant the sample was to stress relaxation. For example, for a cement sample one hour old, the authors measured a stress relaxation from 16 MPa to 6 MPa to occur in one hour. While for a cement sample 70 days old, the authors measured a stress relaxation from 24 MPa to 18 MPa in the same time period.

Lee *et al* [93] investigated the stress relaxation rates between 6 different bone cement brands and different sample ages (1 hour to 42 days). Significant variance was measured between both the different cement brands and different specimen ages. The bone cement sample age however had a greater influence on

the stress relaxation rates compared with cement brand. Figure 2.9 illustrates the stress relaxation result for Palacos® R bone cement over a 48 hour period, based on 7 day old specimens, in saline solution at 37°C.

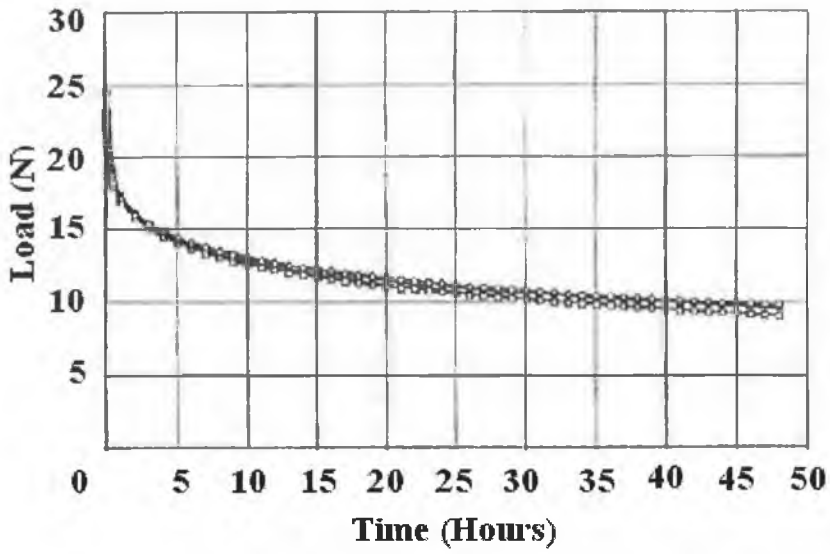

Figure 2.9: Stress relaxation of Palacos® R bone cement over a 48 hour period, based on 7 day old samples in saline solution at 37°C. Adapted from Lee et al [93].

Huiskes [8] reported the stress relaxation rate for a rod of bone cement under an initial tensile stress of 4 MPa, at 37°C, under a constant strain of 1.6×10^{-3}. Extrapolating their measurements, the author postulated the stress would reduce by 90% after 70 days and would be negligible after one year.

Roques *et al* [34, 41] reported the residual strain levels over the first two hours from the initiation of cement mixing. Negligible stress relaxation had occurred over this time period. From such, the authors postulated that when the construct is loaded for the first time by the patient, the residual stresses would be only partially relieved.

Coefficient Of Thermal Expansion

The bone cement coefficient of thermal expansion is central for the accurate

quantification of residual stress. Based on dilatometer experiments using Radiopaque Surgical Simplex® P acrylic cement, Ahmed *et al* [65] measured the coefficient of thermal expansion to be approximately 8 x $10^{-5}{}^{o}C^{-1}$, varying between 7.2 and 8.8 x $10^{-5}{}^{o}C^{-1}$. The authors also derived an expression for the calculation of the coefficient of thermal expansion. For a relatively high Young's modulus of 3.2 GPa, the coefficient of thermal expansion was calculated to be 3.0 x $10^{-5}{}^{o}C^{-1}$, whereas for a relatively low Young's modulus of 2.07 GPa, the coefficient of thermal expansion was calculated to be 4.7 x $10^{-5}{}^{o}C^{-1}$. Figure 2.10 graphically represents Ahmed *et al's* results.

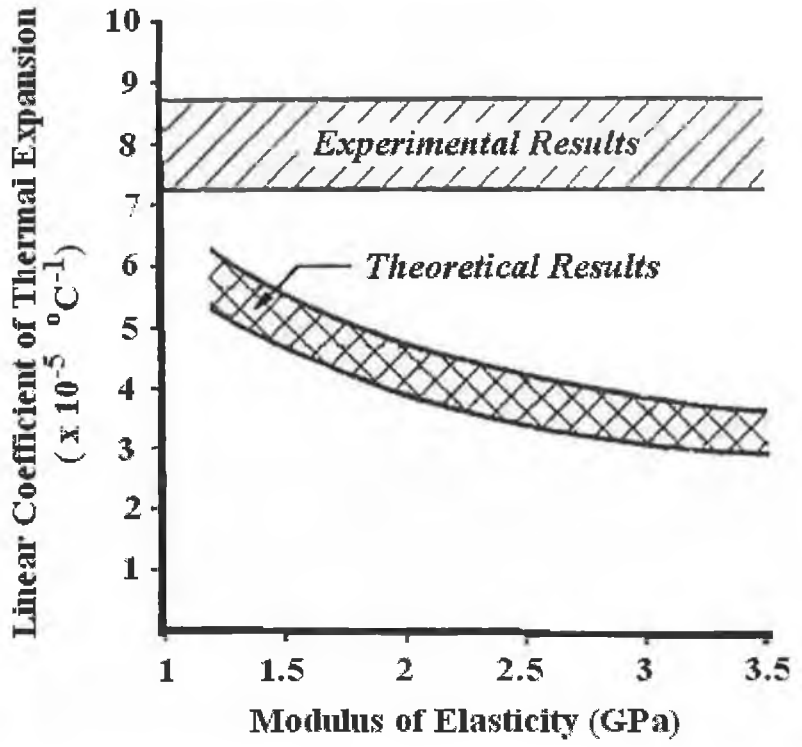

Figure 2.10: Linear coefficient of thermal expansion, both experimental and theoretical findings. Adapted from Ahmed et al [65].

2.3 Residual Stress Development

Bone cement residual stresses are formed after the cement has solidified. When the cement solidifies, it is at an elevated temperature, due to the exothermic reaction. Upon solidification the bone cement mechanically locks with the

contiguous cancellous bone and bonds with the femoral prosthesis. With the passing of time the cement mantle cools to body temperature. However the cement mantle remains constrained and unable to shrink. Due to this constraint, residual stresses are set up in the construct. It has been hypothesised that these residual stresses, coupled with stress concentrators in the cement mantle, such as air pores and contaminates (blood, bone marrow, bone), may raise local stress levels above the fracture strength of fresh bone cement and thereby induce fractures [32, 33]. Evidence of preload cracks have been found in numerous experimental studies [29, 32-35, 41].

2.3.1 Volume Alteration Mechanisms

Since PMMA bone cement was first introduced, it has been known that it undergoes a change in volume during the polymerisation process [96]. It has been hypothesised by many [8, 40, 49, 97] and widely accepted that the chief mechanisms of volume alteration during polymerisation include;

1. Polymerisation shrinkage
2. Pore expansion
3. Thermal expansion followed by thermal contraction

Cement swelling due to liquid absorption *in vivo* has been hypothesised by some authors [40, 49, 98], however research by Haas *et al* [49] and De Wijn *et al* [40] were unsuccessful in measuring any swelling or enlargement effects.

Polymerisation Shrinkage

As mentioned in Section 2.2, bone cements are commercially supplied as packs of polymer powder and vials of liquid monomer. When mixed together, the activator in the powder (benzoyl peroxide) and the initiator in the monomer (N,N-dimethyl-p-toluidine) bring about polymerisation [10]. During the polymerisation process monomers are converted into their corresponding polymeric form. This polymerisation process forms a net density change for the liquid monomer, as it is converted from 0.937 kg/m^3 to a polymer of 1.18 kg/m^3

[8, 98]. It is this density increase for the monomer that is the primary source of polymerisation shrinkage [10, 98, 99]. Therefore, the amount of polymerisation shrinkage is dependent on the quantity of monomer applied, as demonstrated in Figure 2.11. Attempts have been made to control the amount of shrinkage by reducing the amount of monomer, however it has been found that this has a negative effect on the bone cements mechanical properties [8, 49, 52, 99].

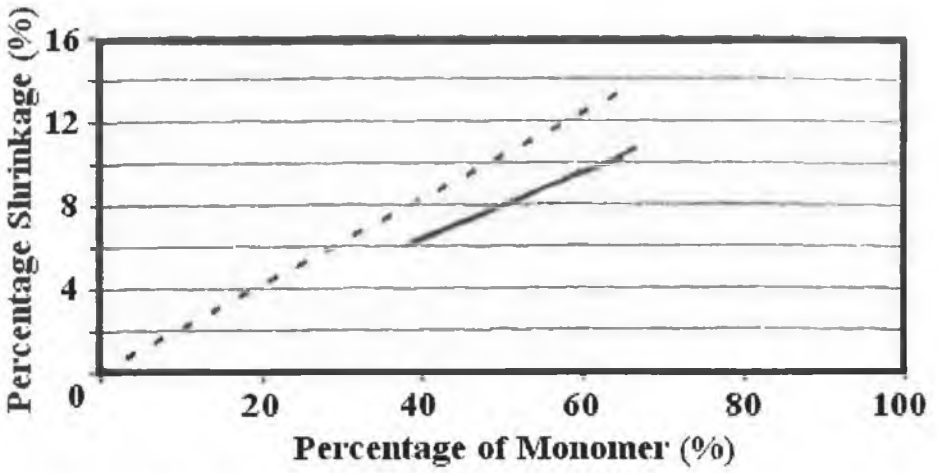

Figure 2.11: Percentage shrinkage versus percentage MMA [98]. Dashed line represents theoretical shrinkage, solid line represents experiment findings.

Silikas *et al* [99] calculated a volumetric shrinkage of 21.1% for the complete conversion of MMA to PMMA. Gilbert *et al* [98] calculated the theoretical polymerisation shrinkage to be 20.6% for the complete conversion of pure monomer to 100% polymer. Basing his calculations on Endurance® (DePuy Orthopedics, Indiana, USA) bone cement, Gilbert *et al* calculated a net polymerisation shrinkage of 7.8%. Loshaek *et al* [100] calculated the theoretical liquid monomer shrinkage to be between 22 to 23%. Assuming a ratio of two parts polymer and one part monomer, the authors calculated a net polymerisation shrinkage of 7.5%. De Wijn *et al* [40] reported a theoretical shrinkage of 22% for the complete conversion of MMA to PMMA. Based on the same 2:1 ratio, De Wijn *et al* calculated a net shrinkage of 7%. Haas *et al* [49] calculated the net polymerisation shrinkage to be between 7.6 to 8%.

Bulk Thermal Expansion And Contraction

The exothermic polymerisation of high-energy unstable monomer to low energy stable polymer releases significant amounts of thermal energy [10]. With respect to volume alteration, this causes the bone cement mass to thermally expand during the exothermic phase and thermally contract during the cooling phase.

Porosity Effects

Pores in the cement mantle, (Figure 2.12), are typically attributed to air that has become entrapped in the powder interstices during mixing [48, 71, 74]. Wixson *et al* [71] identified at least 4 sources of porosity in which air may become entrapped in the bone cement mantle during the cement preparation process. These include [71];

1. "Air initially surrounding the powdered polymer beads
2. Air trapped during the wetting of the power
3. Air stirred into the liquid cement during spatulation
4. Air trapped during transfer to a non-vented cement gun or specimen mold"

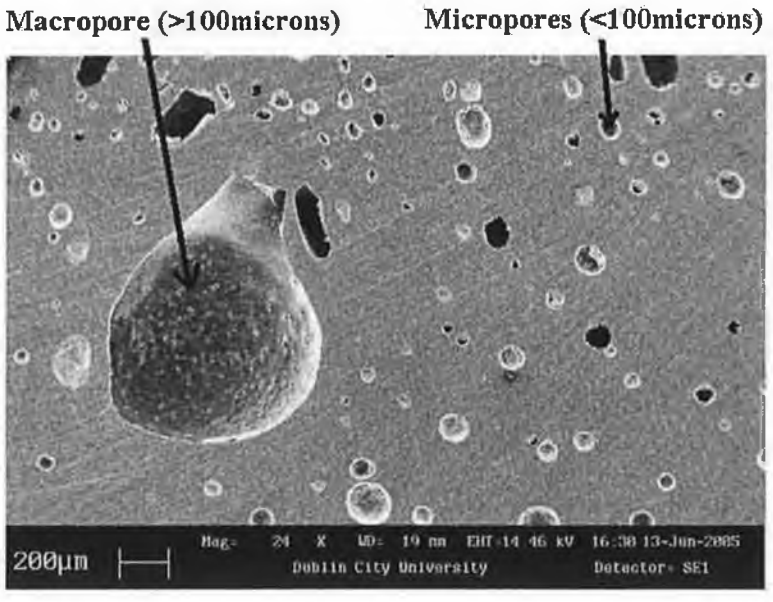

Figure 2.12: A scanning electron micrograph of a typical acrylic bone cement sample, identifying micropores and macropores

Pore Thermal Expansion

During the exothermic phase of the polymerisation process, air pores entrapped enlarge due to thermal expansion. Based on Charles Law, Hamilton *et al* [74] calculated that for a cement initially at room temperature and heated by 60°C, a 22% volumetric expansion of the air pore would result. This represents approximately 1% net volume expansion for a typical 5.3% air pore occupancy. Thermal contraction of the air pores would not occur, as the bone cement would have attained its properties as a solid before the cooling phase commences.

Pore Removal Effects

There is a general consensus that reducing the number of pores in the cement mass improves the cements mechanical properties [42, 45, 48, 71, 101, 102]. To produce less porous cement, centrifugation or vacuum mixing is performed. However, the side effects of such actions are less well understood. It has been hypothesised that by reducing the number of pores in the cement, the amount of pore expansion to counteract polymerisation shrinkage reduces [33, 98]. Therefore an increased percentage of the polymerisation shrinkage is absorbed by external dimensional contraction. Table 2.7 summarises shrinkage results in the literature.

Cement Brand	**Mixing Method**	**Shrinkage (%)**		**Reference**
		Mean	**Std. Dev.**	
Simplex® P	Hand mixed	5.09	0.5	[98] Gilbert *et al*, 2000
Simplex® P	Vacuum mixed	6.67	0.4	
Endurance®	Vacuum mixed	6.5	0.24	
Simplex® P	Centrifuged	7.5	-	[74] Hamilton *et al*, 1988
Simplex® P	Uncentrifuged	2-4	-	
Palacos® R	-	3	-	[103] Rimnac *et al*, 1986
-	Hand mixed	2.7-5.2	-	[49] Haas *et al*, 1975

Table 2.7: Summary of bone cement shrinkage data from the published literature

Orr *et al* [33] established a clear relationship between increased vacuum level and increased mean shrinkage Table 2.8 summarises their experimental findings.

Vacuum Level (kPa)	Mean Shrinkage (%)	Standard Deviation
0	-1.95	0.78
39	-4.92	1.28
72	-6.87	1.54
86	-7.27	0.76

Table 2.8: Relationship between vacuum level and mean shrinkage based on Palacos® R bone cement [33]

Dunne *et al* [101] investigated porosity dissimilarities between vacuumed and non-vacuumed mixed cement. Dunne *et al* noted the non-vacuum mixed cement created numerous micropores and some macropores. The larger of the macropores were in the order of 0.5 mm in diameter. Figure 2.13 illustrates a typical sample of non-vacuum mixed bone cement.

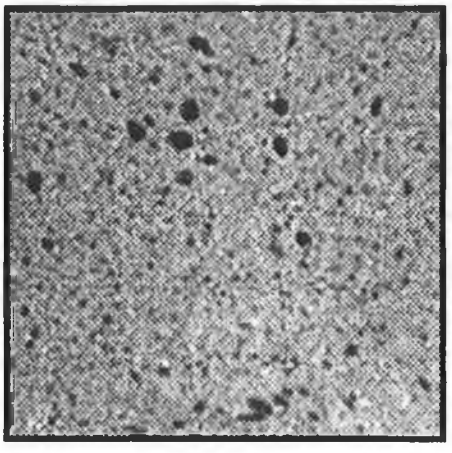

Figure 2.13: Typical sample of non-vacuum mixed bone cement. Reprinted with permission [45].

Upon comparison with vacuum mixed cement, Dunne *et al* [101] noted a dramatic reduction in the number of micropores, however the macropores were

significantly larger, in the order of 1 to 3 mm in diameter. Figure 2.14 illustrates a typical sample of vacuum mixed bone cement.

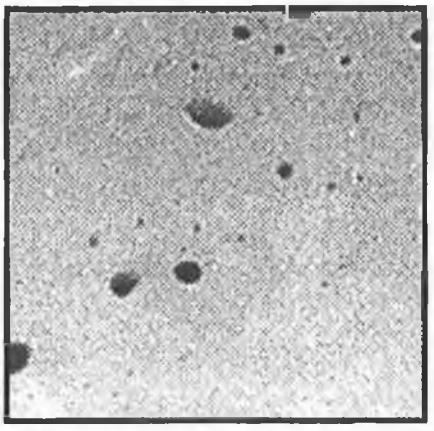

Figure 2.14: Typical sample of vacuumed mixed cement. Reprinted with permission [45].

Wang *et al* [104] similarly reported that vacuum mixing significantly reduced microporosity but not all the vacuum mixing systems investigated were successful in removing the larger pores. Research by Gilbert *et al* [98] may explain this phenomenon. Gilbert *et al* noted that the exterior shell of the polymerising cement solidified before the interior. They noted that when the exterior surfaces of the cement samples were free to move no pores were observed. Conversely it was noted that when the exterior surfaces of the curing cement samples were constrained, pores were found in the cement. Gilbert *et al* concluded that the external constraint on polymerising cement played a significant part in the generation of pores in bone cement. Assuming that the exterior shell of the polymerising cement mantle solidifies before the interior, it would appear that for non-vacuum mixed cement, a part of the polymerisation shrinkage is absorbed by the slight expansion of the numerous micropores. However for the vacuum mixed cement, relatively few pores exist. Due to the polymerisation shrinkage, the few pores that exist greatly increase in size to absorb the polymerisation shrinkage. This may explain why both Wang *et al* [104] and Dunne *et al* [101] noted non-vacuum mixed cement produced

numerous micropores with some macropores, while vacuum mixed cement produced relative few micropores and relative large macropores.

Monomer Evaporation

A number of authors have presented computational or experimental evidence that under conditions of orthopaedic surgery, temperatures in the cement mantle may reach and exceed 100°C [8, 40, 52, 71]. At these temperatures it has been hypothesised that any remaining monomer that has eluded polymerisation may evaporate forming pores. These monomer pores, in a fashion similar to air pores, would reduce the density of the orthopaedic cement thus diminishing the cements mechanical properties.

Wixson *et al* [71] noted that the level of vacuum used was an important variable with respect to monomer evaporation. Wixson *et al* reported that by increasing the vacuum level beyond 80 kPa (600 mmHg) "the monomer tended to boil and bubble up" introducing monomer pores to the viscous cement mass. The authors concluded a vacuum level between 66.7 to 73.3 kPa (500 to 550 mmHg) was the best compromise between air porosity removal and the suppression of monomer evaporation at mixing.

2.3.2 Stress-Locking

Bone cement residual stresses are formed after the cement has attained its properties as a solid. Due to the highly non-linear polymerisation reaction rate and the large number of variables that effect this process, the exact moment of stress-locking is difficult to ascertain [32]. Note that some sources in the literature use the term "stress-locking", while other sources use the word "solidification" to denote the moment when the bone cement has sufficiently polymerised to sustain a stress. The word "solidification" may imply that the bone cement has abruptly changed from a liquid to a solid, which is not the case. After mixing the bone cement it is quite fluid, however over time as polymerisation progresses it becomes progressively more elastic until it has solidified enough to sustain a force. The term "stress-locking" will be used in this

thesis to denote this moment when the bone cement has polymerised sufficiently to sustain a stress.

Experimental work by Ahmed *et al* [65] reported the initial development of stress to coincide "remarkably well with the onset of the rapid rise in temperature" and concluded that the volume alteration that occurred after the onset of the rapid rise in temperature would be responsible for the generation of residual stresses. Debrunner *et al* [97] likewise reported that bone cement remained sufficiently paste-like up until the time of rapid rise in cement temperature.

Whelan *et al* [105] used optical fibre bragg grating sensors to identify the moment at which bone cement was first able to sustain a strain. The first occurrence of strain was noted to occur approximately at the attainment of maximum cement temperature. Roques *et al* [34] cured bone cement about a stainless steel tube. On the internal surface of the stainless tube strain gauges were attached. By monitoring both strain and temperature during cement polymerisation, the first significant measurement of strain approximately coincided with the attainment of peak cement temperature. Figure 2.15 graphically represents a strain and temperature versus time result measured by Roques *et al* [34].

Stachiewicz *et al* [106] noted that the hardening of bone cement occurred in the final stage of polymerisation and coincided approximately with the attainment of maximum temperature. Holm [39] reported that the initiation of residual stress coincided with the attainment of peak cement temperature. Considering the entire body of evidence, it seems that the early findings by Debrunner *et al* [97] and Ahmed *et al* [65] (1976 and 1982 respectively) were inaccurate and that stress-locking approximately coincides with the attainment of peak cement temperature.

2.3.3 Transient Net Volume Alteration

A number of authors have postulated that the cessation of polymerisation approximately coincides with the attainment of peak temperature [8, 105-107].

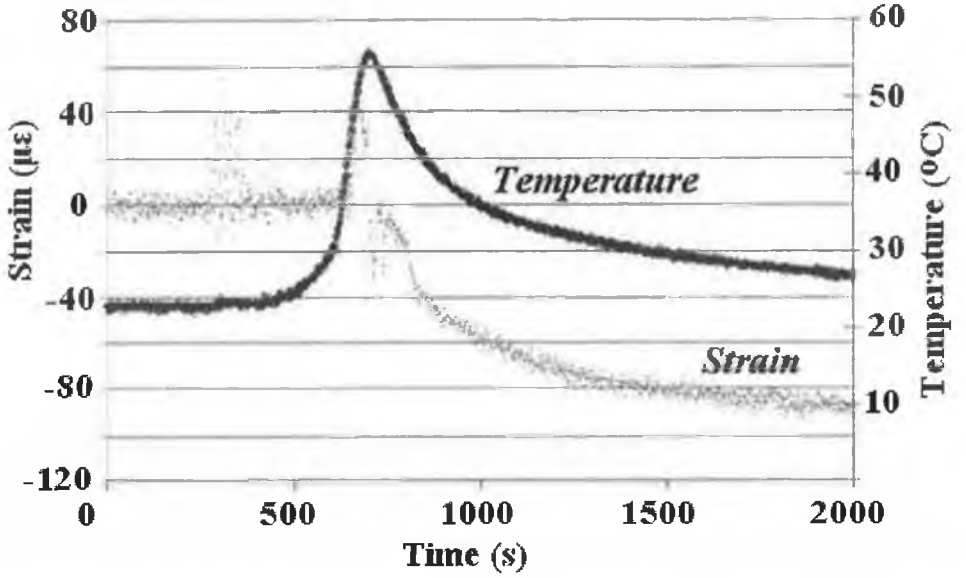

Figure 2.15: Strain (left axis) and temperature (right axis) trace versus time for polymerising CMW® 1 bone cement. Adapted from Roques et al [34].

From this it has been hypothesised that the polymerisation shrinkage and all thermal expansion effects may be ignored, due to the inability of the cement mass to sustain a stress [33]. Due to the aforementioned deductions, most authors that compute cement residual stresses consider thermal shrinkage effects alone [8, 32, 33, 107, 108]. Figure 2.16 illustrates a typical temperature and fraction of polymerisation versus temperature plot.

Research by Orr *et al* [33] has cast doubt as to whether all the polymerisation shrinkage has occurred by the time the cement mass has attained its properties as a solid. Orr *et al* [33] reported longer preload cracks produced for vacuum mixed cement over non-vacuum mixed cement, for cement samples that underwent identical thermal changes. On this basis, higher residual stresses have been postulated for vacuum mixed cement. As both cement samples underwent the same temperature change, it was postulated that polymerisation shrinkage may play a role in the creation of residual stress.

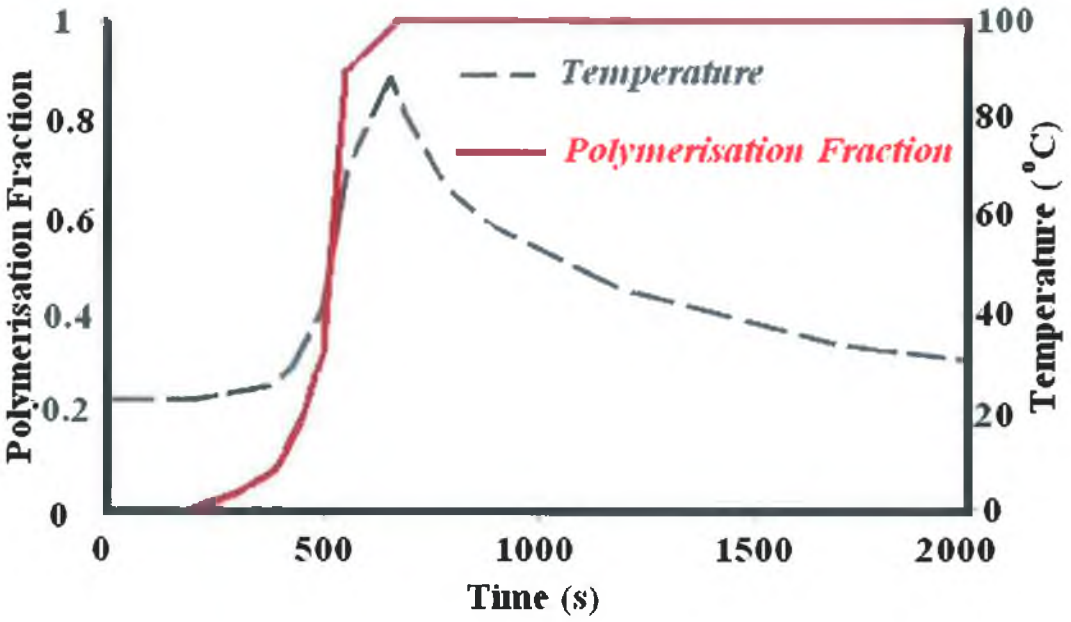

Figure 2.16: A typical plot relating polymerisation fraction and polymerisation temperature with time. Adapted from Lennon et al [107].

2.4 Residual Stress Studies

Published residual stress studies can be categorised into three strands; mathematical studies, finite element studies and experimental studies.

2.4.1 Mathematical Studies

Stachiewicz *et al* [106] derived an mathematical expression to obtain an estimate of the hoop stresses produced *in vivo*. To represent the stem a relatively unyielding solid steel core was assumed. To represent the cement mantle, a bone cement cylinder was assumed. Femoral effects were ignored. Based on the assumption that bone cement obeyed Hooke's law, Stachiewicz *et al* derived Equation 2.2. This equation calculated the hoop stress at the stem-cement interface.

$$\sigma_{\theta c} = \left\{1 + \left[\frac{R^2 - 1}{R^2 + 1}\right]\left[\nu_c + (1 - \nu_s)\frac{E_c}{E_s}\right]\right\}^{-1} \frac{S.E_c}{3} \qquad (2.2)$$

Where

$$R = \frac{D_o}{D_i} \qquad (2.3)$$

The subscripts "*c*" and "*s*" represent *cement* and *stem* respectively, while "S" represents percentage volume shrinkage. Table 2.9 summarises results based on a cement's Young's modulus of 2.1 GPa, cement's Poisson's ratio of 0.3, stem's Young's modulus of 193 GPa, stem's Poisson's ratio of 0.3 and a diameter ratio of 1.5. For the diameter ratio calculations, a shrinkage of 2.2% was assumed.

Variable	Max. Tensile Hoop Stress (MPa)
S = 1%	6.17
S = 2%	12.34
S = 3%	18.51
R = 1	15.5
R = 1.5	13.6
R = 2	13.1

Table 2.9: Calculated residual hoop stresses based on Equation 2.2, developed by Stachiewicz et al [106]

Stachiewicz *et al* [106] also investigated the magnitude of volumetric shrinkage due to thermal cooling. Stachiewicz established that a 1% volumetric shrinkage occurred for every 50°C temperature drop. Thus for a pure thermal shrinkage from 87°C to body temperature, Stachiewicz *et al* predicted a thermal hoop stress of 6.2 MPa.

Orr *et al* [33] similarly developed a mathematical representation of a cement cylinder shrunk about a solid steel core. Likewise, femoral effects were ignored. From Lamé's equations, the authors derived an expression to calculate the

circumferential stress at the stem-cement interface, assuming plane stress conditions, (Equation 2.4).

$$\sigma_{\theta c} = \frac{E_c S}{3}\left[\left(\frac{1+R^2}{1-R^2}\right)\left(\frac{E_c}{E_s}(\nu_s - 1) - \nu_c + \frac{1+R^2}{1-R^2}\right)^{-1}\right] \qquad (2.4)$$

Thermal shrinkage "S" was defined by:

$$S = 3(\alpha_c(T_c - T_a) - \alpha_s(T_s - T_a)) \qquad (2.5)$$

Where "T" denotes *temperature* and the subscript "a" denotes *ambient*. Based on Equation 2.4, the authors calculated the peak circumferential residual stresses for vacuumed and non-vacuumed cement at the stem-cement interface over a temperature range of 60 to 140°C. Bone cement material properties representative of Palacos® R bone cement were assumed, namely a Poisson's ratio of 0.455, thermal expansion coefficient of 8 x 10^{-5}°C^{-1}, Young's modulus of 2.11 GPa for non-vacuum mixed cement, and 2.65 GPa for vacuum mixed cement. Figure 2.17 illustrates the residual stress results based on Equation 2.4.

Due to load bearing activities, such as walking, axial loads will be induced in the cement mantle. For this reason Orr *et al* [33] adapted Equation 2.4 to consider plane strain conditions, as this condition may be more representative of *in vivo* conditions (Equation 2.6).

$$\sigma_{\theta c} = E_c \frac{S}{2(1-\nu)}\left[\left(\frac{1+R^2}{1-R^2}\right)\left(\frac{E_c}{E_s}(\nu_s - 1) - \nu_c + \frac{1+R^2}{1-R^2}\right)^{-1}\right] \qquad (2.6)$$

Based on Equation 2.6, circumferential stresses in the range of 22 to 70 MPa were calculated over a 60 to 140°C temperature range. The authors also established a mathematical relationship between the level of vacuum and resultant residual stresses. Applying measured shrinkages to their mathematical

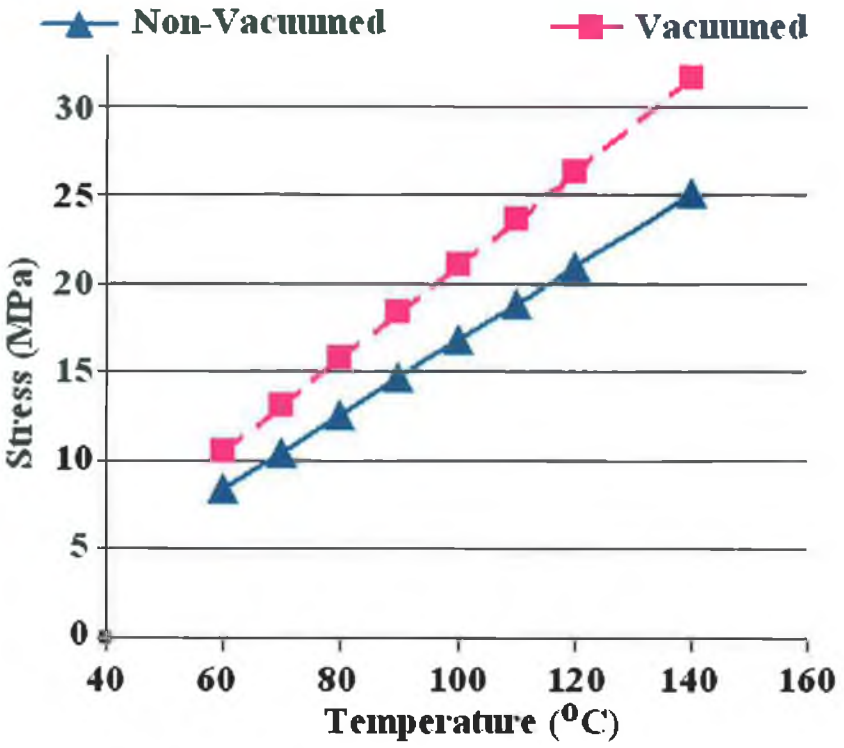

Figure 2.17: Circumferential residual stresses (MPa) versus temperature (°C) [33]. Solid line represents non-vacuumed cement. Dashed line represents vacuumed cement.

model, hoop residual stresses of 20 to 88 MPa were calculated for vacuum levels of 0 to 72 kPa respectively.

2.4.2 Finite Element Studies

Huiskes and De Wijn [109] calculated residual stress magnitudes based on a plane strain axisymmetric model of a cement cylinder about a rigid stem. Femoral effects were ignored. The authors assumed a certain temperature distribution at the moment of stress-locking. The temperature profile assumed that the interior of the cement mantle attained a higher temperature than the edges. Figure 2.18 illustrates a typical temperature distribution assumed.

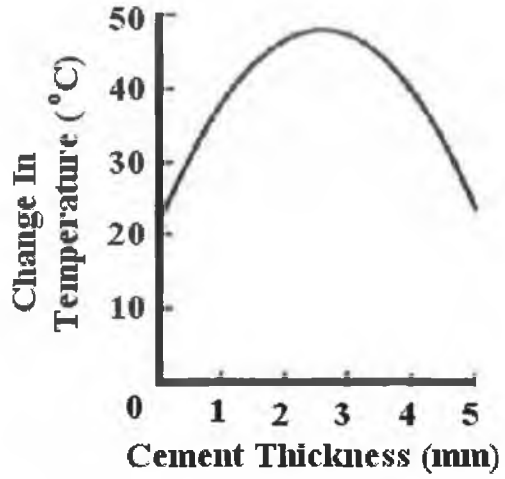

Figure 2.18: Typical change in temperature distribution assumed by Huiskes and De Wijn [109]

The bone cement was assumed to have a Young's modulus of 2 GPa, Poisson's ratio of 0.3 and a coefficient of thermal expansion of 5 x 10^{-5}°C^{-1}. The authors computed a radial compression stress at the stem-cement interface of approximately 2.5 MPa and a tensile hoop stress of approximately 3.5 MPa at approximately the centre of the cement mantle. Figure 2.19 illustrates a typical result reported.

Ahmed *et al* [110] conducted an axisymmetric FEA study consisting of three coaxial cylinders to evaluate the effect of cancellous or cortical bone at the cement-bone interface. To model the presence of cancellous bone, a bonded cement-bone interface was assumed. To model the presence of cortical bone, a debonded cement-bone interface was assumed. Similar to Huiskes and De Wijn [109], a temperature distribution was assumed at the moment of stress-locking. However, contrary to recent practice, the authors assumed stress-locking to occur at the onset of the rapid rise in cement temperature, not the peak. For the condition of cancellous bone, a radial displacement of up to 15 μm was calculated at the stem-cement interface. Residual stresses varied between ±2 MPa, dependent on interface condition.

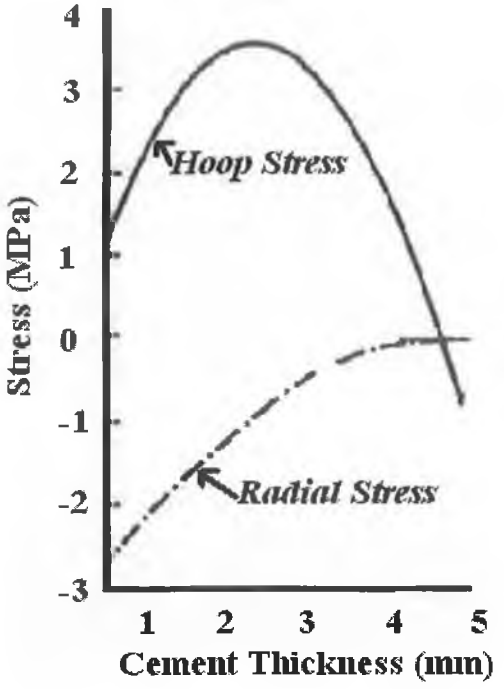

Figure 2.19: Typical residual stress result by Huiskes and De Wijn [109]

Mann *et al* [111] investigated thermal shrinkage effects based on an axisymmetric model, representative of a bone cement cylinder about a solid titanium alloy stem. Femoral effects were not included. The bone cement material was assumed to have a Young's modulus of 2.2 GPa, Poisson's ratio of 0.3 and a coefficient of thermal expansion of 4.7 x $10^{-5o}C^{-1}$. The model consisted of 91 elements. A uniform thermal difference of -60°C was applied to the entire bone cement cylinder. Results revealed a maximum tensile longitudinal stress of approximately 6.0 MPa, maximum tensile hoop stress of approximately 5.5 MPa, and finally a compressive radial stress of approximately -3 MPa at the stem-cement interface. Comparing their finite element results with previous experimental findings, the authors estimated the coefficient of friction between the stem and bone cement mantle to be between 0.25 to 0.35.

Lennon and Prendergast [32] developed a finite element model to compute transient temperature distributions and residual stresses. The 3-D finite element model was based on a previous experimental model that investigated damage accumulation. The model consisted of a medial and lateral strip of bone cement

encased between a strip of bovine cancellous bone and a representative stem. The system was held together by two aluminium support frames. These aluminium frames in turn contained windows that permitted the cement to be viewed, (Figure 2.20). Note that although a three dimensional formulation, the model was essentially two dimensional in character, and did not take into account the development of hoop stress.

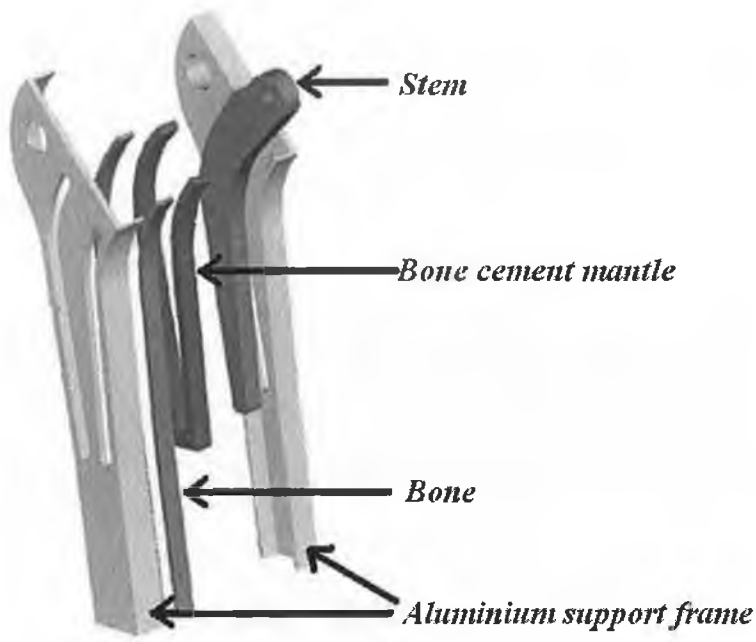

Figure 2.20: Schematic of FE model employed by Lennon and Prendergast [32] to compute residual stresses. Image adapted from Lennon and Prendergast [32].

Lennon and Prendergast [32] initially conducted a transient thermal analysis to ascertain the temperature distribution at the moment of assumed stress-locking. To implement this, the authors based the cement generation of heat during polymerisation on a theoretical model developed by Baliga *et al* [55]. Baliga *et al* [55] developed an expression (Equation 2.7) that described the heat produced during polymerisation as a function of temperature and fraction of monomer polymerised, where S_p represents the rate of heat generated by the bone cement during its polymerisation, R is a function of the instantaneous local temperature, β represents the degree of polymerisation and where m and n are constants independent of temperature.

$$S_p = R\beta^m(1-\beta)^n \tag{2.7}$$

Results from the thermal analysis by Lennon and Prendergast [32] predicted the middle of the cement layer to exhibit a greater and more rapid rise in temperature than the cement near the interfaces. A peak temperature of 53°C was predicted at the centre of the cement mantle, a peak temperature of 30°C was predicted for the stem-cement interface and a peak temperature of 42°C was predicted for the cement-bone interface. The authors also noted that these locations did not reach their peak temperature at the same time. A 38 second interval existed between the first element that attained peak temperature, (located at the centre of the cement mass) and the last element that attained peak temperature, (located at the stem-cement interface). The model calculated complete polymerisation to occur almost simultaneously at 697 seconds. However the peak temperature was predicted at 536 seconds, some 161 seconds (2.7 minutes) before complete polymerisation. As a consequence, the authors conducted two analyses for the calculation of residual stress. One based on the assumption that stress-locking occurred with the attainment of peak temperature, i.e. approximately 536 seconds, and another based on the assumption that stress-locking occurred at the end of polymerisation, i.e. approximately 697 seconds. Assuming stress-locking occurred at the peak temperature during polymerisation, the maximum principal stresses ranged from 4 to 7 MPa. Assuming stress-locking occurred at the end of polymerisation, the maximum principal stresses ranged from 1 to 2 MPa.

Li *et al* [108] computed residual stresses based on cylindrical representative geometries. To represent the stem, a solid cylinder of diameter 16 mm was assumed. About this a 5 mm thick cement mantle was assumed. Finally, about the cement mantle an 8 mm thick cylinder, representative of the femur was assumed. Similar to Lennon and Prendergast [32], the numerical model that described the heat production during polymerisation was a function of temperature and fraction of monomer polymerised. Li *et al* [108] reported maximum hoop stresses of 15 MPa, axial stresses of 10 MPa and radial stress of -5 MPa. However the temperature profile at the moment of stress-locking was not specified.

2.4.3 Experimental Studies

Experimental studies in the literature may be categorised into two strands, namely, investigations to determine if residual stresses are sufficient to induce fracture damage in unloaded bone cement mantles, and investigations which endeavour to quantify the bone cement residual stresses.

Fracture Damage

While investigating microdamage accumulation, McCormack and Prendergast [29] noted the occurrence of fracture damage in the bone cement mantle prior to any mechanical loading. The authors recorded 118 cracks from 6 specimens and noted that all the pre-load cracks emanated from pores within the bulk cement. Under cyclic loading, these pre-load cracks grew and were more significant after 5 millions cycles than load-initiated cracks.

Lennon and Prendergast [32] postulated the pre-load cracks observed by McCormack and Prendergast [29] were the consequence of cement residual stresses. The authors specifically looked for the occurrence of preload cracks over 5 experiments based on the experimental rig as illustrated in Figure 2.20. Hand mixed Simplex® Rapid cement was utilised for all experiments. Results revealed preload cracks occurred in almost every region of the cement mantle for all 5 experiments. The authors noted that the cracks were predominantly oriented normal to the interfaces and in some instances the cracks were complete across the mantle. The authors concluded that residual stresses coupled with stress concentrators to have sufficient stress to form cracks in the cement mantle prior any functional loading.

Orr *et al* [33] investigated whether thermal cooling alone from the moment of stress-locking was sufficient to form cracks in bone cement. To represent the stem, a 316L stainless steel No. 2 Morse taper mandrel was utilised. To represent the cement mantle, rings of Palacos® R bone cement were produced. The cement rings were 30 mm in outside diameter, internally reamed to fit the Morse taper and 7 mm thick. Femoral effects were ignored in the model. To mimic the thermal cooling effects after stress-locking, each prepolymerised cement ring

was heated in an oven to a predefined temperature. The cement ring was assembled to the Morse taper and the assembly placed in a thermostatically controlled water bath at 37°C. After 24 hours the bone cement ring was removed from the Morse taper and examined using a scanning electron microscope. Figure 2.21 illustrates the No. 2 Morse taper with a bone cement ring assembled.

Figure 2.21: No.2 Morse taper mandrel with an acrylic bone cement ring assembled. Reprinted with permission of Orr et al [33].

To investigate what effect different stress-locking temperatures may have, the experiment was repeated at different assembly temperatures i.e. 60, 80, 100 and 120°C. To investigate if vacuum mixing had an effect, the experiment was repeated using cement samples created from atmospheric mixing conditions and cement rings produced from different vacuum levels i.e. 39, 72 and 86 kPa. Results revealed cracks were present in all samples assembled and cooled from 80°C and above. On examination of the crack lengths, it was observed that the cement samples assembled at higher temperatures produced longer cracks. Results also revealed that samples created with greater vacuum levels produced longer cracks. The induced cracks radiated predominantly from the cement-Morse taper interface, in a direction perpendicular to interface, as illustrated in

Figure 2.22. From this the authors postulated that tensile hoop stresses were the dominant residual stress generated in this experiment.

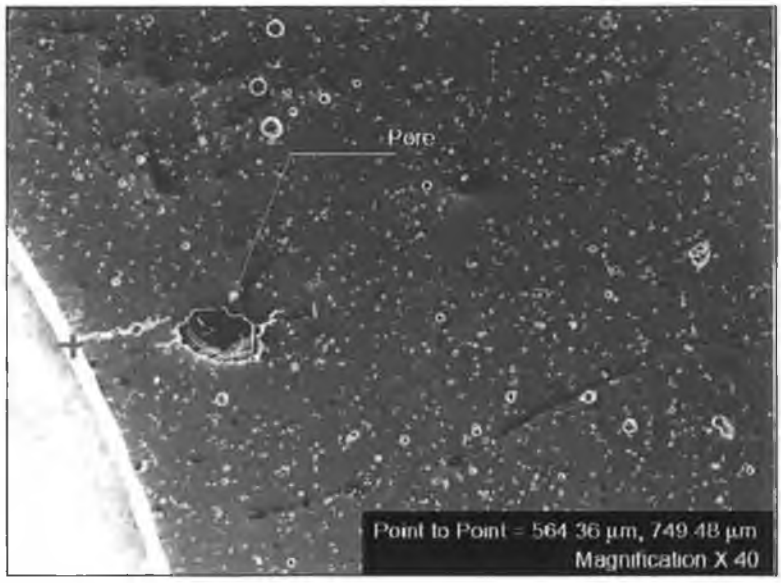

Figure 2.22: Typical crack found by Orr et al [33] due to thermal cooling. Reprinted with permission.

Roques *et al* [34] employed acoustic emission techniques to "listen" to polymerising cement to investigate the possible residual stress relief mechanisms. The acoustic emission sensor was applied to the inside of a hollow stainless steel tube 125 mm long, 12 mm in external diameter and 1 mm thick. About this stem a 2 mm thick CMW® 1 cement mantle was polymerised. The authors reported evidence of both cracking and sliding, after the cement had reached peak temperature.

Residual Stress Quantification

The earliest work found in the published literature that attempted the measurement of transient and residual strains due to bone cement polymerisation was by Ahmed *et al* [65] in 1982. The authors correlated the thermal history of polymerising bone cement with the residual strain history. To achieve this, two strain gauges were applied to the inner surface of a stainless steel tube, 21.4 mm outside diameter and 1.2 mm thick to measure hoop strain. Thermocouples were

bonded beside the strain gauges to measure temperature. Stainless steel beads of 100 μm were sintered to the outside of the tube to ensure a mechanical lock at the stem-cement interface. This instrumented cylinder was used to represent the stem. To represent the femur, a cylinder of cardboard 37.4 mm in internal diameter, slit axially at 90 degree intervals and held in shape by rubber bands was employed. This resulted in an 8 mm thick bone cement mantle between the instrumented stem and cardboard mould. From 4 experiments, the onset of residual strain was reported to correspond with the onset of rapid rise in cement temperature. The peak stress of +1.8 MPa measured in the stem was reported to coincided with the moment of peak temperature in the cement. One hour after the mixing of the cement, a residual stress of -0.5 MPa was reported. Bearing in mind that it is now known that bone cement remains paste like until the approximate peak in temperature (Section 2.3.2), it is likely that thermally induced apparent strains in the strain gauges were the primary source for the registration of stress at the onset of temperature rise and the occurrence of peak stress at the moment of peak temperature. The measurement of -0.5 MPa one hour after the initiation of mixing is most likely to be credible as the assembly would have returned to ambient temperature.

Nuno and Amabili [38] created 4 bone cement cylinders of 20 mm inside diameter, 30 mm outside diameter and 140 mm long about a representative stem and femur. On removal of the cement cylinder from the stem, the authors noted a diametrical shrinkage. The authors bonded 4 triaxial rosettes strain gauges to the external surface of the cement mantle and reintroduced the stem. From 4 tests, the measured hoop strains ranged from 1402 με to 2240 με. Nuno and Amabili [38] did not calculate a stress range from this, however assuming a Young's modulus of 2.65 GPa, this represented a stress of approximately 3 to 6 MPa.

Li *et al* [108] measured the residual stresses of prepolymerised bone cement rings cooled about an aluminium thick walled cylinder based on the photoelastic method. The outer diameter of the aluminium cylinder was 33 mm and was 7 mm thick. The outer diameter of the cement ring was 61 mm. Residual stresses of approximately 6 MPa were reported.

In a similar manner to Ahmed *et al* [65], Roques *et al* [34] recorded polymerisation induced strain and cement temperature versus time for polymerising CMW® 1 bone cement. To represent the stem, a hollow polished stainless steel tube 125 mm long, 12 mm in external diameter and 1 mm thick was utilised. On the internal surface of the stainless steel tube, strain gauges were attached to form a full Wheatstone bridge circuit. Two k-type thermocouples were set onto the stem beside the strain gauges to monitor temperature. To represent the femur, a composite femur by Sawbones Europe AB (Malmo, Sweden) of 16 mm internal diameter was utilised. CMW® 1 bone cement was mixed under atmospheric conditions and added to the system to form the cement mantle. From 7 experiments, residual strain measurements varied from -98 με to +98 με.

To measure the individual hoop and axial strains, strain gauges were applied to a similar tube to form a quarter-bridge circuit [41]. To represent the femur, a Tufnol tube of 16 mm internal diameter and 20 mm external diameter was utilised. From 4 repetitions of the experiment, the hoop strains varied from -106 με to +38 με, while the longitudinal strains varied from -138 με to -25 με.

To obtain a relationship between the strain data experimentally obtained and the residual stresses in the cement mantle, finite element analysis was employed. Assuming bonded conditions for both the stem-cement and cement-tufnol interfaces, the authors applied a shrinkage of 6% to the cement mantle, such that it resulted in a hoop strain of -100 με in the stem. From this finite element methodology, the authors reported a maximum residual stress of 11.85 MPa for the cement mantle. Table 2.10 summarises some of the residual stress studies in the published literature that aimed to quantify the bone cement residual stress levels.

2.5 Residual Stress Under Load Conditions

From a search of the published literature, only one research team has attempted to investigate the impact of residual stresses under loaded joint conditions. In two similar papers, Nuno and Amabili [38] and Nuno and Avanzolini [112] used

Method	Comment	Residual Stress (MPa)	Author(s)
Theoretical equation	Femoral effects not included	6 to 18.5	Stachiewicz et al, (1976) [106]
Theoretical equation	Femoral effects not included	8 to 32 (Plane stress) 22 to 70 (Plane strain) 20 to 88 (0 to -72 kPa)	Orr *et al,* (2003) [33]
Finite Element Analysis	Femoral effects not included	3.5 (Plane strain)	Huiskes and De Wijn, (1979) [109]
Finite Element Analysis	Femoral effects not included	6 (Axial stress) 5.5 (Hoop stress) -3 (Radial stress)	Mann *et al,* (1991) [111]
Finite Element Analysis	Strips of bone cement to represent cement mantle	1 to 7	Lennon and Prendergast, (2002) [32]
Finite Element Analysis	Axisymmetric model	10 (Axial stress) 15 (Hoop stress) -5 (Radial stress)	Li *et al,* (2004) [108]
Experimental	Femoral effects not included	-0.5 (Measured after 1 hour from mixing)	Ahmed *et al,* (1982) [65]
Experimental	Femoral effects not included	3 to 6	Nuno and Amabili, (2002) [38]
Experimental	Photoelastic method based on concentric cylinders	6	Li *et al,* (2004) [108]
Experimental	Stress derived from FEA of experimental work	10 to 12	Roques *et al,* (2004) [34]

Table 2.10: Summary of residual stress studies in the published literature

finite element techniques to investigate whether the inclusion of residual stresses significantly effected the cement mantle and interface stress magnitude and distribution for a loaded artificial hip joint. Figure 2.23 illustrates the finite element model and dimensions assumed. The finite element model assumed bonded conditions for the cement-bone interface and debonded conditions for the stem-cement interface. The model contained approximately 4,300 elements. To represent polymerisation shrinkage, a mechanical interference of 5 μm was imposed at the stem-cement interface nodes, corresponding to a radial stress of 2.4 MPa. To represent a physiological load, a transverse and axial load of 600 N was applied to the model, as illustrated in Figure 2.23.

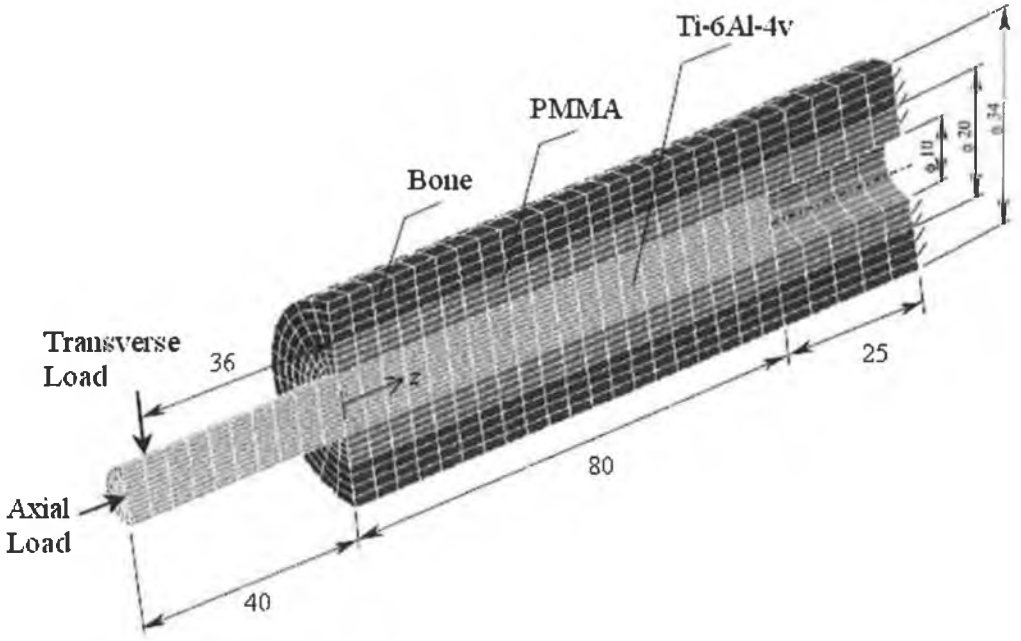

Figure 2.23: Finite element model employed by Nuno and Amabili [38] and Nuno and Avanzolini [112] to investigate the impact of residual stress on a loaded artificial hip joint (units in mm's). Image adapted from Nuno and Avanzolini [112].

Results revealed that the inclusion of residual stress had a significant impact on the stress magnitude and distribution, with parts of the interface experiencing a 4 fold increase in stress. The peak von Mises stress rose from approximately 4.5 MPa without residual stresses to approximately 5.8 MPa including residual

stresses. The authors concluded that the inclusion of residual stresses were necessary to accurately calculate the cement and interface stresses for an artificial hip joint under physiological load conditions, for the early post-operative period.

2.6 Concluding Remarks

Since orthopaedic bone cement was first successfully used in a hip arthroplasty by Sir John Charnley, bone cement has received an extensive amount of research. However certain aspects have remained poorly understood. One such aspect is the quantification of the residual stresses as a result of the polymerisation process and its consequences. This subject has often been neglected primarily due to the assumption that the residual stresses within the bone cement mantle are low and quickly relax to negligible levels, due to the bone cements viscoelastic nature. However the relatively recent discovery of fractures in preloaded bone cement mantles has focused attention on the residual stresses.

Research involving bone cement is complicated by the large number of different bone cement brands commercially available, the large number of cement mixing devices commercially available, and bone cements inherent sensitivity to initial conditions and environmental parameters. As a consequence, significant variability exists in almost every area of research involving bone cement, including residual stresses.

A number of relatively recent reports have documented bone cement mantle fracture damage before any functional loading. However issues relate to how well the model represents the *in vivo* scenario. Peak residual stress magnitudes predicted in the literature vary from 1 to 88 MPa. However, issues again relate to how well the model represents the *in vivo* scenario.

Due to the significant variance in residual stress levels, and issues relating to the methods and models employed, Chapter 3 is focused upon the experimental measurement of transient and resultant residual strains based on a representative

femoral construct. The developed experimental femoral model was based upon the experimental work by Ahmed *et al* [65] and Roques *et al* [34]. A number of advances were made to more accurately represent the *in vivo* scenario, to record more data, and to improve the reliability of the data. Chapter 3 however is primarily focused upon the investigation of factors that may affect the magnitude of residual strains. Factors such as vacuum mixing, cement pressurisation and cement brand were investigated. From such an analysis, it is hoped to establish a methodology that may reduce residual stress levels and hence reduce the extent of fracture damage before functional loading.

Chapter 4 is primarily concerned with the establishment of a finite element analysis methodology for the quantification of the bone cement mantle residual stress levels. The experimental model of Chapter 3 was modelled and results compared with the experimental results to verify the finite element model. Finally, Chapter 5 was primarily concerned with the prediction of residual stress levels *in vivo* and the prediction of stress levels during rehabilitation i.e. residual stresses in conjunction with load bearing stresses due to gait.

Chapter 3

Experimental Investigation Of Bone Cement Residual Stresses

3.1 Introduction

The objectives of this chapter are three fold. Firstly to experimentally investigate the hypothesis that vacuum mixing may increase the residual stress levels. Secondly to investigate if pressurisation of the bone cement mantle during polymerisation affects the residual stress levels. Thirdly and finally to investigate if any significant difference exists in the residual stress levels between two bone cement brands.

3.2 Materials And Methods

An experimental system was designed to approximately reproduce the thermo-mechanical conditions which occur during polymerisation of bone cement in a femoral cemented hip arthroplasty. The objective of the experimental model was to measure and log the individual hoop and axial strains, in conjunction with the temperature, of a representative femoral construct, during and after polymerisation.

3.2.1 Materials

Experimental Model Of Femoral Stem

To represent the stem, a 316L stainless steel tube, 1 mm thick of 14.6 mm external diameter and 70 mm long was manufactured. 316L stainless steel was selected as many femoral stems are made from this material, for example the Exeter™ femoral prosthesis by Stryker®-Howmedica-Osteonics (Stryker Corporation, MI, USA) [113]. The Exeter™ femoral prosthesis was the most popular cemented stem prosthesis in 2003 and 2004 for England and Wales, according to their NJR [4, 114]. To prevent cement penetrating the interior of the tube during insertion, the base of the stem was closed with a circular piece of 316L stainless steel, (Figure 3.1). For the remainder of this document, this stainless steel tube will be referred to as the "representative stem".

Figure 3.1: 316L stainless steel tube used to represent the femoral prosthesis in the experimental model

Experimental Model Of The Femur

To achieve research objectives, a large number of experiments were required. A synthetic test material was selected in preference to femoral cadavers as synthetic

materials are less variable in mechanical properties and dimensions. Synthetic test materials also do not require ethical approval prior to laboratory testing.

To represent the femoral bone, a composite material of e-glass filled epoxy was selected (Sawbones Europe AB, Sweden). E-glass filled epoxy was chosen as this composite was specifically developed to mechanically represent human cortical bone [115]. E-glass/epoxy cylinders of 25.4 mm internal diameter and 4.8 mm thickness were obtained. These cylinders were sectioned into cylinders 60 mm long. To simulate the presence of cancellous bone and provide a mechanical lock between the cement mantle and e-glass/epoxy, 90 diameter 1.2 mm holes were drilled radially at 45° to the tube axis, (Figure 3.2). For the remainder of this document, these edited e-glass/epoxy cylinders will be referred to as the "representative femur".

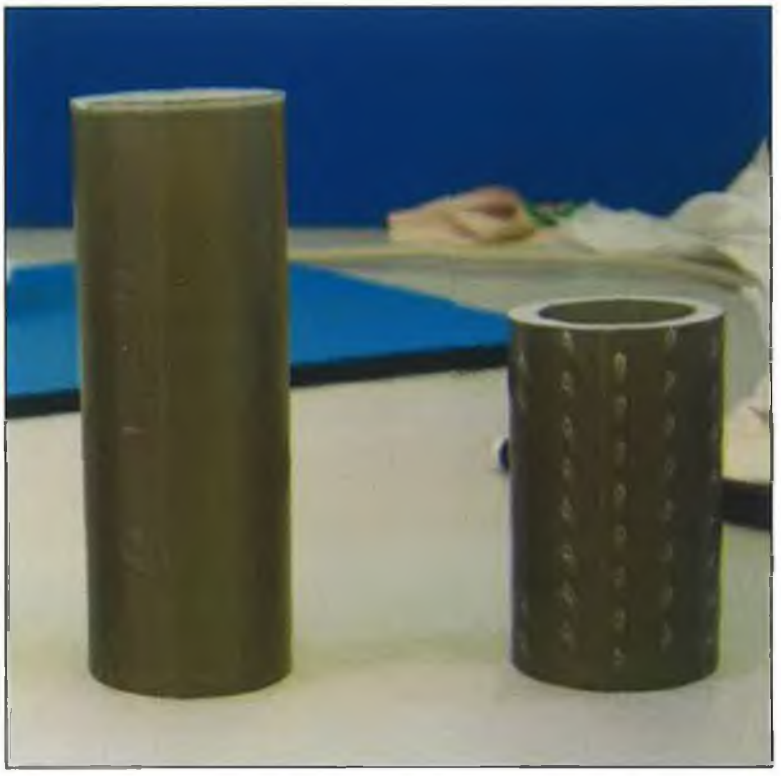

Figure 3.2: E-glass/epoxy cylinders; (Left) Unedited cylinder; (Right) Modified cylinder used to represent the femur in the experimental model

Bone Cement

To investigate the effects of vacuum mixing and pressurisation, CMW® 1 Gentamicin (CMW Laboratories Ltd., UK) bone cement was selected. CMW® 1 was chosen as this brand has a long clinical history and is popular. From the Australia Orthopaedic Association, national joint replacement registry annual 2004 report, CMW® 1 was the fifth most utilised cement brand for the Australian market [5]. CMW® 1 has been in use for over 40 years and therefore has an extensive history [116]. CMW® 1 Gentamicin is similar to CMW® 1 but has one gram of gentamicin antibiotic added per 40 gram polymer powder unit. CMW® 1 Gentamicin has been on the market for over 10 years [117].

SmartSet® HV Gentamicin (CMW Laboratories Ltd., UK) is promoted as having a longer working time and shorter setting time compared to other popular cement brands [118]. From this, SmartSet® HV Gentamicin was selected to investigate the effect of a different cement brand on the residual strain levels.

For the cement prepared under atmospheric conditions, the cement was mixed using an open bowl and spatula arrangement. For the vacuum mixed experiments, the bone cement was mixed using the CEMVAC® disposable tube vacuum mix system (CMW Laboratories Ltd., UK), set at its maximum vacuum level of -86 kPa.

Experimental Rig

An experimental rig was required to fulfil a number of objectives. The experimental rig was required to;

1. Support the representative femur during cement and stem insertion
2. Ensure the representative stem was concentric with the representative femur after insertion
3. Support the assembly during cement pressurisation

Figure 3.3 illustrates the experimental rig utilised, with the representative stem and femur assembled. The experimental rig consisted of a pressuriser, guide fins,

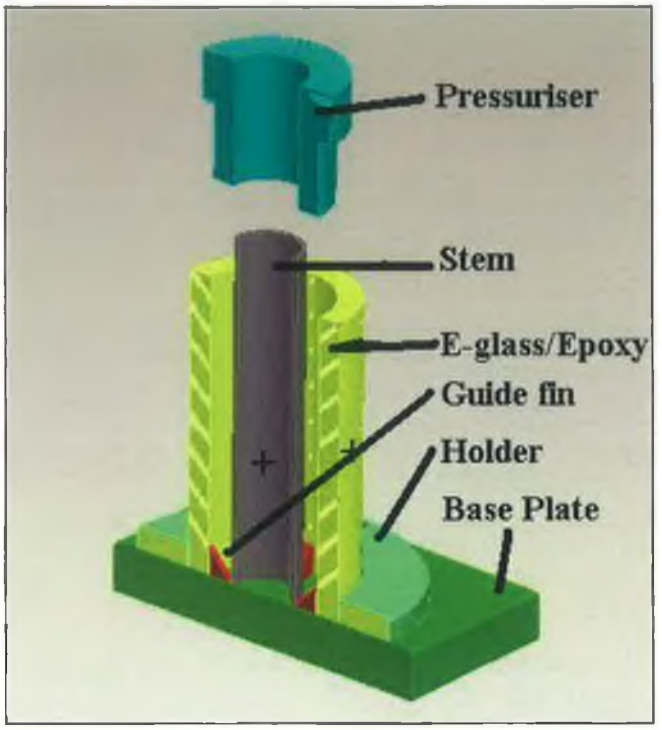

Figure 3.3: CAD cross-section isometric view of experimental rig, with the assembly of the representative stem and femur included

e-glass/epoxy holder and base plate. Aluminium was utilised for each part of the rig. A 1 mm clearance was designed between the representative femur and rig holder. This was to ensure the holder did not adversely interfere with the flow of cement into the drilled holes of the e-glass/epoxy, representative of the cancellous bone structure. Four guide fins where adhered to the base plate to ensure the representative stem was concentric with the representative femur. The 4 guide fins were 1 mm thick and 5 mm high. The pressuriser was designed to freely move between the representative stem and femur. A clearance of 0.2 mm existed between the pressuriser and both the representative stem and femur.

3.2.2 Strain Measurement

Strain Gauges

One of the main objectives of the experimentation is to measure both the hoop

and axial strains during and after polymerisation of the bone cement mantle. The bone cement is in a fluid state initially and therefore it is not possible to directly measure using strain gauges the cements transient and resultant residual strains. To overcome this, the hoop and axial strains induced in the interior of the stainless steel tube and exterior of the e-glass/epoxy composite were measured. This method of measuring the transient and resultant residual strains is based upon similar experimental work by Ahmed *et al* [65] and Roques *et al* [34].

To measure the individual hoop and axial strains, two strain gauges are required for the interior of the stainless steel tube and the exterior of the e-glass/epoxy composite. As the direction of the principal stresses are assumed known (due to model symmetry) and orthogonal to each other, tee rosette strain gauges were selected for both the representative stem and femur in order to ensure the gauges were orthogonal to each other. For the inside of the stainless steel tube, due to physical constraints, a relatively small strain gauge of grid 1.57 mm by 2.03 mm was selected. For the exterior of the e-glass/epoxy, a relative large strain gauge of grid 6.35 mm by 7.37 mm was selected. The relatively larger strain gauge had the advantage of reduced installation complexity.

Due to the exothermic reaction of the bone cement during polymerisation, both the stainless steel tube and e-glass/epoxy composite will undergo a change in temperature. As the strain gauges were bonded to these materials, they also undergo a variation in temperature during polymerisation. This is noteworthy, as temperature variation is the greatest source of apparent strain [119]. Apparent strain is any change in resistance that is not caused by the applied force [120]. Appendix C contains strain gauge and measurement circuit principles.

To reduce apparent strains, A-Alloy (constantan) strain gauges were selected. A-Alloy strain gauges can be processed by the manufacturer to have the same coefficient of thermal expansion as the substrate material [119, 121]. In theory, if both the strain gauge and the substrate material have the same coefficient of thermal expansion, they will both thermally expand and contract at the same rate, significantly reducing apparent strain levels. In addition, A-Alloy's gauge factor is relatively insensitive to varying temperature.

The strain gauge Self Temperature Compensation (STC) of 16 x $10^{-6o}C^{-1}$ (9.0 x $10^{-6o}F^{-1}$) was selected for the representative stem, as the coefficient of thermal expansion of 316L is 16 x $10^{-6o}C^{-1}$ [122]. Following the same methodology, the strain gauge STC of 11 x $10^{-6o}C^{-1}$ (6.0 x $10^{-6o}F^{-1}$) was selected for the representative femur, as the reported coefficient of thermal expansion of e-glass/epoxy is 11 x $10^{-6o}C^{-1}$ [123].

The 350 Ω grid resistance was selected over the 120 Ω grid resistance, as the higher-resistance gauge produces less self-heating effects by a factor of three for the same applied voltage [119, 121]. The higher gauge resistance also has the advantage of decreasing unwanted signal variations caused by lead wire resistance changes with temperature fluctuations.

With the above design parameters considered, the tee rosette strain gauge CEA-09-062UT-350 (Vishay Measurement Group Ltd., UK) was selected for the representative stem. The strain gauge CEA-06-250UT-350 was selected for the representative femur. The stem strain gauge was bonded 25 mm from the base, while the e-glass/epoxy strain gauge was bonded 30 mm from the base. M-Bond 200 adhesive (Vishay Measurement Group Ltd., UK) was utilised to adhere the gauges. Figure 3.4 illustrates the selected stem tee rosette strain gauge before application to the representative stem.

Circuit Configuration

To measure the individual hoop and axial strains in both the representative stem and femur, a quarter-bridge circuit was implemented for each strain gauge. The STC strain gauges would reduce the apparent thermal strains of the system. However, significant error may still occur [119, 121]. To further compensate for temperature variation during cement polymerisation, a quarter-bridge circuit with temperature compensation was implemented for both the representative femurs axial and hoop strain gauges.

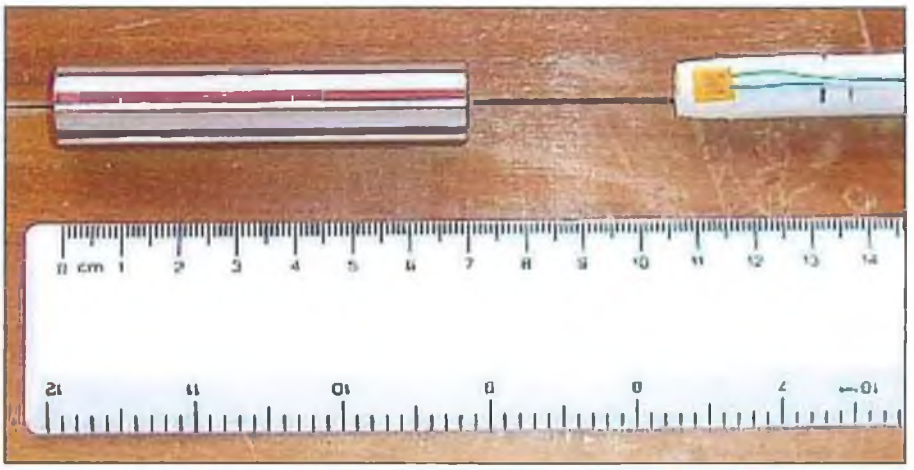

Figure 3.4: Tee rosette strain gauge before application to the representative stem

To implement a quarter bridge with temperature compensation, a second strain gauge is required [119, 120, 124]. The second strain gauge is referred to as the *dummy strain gauge*. The dummy strain gauge should be free from any mechanically induced strain, but yet should always be at the same temperature as the active strain gauge. In principle, when both the active and dummy strain gauges undergo the same temperature change, both gauges will experience the same apparent strains. From the circuit layout illustrated in Figure 3.5, both apparent strains from the strain gauges will cancel each other out, and the bridges state of balance will, in theory, remain unaffected by change in temperature.

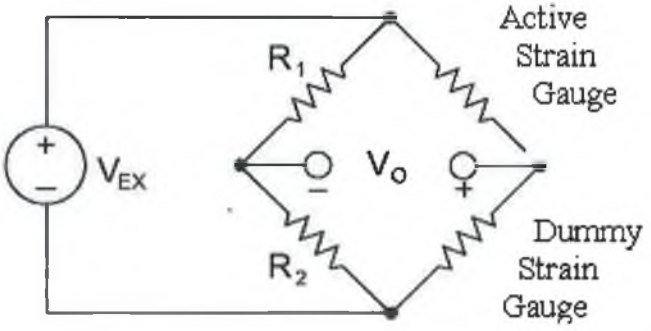

Figure 3.5: Quarter bridge circuit schematic with dummy strain gauge temperature compensation

To implement dummy strain gauge compensation, the dummy gauge was applied

to a 1 mm thick detached piece of e-glass/epoxy. This in turn was applied to the exterior of the representative femur with highly conductive Ceramique™ thermal paste (Arctic Silver Inc., CA, USA). Figure 3.6 illustrates the dummy strain gauge assembly applied to the exterior of the representative femur. This configuration permitted the dummy gauge to closely track the temperature of the active strain gauge but yet remain mechanically isolated from the representative femur, as the thermal paste is not adhesive nor solidifies. The temperatures of the e-glass/epoxy active and dummy strain gauges were measured over a number of experiments. The maximum temperature difference between the e-glass/epoxy active and dummy strain gauge was always less than $\pm 2^{\circ}C$.

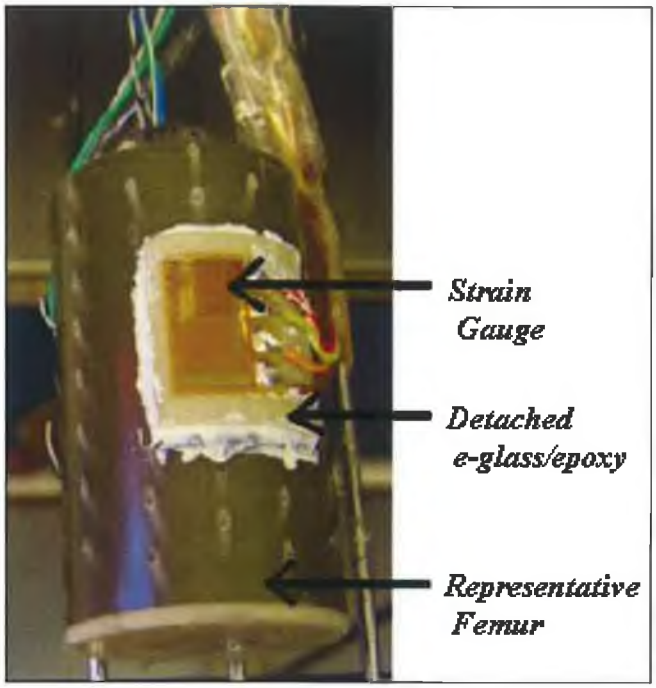

Figure 3.6: Dummy strain gauge assembly applied the exterior of the representative femur. Note the strain gauge is bonded to the thin detached piece of e-glass/epoxy which in turn is applied to the representative femur with thermal paste.

Dummy circuit compensation was attempted for the representative stem. However, due to physical constraints it was unsuccessful. Therefore regular quarter-bridge circuits were implemented for the hoop and axial strain gauges applied to the representative stem.

Circuit Excitation Voltage

For greatest sensitivity to strain, the highest practical excitation voltage should be applied to the Wheatstone bridge circuit [119]. However excessive voltage would induce self heating effects in the strain gauge, which in turn would induce thermal apparent strain errors and instability.

A strain gauge power density of 1.6 to 3.1 kW/m^2 is recommended for a "moderate" level of accuracy from self heating effects [119]. Equation 3.1 relates strain gauge power density with excitation voltage, where "V" represents bridge excitation voltage, "R" represents the gauge resistance and "A" represents the grid area of the strain gauge.

$$\text{Power Density} = \frac{V^2}{4RA} \tag{3.1}$$

Due to the small grid area of the strain gauges bonded to the interior of the representative stem, these gauges were the most susceptible to self heating effects. From Equation 3.1, an excitation voltage of 3.5 V was selected. This resulted in a power density of 2.74 kW/m^2. To reduce equipment costs and virtual instrument programme complexity, the same voltage level was applied to the representative femur strain gauges.

A number of validation tests (n = 5) where performed to confirm this voltage level did not induce noteworthy adverse effects in the strain gauge measurements. These tests involved the application of the selected circuit excitation voltage (3.5 V) to the strain gauges and monitoring of measurements for apparent strains due to self heating effects.

3.2.3 Temperature Measurement

To correlate polymerisation temperature with residual stress, 7 J-type thermocouples, model 401-307 (TC Ltd, UK) were utilised. These thermocouples

were selected as they were of exposed tip form and of light gauge wire, with a wire diameter of 0.2 mm. This combination permitted a relatively fast thermocouple response time (63% of temperature < 1 second) with reduced thermal contamination side effects due to the physical presence of the thermocouple in the system [120].

The thermocouples were positioned in different locations from experiment to experiment to establish the thermal profile of the construct throughout polymerisation history. However, a thermocouple was consistently placed beside both active tee rosette strain gauges to monitor strain gauge transient temperatures. To measure cement mantle temperatures, the thermocouples were typically pushed through the 1.2 mm diameter holes drilled in the representative femur. For interface temperature measurements, the thermocouples were typically preset in place with adhesive during experiment set-up.

For the remainder of this document, the representative stem with applied thermocouple(s) and bonded tee rosette strain gauge will be referred to as the "instrumented stem". Likewise the representative femur with applied thermocouple(s) and bonded active and dummy strain gauges will be referred to as the "instrumented femur".

3.2.4 Data Acquisition

To measure the strain gauge and thermocouple voltages, the NI4351 (National Instrument Inc., TX, USA) data acquisition system was employed. The NI4351 data acquisition system was designed specifically for high-accuracy thermocouple measurement and low analogue voltage measurement [125]. National Instruments report an accuracy of $\pm 0.59^{\circ}C$ for J-type thermocouples with this system. The strain gauge analogue voltages were digitised with 24-bit accuracy.

To simultaneously record the 7 thermocouple inputs and 4 strain gauge inputs, a Labview v7.1 programme was developed. The Labview code is presented in

Appendix D. Due to the large number of applied signals and 24-bit accuracy, the cycle frequency for each port measurement was approximately 7 seconds. The Labview programme exported all data into Microsoft excel format files for analysis.

3.2.5 Experimental Procedure

The experimental rig with assembled instrumented stem and femur was placed in an oven at 37°C for a minimum of 8 hours before the start of each experiment. The data acquisition system was activated a minimum of 4 hours before the initiation of the experiment, as recommend by National Instruments [125].

Figure 3.7 illustrates the oven and data acquisition utilised. Note the oven in the right of the image with the instrumented femur inside. Note the boxes on top of the oven and PC tower, which contained the Wheatstone bridge circuitry and the data acquisition input-boxes.

Figure 3.7: Oven and data acquisition system

To commence the experiment, the data acquisition programme was reset to time zero. At the same time the bone cement mixing commenced. For the cement

prepared under atmospheric conditions, the bone cement was mixed for approximately 50 seconds at approximately two beats per second, using an open bowl and spatula arrangement. For the vacuum mixed experiments, the bone cement was mixed using the CEMVAC® disposable vacuum tube cement mixing system (CMW Laboratories Ltd., UK) as per manufacturer's instructions. The maximum vacuum level of -86 kPa was applied for all vacuum mixed experiments. Figure 3.8 illustrates the utilised CEMVAC® disposable vacuum tube cement mixing system.

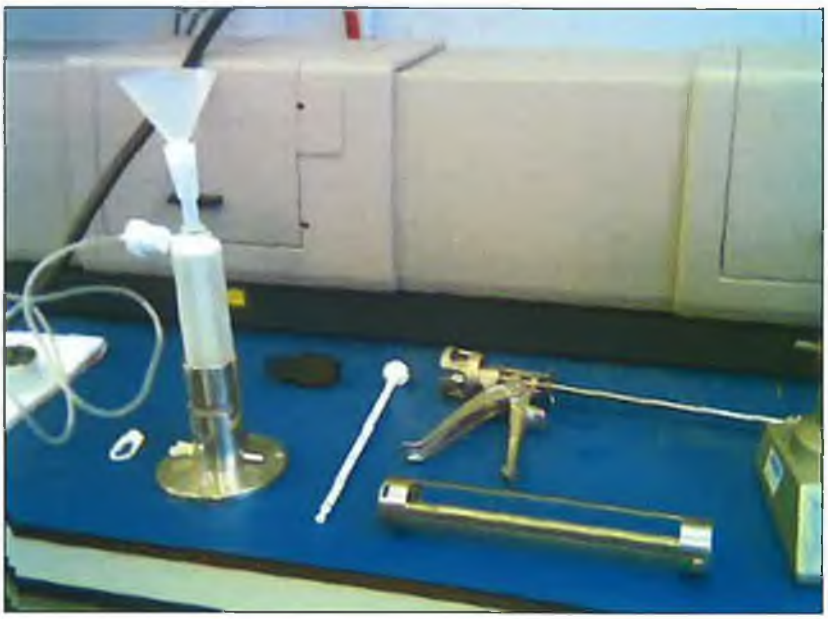

Figure 3.8: CEMVAC® disposable vacuum tube mixing system

After the cement was mixed, the oven door was opened to allow access to the instrumented femur. For the vacuum mixed experiments, the cement was injected into the instrumented femur in a retrograde fashion, as performed by surgeons conforming to modern cementing techniques [17]. For the bowl and spatula mixed cement, the cement was poured or scooped into the instrumented femur. Once this step was complete, the instrumented stem was pushed down into the viscous polymerising bone cement mass. This process extruded the bone cement into the representative cancellous bone structure. Over the final 5 mm displacement before the stem came into contact with the base plate, the 4 guide fins aligned the instrumented stem ensuring an even cement mantle, (Figure 3.9).

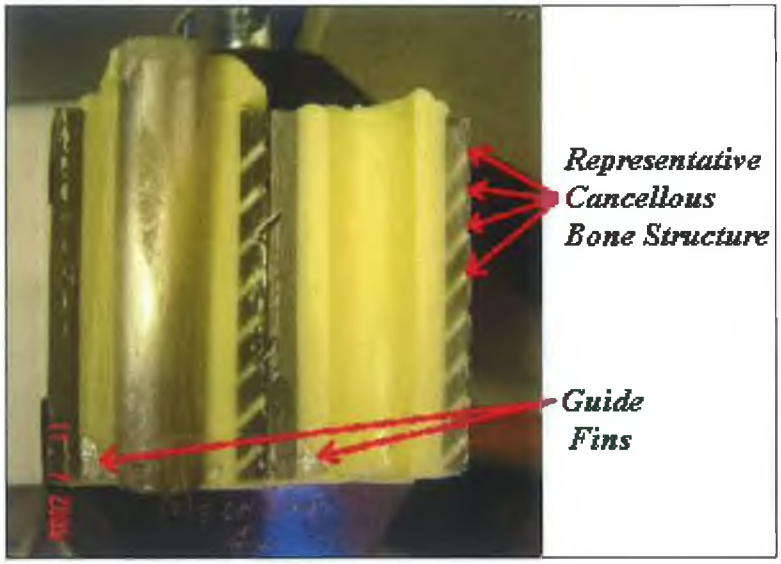

Figure 3.9: Representative femoral construct at breakdown. Note cement ingress into the representative cancellous bone structure and guide fins at base of cement mantle used to ensure an even cement mantle.

Once the instrumented stem was in place, the thermocouples were plunged into the viscous cement mantle at predefined positions and depths. For the pressurised experiments, the pressuriser was next utilised to manually pressurise the viscous cement mantle, (Figure 3.10). Hand pressure was applied (measured between 50 to 80 N based on separate measurements), to the pressuriser to pressurise the cement between -145 kPa and -235 kPa (calculated from above force).

Pressurisation was conducted until the bone cement extruded through the 1.2 mm diameter holes, representative of the cancellous bone structure. After pressurisation, the pressuriser was removed. Finally to complete the experiment the oven door was closed. For a typical experiment, the over door remained opened for approximately 2 to 3 minutes. All strains and temperatures were recorded for a minimum of 3 hours from the initiation of cement mixing.

3.2.6 Validation

Strain Measurement Validation

To validate the strain measurement system, three different weights of known

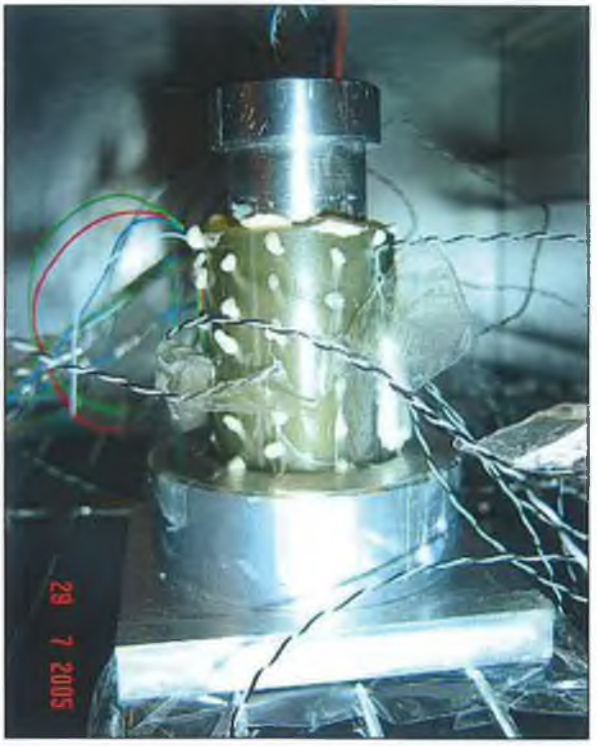

Figure 3.10: Representative femoral construct after pressurisation. Note cement extrusion from representative cancellous bone structure and pressuriser on top of cement mantle

magnitude were applied axially to both the instrumented stem and femur. Taking advantage of the regular geometries, classical mathematical techniques were applied to calculate the compressive axial strains and the indirect tensile hoop strains in the instrumented cylinders. The strain gauge results displayed and logged by the data acquisition system were in line with the calculated theoretical values for each of the three different axial loads applied for both instrumented cylinders.

Thermocouple Measurement Validation

To validate the temperature measurement system, each thermocouple was applied to a beaker of water containing crushed ice cubes. The temperature results displayed and logged by the data acquisition system (approximately $0^{o}C$) was in line with the expected temperature of the ice/water mix.

Instrumented Stem Apparent Strains

Temperature variation is the greatest source of strain gauge error [119]. To establish the degree of erroneous apparent strains experienced by the instrumented stem, knowledge of the transient temperature history of the instrumented stem under experimental conditions was required. To establish this thermal history, a preliminary experiment using CMW® 1 Gentamicin bone cement was performed. From this preliminary experiment, (confirmed by numerous later cemented experiments) it was established that the stem remained at oven temperature (37°C) until it was plunged into the viscous polymerising bone cement. As the cement had not yet significantly exothermed, it was below 37°C and cooled the stem until it reached approximately 33°C. After this, the cement exotherm began to generate significant amounts of thermal energy and the stem rapidly increased in temperature until it reached its maximum temperature of approximately 83°C. After this point the stem gradually declined in temperature until approximately 1.5 hours later when it had returned to ambient oven temperature of 37°C.

To establish the degree of apparent strain, the instrumented stem, free from any mechanical constraints, was placed in the oven. The temperature of the oven was manually changed to simulate the thermal history under experimental conditions. To ensure these tests would not adversely degrade the M-Bond adhesive (adhesive used to bond strain gauge to stem), a maximum temperature of 75°C was employed. Figure 3.11 illustrates a typical apparent strain versus temperature result for the instrumented stem.

From Figure 3.11 it is evident that despite matching the self temperature compensation of the bonded strain gauge with the coefficient of thermal expansion of the substrate material, thermal apparent strains still occur. These thermal apparent strains may be due to a number of reasons, namely:

- The coefficient of thermal expansion of the stem may not exactly match the strain gauge coefficient of thermal expansion

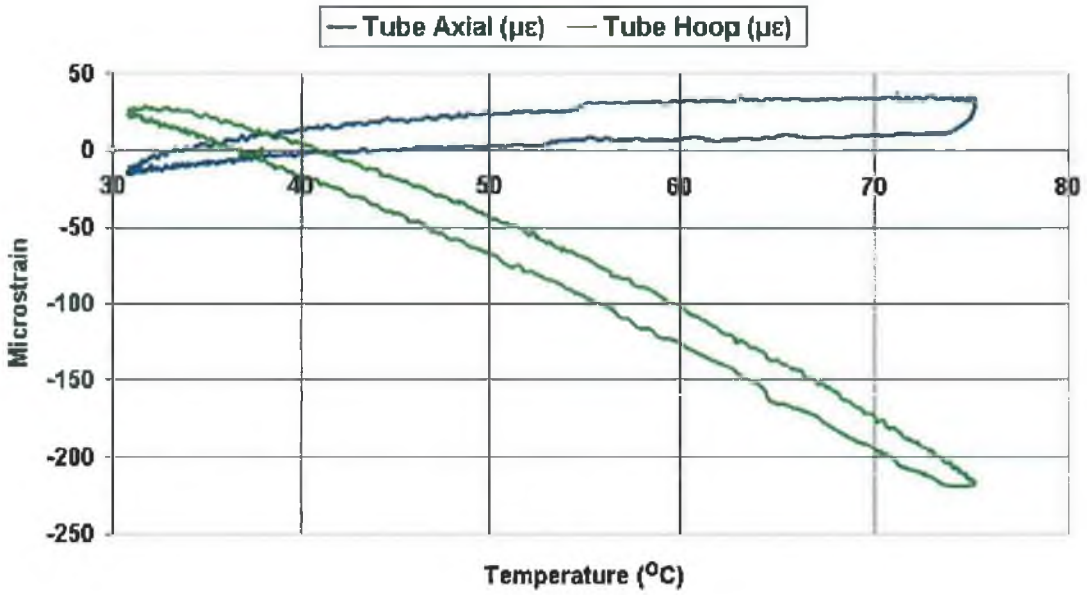

Figure 3.11: Apparent strain levels for instrumented stem under simulated experimental conditions

- The M-Bond adhesive thermal expansion may introduce apparent strain errors
- The gauge factor of the strain gauge changes with temperature
- The resistance of the lead wires changes with temperature
- Hysteresis

From Figure 3.11 it is also evident that apparent strains are not present when the system is brought back to initial temperature. Therefore there are no erroneous apparent strains at the end of the thermal history when the system has returned to 37°C. Approximately 20 experiments were performed to confirm this finding.

To summarise, the measured strains during the exothermic phase of the experiments will consist of residual strain plus apparent strain, but the measured strains after the system has returned to 37°C will consist of residual strain only. For this reason, all reported residual strains were taken 3 hours after the initiation of the experiment to ensure no apparent strains were included.

Instrumented Femur Apparent Strains

To establish the degree of apparent strains experienced by the instrumented femur, its transient temperature history under experimental conditions was initially required. From the preliminary cemented experiment performed, the representative femur remained at its initial temperature of 37°C until the cement was introduced to the system. After this point, the composite gradually declined in temperature until it reached it lowest temperature of approximately 32°C. After this point, the representative femur increased in temperature until it reached its maximum temperature of approximately 55°C. Over the next 1.5 hours the representative femur gradually declined in temperature until it reached ambient oven temperature of 37°C.

Similar to the instrumented stem, to establish the degree of apparent strain, the instrumented femur, free from any mechanical constraints, was placed in the oven and the temperature was manually changed to simulate the thermal history under experimental conditions. Figure 3.12 illustrates a typical apparent strain versus temperature result for the instrumented femur.

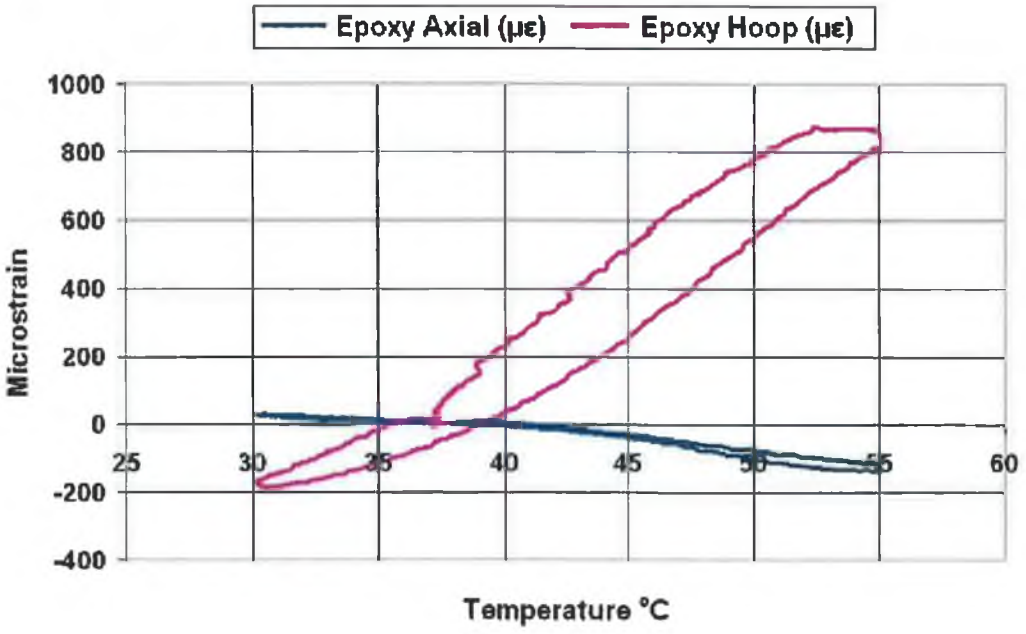

Figure 3.12: Apparent strain versus temperature for the instrumented femur

Despite employing both strain gauge self-temperature-compensation and quarter-bridge with temperature compensation, apparent strains were still present, most notably in the hoop direction. From this result, the author hypothesised that the difference between the level of hoop and axial apparent strains may be due to a different coefficient of thermal expansion for the axial and hoop directions, as the representative femur is a composite material of epoxy matrix and short e-glass fibre reinforcement. If the short e-glass fibres were orientated in a specific direction the mechanical properties of the composite material would not be isotropic.

The author contacted the manufacturer of the e-glass/epoxy cylinders (Sawbones Europe AB, Sweden), and from a personal communication with a representative (Mr. Peter Asker) it was established that the short e-glass fibres of the e-glass/epoxy cylinders were orientated along the axial direction. To confirm the orientation of the e-glass, a number of samples of the e-glass/epoxy composite were examined under a scanning electron microscope. Evidence of e-glass fibre orientation along the longitudinal direction was confirmed, (Figure 3.13). The manufacturer of the composite cylinder did not document this property on its mechanical properties web page or any other part of its web site.

Similar to the instrumented stem, and evident in Figure 3.12, no apparent strains exist after the instrumented femur had returned to 37°C. Therefore, all reported residual strains were taken 3 hours after the initiation of the experiment to ensure no apparent strains were present.

3.3 Results

A total of 29 experiments were performed. Table 3.1 categorises the experiments performed. Results have been divided into two sections, *thermal results* and *residual strain results*. Note the limited number of vacuum mixed experiments performed were due to budget constraints.

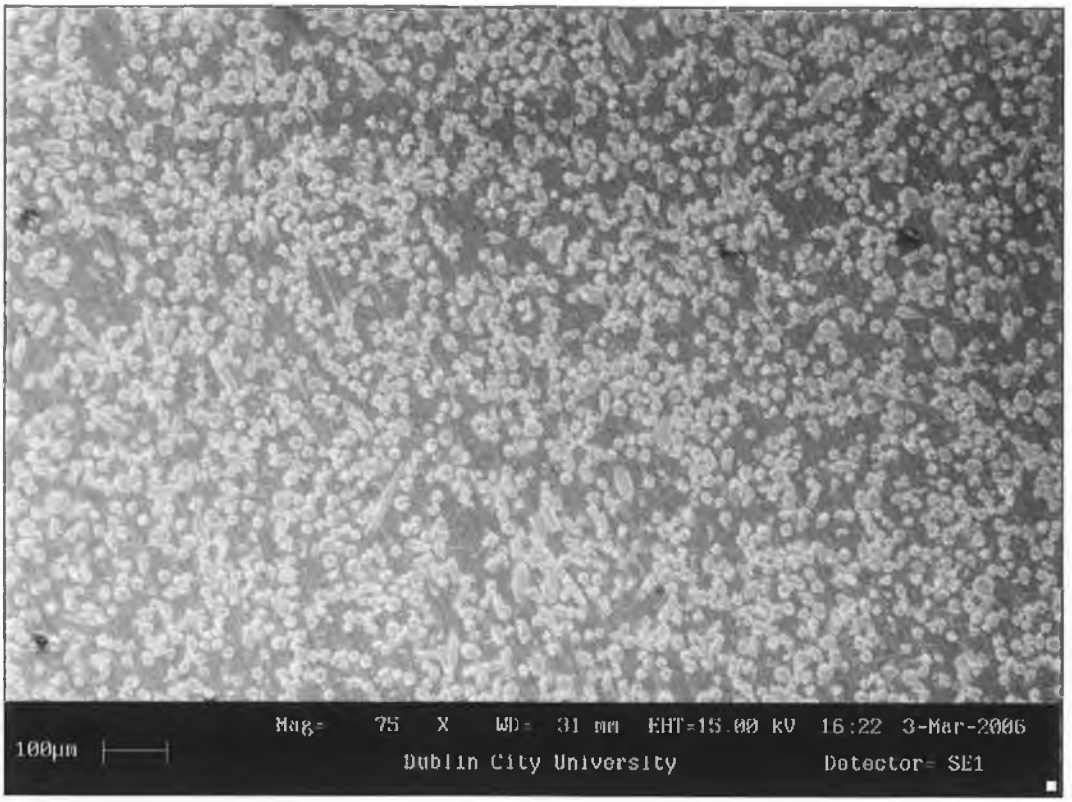

Figure: 3.13: Scanning electron microscope image of e-glass/epoxy composite taken approximately transverse to the axial direction

Cement Brand	Vacuum	Pressure	Comment	No. of experiments
SmartSet® Gentamicin	No	No		5
CMW® 1 Gentamicin	No	No		5
CMW® 1 Gentamicin	Yes	No		3
CMW® 1 Gentamicin	No	Yes		8
CMW® 1 Gentamicin	Yes	Yes		3
CMW® 1 Gentamicin	No	No	Solid stem	2
CMW® 1 Gentamicin	No	No	Debonded stem-cement interface	1
CMW® 1 Gentamicin & SmartSet® Gentamicin	No	No	Debonded e-glass/epoxy–cement interface	2

Table 3.1: Summary of experiments performed

3.3.1 Thermal Results

CMW® 1 Gentamicin Transient Thermal History

Figure 3.14 illustrates a thermal result for CMW® 1 Gentamicin bone cement over the first 600 seconds (10 minutes).

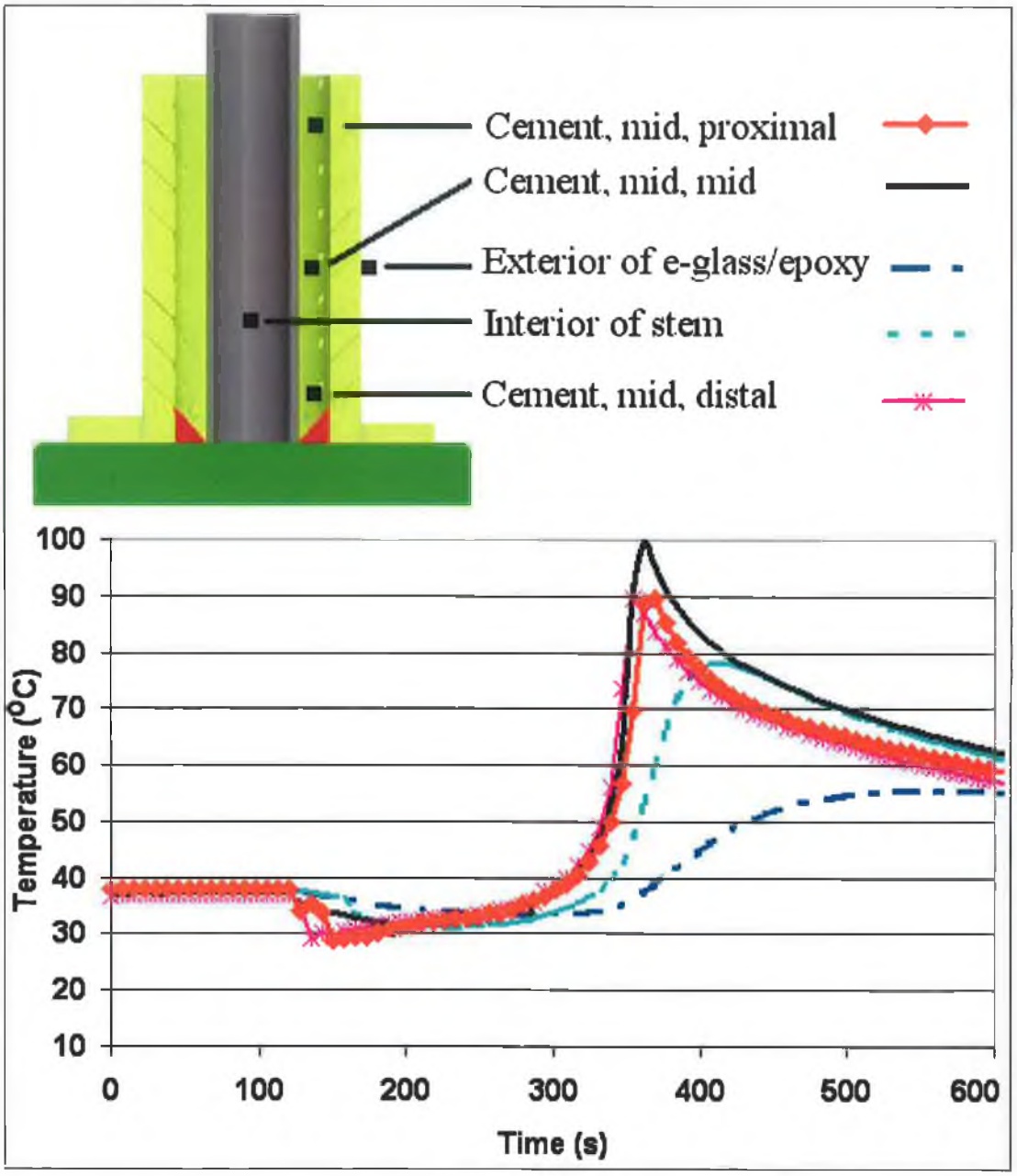

Figure 3.14: Transient thermal result for polymerising CMW® 1 Gentamicin bone cement over the first 600 seconds (10 minutes). Note thermocouple locations are indicated on CAD solid model image.

When the cement was initially introduced to the representative femoral model, it was cooler than both the stem and femur. Therefore for the initial period until approximately 200 seconds, both the representative stem and femur decreased in temperature while the cement mass increased in temperature. After this point the cement mass continued to slowly rise in temperature, rising above that of both the representative stem and femur. After reaching approximately 40°C, the cement mass increased in temperature at a rapid rate. The temperature continued to rise at this rapid rate until the peak cement temperature was reached. After this time the cement began to cool and after approximately 5,400 seconds (1.5 hours) the entire system returned to 37°C. Figure 3.15 illustrates a typical thermal history result over the first 5,400 seconds. Appendix E contains a sample of other CMW® 1 Gentamicin bone cement thermal results over the first 5,400 seconds.

SmartSet® HV Gentamicin Transient Thermal History

SmartSet® HV Gentamicin is promoted as having a longer working time and shorter setting time, compared with other leading brands of cement [118]. This statement is in line with the experimental findings. For CMW® 1 Gentamicin the temperature knee point, i.e. the point when the temperature rate changed from a slow gradual increase in temperature to a rapid increase in temperature, occurred at approximately 40°C. For SmartSet® HV Gentamicin, the knee point occurred at approximately 50°C. Overall polymerisation took approximately 120 seconds longer compared with CMW® 1 Gentamicin, (Figure 3.16). Similar to CMW® 1 Gentamicin, the construct took approximately 5,400 seconds (1.5 hours) to return to 37°C. Appendix F contains a sample of other SmartSet® HV Gentamicin thermal results over the first 800 seconds.

CMW® 1 Gentamicin, Non-Vacuumed, Non-Pressurised

Table 3.2 summarises laboratory conditions and experimental findings, for CMW® 1 Gentamicin non-vacuum mixed, non-pressurised experiments. Experiment number 6 had release agent applied to the interior of instrumented femur. This was performed to investigate the effect of a debonded femur-cement

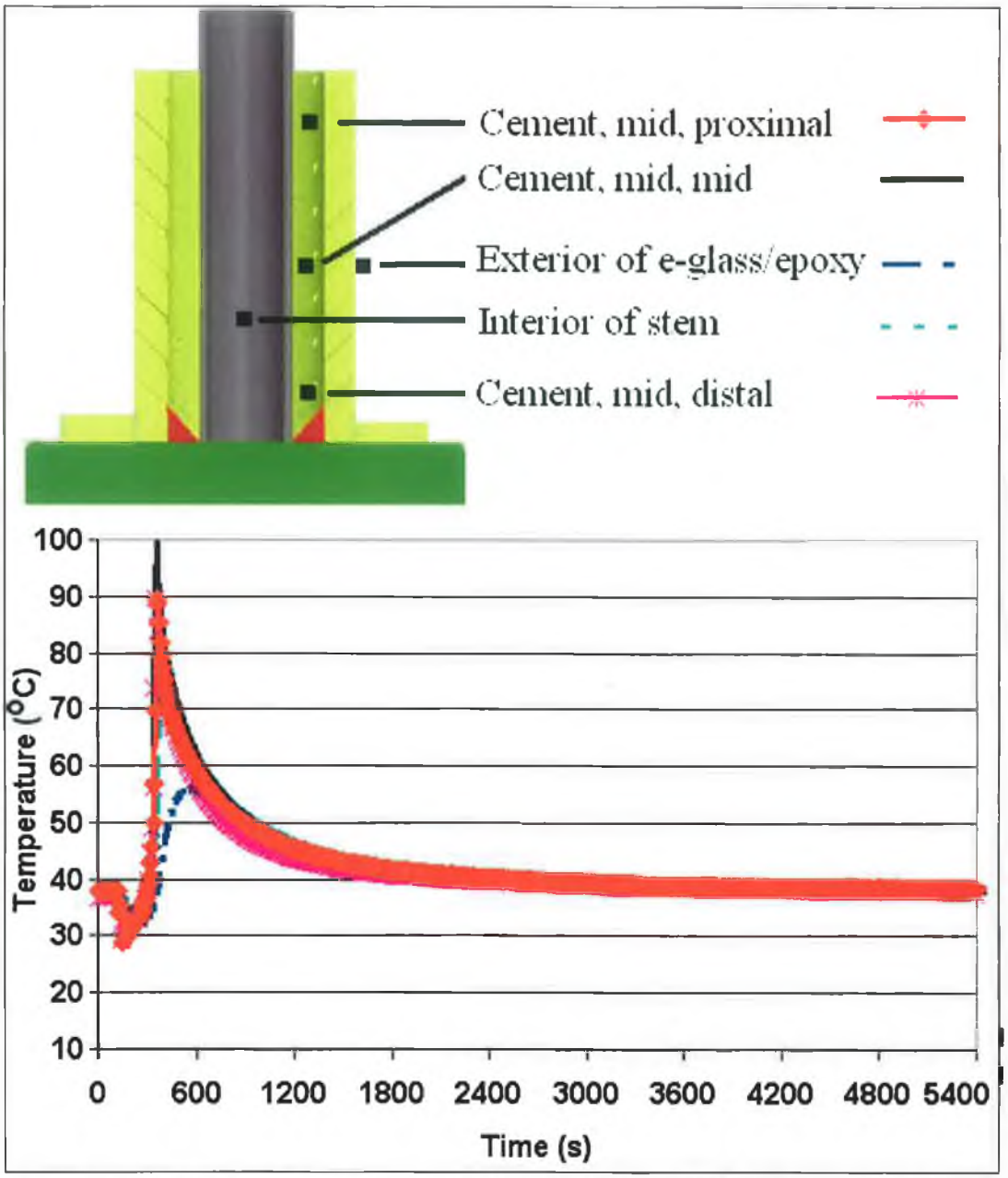

Figure 3.15: Typical thermal history for polymerising CMW® 1 Gentamicin bone cement over the first 5,400 seconds (1.5 hours). Note thermocouple locations are indicated on CAD solid model image.

interface. It is postulated that the release agent would not have any noteworthy thermal consequence, and therefore has been included in Table 3.2. From 6 experiments, the mean peak cement temperature was 98.3°C ± 6.3°C. The mean peak representative stem temperature measured beside the strain gauge was

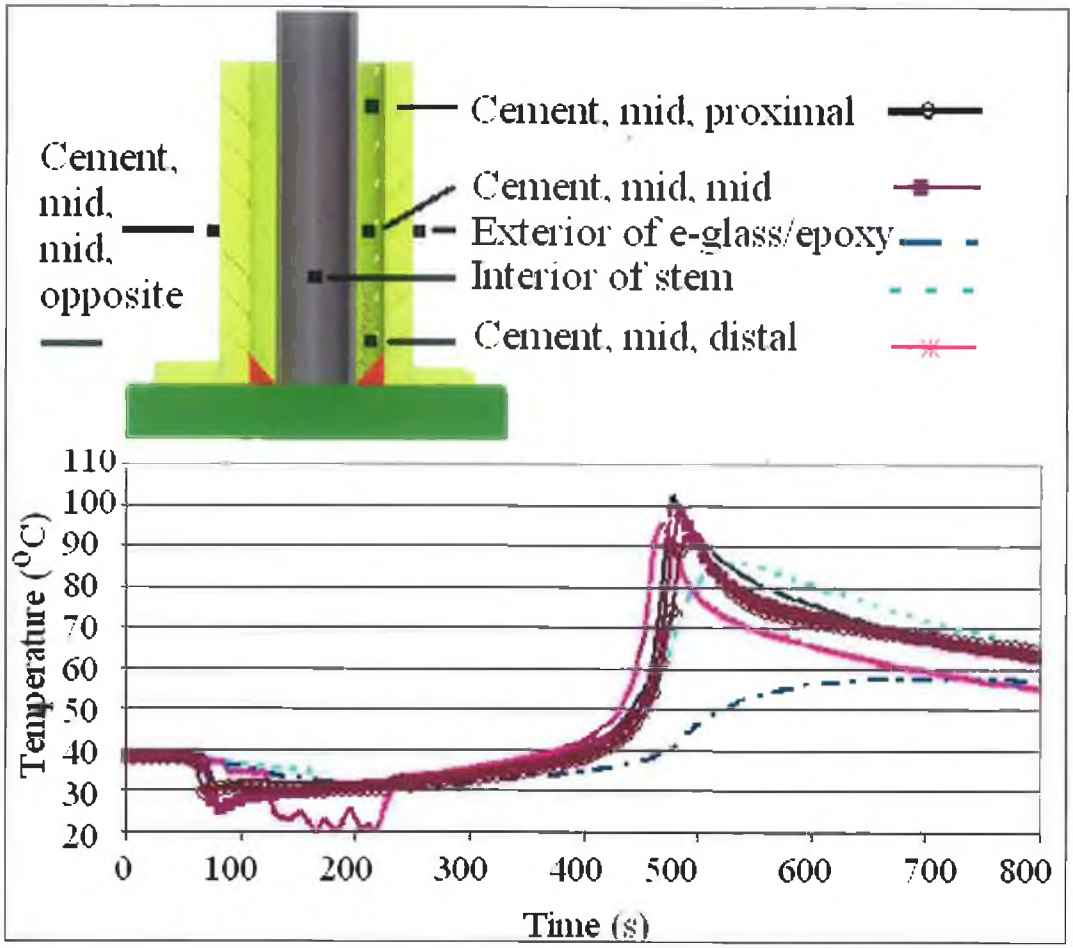

Figure 3.16: Typical thermal history for polymerising SmartSet® HV Gentamicin bone cement over the first 800 seconds (13.3 minutes). Note thermocouple locations are indicated on CAD solid model image.

Experiment Number	Exp. 1	Exp. 2	Exp. 3	Exp. 4	Exp. 5	Exp. 6[a]	Mean	Std. Dev.
Lab. temperature (°C)	25.5	24	22.5	25.3	26	26.5	25.0	1.5
Lab. relative humidity	53%	49%	41%	58%	55%	40%	49%	7.4%
Peak cement temp (°C)	97	97	102	93	109	92	98.3	6.3
Time of peak cement temp (s)	298	318	324	309	279	325	308.8	17.8
Peak stem temp (°C)	82	88	85	88	74	84	83.5	5.2
Time of peak stem temp (s)	338	365	369	362	324	378	356.0	20.6
Peak femur temp (°C)	57	57	56	57	58	56	56.8	0.8
Time of peak femur temp (s)	504	484	550	505	475	543	510.2	30.5

Table 3.2: CMW® 1 Gentamicin thermal results for non-vacuum mixed, non-pressurised experiments

[a] Release agent applied to interior of instrumented femur

83.5°C ± 5.2°C, while the mean peak instrumented femur temperature measured beside the active strain gauge was 56.8°C ± 0.8°C.

SmartSet® HV Gentamicin, Non-Vacuumed, Non-Pressurised

Table 3.3 summarises laboratory conditions and experimental findings for SmartSet® HV gentamicin non-vacuum mixed, non-pressurised experiments. Experiment number 12 had release agent applied to the interior of the instrumented femur. This was performed to investigate the effect of a debonded femur-cement interface. It is postulated that the release agent would not have any noteworthy thermal consequence and therefore has been included in Table 3.3.

Experiment Number	Exp. 7	Exp. 8	Exp. 9	Exp. 10	Exp. 11	Exp. 12[b]	Mean	Std. Dev.
Lab. temperature (°C)	19.5	23.3	23.8	21	21	23	21.9	1.7
Lab. relative humidity	44%	47%	53%	35%	38%	49%	44%	6.8%
Peak cement temp (°C)	102	91	97	107	89	113	99.8	9.3
Time of peak cement temp (s)	476	422	400	369	543	391	433.5	64.8
Peak stem temp (°C)	86	90	90	88.3	83.9	89	87.9	2.4
Time of peak stem temp (s)	529	460	467	414	572	414	476.0	63.3
Peak femur temp (°C)	58	62	60	60	59	56	59.2	2.0
Time of peak femur temp (s)	711	588	603	519	633	618	612.0	62.6

Table 3.3: SmartSet® HV Gentamicin thermal results for non-vacuum mixed, non-pressurised experiments

[b] Release agent applied to interior of instrumented femur

SmartSet® HV Gentamicin bone cement produced about a 120 second longer "working time" compared with CMW® 1 Gentamicin. This is consistent with DePuy's claim that SmartSet® allows for a longer working time [118]. No statistically significant thermal difference was measured between both cement brands for peak cement temperature and peak stem temperature (t-test, $p<0.05$). However, the instrumented femur did measure a statistically significant higher peak temperature for SmartSet® HV Gentamicin over CMW® 1 Gentamicin. This

may be due to the longer period of time at elevated temperature produced by SmartSet® HV Gentamicin

CMW® 1 Gentamicin, Non-Vacuumed, Pressurised

Table 3.4 summarises laboratory conditions and experimental findings for CMW® 1 Gentamicin non-vacuum mixed, pressurised experiments.

Experiment number	Exp 13	Exp 14	Exp 15	Exp 16	Exp 17	Exp 18	Exp 19	Exp 20	Mean	Std. Dev.
Lab. temperature (°C)	N/A	22.2	21.5	22	28	26	26	24	24.2	2.5
Lab. relative humidity	N/A	40%	36%	49%	51%	53%	37%	38%	43%	7.3%
Peak cement temp (°C)	96	89	95	90	104	90	100	103	95.9	6.0
Time of peak cement temp (s)	477	364	431	338	271	295	325	347	356.0	68.3
Peak stem temp (°C)	N/A	84	86	78	84	83	84	82	83.0	2.5
Time of peak stem temp (s)	437	409	451	390	309	325	355	384	382.5	50.6
Peak femur temp (°C)	52	50	56	55	58	58	58	57	55.5	3.0
Time of peak femur temp (s)	762	550	597	523	445	483	506	535	550.1	96.8

Table 3.4: CMW® 1 Gentamicin thermal results for non-vacuum mixed, pressurised experiments

No statistically significant thermal difference was measured for the peak cement, instrumented stem and femur temperatures, between CMW® 1 Gentamicin non-vacuumed, non-pressurised and CMW® 1 Gentamicin non-vacuumed, pressurised experiments (t-test, $p<0.05$). Therefore from the experiments performed, results reveal pressurisation does not have any statistically significant thermal consequence.

CMW® 1 Gentamicin, Vacuum-Mixed, Non-Pressurised

Table 3.5 summarises laboratory conditions and experimental findings for CMW® 1 Gentamicin, vacuum-mixed, non-pressurised experiments. Due to resource constraints, fewer vacuum mixed experiments were performed than

non-vacuum mixed experiments. For experiment number 24, release agent was applied to the exterior of the instrumented stem. This was performed to investigate the effect of a debonded stem-cement interface. It is postulated that the release agent would not have any noteworthy thermal consequence and therefore has been included in Table 3.5.

Experiment Number	Exp. 21	Exp. 22	Exp. 23	Exp. 24[c]	Mean	Std. Dev.
Lab. temperature (°C)	23.5	25.5	25	22	24	1.6
Lab. relative humidity	49%	44%	55%	71%	55%	11.7%
Peak cement temp (°C)	98	98	96	83	93.8	7.2
Time of peak cement temp (s)	325	338	286	363	328.0	32.1
Peak stem temp (°C)	N/A	85	80	62	75.7	12.1
Time of peak stem temp (s)	411	357	324	457	387.3	58.7
Peak femur temp (°C)	54	56	57	54	55.3	1.5
Time of peak femur temp (s)	464	477	444	464	462.3	13.6

Table 3.5: CMW® 1 Gentamicin thermal results for vacuum-mixed, non-pressurised experiments

[c] Release agent applied to exterior of instrumented stem

On comparison between CMW® 1 Gentamicin vacuumed, non-pressurised and CMW® 1 Gentamicin non-vacuumed, non-pressurised, results indicate vacuum mixing may produce slightly lower peak temperatures. The mean vacuum mixed peak cement temperature (93.8°C) was 4.5°C below the mean non-vacuum mixed cement (98.3°C). Likewise, the mean peak stem temperature for vacuum temperature (75.7°C) was 8°C below the mean non-vacuum mixed cement (83.5°C). Finally the mean peak instrumented femur temperature for vacuum mixed cement (55.3°C) was 1.5°C below the mean non-vacuum mixed experiments (56.8°C). However, it is noted that no statistical thermal difference was measured for the peak cement, instrumented stem, and femur temperatures between CMW® 1 Gentamicin non-vacuumed non-pressurised and CMW® 1 Gentamicin vacuum mixed non-pressurised experiments (t-test, $p<0.05$). Therefore, to summarise, there is no statistically significant thermal difference between vacuum mixed and non-vacuum mixed results. However looking at the

means, there is an indication that vacuum mixing may slightly reduce peak temperatures. A greater sample number would be required to confirm if vacuum mixing reduces peak exotherm temperatures. Note Lidgren *et al* [126] also observed a slight reduction in peak temperature for vacuum mixed cement over non-vacuum mixed cement.

CMW® 1 Gentamicin, Vacuum-Mixed, Pressurised

To investigate if the combined actions of vacuum-mixing and pressurisation would have an affect on the thermal profile, three vacuum mixed with pressurisation experiments were performed with CMW® 1 Gentamicin bone cement. As mentioned previously, budget limitations restricted the number of vacuum mix experiments performed. Table 3.6 summarises laboratory conditions and experimental results.

Experiment Number	Exp. 25	Exp. 26	Exp. 27	Mean	Std. Dev.
Lab. temperature (°C)	25	18	24	22	3.8
Lab. relative humidity	37%	61%	48%	49%	12%
Peak cement temp (°C)	87	100	98	95.0	7.0
Time of peak cement temp (s)	331	362	271	321.3	46.3
Peak stem temp (°C)	70	79	73	74.0	4.6
Time of peak stem temp (s)	424	414	309	382.3	63.7
Peak femur temp (°C)	58	56	57	57.0	1.0
Time of peak femur temp (s)	505	558	422	495.0	68.5

Table 3.6: CMW® 1 Gentamicin thermal results for vacuum-mixed, pressurised experiments

No statistically significant thermal difference was measured for peak cement temperature and peak instrumented femur temperature between the CMW® 1 Gentamicin non-vacuumed, non-pressurised and CMW® 1 Gentamicin vacuum-mixed and pressurised experiments (t-test, $p<0.05$). However, the instrumented stem did measure a statistically significant lower temperature. It is postulated that this measured statistical difference is possibly due to a loose thermocouple, as no statistical difference was measured for the bone cement, and it is the bone cement

that heats the stem. Therefore, from this suite of experimental results, it is inferred that the combined action of vacuum mixing and pressurisation does not have any statistically significant thermal consequence.

Solid Stem (CMW® 1 Gentamicin, Non-Vacuumed, Non-Pressurised)

Two experiments were performed using a solid 316L stainless steel cylinder of equal external diameter and length to the instrumented stem, to investigate the effect of a solid stem compared to the instrumented stem. Table 3.7 summarises laboratory conditions and experimental findings, for the solid stem experiments (CMW® 1 Gentamicin non-vacuum mixed, non-pressurised).

Experiment Number	Exp. 28	Exp. 29
Lab. temperature (°C)	23	22.5
Lab. relative humidity	35%	38%
Peak cement temp (°C)	86	79
Time of peak cement temp (s)	437	412
Peak stem temp (°C)	N/A	N/A
Time of peak stem temp (s)	N/A	N/A
Peak femur temp (°C)	52.4	50.5
Time of peak femur temp (s)	554	529

Table 3.7: Thermal results for solid representative stem experiments

The increased heat capacity of the stem reduced the peak cement temperature by approximately 13°C and the instrumented femur peak temperature by approximately 4°C. The solid stem also had the effect of extending the "working time" of the cement by approximately 120 seconds, as the cement took longer to reach the knee point temperature, i.e. the point when the temperature rate changed from a slow gradual increase to a rapid increase in temperature, (Figure 3.17).

Overview Of Thermal Experimental Results

The location of 4 thermocouples were varied from experiment to experiment to

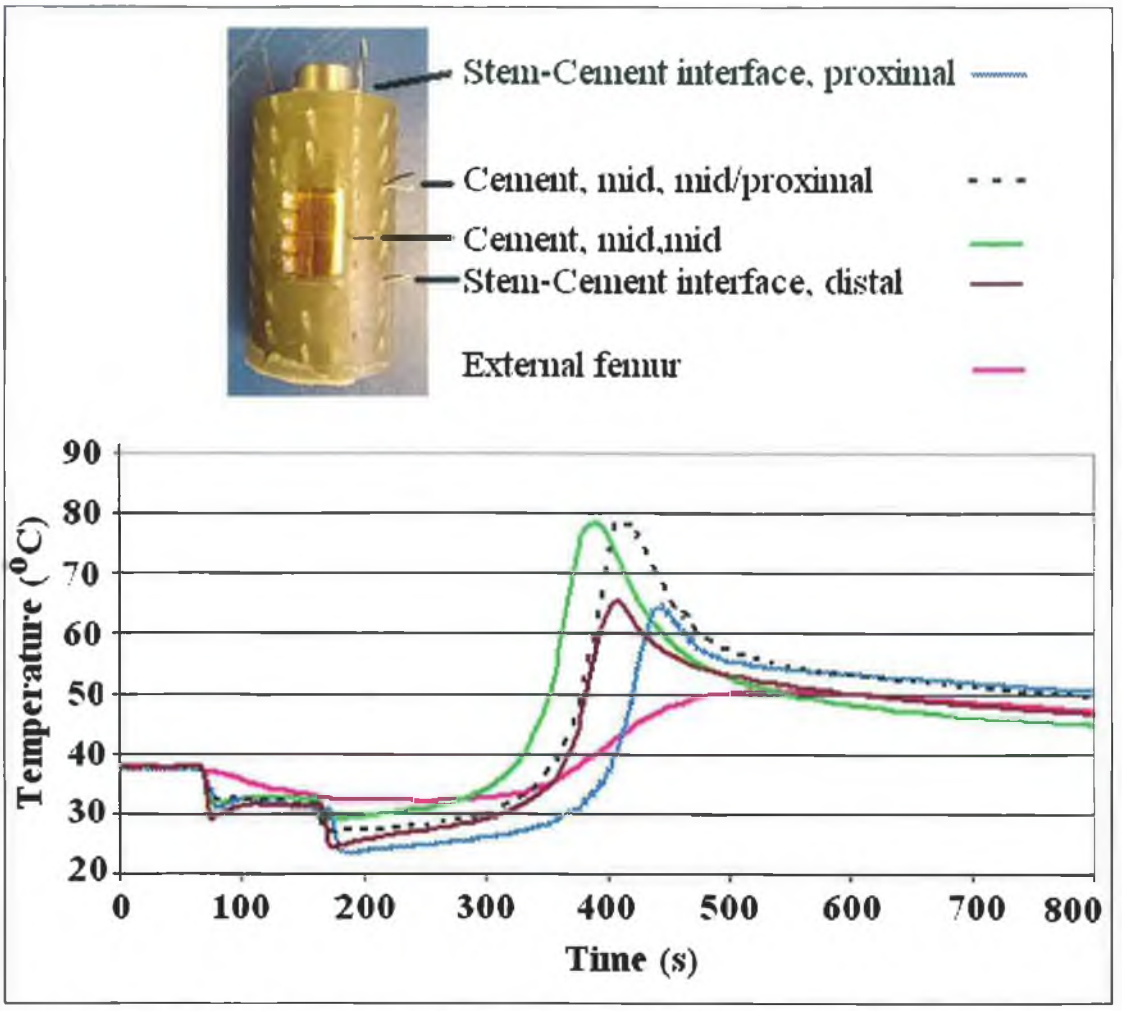

Figure 3.17: Solid representative stem transient thermal history, taken from experiment number 29. Note thermocouple locations are indicated on top of image.

gain an understanding of the temperature history for the entire construct. From this it was noted that the cement at the interfaces were approximately 10 to 20°C below the cement temperature at the centre regions. Also, the majority of the experiments revealed that different locations within the cement mass reached peak temperature at different times. Typically, the cement mass at the distal region reached peak temperature 15 seconds before the cement mass at the proximal region. Table 3.8 summaries the average thermal results for the different initial conditions considered.

Cement Brand	Vacuum	Pressure	No. Of Experiments	Mean Peak Cement Temp. (°C)	Mean Time Of Peak Temp (s)
SmartSet® Gentamicin	No	No	6	99.8	433
CMW® 1 Gentamicin	No	No	6	98.3	309
CMW® 1 Gentamicin	Yes	No	4	93.8	328
CMW® 1 Gentamicin	No	Yes	8	95.9	356
CMW® 1 Gentamicin	Yes	Yes	3	95.0	321
CMW® 1 Gentamicin (Solid Stem)	No	No	2	82.5	424

Table 3.8: Summary of mean experimental thermal results

3.3.2 Strain Results

Instrumented Femur Transient Results

A strain and temperature versus time result measured by the instrumented femur is illustrated in Figure 3.18. The slight hoop tensile force occurring between 66 and 88 seconds is due the insertion of the instrumented stem. As the cement is in a viscous state, the tensile hoop strains return to 0 με after insertion. After approximately 240 seconds, the exterior of the instrumented femur begins to increase in temperature due to the exotherm of the cement. Thus the associated tensile strains were primarily due to thermal apparent strains. At 291 seconds (7 seconds before peak cement temperature), both the axial and hoop strain slopes changed significantly, even though the representative femur temperature is continuing to increase slowly. It is postulated that this change in slope is due to mechanical strain and signifies the initiation of residual strain. For the hoop strain, the temporary inflection of the curve at approximately 460 seconds

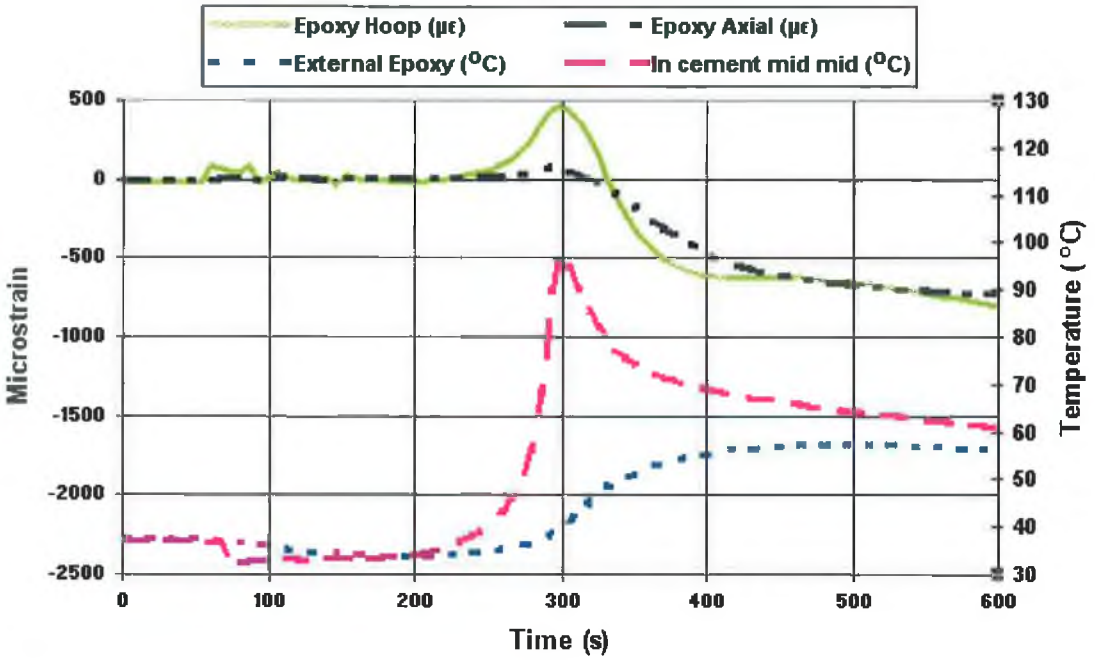

Figure 3.18: Instrumented femur transient strains with associated temperatures over the first 600 seconds (10 minutes). Data taken from experiment number 1 (CMW® 1 Gentamicin, non-vacuumed, non-pressurised).

coincides with the attainment of peak temperature in the femur and is due to apparent strain effects.

Figure 3.19 illustrates a typical instrumented femur result over the first 10,800 seconds (3 hours). From Section 3.2.6, it is evident that the axial strain gauge is less sensitive to thermal effects than the hoop strain gauge. From the validation testing, a maximum thermal strain of approximately 150 με at 55°C was induced due to thermal effects. As the residual axial strains are of significantly greater magnitude than the apparent strains, the measured transient axial strains relay an approximate depiction of the transient strains induced in the representative femur due to cement polymerisation over the curing process. Appendix G contains a sample of instrumented femur transient strain results with associated temperatures over the first 10,800 seconds.

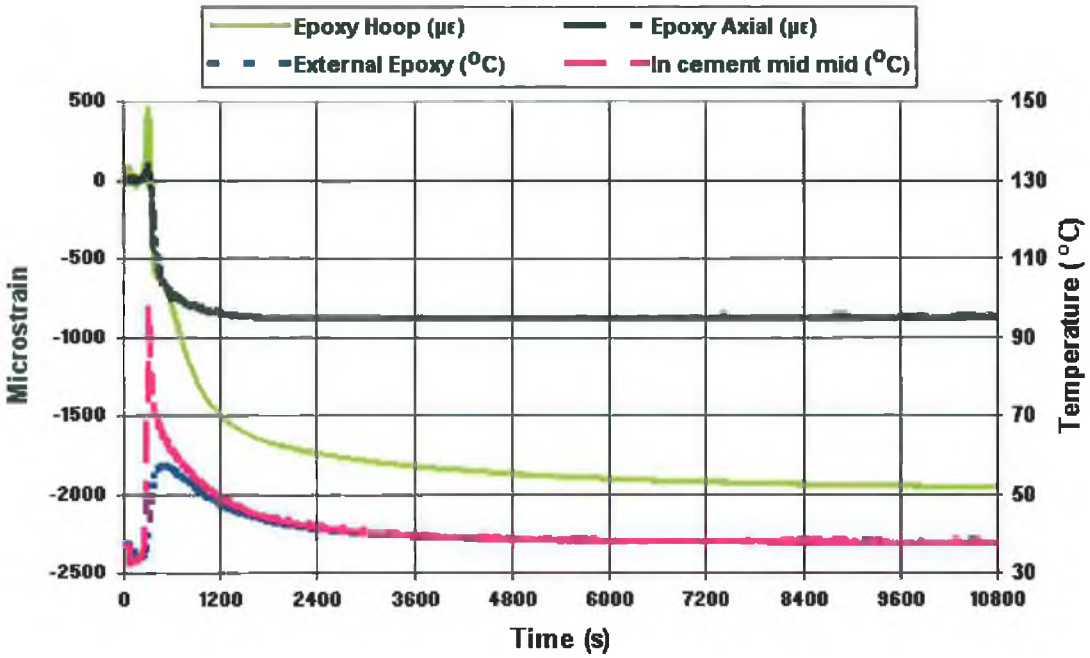

Figure 3.19: Typical instrumented femur strain result with associated temperatures over the first 10,800 seconds (3 hours). Data taken from experiment number 1 (CMW® 1 Gentamicin, non-vacuumed, non-pressurised).

Instrumented Stem Transient Results

Figure 3.20 illustrates a transient strain and associated temperatures versus time result, measured by the instrumented stem over the first 600 seconds (10 minutes). Unlike the instrumented femur, the instrumented stem did not measure any associated strains from the plunging of the stem into the viscous cement mass. This is because the representative stem is much less compliant compared to the representative femur, as the Young's modulus of the representative stem material is approximately 193 GPa [122], while the Young's modulus of the representative femur is approximately 7.6 GPa [115].

For the hoop strain results, both the apparent strain and residual mechanical strain were negative. Therefore it was difficult to distinguish the moment of stress-locking. For the axial strain results, the apparent strain was positive, while the residual mechanical strain was negative. On examination of the transient axial strain result, at 291 seconds (7 seconds before peak cement temperature)

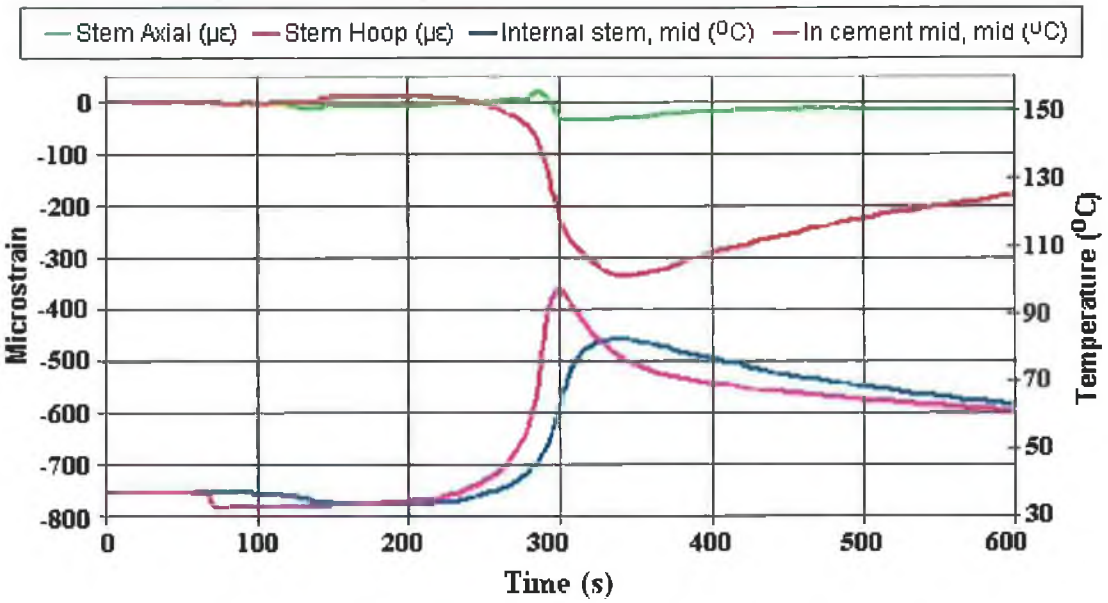

Figure 3.20: Instrumented stem results with associated temperatures over the first 600 seconds (10 minutes). Data taken from experiment number 1 (CMW® 1 Gentamicin, non-vacuumed, non-pressurised).

the slope of the trace changes drastically, even though the instrumented stem temperature is steadily increasing. It is postulated that this change in slope is due to mechanical strain, and signifies the initiation of residual strain. This result is in line with the findings of the instrumented femur, which also first appeared to register mechanical strain 7 seconds before the attainment of peak cement temperature. This result also implies that the bone cement stress-locked some time shortly prior to the first measurement of residual strain. Figure 3.21 illustrates a transient strain and temperature versus time result measured by the instrumented stem over the first 10,800 seconds (3 hours). Appendix H contains a sample of other instrumented stem transient strain results with associated temperatures over the first 10,800 seconds.

CMW® 1 Gentamicin, Non-Vacuumed, Non-Pressurised

Table 3.9 summarises the instrumented stem and femur strain gauge measurements for CMW® 1 Gentamicin non-vacuum mixed, non-pressurised experiments. As mentioned previously, to ensure the reported residual strains did

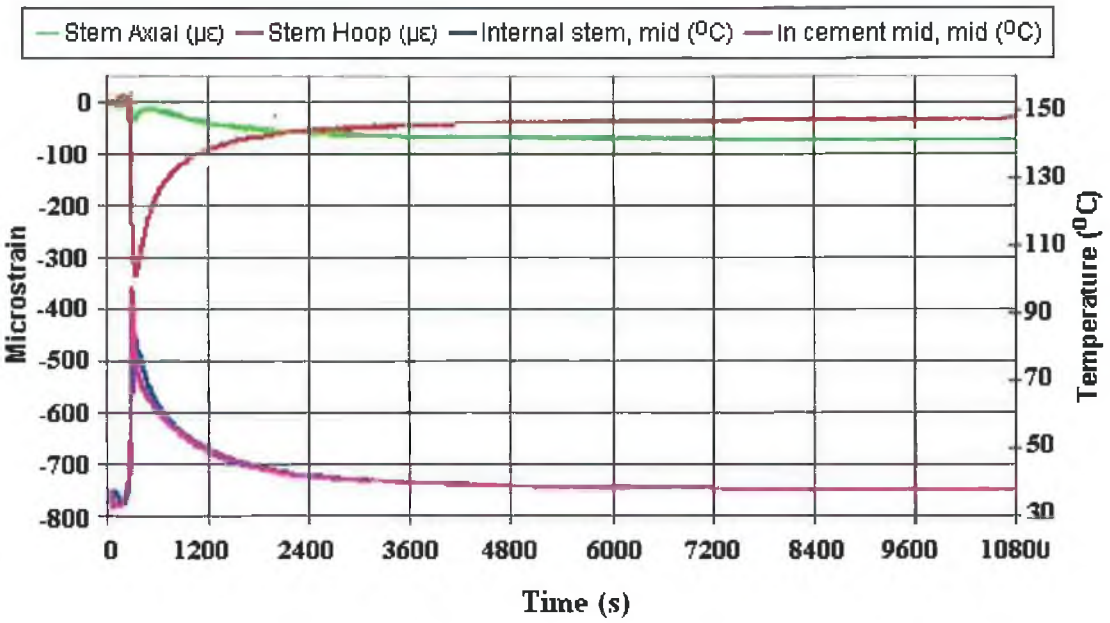

Figure 3.21: Typical instrumented stem strain result with associated temperatures over the first 10,800 seconds (3 hours). Data taken from experiment number 1 (CMW® 1 Gentamicin, non-vacuumed, non-pressurised).

not include any thermal apparent strains, all strain measurements were taken 3 hours after the initiation of mixing.

Experiment Number	Exp. 1	Exp. 2	Exp. 3	Exp. 4	Exp. 5	Mean	Std. Dev
Peak cement temp (°C)	97	97	102	93	109	99.6	6.1
Femur axial (με)	-874	-711	-437	-450	-774	-649.2	196.6
Femur hoop (με)	-1958	-2153	-1295	N/A	N/A	-1802	449.8
Stem axial (με)	-72	-97	-84	-71	-56	-76	15.4
Stem hoop (με)	-31	-52	-49	-57	-65	-50.8	12.6

Table 3.9: CMW® 1 Gentamicin residual strain results for non-vacuumed, non-pressurised experiments

From Table 3.9 it is evident that for the instrumented femur, both the hoop and axial directions registered compression. This was anticipated, as stress-locking occurs at an elevated temperature. After stress-locking, as the bone cement

mantle cools, it wants to reduce in volume due to thermal shrinkage. However the cement mantle is constrained from doing so, due to the mechanical lock between the cement mantle and representative femur. Thus hoop and axial compression is induced in the instrumented femur.

The instrumented stem also registered hoop and axial compression. The axial compression was due to the thermal shrinkage of the cement mantle. From examination of the experiments at breakdown, the cement mantle appeared to be adhered to the instrumented stem. This bond therefore would transfer the shrinkage loads from the cement mantle to the stem. It is postulated that the hoop compression is due to the combination of two factors. Firstly, the e-glass/epoxy composite has a much lower Young's modulus (approximately 7.6 GPa [115]) compared to the 316L stainless steel (approximately 193 GPa [122]). Therefore it is much less stiff and will strain significantly under the residual load, allowing the cement mantle to shrink onto the stem inducing compression. Secondly, the coefficient of thermal shrinkage of both the cement mantle and e-glass/epoxy is much greater than that of the 316L stainless steel. Therefore on cooling both materials may shrink onto the instrumented stem, inducing compression.

SmartSet® HV Gentamicin, Non-Vacuumed, Non-Pressurised

Table 3.10 summarises the instrumented stem and femur strain gauge measurements for non-vacuum mixed, non-pressurised SmartSet® HV Gentamicin bone cement experiments.

Experiment Number	Exp. 7	Exp. 8	Exp. 9	Exp. 10	Exp. 11	Mean	Std. Dev
Peak cement temp (°C)	102	91	97	107	89	97.2	7.5
Femur axial (με)	-137	-263	-633	-629	-356	-403.7	221.7
Femur hoop (με)	-1084	-702	-1778	-2067	-1252	-1376.7	546.6
Stem axial (με)	-86	-79	-92	-44	-92	-78.8	20.3
Stem hoop (με)	-89	-59	-78	-84	-38	-69.5	21.3

Table 3.10: SmartSet® HV Gentamicin residual strain results for non-vacuumed, non-pressurised experiments

Results reveal no statistical difference between the CMW® 1 Gentamicin non-vacuumed non-pressurised and the SmartSet® HV Gentamicin non-vacuumed non-pressurised residual strain results (*t*-test, $p<0.05$). Therefore results indicate both CMW® 1 Gentamicin and SmartSet® HV Gentamicin both produce similar residual stress levels.

CMW® 1 Gentamicin, Non-Vacuumed, Pressurised

Table 3.11 summarises the instrumented stem and femur strain gauge measurements for CMW® 1 Gentamicin non-vacuumed, pressurised experiments.

Experiment Number	Exp. 13	Exp. 15	Exp. 16	Exp. 17	Exp. 18	Exp. 19	Mean	Std. Dev
Peak cement temp (°C)	96	95	90	104	90	100	95.8	5.5
Femur axial (με)	-255	-25	-120	-490	-382	-354	-271.0	173.6
Femur hoop (με)	348	237	102	N/A	N/A	-492	48.8	374.3
Stem axial (με)	-67	-67	-41	-128	-120	-119	-90.3	36.5
Stem hoop (με)	-106	-135	-138	-57	-47	-79	-93.7	38.9

Table 3.11: CMW® 1 Gentamicin residual strain results for non-vacuumed, pressurised experiments

Upon comparison between the CMW® 1 Gentamicin non-vacuumed, non-pressurised with the current results, pressurisation of the curing cement mass had a statistically significant effect on both the femur axial and hoop strains (*t*-test, $p<0.05$). Note the average representative femur axial strains reduced from -649 με to -271 με and the hoop strains from -1802 με to 49 με. With respect to the instrumented stem average strain results, the axial strains increased from -76 με to -90 με and the hoop strains from -51 με to -94 με. The stem hoop strain increase was statistically significant while the stem axial was not statistically significant.

CMW® 1 Gentamicin, Vacuum Mixed, Non-Pressurised

Table 3.12 summarises the instrumented stem and femur strain gauge

measurements for CMW® 1 Gentamicin vacuum mixed, non-pressurised experiments.

Experiment Number	Exp. 21	Exp. 22	Exp. 23	Mean	Std. Dev
Peak cement temp (°C)	98	98	96	97.3	1.2
Femur axial (με)	-136	-974	-1045	-718.3	505.6
Femur hoop (με)	-1220	-1562	-1764	-1515.3	275.0
Stem axial (με)	-35	-72	-102	-69.7	33.6
Stem hoop (με)	-147	N/A	-174	-160.0	19.1

Table 3.12: CMW® 1 Gentamicin residual strain results for vacuum-mixed, non-pressurised experiments

Results reveal no statistical difference between the CMW® 1 Gentamicin non-vacuumed non-pressurised and the current residual strain results (t-test, $p<0.05$). Therefore results indicate vacuum mixing bone cement does not significantly alter the residual stress levels.

CMW® 1 Gentamicin, Vacuum Mixed, Pressurised

Table 3.13 summarises the instrumented stem and femur strain gauge measurements for CMW® 1 Gentamicin vacuum mixed and pressurised experiments.

Experiment Number	Exp. 25	Exp. 26	Mean	Std. Dev
Peak cement temp (°C)	87	100	93.5	9.2
Femur axial (με)	-38	-845	-441.5	570.6
Femur hoop (με)	113	-1160	-523.5	900.1
Stem axial (με)	-64	-95	-79.5	21.9
Stem hoop (με)	-113	-11	-62.0	72.1

Table 3.13: CMW® 1 Gentamicin residual strain results for vacuum mixed, pressurised experiments

Due to variance, a greater sample number would be required before any conclusion(s) regarding the combined actions of vacuum mixing and pressurisation on the resultant residual strain levels, compared with

non-vacuumed non-pressurised experiments, may be drawn. However it is postulated that a significant effect would occur due to the pressurisation action.

Solid Stem (CMW® 1 Gentamicin, Non-Vacuumed, Non-Pressurised)

Table 3.14 summarises the instrumented femur strain gauge measurements for CMW® 1 Gentamicin non-vacuum mixed, non-pressurised experiments performed with a solid representative stem. These experiments were performed to investigate the effect of an increased stem heat capacity.

Experiment Number	Exp. 28	Exp. 29	Mean	Std. Dev
Peak cement temp (°C)	86	79	82.5	4.9
Femur axial (με)	-795	-705	-750.0	63.6
Femur hoop (με)	-1731	-1568	-1649.5	115.3

Table 3.14: Residual strain results for solid stem experiments (CMW® 1 Gentamicin, non-vacuumed, non-pressurised)

Results indicate the use of a solid stem has a negligible impact on the residual strain levels compared with CMW® 1 Gentamicin, non-vacuumed, non-pressurised experimental results, however a greater sample number would be required to confirm these indications.

Debonded Interface

A number of experiments were performed to investigate the effect of a debonded interface. Table 3.15 summarises the initial conditions and measured residual strains. For experiment number 6, the debonded cement-femur interface induced negligible strains in the instrumented femur and appears to have increased the residual strains in the instrumented stem. This may be explained by the thermal shrinkage of the bone cement mantle. It is postulated that, as the cement is debonded from the instrumented femur, it separates from the instrumented femur and shrinks onto the instrumented stem. Therefore the instrumented femur registers no strain while the instrumented stem registers a relatively high residual strain.

Experiment Number	Exp. 6	Exp. 13	Exp. 24
Debonded Interface	Cement-Femur	Cement-Femur	Stem-Cement
Cement brand	CMW 1	SmartSet	CMW 1
Pressurisation	No	Yes	No
Vacuum-mixed	No	No	Yes
Peak cement temp (°C)	92	113	83
Femur axial (με)	-12	-127	-890
Femur hoop (με)	12	-149	-402
Stem axial (με)	-133	-67	-4
Stem hoop (με)	-73	-50	-112

Table 3.15: Residual strain results for debonded interface experiments

For experiment number 13, the release agent didn't seem to be completely effective, as compressive residual strains were induced in the instrumented femur. The adherence of the cement may be due to the pressurisation of the cement mantle. The pressurisation may have forced the viscous cement to form a partial physical lock with the instrumented femur.

Experiment number 24 had release agent applied to the stem-cement interface. This had the effect of reducing stem axial strains to a negligible level. It is postulated that the cement was unable to adhere to the stem, thus allowing the cement to slide over the stem. The instrumented stem measured significant hoop strains. It is postulated that this may be due to the shrinkage of the cement mantle in the hoop direction onto the stem. The instrumented femur registered significant hoop and axial strains, however the axial strain was significantly greater than the hoop strain. In every other non-pressurised experiment, the hoop strain was significantly greater than the axial strain. This may be due to the representative femur taking the entire axial shrinkage load, as the stem-cement interface was unable to support the axial shrinkage. These experiments support the hypothesis that shrinkage is the primarily factor in the generation of residual stress. Table 3.16 summarises the mean residual strain results.

3.4 Discussion

Peak Temperatures

No statistically significant peak temperature difference was measured between

Cement (Comment)	Vacuum	Pressure	No. Of Experiments	Stem Axial (με)	Stem Hoop (με)	Epoxy Axial (με)	Epoxy Hoop (με)
SmartSet® Gentamicin	No	No	5	-79	-70	-404	-1377
CMW® 1 Gentamicin	No	No	5	-76	-51	-649	-1802
CMW® 1 Gentamicin	No	Yes	6	-90	-94	-271	49
CMW® 1 Gentamicin	Yes	No	3	-70	-160	-718	-1515
CMW® 1 Gentamicin	Yes	Yes	2	-80	-62	-442	-524
CMW® 1 Gentamicin (Solid Stem)	No	No	2	N/A	N/A	-750	-1650

Table 3.16: Summary of mean residual strain results

vacuum mixed and non-vacuum mixed cement. Likewise no statistically significant peak temperature difference was measured between pressurised and non-pressurised experiments. Thus from the experimental work performed, it is evident that both vacuum-mixing and pressurisation have negligible effects on the cement thermal profile during polymerisation.

No statistically significant thermal difference was measured between CMW® 1 Gentamicin and SmartSet® HV Gentamicin for both cement and stem peak temperature magnitudes. However, the instrumented femur did measure a statistically significant higher peak temperature for SmartSet® HV Gentamicin compared to the CMW® 1 Gentamicin experiments. It is postulated that this is due to the longer period of time the cement was at an elevated temperature, due to SmartSet® HV Gentamicin's slower polymerisation rate.

Time To Peak Temperature

A statistically significant time difference was measured between CMW® 1

Gentamicin and SmartSet® HV Gentamicin bone cements. SmartSet® HV Gentamicin reached its peak cement temperature approximately 120 seconds after CMW® 1 Gentamicin. This is consistent with DePuy's claim that SmartSet® allows for greater working time [118].

Residual Strain

The first measurement of residual strain typically occurred 7 seconds before the attainment of peak cement temperature. Over half the experiments first recorded residual strain to occur between 6 and 8 seconds before the attainment of peak cement temperature. Only one experiment from 29 recorded residual strain initiation after the attainment of peak cement temperature. These results are similar to experimental findings by a number of authors [39, 105, 106] who reported the first occurrence of residual strain to approximately coincide with the attainment of maximum temperature in the cement.

Effect Of Cement Brand

No statistically significant residual strain differences were measured between CMW® 1 Gentamicin and SmartSet® HV Gentamicin bone cements. This was to be expected as both cements produced similar peak temperatures at the moment of stress-locking.

Effect Of Vacuum Mixing

No statistically significant change in residual strain was measured between cement mixed under vacuum conditions with cement mixed under atmospheric conditions. This is significant, as previous research established a clear relationship between pore reduction mixing methods and increased cement shrinkage [33, 74, 98]. Orr *et al* [33] reported almost 4 times more shrinkage (7.3%) for -86 kPa vacuum mixed cement over non-vacuum mixed cement (1.95%), which laid the foundation for the premise that greater vacuum levels may induce greater residual stress. The fact that no significant increase in cement residual strain was recorded between non-vacuum mixed cement and cement

prepared under a vacuum of -86 kPa suggests that the dominant shrinkage mechanism after the cement has attained its properties as a solid is thermal shrinkage.

Effect Of Pressurisation

Noteworthy residual strain differences were measured between the experiments involving non-pressurised and pressurised bone cement mantles. The average instrumented femur hoop strains were reduced from -1656 με to -116 με by pressurisation. This is associated with a significant relief of compressive hoop stress in the bone analogue material due to pressurisation. The average instrumented stem hoop strains increased from -71 με to -86 με. This points to a small net compressive effect on the stem hoop stresses due to pressurisation. For the axial strains, the average instrumented femur values were reduced from -690 με to -280 με, while the average axial instrumented stem strains slightly increased from -74 με to -88 με. Thus the overall pressurisation effect appears to be a significant reduction in the residual strains in the representative femur, with a slight increase in residual strains for the representative stem.

These changes may be explained when one considers the state of stress induced in the representative stem and femur by the pressurised cement just before the moment of stress-locking. At this moment the bone cement is under compression, due to the applied load. This in turn induces a compressive hoop stress on the stainless steel tube and a tensile hoop stress in the e-glass/epoxy. At the moment of stress-locking the tube remains in hoop compression and the e-glass/epoxy in hoop tension. As the bone cement cools it shrinks due to thermal contraction. Thus for the e-glass/epoxy, the hoop strains change from hoop tension to hoop compression. As the Young's modulus of the e-glass/epoxy is much lower than that of the stem, both the cement mantle and e-glass/epoxy contract about the stem inducing hoop compression. Thus for the experimental model employed, pressurisation reduced the e-glass/epoxy hoop strains (average measured reduction of 1540 με) and increased the tube hoop compression strains (average measured increase of 15 με).

It is hypothesised that for the *in vivo* scenario, after the cement solidifies and cools, hoop compression would be induced in the femur and hoop tension in the stem. This is because the Young's modulus of femoral bone is much greater than that of the e-glass/epoxy. Therefore *in vivo* the cement mantle and femur will not shrink onto the stem as for our experimental model, but induce tensile hoop loading to the stem, due to negligible hoop contraction in the femur. Thus, it is hypothesised based on experimental findings, that pressurisation of the curing cement mantle *in vivo* will reduce both residual stresses in the femur and stem.

Limitations

The experimental model attempted to represent the *in vivo* scenario as closely as feasible, but yet measure the transient temperatures and residual strains. A number of differences exist between the *in vitro* model utilised and a typical cemented femoral arthroplasty. The more significant of these differences may be enumerated as follows;

1. The bone cement mantle was 5.4 mm thick in the *in vitro* model. While bone cement mantles of this thickness do occur, typical modern cementing techniques employ thinner cement mantles, at approximately 3 mm thick. The relatively thick cement mantle was a deliberate design feature to maximise the cement polymerisation temperature and therefore to maximise residual strain levels, while still remaining within cement mantle thicknesses found *in vivo*.

2. A 316L stainless steel tube of 1 mm thickness was utilised to represent the femoral prosthesis. This was employed in order to measure the transient residual strains. *In vivo,* the stem would be solid and therefore have a much greater "heat sink" capacity. Two experiments were performed with a non-instrumented solid stem to investigate this effect. Results indicate that the use of the instrumented stem instead of a solid stem had the effect of increasing the peak cement temperature by approximately 13°C (from approximately 82°C with the solid stem to approximately 95°C with the instrumented stem) and increasing the

instrumented femur peak temperature by approximately 4°C (from approximately 52°C with the solid stem to approximately 56°C with the instrumented stem). The instrumented stem also had the effect of reducing the "working time" of the cement by approximately 120 seconds, as the cement took a shorter period of time to reach the knee point temperature (when the temperature rate changes from a slow gradual temperature increase to a rapid temperature increase).

3. To represent the femur, a cylinder of e-glass/epoxy composite, manufactured by Sawbones Europe AB, Sweden, was utilised. While this cylinder was designed by Sawbones to represent the mechanical properties of bone, it had a number of limitations. The more significant of these included; the transverse Young's modulus of approximately 3 GPa for e-glass/epoxy compared with approximately 9 GPa for femoral bone and the specific heat capacity of approximately 880 J/kg-K for the e-glass/epoxy, compared with approximately 1,300 J/kg-K for femoral bone.

4. For the *in vitro* model, the exterior of the representative femur was in contact with air at 37°C. *In vivo* the exterior of the femur is in contact with body tissue (fascia, muscle, fat etc). The aforementioned tissue would have a much greater thermal conductivity and heat capacity compared with air. Also this tissue would have a blood supply. Therefore it is postulated that due to the aforementioned reasons, the exterior of the femur *in vivo* would remain close to 37°C throughout bone cement polymerisation. From the experimental work, the exterior of the representative femur reached a typical peak temperature of 56°C. While the exterior of the representative femur could have been encased in a fluid of 37°C, this was not implemented to ensure the reliable operation of the strain gauges.

Despite these limitations, the *in vitro* model employed represents the most anatomically representative experimental model utilised to date to quantify the

transient level of residual strains in the femoral construct due to cement polymerisation. The *in vitro* model utilised was the first to;

1. Simulate the presence of the cancellous bone structure, and ensure a mechanical lock between the cement mantle and the representative femur.

2. To perform the experimentation at body temperature (37°C).

3. To record the transient residual strains induced in the representative femur.

3.5 Chapter Summary

This chapter reported the transient temperatures and strains induced in a representative femoral construct during bone cement polymerisation and up to three hours from the initiation of mixing. The experimental findings may be enumerated as follows;

1. Vacuum mixing does not significantly effect the cement temperatures during polymerisation.

2. Pressurisation does not significantly effect the cement temperatures during polymerisation.

3. CMW® 1 Gentamicin and SmartSet® HV Gentamicin bone cements both produced equally high peak cement temperatures.

4. The first registration of residual strain occurs approximately 7 seconds before the attainment of peak cement temperature. This indicates stress-locking occurred some time shortly previous to this point i.e. 7 seconds before peak temperature.

5. No statistically significant residual stress differences were measured between CMW® 1 Gentamicin and SmartSet® HV Gentamicin.

6. Vacuum-mixing bone cement does not appear to increase residual stress levels. This result implies that thermal shrinkage is the dominant process for residual stress formation.

7. Pressurisation of the polymerising cement mantle had a distinct effect on the residual strain magnitudes. Experimental results indicate that a significant reduction in residual stresses may be achieved *in vivo* by cement mantle pressurisation.

Chapter 4

Finite Element Analysis Of *In Vitro* Residual Stresses

4.1 Introduction

The objective of this chapter is to develop a finite element model of the experimental apparatus, and use it to validate the analysis methodology, which can be applied to more geometrically complex situations.

In order to establish a modelling methodology for the prediction of residual stresses, the following steps were followed;

1. Simple geometry and uniform temperature distribution
   - Compared to published Morse taper experimental results
   - Compared to a theoretical model
2. Simple geometry with heat generation abilities
   - Compared to experimental results and the literature
3. Physiological geometry with heat generation

Figure 4.1 outlines the modelling development for the prediction of residual stress and the fulfillment of thesis objectives.

Figure 4.1: Flow chart of model development and the fulfillment of thesis objectives

4.2 Preliminary Finite Element Analysis: Morse Taper Experiments

As a foundation for the development of a future model, and to establish confidence in the finite element methodology, the experimental work published by Orr *et al* [33] was initially modelled. Orr *et al* [33] investigated whether thermal cooling alone from the moment of stress-locking was sufficient to form cracks in bone cement. Section 2.4.3 summarises the experimental methodology and results. As the Morse taper and bone cement ring were of known uniform temperature at the moment of assembly (representative of the moment of stress-locking) and as femoral effects were ignored due to the assumption of the debonded cement-femur interface, this allowed for a relatively simple finite element model.

4.2.1 Model Definition

The objectives of this research include the modelling of an anatomically representative femoral hip construct, as defined in Section 1.5. Due to the femurs complex geometry, symmetry may not be employed to reduce the anatomical model from 3-D to 2-D. Therefore, as a foundation to future modelling, and to impart confidence in the finite element methodology, the experimental work published by Orr *et al* [33] was modelled in 3-D. To validate the methodology, the FEA results were compared with both the experimental findings published by Orr *et al,* and a theoretical model developed from thick wall cylinder theory.

The ANSYS FEA software product, developed by ANSYS Inc., (PA, USA) was selected to perform all finite element modelling. ANSYS is a comprehensive, general-purpose, finite element package and a leading FEA programme for over 20 years [127]. ANSYS has the capability to model problems in areas of structural mechanics, thermal analysis, fluid mechanics, acoustics and electromagnetics. ANSYS may also perform static or transient, linear or non-linear and coupled field problems. Pertaining to this research the more important

capabilities of ANSYS include its ability to solve mechanical, thermal, contact and coupled environment problems.

Geometry

The Morse taper and bone cement sample geometries were developed and assembled with Pro-Engineer 2001 (PTC Inc., MA, USA). Material geometries were matched with those reported by Orr *et al* [33], and defined in Section 2.4.3. To reduce the number of nodes required to mesh the Morse taper geometry, a 21 mm segment of the Morse taper total geometry was considered. It is postulated that this assumption would not affect the residual stress levels, as the Morse taper has a Young's modulus approximately 90 times that of the bone cement. A taper of 0.05 mm per mm exists for the Morse taper utilised in the experimental work [128, 129]. Therefore over the 7 mm contact length of the cement sample, a taper of 0.35 mm existed. Due to this relatively small taper, a regular non-tapered solid cylinder was assumed. The assembled geometries were imported into ANSYS v7.1.

Element

The choice of element used to model the system is important, as it defines what the finite element software will calculate at each node. It also has a bearing on the mesh distribution and accuracy of the model. To enable the same methodology to be applied to later models in the mechanical environment, the chosen element to mesh the Morse taper must also be suitable for the 3-D anatomically representative model, as discussed in research objectives, (Section 1.5).

To model the anatomical geometry effectively the mechanical environment element must have the ability to calculate displacement, (UX, UY and UZ) and temperature (TEMP) at each node. Due to the relatively complex geometry of the femur, cement mantle and stem, the element must also have the ability to mesh complex geometries. In conjunction with this, the chosen element must be compatible with a similar thermal element to permit coupled field analysis.

Future models will employ coupled field analysis to initially model the bone cement exothermic reaction during polymerisation in the thermal environment and subsequently model and predict the level of residual stress in the mechanical environment.

A number of different elements fulfil the given criteria. These elements include SOLID45 (hexahedral 8-node brick element), SOLID92 (tetrahedral 10-node element) and SOLID95 (hexahedral 20-node brick element) [130]. The SOLID92 element was selected due to its multi-node tetrahedral structure. This structure permits the element to mesh curved boundaries and tolerate irregular shapes without much loss of accuracy [130], required for the 3-D modelling of the artificial hip construct in later models. Research by Ramos *et al* [131] evaluated and compared tetrahedral versus hexahedral finite element elements based on a femur geometry. The authors concluded tetrahedral linear elements were more accurate than hexahedral elements. Figure 4.2 graphically describes the chosen 10-node tetrahedral element, SOLID92.

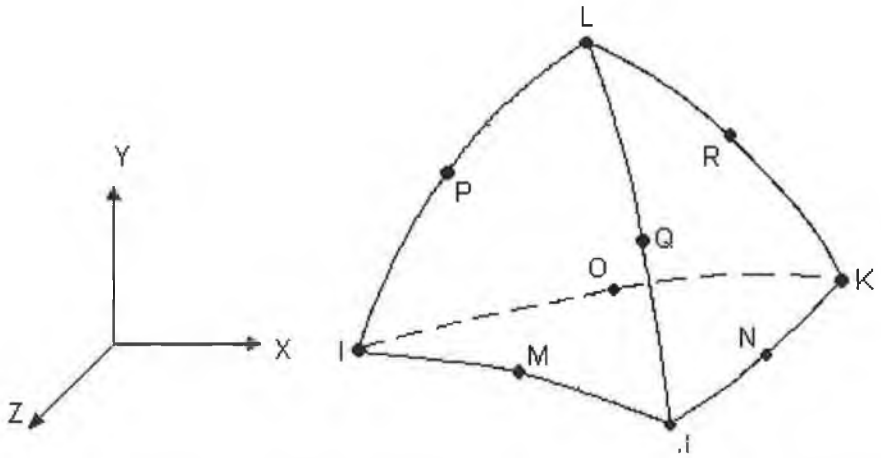

Figure 4.2: Line diagram of SOLID92 element. Adapted from ANSYS [130].

Mesh

The accuracy of a finite element model will depend, amongst other variables, on the density of the mesh. The maximum number of nodes allowed with the DCU ANSYS license is 32,000 nodes. The residual stresses of the Morse taper were of

secondary importance, therefore a less dense mesh was applied to the Morse taper geometry (approximately 7,000 nodes), compared to that of the bone cement sample (approximately 22,000 nodes). Figure 4.3 illustrates the model post meshing. The mesh density was controlled by setting the maximum element size for each volume and meshing each volume separately. Free meshing was utilised.

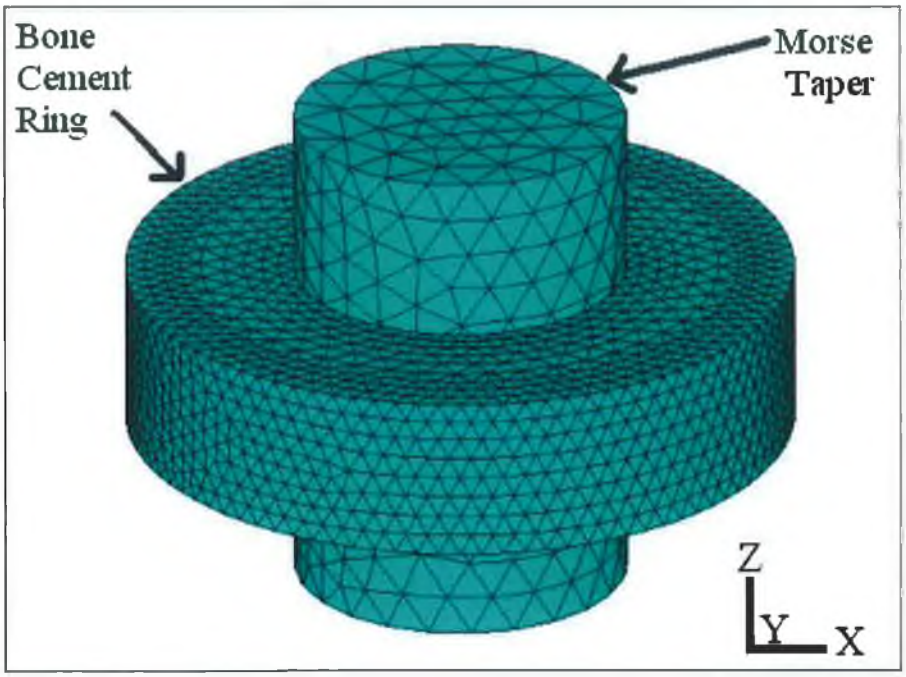

Figure 4.3: 3-D meshed model of Morse taper with cement ring assembled

Contact

To include the frictional effects between the Morse taper and bone cement ring, the ANSYS contact analysis feature was utilised. Contact problems fall into two general categories, rigid-to-flexible and flexible-to-flexible. Rigid-to-flexible analysis requires less computational resources compared with flexible-to-flexible [130]. As the stainless steel of the Morse taper had a Young's modulus approximately 90 times that of bone cement, rigid-to-flexible contact was utilised to increase efficiency.

ANSYS supports three contact methods, node-to-node, node-to-surface and surface-to-surface. From ANSYS literature, surface-to-surface nodes are recommended for modelling interference fit problems, as surface-to-surface elements handle sliding effects and are generally more computational efficient [130]. Thus surface-to-surface contact elements were utilised. To mesh the surfaces, the ANSYS v7.1 "Contact Wizard" was utilised. Post meshing, the Morse taper surface was meshed with 778 TARGE170 elements, while the bone cement contact surface was meshed with 1,828 CONTA174 elements.

4.2.2 Material Properties

In line with Orr *et al* [33] experimental work, material properties representative of 316L stainless steel and Palacos® R non-vacuum mixed bone cement were assumed for the relevant materials. Both materials were assumed to be linearly isotropic and homogeneous. Table 4.1 summarises the material properties assumed.

	Morse Taper (Stainless Steel 316L)	**Bone Cement (Palacos® R Non-Vacuumed)**
Young's modulus (E)	193 GPa [122]	2.11 GPa [33]
Poisson's ratio (ν)	0.28 [132]	0.455 [33]
Expansion coefficient (α)	$1.6 \times 10^{-5}\ °C^{-1}$ [122]	$8.0 \times 10^{-5}\ °C^{-1}$ [65]

Table 4.1: Material properties assumed for Morse taper and bone cement ring

4.2.3 Boundary Conditions And Loading

All temperature loads were applied as body loads, of uniform magnitude over the full component volume. The cement samples were set with an initial peak temperature of 60°C, 80°C, 100°C or 120°C over a number of different analyses, while the stem always assumed an initial temperature of 20°C. Both materials always assumed a final temperature of 37°C.

The Morse taper geometry was constrained in a manner that allowed the geometry to freely expand, but yet prevented free body motion. To achieve this, the lower face of the Morse taper was fixed in the UZ plane. To prevent free motion along the X direction, the Morse taper frontal quadrant line was fixed in the X direction. Finally to prevent rotation about this line the bottom-mid-left quadrant keypoint was fixed in the Y direction.

To enable a comparison with the plane stress theoretical model derived from thick wall cylinder theory, (see Appendix I for theoretical model development), a coefficient of friction of 0.01 was assumed at the interface. It is postulated that the coefficient of friction between the mandrel and cement sample would be relatively low, as the bone cement samples were not cured about the mandrel but gently placed about it. In conjunction with this, the taper of the mandrel may prevent full contact between both geometries, thus reducing friction. The Augmented-Lagrange contact algorithm was utilised to model interface conditions. This algorithm was selected due to its ability to model stick (shear stress is less than friction times normal stress), slip (shear stress is greater than friction times normal stress), and open (normal stress = 0) conditions [130].

4.2.4 Results

Figure 4.4 illustrates the von Mises stress distribution and magnitude for the assembly temperature of 100°C. The stress distributions for the 60°C, 80°C and 120°C assembly temperatures were of similar format i.e. peak stress at cement-stem interface.

From Figure 4.4, it is evident that the peak calculated residual stresses occur at the Morse taper-cement interface. A plot of the hoop and radial stresses also reveal the peak stresses to occur at the interface. This result is in agreement with the experimental findings of Orr *et al* [33]. Figure 4.5 illustrates the peak residual stress magnitude (stress at interface) calculated from the 3-D finite element model over the temperature range considered.

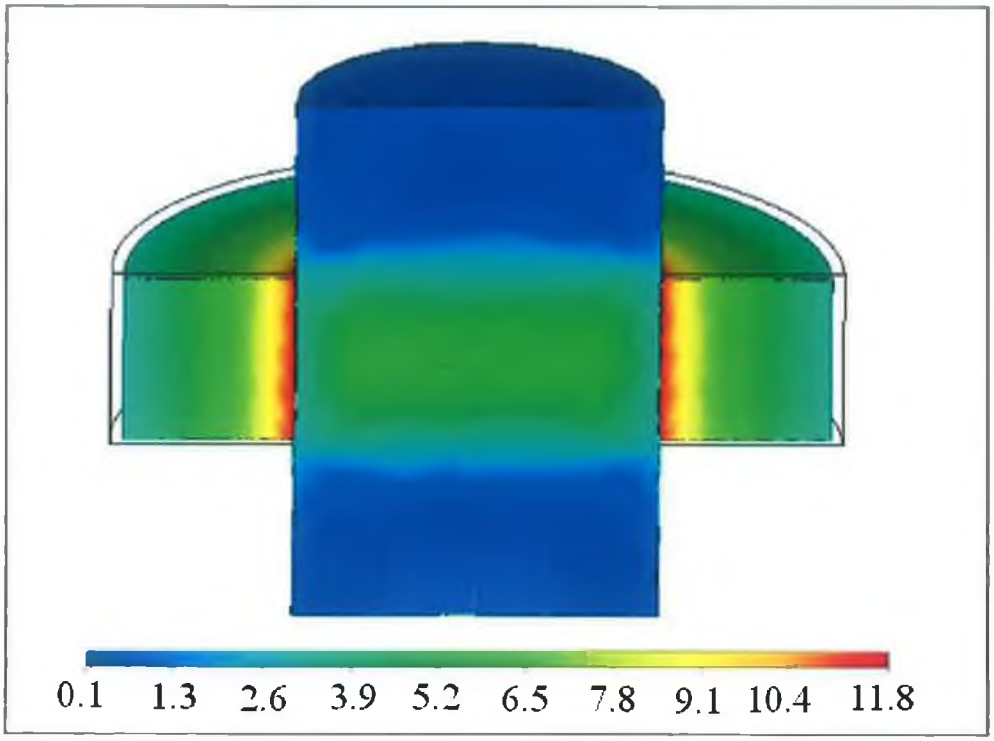

Figure 4.4: Cross sectional view of von Mises stresses (MPa) induced from an assembly temperature of 100°C. Note displacements were magnified by a factor of 10.

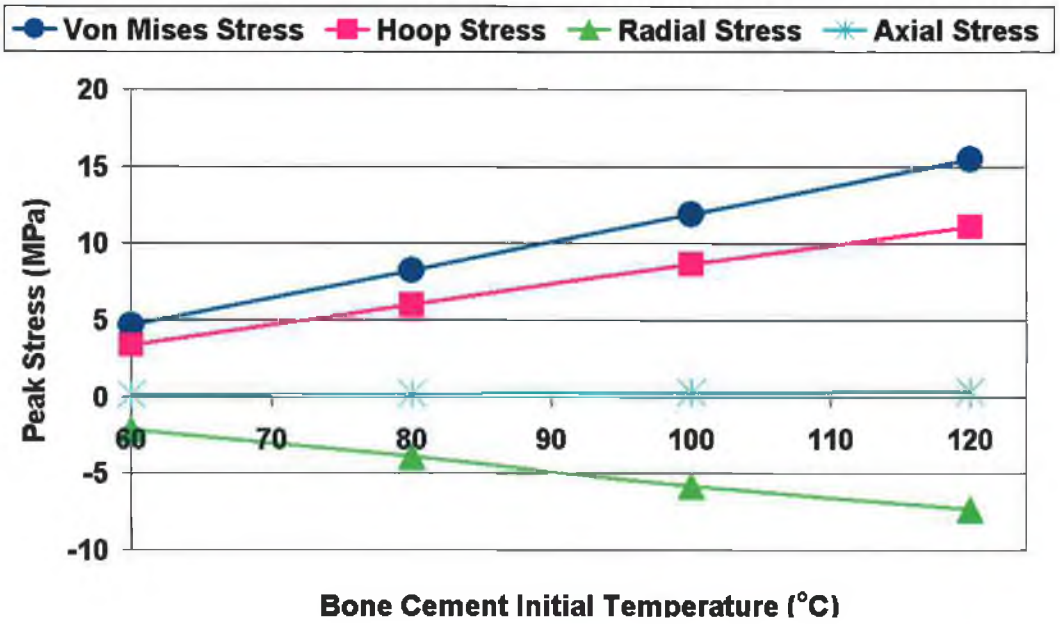

Figure 4.5: Peak residual stresses versus assembly temperature, predicted by finite element model

From Figure 4.5, it is evident that the hoop stresses were the most significant of the principal stresses and are tensile in nature. This is in line with the experimental findings published by Orr *et al* [33].

4.2.5 Validation

From the experimental work published by Orr *et al* [33], no experimental measurements were made to quantify the level of residual stresses in the bone cement samples. To validate the finite element methodology and results, a mathematical model was developed from thick wall cylinder theory to independently calculate the bone cement residual stresses (Appendix I). Table 4.2 compares the peak residual stresses predicted by the finite element model and the mathematical model.

Finite Element Model Results				
Temperature (°C)	**60**	**80**	**100**	**120**
Von Mises Stress	4.63	8.22	11.9	15.5
Hoop Stress	3.36	6.01	8.65	11.1
Radial Stress	-2.19	-3.91	-5.85	-7.32
Axial Stress	0.1	0.2	0.28	0.37
Mathematical Model Results				
Temperature (°C)	**60**	**80**	**100**	**120**
Von Mises Stress	4.88	8.59	12.28	15.98
Hoop Stress	3.49	6.13	8.77	11.41
Radial Stress	-2.09	-3.68	-5.26	-6.84
Axial Stress	0	0	0	0

Table 4.2: Comparison between finite element model results and mathematical model results

From Table 4.2 it is evident that a correlation exists between the peak residual stresses calculated by the finite element model and the mathematical model. Likewise on comparison between the stress distributions calculated by the finite element model and the mathematical model, clear correlation exists. From Table 4.2, the average difference between both models was 0.3 MPa. Both stress

distributions and magnitudes are consistent with published findings by Orr *et al* [33].

4.3 Finite Element Analysis Of Experimental Work

From the experimental results reported in Chapter 3, a non-uniform temperature profile is known to exist for the representative stem, cement mantle and femur. As the temperature history of the experimental construct was measured during experimentation, a temperature profile in line with that measured at stress-locking could have been directly applied to the finite element model and the residual stresses calculated in the mechanical environment of ANSYS, in line with the finite element methodology performed in the previous section (Section 4.2). However future objectives require the calculation of residual stresses for the *in vivo* scenario. Measurements pertaining to the temperature history during THA do exist in the published literature, however they are limited and not sufficient for the calculation of residual stress. Therefore, an independent finite element thermal analysis technique was implemented to define the temperature distribution at the moment of stress-locking. After verification with the measured experimental work, the thermal profile at the moment of assumed stress-locking was applied as the initial condition to a mechanical analysis (similar in methodology to that performed in Section 4.2), to quantify the residual stresses. Figure 4.6 outlines the flow chart for the FEA procedure employed for the calculation of residual stress. This procedure is termed indirect coupled field analysis [130].

4.4 Model Definition

Geometry

The maximum number of nodes allowed under the DCU ANSYS license agreement was 32,000 nodes. To increase the node density for the stem-cement-femur representative construct, the aluminium support frame and guide fins were

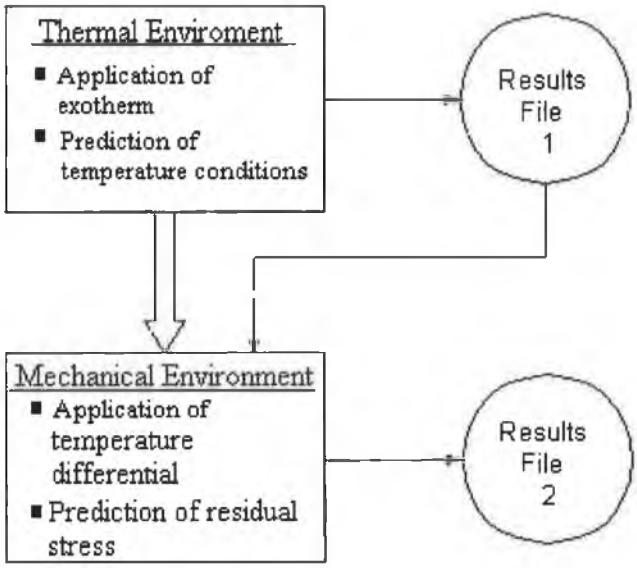

Figure 4.6: Flow chart of finite element methodology for the quantification of residual stress

not included in the 3-D finite element model. It is postulated that these parts would have negligible influence on the results, as they only contacted the stem-cement-femur construct at the base and were employed only as an aid to the procedure.

The inclusion of the diameter 1.2 mm holes drilled into the representative femur to simulate the presence of the cancellous bone structure were not incorporated into the finite element model. It is postulated that this limitation would have a negligible effect on the results, due to the small diameter associated with these holes. Figure 4.7 illustrates the CAD model developed in Pro-Engineer Wildfire 2.0 (PTC Inc., MA, USA) representative of the experimental model. Similar to the Morse taper assembly, the geometry created in Pro-Engineer was imported into ANSYS.

Element

The mechanical environment element SOLID92 was selected for the structural simulations for the reasons discussed in Section 4.2.1. From coupled field analysis, this element is only compatible with SOLID87 in the thermal

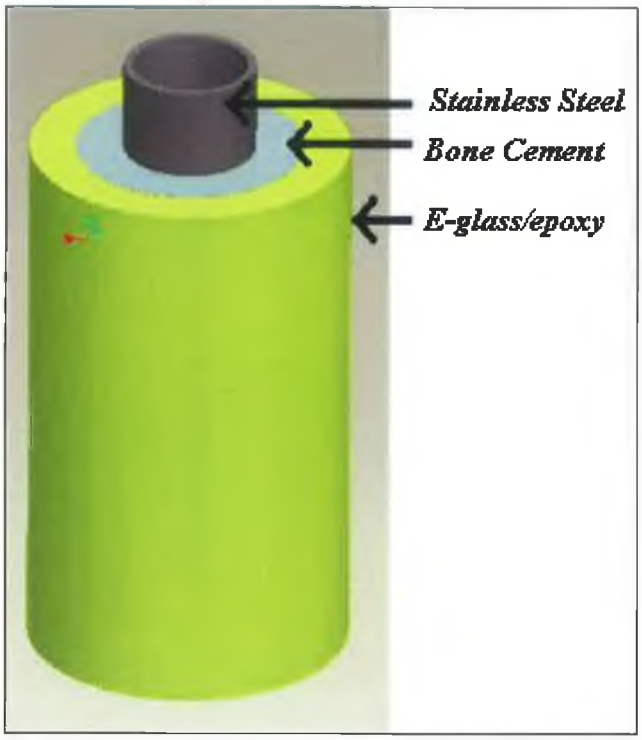

Figure 4.7: 3-D CAD model of experimental construct

environment [130]. SOLID87 has one degree of freedom at each node, i.e. temperature. The element is applicable to a 3-D, steady-state or transient thermal analysis. Similar to SOLID92, SOLID87 is a 10 node, tetrahedral element with mid-nodes, (Figure 4.8).

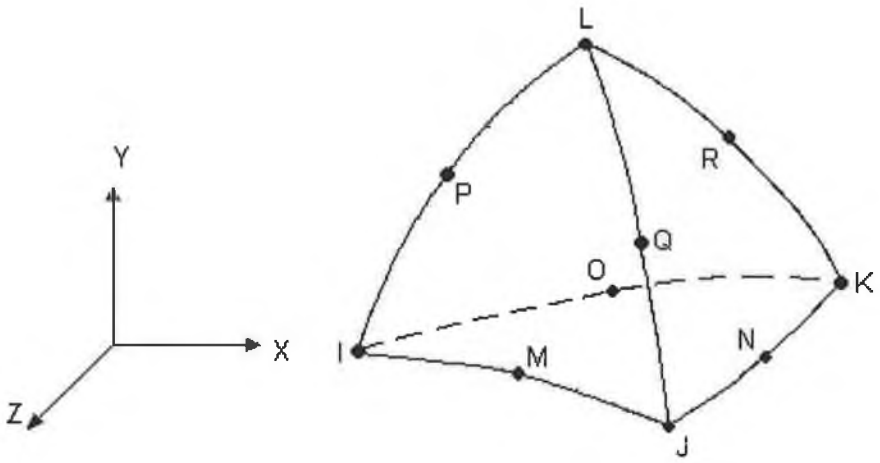

Figure 4.8: Geometry of SOLID87 element. Adapted from ANSYS help [130]

Mesh

In line with the meshing methodology employed for the Morse taper model, the mesh density was controlled by setting the maximum element size for each volume and free meshing each volume separately. The bone cement mantle was meshed with a higher mesh density compared to the representative stem and femur, as this constituent was of primary interest. After meshing, the representative stem contained approximately 5,000 nodes, the cement mantle approximately 16,000 nodes, and the representative femur approximately 7,000 nodes. Figure 4.9 illustrates the finite element model after meshing.

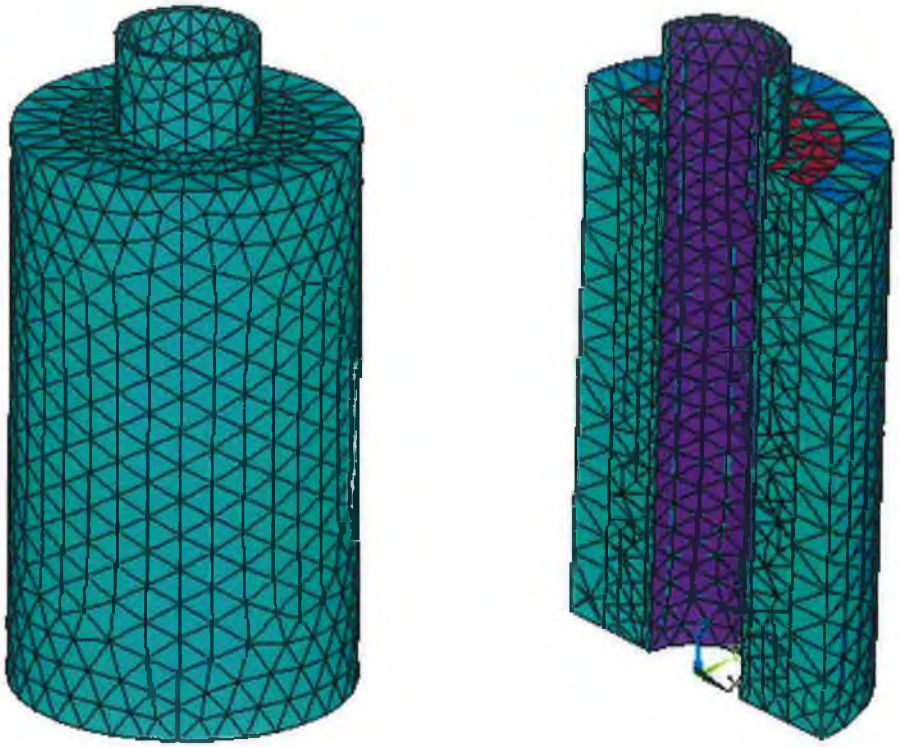

Figure 4.9: 3-D experimental model after meshing with element SOLID87

Contact Analysis

To permit the modelling of interface conditions, flexible-to-flexible, surface-to-surface contact elements, TARGET170 and CONTA174, were applied to the construct. To mesh the surfaces, the ANSYS v9.0 "Contact Wizard" was utilised. After meshing the model contained approximately 4,000 contact nodes.

4.5 Material Properties

4.5.1 Dilatometer Measurements

The coefficient of thermal expansion of CMW® 1 Gentamicin bone cement plays a critical role in the prediction of residual stress. Despite the widespread use of bone cement over the past 40 years, only one source could be located from public literature that reported the measurement of bone cement coefficient of thermal expansion. Based on dilatometer experiments, Ahmed *et al* [65] measured the coefficient of thermal expansion to be approximately 8 x $10^{-5o}C^{-1}$. However, these experiments were based on a Simplex® P bone cement and performed in 1982.

CMW® 1 Gentamicin Coefficient Of Thermal Expansion

To quantify the linear coefficient of thermal expansion for CMW® 1 Gentamicin bone cement, dilatometer experiments were performed. All experiments were performed with the DIL402 (Netzsch-Geratebau GmbH, Germany) dilatometer. The bone cement samples were taken from the experimental work performed in Chapter 3. The bone cement samples were approximately 25 x 4 x 4 mm in geometry, (Figure 4.10).

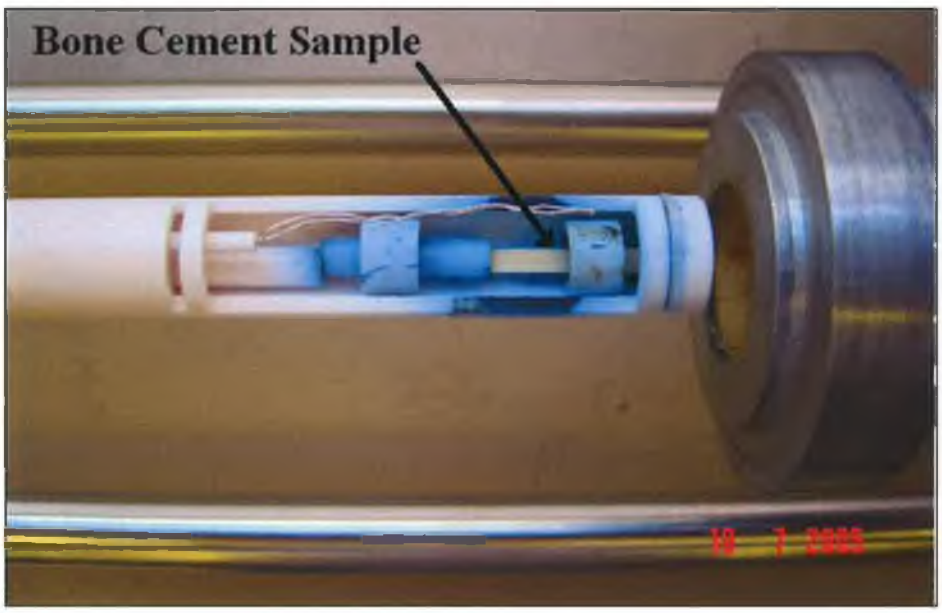

Figure 4.10: Bone cement sample within dilatometer

Twenty four dilatometer experiments were performed with CMW® 1 Gentamicin bone cement. The cement sample mixing condition (vacuum mixed or non-vacuum mixed), curing condition (pressurised or non-pressurised) and sample age were noted. Table 4.3 summarises the initial conditions and the measured coefficient of thermal expansion.

Vacuum	**No**	**Yes**	**No**	**Yes**
Pressurisation	**No**	**No**	**Yes**	**Yes**
	Coefficient x 10^{-6} °C^{-1} (Sample age from mixing)	**Coefficient x 10^{-6} °C^{-1} (Sample age from mixing)**	**Coefficient x 10^{-6} °C^{-1} (Sample age from mixing)**	**Coefficient x 10^{-6} °C^{-1} (Sample age from mixing)**
No.1	100.2 (90 days)	87.8 (27 days)	82.1 (15 days)	85.9 (57 days)
No.2	84.7 (32 days)	83.1 (1 hour)	81.6 (9 days)	78.7 (50 days)
No.3	98.3 (33 days)	81.1 (4 hours)	84.5 (9 days)	82.3 (49 days)
No.4	91.9 (2 hours)	101.4 (30 min)	86.0 (58 days)	88.4 (58 days)
No.5	81.5 (4 days)	89.2 (5 hours)	87.9 (60 days)	90.8 (51 days)
No.6		102.7 (2.5 days)		
No.7		101.6 (30 min)		
No.8		94.8 (5 hours)		
No.9		93.3 (1.5 days)		
Mean	**91.3**	**92.8**	**84.4**	**85.2**
Std. Dev	**8.2**	**8.1**	**2.7**	**4.8**

Table 4.3: Dilatometer experimental results for CMW® 1 Gentamicin bone cement

From the dilatometer experiments performed, it is apparent that the sample age and mixing condition had a negligible impact on the cements coefficient of thermal expansion. Conversely, pressurisation appeared to have the statistically significant (*t*-test, $p<0.05$) effect of lowering the cements coefficient of thermal expansion from 92.3 x 10^{-6}°C^{-1} (mean non-pressurised) to 84.8 x 10^{-6}°C^{-1} (mean pressurised). However, due to the porous nature of the bone cement and the large assortment of variables that significantly affect its mechanical properties a larger sample number would be required to confirm this finding.

Non-pressurised conditions are considered for the finite element model of the experimental work. Thus the mean coefficient of thermal expansion found for all the non-pressurised bone cement samples i.e. 92 x 10^{-6}°C^{-1}, was assumed for the thermal expansion of CMW® 1 Gentamicin bone cement.

SmartSet® HV Gentamicin Coefficient Of Thermal Expansion

To quantify the linear coefficient of thermal expansion for SmartSet® HV Gentamicin bone cement, 16 dilatometer experiments were performed. Eight non-pressurised bone cement samples and 8 pressurised bone cement samples. Table 4.4 summarises the cement samples initial conditions and dilatometer measurements.

Vacuum	**No**	**No**
Pressurisation	**No**	**Yes**
	Coefficient x 10^{-6} $^{o}C^{-1}$	**Coefficient x 10^{-6} $^{o}C^{-1}$**
No.1	68.1	70.3
No.2	69.1	76.3
No.3	68.9	74.0
No.4	74.0	69.6
No.5	75.4	65.3
No.6	70.3	78.8
No.7	68.8	74.6
No.8	80.0	78.8
Mean	**71.8**	**73.5**
Std. Dev	**4.0**	**4.4**

Table 4.4: Dilatometer experimental results for SmartSet® HV Gentamicin bone cement

From the 16 dilatometer experiments performed, results indicate no statistically significant difference between pressurised and non-pressurised SmartSet® HV Gentamicin linear coefficient of thermal expansion (*t*-test, $p<0.05$). On comparison between all the CMW® 1 Gentamicin bone cement experiments with all the SmartSet® HV Gentamicin bone cement experiments, SmartSet® HV Gentamicin had a statistically significantly lower coefficient of thermal expansion.

E-glass/epoxy Coefficient Of Thermal Expansion

The coefficient of thermal expansion of the utilised e-glass/epoxy was not documented by the manufacturer (Sawbones Europe AB, Sweden). Due to the materials composite nature and the fact that the e-glass fibres were orientated

along the axial direction, different coefficients of thermal expansions would exist between the axial and transverse directions, as discussed in Section 3.2.6. In conjunction with this, there exists a significant disparity in the coefficient of thermal expansion between the epoxy matrix coefficient of thermal expansion, (100 x $10^{-6}{}^{o}C^{-1}$ [133]) and the coefficient of thermal expansion of the e-glass reinforcement (5 x $10^{-6}{}^{o}C^{-1}$ [134]). Therefore the volume fraction of the reinforcement and the orientation of the reinforcement will have a direct impact on the materials coefficient of thermal expansion. The manufacturer of the representative femur was contacted to establish the volume fraction of reinforcement employed. However, this proved to be unfruitful.

To determine the coefficient of thermal expansion of the representative femur, 10 dilatometer experiments were performed. Due to sample size restraints, i.e. a sample size of at least 18 x 4 x 4 mm is required by the dilatometer, only samples from the longitudinal direction could be measured, as the e-glass/epoxy cylinder obtained was neither 18mm radially thick nor sufficiently thick to obtain samples in the hoop direction. Thus, only the longitudinal coefficient of thermal expansion could be measured. Table 4.5 summarises the dilatometer measurement results. For the finite element model, the mean coefficient of thermal expansions (37.9 x $10^{-6}{}^{o}C^{-1}$), was assumed for the representative femur longitudinal direction.

	Coefficient Of Thermal Expansion (x $10^{-6}{}^{o}C^{-1}$)
No.1	29.6
No.2	25.5
No.3	35.0
No.4	43.1
No.5	31.8
No.6	47.5
No.7	52.3
No.8	33.0
No.9	33.6
No.10	47.8
Mean	**37.9**
Std. Deviation	**9.1**

Table 4.5: Dilatometer experimental results for e-glass/epoxy in the longitudinal direction

4.5.2 316L Stainless Steel Material Properties

Table 4.6 summarises the material properties assumed for the 316L stainless steel tube. The representative stem was assumed to be linearly isotropic and homogeneous. All material properties were assumed to be independent of temperature for the temperature range considered.

Young's modulus (GPa)	Poisson's ratio	Coefficient of thermal expansion (10^{-6} °C^{-1})	Density (kg/m^3)	Specific heat capacity (J/kgK)	Conductivity (Wm/K)
193 [122]	0.28 [132]	16 [122]	8000 [122, 132]	500 [122]	16.3 [122]

Table 4.6: 316L stainless steel tube mechanical and thermal properties

4.5.3 Acrylic Bone Cement Material Properties

The mechanical properties of orthopaedic bone cement reported in the literature varies significantly, as discussed in Section 2.2.6. For example Tanzi *et al* [78] reported a Young's modulus of 1.99 GPa for bowl and spatula mixed CMW® 1 bone cement, while Harper and Bonfield [47] reported a Young's modulus of 2.96 GPa for the same cement (CMW® 1) with the same mixing method (bowl and spatula). For this reason, the mechanical properties assumed for the bone cement were not taken from experiments performed using CMW® 1 Gentamicin bone cement only, but from typical values found in the literature and typically used by previous researchers who performed FEA involving bone cement. Table 4.7 summarises the bone cement properties assumed for the finite element model. The bone cement was assumed to be linearly isotropic and homogeneous. All material properties were assumed to be independent of temperature for the temperature range considered.

Young's modulus (GPa)	Poisson's ratio	Coefficient of thermal expansion (10^{-6} °C^{-1})	Density (kg/m^3)	Specific heat capacity (J/kgK)	Conductivity (Wm/K)
2.6 [110]	0.43 [33]	92*	1190 [32, 33, 57]	1450 [32]	0.17 [57, 135]

Table 4.7: Bone cement assumed mechanical and thermal properties

*Measured experimentally, see Section 4.5.1

4.5.4 E-glass/epoxy Material Properties

Due to the orientation of the e-glass reinforcement in the axial direction, as discussed in Section 3.2.6, the e-glass/epoxy cylinder cannot be assumed isotropic. However the mechanical properties in the transverse directions i.e. hoop and radial directions, will have similar properties as the e-glass fibres were orthogonal to both directions. Thus transverse isotropy was assumed for the e-glass/epoxy cylinder. Table 4.8 summarises the mechanical and thermal properties assumed for the e-glass/epoxy material. The e-glass/epoxy was assumed to be homogeneous. All material properties were assumed to be independent of temperature for the temperature range considered.

	Axial	Transverse
Young's modulus (GPa)	7.6 [115]	3.0 *(Note 1)*
Shear modulus (GPa)	3.0 *(Note 2)*	1.2 *(Note 2)*
Poisson's ratio	0.26 *(Note 3)*	0.26 *(Note 3)*
Coefficient of thermal expansion (10^{-6} °C^{-1})	37.9*	80 *(Note 4)*
Density (kg/m^3)	1700 [115]	1700 [115]
Specific heat capacity (J/kgK)	878 *(Note 5)*	878 *(Note 5)*
Conductivity (Wm/K)	0.6 *(Note 6)*	0.4 *(Note 6)*

Table 4.8: E-glass/epoxy assumed mechanical and thermal properties

*Measured experimentally, see Section 4.5.1

Note 1: The manufacturer of the e-glass/epoxy did not specify the transverse Young's modulus [115]. As the e-glass fibres were known to be orientated in the longitudinal direction, it was postulated that the matrix material (epoxy) would provide the principal stiffness in the transverse directions. Epoxy has a Young's modulus of 2.6 GPa [133]. A representative value of 3.0 GPa was assumed for the transverse Young's Modulus of the representative femur.

Note 2: Shear modulus calculated by $G = \frac{E}{2(1+\nu)}$ [37]

Note 3: From a personal communication with a representative (Mr. Peter Asker) of the e-glass/epoxy cylinder manufacturer (Sawbones Europe AB, Sweden), it was conveyed that the composite material had a Poisson's ratio of 0.26.

Note 4: The coefficient of thermal expansion of epoxy is 100 x $10^{-6}{}^{o}C^{-1}$ [133]. The coefficient of thermal expansion of e-glass is 5 x $10^{-6}{}^{o}C^{-1}$ [134]. The coefficient of thermal expansion of the representative femur longitudinally was measured at 37.9 x $10^{-6}{}^{o}C^{-1}$. As the e-glass fibres were orientated longitudinally, the transverse coefficient of thermal expansion must be greater than the axial coefficient. It is postulated that the matrix material (epoxy) would dominate the transverse coefficient of thermal expansion rate. From this the coefficient of thermal expansion of 80 x $10^{-6}{}^{o}C^{-1}$ was assumed to occur in the transverse direction.

Note 5: To establish the representative femurs heat capacity, the weight percentage of reinforcement filler is required. To solve for this, the composite "rule of mixtures" equation was adopted, (Equation 4.1) [136].

$$X_c = X_m V_m + X_f V_v \qquad (4.1)$$

Where "X" represents a certain mechanical property and "V" represent the density fraction. The subscript "c" represents the *composite material* i.e. representative femur, the subscript "m" represents the *matrix material* i.e. epoxy, and the subscript "f" represents the *filler material* i.e. e-glass. The manufacturer of the representative femur state the density of the e-glass/epoxy composite to be 1700 kg/m^3 [115]. E-glass has a reported density of 1200 kg/m^3 [134] and the epoxy has a reported density of 2600 kg/m^3 [133]. Using the rule of mixtures, the representative femur was calculated to be composed of approximately 64% weight e-glass fibre and thus 36% weight epoxy matrix. With the mixture ratios established, and the specific heat capacity of the epoxy (1000 J/kg-K [133]) and e-glass (810 J/kg-K [134]) known, the rule of mixtures was again applied to establish the representative femur's specific heat capacity. A specific heat capacity of 878 J/kg-K was calculated for the composite cylinder.

Note 6: The reported thermal conductivity of epoxy is 0.2 W/m-K [133]. The reported thermal conductivity of the e-glass fibre is 1.3 W/m-K [134]. As the fibres were orientated longitudinally, a greater thermal conductivity would occur in the axial direction compared to the transverse directions. Also, as the e-glass fibres were completely encapsulated by the epoxy, it is postulated that the conductivity would be biased more towards the epoxy value than the e-glass value. With this considered, a conductivity of 0.6 W/m-K was assumed for the axial direction and the thermal conductivity of 0.4 W/m-K was assumed for the transverse directions.

4.6 Boundary Conditions And Loads

To quantify the residual stresses, it is first required to establish the temperature profile at the moment of stress-locking. To define this, a transient thermal analysis was performed. The thermal profile at the time of assumed stress-

locking was then applied as the initial condition to a mechanical analysis to define the residual stress magnitude.

4.6.1 Transient Thermal Analysis

Exotherm Profile

The exothermic reaction profile quantifies the thermal energy released during polymerisation. To model the exothermic reaction, a methodology similar to that employed by Huiskes [8] and Swenson *et al* [56] was implemented. In this methodology the bone cement total thermal energy released per unit volume (J/m^3) and the rate of energy release was measured experimentally. This measured profile was then applied to the finite element model to quantify the exothermic reaction.

Swenson *et al* [56] based their exothermic profile on experimental work performed by Amstutz and Gruen [137]. Amstutz and Gruen based their measurements on Simplex® P bone cement. A search of the published literature was performed to locate any research performed that profiled the exothermic rate for CMW® 1 Gentamicin bone cement. From an extensive literature search, no such data could be located.

Numerous authors have performed Differential Scanning Calorimetry (DSC) experiments to measure the rate of energy release for polymerising bone cement and to define the total thermal energy released [57-60, 138-140]. To quantify the rate of energy released for polymerising CMW® 1 Gentamicin bone cement and to define the total thermal energy released per unit volume, DSC experiments were performed. All the DSC experiments were performed with a Pyris 6 Differential Scanning Calorimeter (PerkinElemer Inc., CT, USA). The DSC measures the thermal energy flow into or from the cement sample, while the temperature remains fixed or follows a prescribed temperature history. The DSC measurements may be slightly conservative, as any polymerisation that takes place before the DSC machine begins would be unaccounted for. From the DSC

experiments performed, this time period was typically measured to be the first 110 seconds after the initiation of mixing. This time period accounted for the mixing of the cement, the placement of the cement sample onto a tray, the weighing of the cement sample, the placement of the sample into the DSC machine and finally after the initiation of the machine, the length of time required for the DSC to established thermal equilibrium (approximately 30 seconds).

To enable a comparison with DSC research by Yang *et al* [59, 60], a number of different DSC thermal profiles were implemented. Yang *et al* based their experiments on Simplex® P bone cement. Table 4.9 summarises the DSC programmed thermal profiles and the measured exotherm results.

DSC Programmed Thermal Profiles	**Number Of Experiments**	**Total Thermal Energy Liberated (x 10^6 J/m^3)**	
		Mean	**Standard Deviation**
Isothermal at 25°C	3	59.1	13.4
Isothermal at 37°C	3	126.3	4.6
Isothermal 30°C for first 90s, remainder 10°C/min	1	125.5	-

Table 4.9: Differential scanning calorimetry programmed thermal profiles and the measured exotherm results based on CMW® 1 Gentamicin bone cement

A significantly lower quantity of thermal energy was released under isothermal conditions of 25°C compared with the remainder of the DSC experiments. This is in line with published results by Yang *et al* [59, 60], who reported the total thermal energy liberated at isothermal 25°C to be 86 x 10^6 J/m^3, while with a heating rate of 10°C per minute, the total thermal energy liberated was 129 x 10^6 J/m^3 based on Simplex® P bone cement. Yang *et al* [60] postulated that the lower total thermal energy liberated at lower temperatures may be due to a greater

proportion of the monomer not being converted to polymer as a consequence of the low temperature condition.

From the experimental work discussed in Chapter 3, the CMW® 1 Gentamicin bone cement went from approximately 34°C to peak temperature at an average rate of 30°C/min ± 7.2°C/min. A number of DSC experiments were attempted with the heating rate of 30°C/min and at 20°C/min, to increase the representativeness of the DSC thermal profile to that of the experiments. However, with these thermal profiles the initial part of the exotherm was missed by the DSC, and for this reason these results have not been included.

The DSC exotherm measurement for the thermal history of isothermal 30°C for the first 90 seconds and a heating rate of 10°C/min for the remainder of the experiment was selected to represent the polymerisation exotherm of bone cement for the finite element model. This result was selected as the DSC applied thermal history was most representative of the experimental condition. Figure 4.11 illustrates the DSC result for this condition. Note that the total thermal energy liberated (area under curve) for this temperature history was very similar to that obtained for isothermal 37°C conditions. This may indicate 126 MJ/m^3 to be approximately the maximum thermal output for CMW® 1 Gentamicin bone cement.

The ANSYS function HGEN (Heat GENeration) was utilised to apply the heat generation rate. Due to the non-linear nature of the exothermic reaction, the *tabular input* method in ANSYS v9.0 was employed. A tabular input (data point) was taken every 5 seconds. Ramped conditions were assumed between data points. Figure 4.12 illustrates the exotherm profile applied to the finite element bone cement volume.

Coefficient Of Thermal Convection

From the exothermic reaction of the polymerising bone cement, the stem-cement-femur construct will exceed ambient temperature, i.e. 37°C. Therefore heat loss will occur due to thermal convection. From the literature, previous

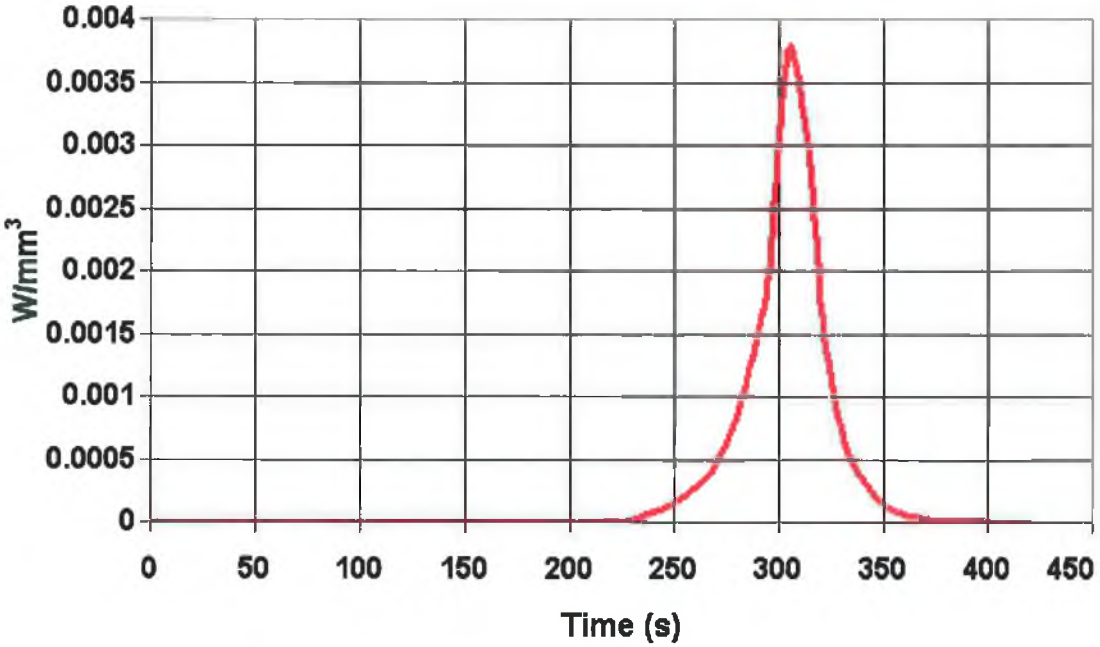

Figure 4.11: DSC exotherm result for CMW® 1 Gentamicin from the DSC thermal history of 30°C for the first 90 seconds (until approximately 200s from start of mixing) and 10°C/min for the remainder of the experiment

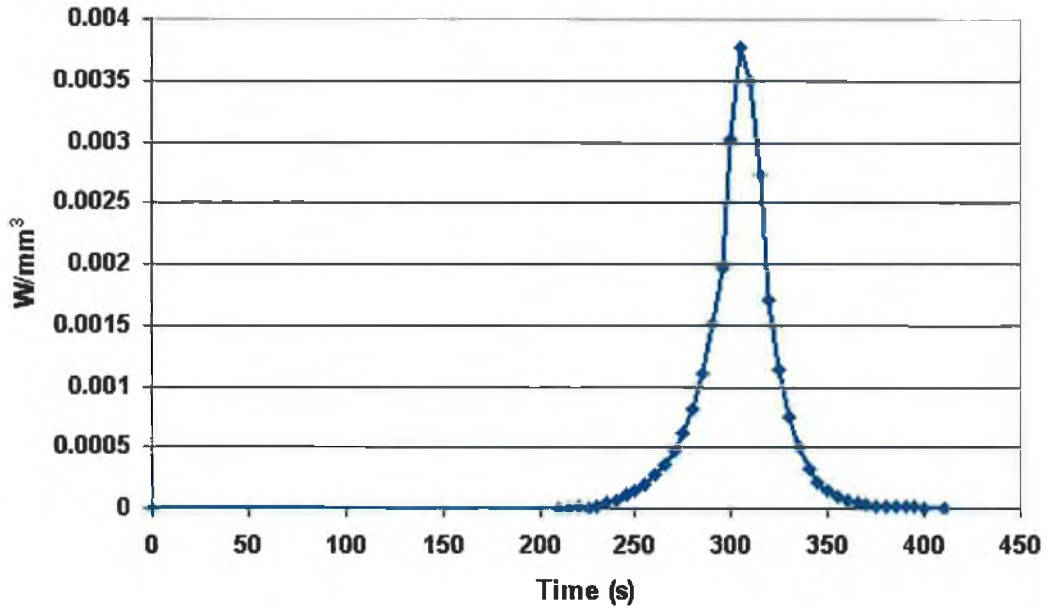

Figure 4.12: Exotherm profile applied to FE model

researchers who have performed transient thermal analyses, have assumed coefficients of thermal convection of 5 W/m^2K [139], 20 W/m^2K [32] and 40 to

60 W/m^{2}K [57]. However in all cases the authors did not give any justification for these values.

Equation 4.2 relates the approximate free thermal convection coefficient for a vertical cylinder, surrounded by air at atmospheric pressure, at a moderate temperature, under laminar air flow conditions [141].

$$h = 1.42\left(\frac{\Delta T}{L}\right)^{1/4} \tag{4.2}$$

Where "h" denotes the *coefficient of thermal convection* (W/m^2°C), "ΔT" denotes the *temperature difference* between the cylinder wall and the ambient air temperature, and "L" denotes the *length of cylinder*. Based on Equation 4.2, a convection coefficient of 5.1 W/m^{2}K was calculated and applied to the exterior surfaces of the representative femur, and 3 W/m^{2}K was calculated and applied to the interior surfaces of the stainless steel tube. Appendix J contains the mathematical details of these calculations. From Equation 4.2, as L becomes shorter, the coefficient of convection becomes larger. Based on this observation, a coefficient of thermal convection of 10 W/m^{2}K was assumed to the top surface of the bone cement mantle that was in direct contact with air.

To maximise the mesh density of the stem-cement-femur construct, the aluminium rig was not included in the finite element model, as discussed in Section 4.3. However the base surfaces of the construct were in direction contact with the aluminium experimental rig. To simulate the heat loss due to thermal conduction between the construct and the aluminium base plate of the rig, a convection coefficient of 50 W/m^{2}K was assumed and applied to the base surfaces of the construct that were in direct contact with the aluminium base plate. All convection loads assumed an ambient air temperature of 37°C.

Thermal Interface Conditions

From the literature, previous researchers who performed transient thermal analyses have assumed a perfect thermal bond between the stem-cement and

cement-femur interfaces [8, 32, 142]. However, it is proposed that for the experimental work performed, a perfect thermal bond would not exist at the interfaces due to contaminates and microscopic air voids between the cement mass and interface material.

Bone cement has a thermal conductivity of approximately 0.17 W/mK [57, 135]. Air has a conductivity of 0.024 W/mK [141]. An interface conductivity of 0.14 W/mK was assumed for the stem-cement interface while an interface conductivity of 0.08 W/mK was assumed for the e-glass/epoxy-cement interface. A greater thermal resistance was applied to the e-glass/epoxy-cement interface, as the internal surface of the composite cylinder was significantly more rough than the external surface of the stainless steel tube. It is well established that rough surfaces have a higher interface thermal resistance than smooth surfaces [143].

Contact elements TARGE170 and CONTA174 were applied to the 3-D model to model interface conductivity conditions. For both interfaces, the Augmented-Lagrange contact algorithm was utilised to solve interface conditions.

Initial Conditions

In line with the experimental work documented in Chapter 3, the representative stem and femur were assigned an initial temperature of 37°C. From the experimental work, the bone cement was measured to be approximately 27°C when it first contacted the representative femoral construct. Therefore the bone cement assumed an initial temperature of 27°C. Due to the cement mixing process, the bone cement did not come into contact with the representative stem and femur until approximately 70 seconds after the initiation of mixing. For presentational reasons, all initial temperatures of the transient model remained fixed from 0 seconds (initiation of mixing) until 70 seconds. All material thermal properties were assumed to be independent of temperature for the temperature range considered. A maximum time step of 5 seconds was imposed on the transient thermal analysis time stepping algorithm.

4.6.2 Mechanical Analysis

From the experimental work performed in Chapter 3, the average first registration of residual strain occurred at approximately 7 seconds before the attainment of peak cement temperature (Section 3.3.2). This indicates that the bone cement must have sufficiently solidified to support a load some time shortly previous to this time. The sample rate from the data acquisition system used in the experimental work was approximately 7 seconds. Therefore to enable a comparison between the experimental data and the finite element model, the moment of stress-locking had to be assumed either at 7 or 14 seconds before the attainment of peak temperature. From the measured thermal data it is known that the bone cement changes temperature rapidly at this phase i.e. shortly before the attainment of peak temperature. As only a slight residual strain was first measured at 7 seconds before peak temperature, it was postulated that stress-locking would occur closer to 7 seconds before peak cement temperature than 14 seconds. Therefore, for the finite element model, stress-locking was assumed to occur 7 seconds before the attainment of peak cement temperature.

Mechanical Interface Conditions

To simulate the presence of cancellous bone and to ensure a mechanical lock between the cement mantle and the representative femur, 90 diameter 1.2 mm holes were drilled radially at 45° to the cylinder axis in the experimental model. Therefore for the finite element model, the e-glass/epoxy-cement interface assumed bonded conditions.

With respect to the stem-cement interface, previous residual stress finite element models by Mann *et al* [111] and Nuno *et al* [38, 112] have assumed debonded conditions, while research by Lennon and Prendergast [32] and Roques *et al* [34] assumed perfectly bonded conditions. Bone cement does have some have some adhesive characteristics. However, as discovered by Dr. Hasboush in 1951, the first person to use acrylic bone cement for a hip arthroplasty (Section 1.1.3), it does not have sufficient adhesive properties for a hip arthroplasty application. For this reason, in clinical use, bone cement is not used as an adhesive but to form a mechanical lock between the prosthesis and the contiguous bone.

Evidence of a debonded stem-cement interface also appears in autopsy findings. Goldring *et al* [144] reported the occurrence of a thick fibrous membrane with numerous macrophages and giant cells at the cement-stem interface. Fornasier *et al* [145] examined 5 retrieved THR's between 7 weeks and 5 years old. For each case, a thin layer of connective tissue was present between the stem prosthesis and the bone cement mantle. Roques [41] reported evidence of slipping, and cracking based on an acoustic emission method. From this body of evidence, it was postulated that debonded conditions at the stem-cement interface would be more representative of reality than the perfectly bonded interface assumption. However this method is limited in that it does not include the element of adhesion associated with bone cement. To the best of the author's knowledge, all FE models assuming the debonded condition in the literature do not account for the adhesive element associated with bone cement.

From the literature, the reported coefficient of friction between bone cement and typical stem material varies between 0.15 to 0.35 [111, 146, 147]. It is postulated that the upper end of this range would be more representative of experimental conditions as the bone cement would have moulded and set about the stem. In line with research by Lennon and Prendergast [146], a coefficient of friction of 0.32 was assumed for the stem-cement interface. No data pertaining to differences between static and dynamic coefficients of friction could be found in the literature. A static to dynamic ratio of 1 was assumed.

Contact elements TARGE170 and CONTA174 were applied to model interface conditions. For the stem-cement interface the Augmented-Lagrange contact algorithm was utilised, due to its ability to model stick (shear stress is less than friction times normal stress), slip (shear stress is greater than friction times normal stress), and open (normal stress = 0) conditions. According to ANSYS documentation, the MPC algorithm is the recommended algorithm to implement bonded conditions [130]. Therefore for the e-glass/epoxy-cement interface, the MPC algorithm was employed to model the bonded interface condition.

4.7 Finite Element Analysis Results

4.7.1 Transient Thermal Results

Figure 4.13 illustrates the transient thermal simulation result over the first 600 seconds.

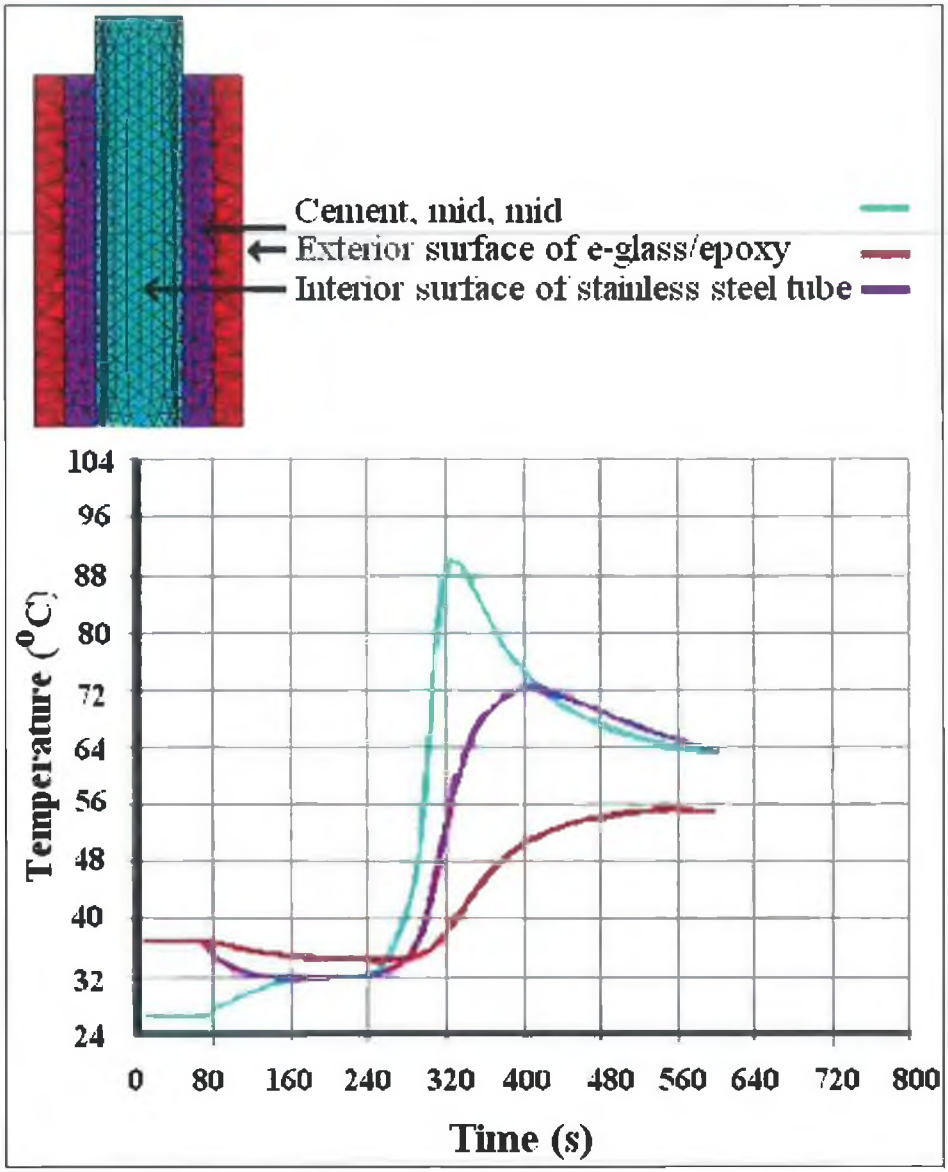

Figure 4.13: FEA transient thermal result over first 600 seconds

Time 0 seconds coincides with the initiation of bone cement mixing. After 70 seconds it was assumed that the bone cement had been added to the representative femoral construct and thermal transfer initiates. Between 70 to 220

seconds, the bone cement increases in temperature while both the stainless steel tube and e-glass/epoxy reduce in temperature. This is primarily due to thermal conduction effects. After 220 seconds the bone cement begins to significantly exotherm and at 327 seconds the bone cement mass has reached its peak temperature of 91°C. Figure 4.14 illustrates the temperature distribution at the moment of peak cement temperature.

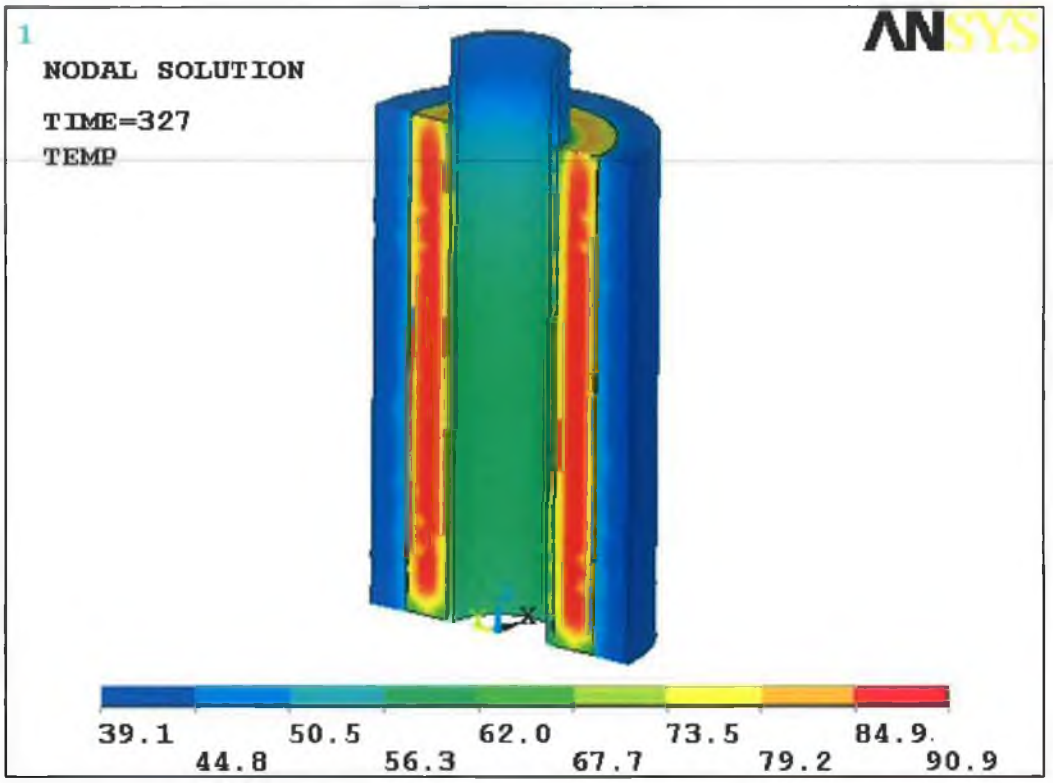

Figure 4.14: Cross sectional view of finite element result at 327 seconds after initiation of mixing. Units are in degrees Celsius.

Table 4.10 compares the finite element model peak temperature results with the mean experimental peak temperature results based on all the CMW® 1 Gentamicin experiments performed utilising the instrumented stem.

As discussed in Section 4.6.2, stress-locking was assumed to occur 7 seconds before the attainment of peak cement temperature. Thus stress-locking was assumed to occur at 320 seconds. Figure 4.15 illustrates the FE predicted thermal distribution at the moment of assumed stress locking.

	Mean Experimental (Std. Dev)	Finite Element Analysis
Peak cement temp. (°C)	95.6 (6.3)	91
Time of peak cement temp. (s)	335 (50)	327
Peak stem temp. (°C)	80.8 (6.7)	73
Time of peak stem temp. (s)	379 (45)	405
Peak femur temp. (°C)	55.9 (2.2)	57
Time of peak femur temp. (°C)	518 (72)	550

Table 4.10: Comparison of peak temperatures attained and time of occurrence between mean experimental results (all CMW® 1 Gentamicin experiments performed with instrumented stem) and FEA results

Table 4.11 compares the mean temperatures from the CMW® 1 Gentamicin experimental work at approximately 7 seconds before the attainment of peak cement temperature and the FEA result at 7 seconds before the attainment of peak cement temperature.

	Mean Experimental (Std. Dev)	Finite Element Analysis
Cement temp. (°C)	85.4 (7.5)	89
Stem temp. (°C)	51.3 (7.9)	53
Femur temp. (°C)	38.3 (3.0)	38
Stem-cement interface (thermocouple in cement) (°C)	71.3 (6.0)	72
Cement-femur interface (thermocouple in cement) (°C)	71.1 (2.5)	74

Table 4.11: Comparison between mean experimental temperatures and FEA result, both at 7 seconds before the attainment of peak temperature

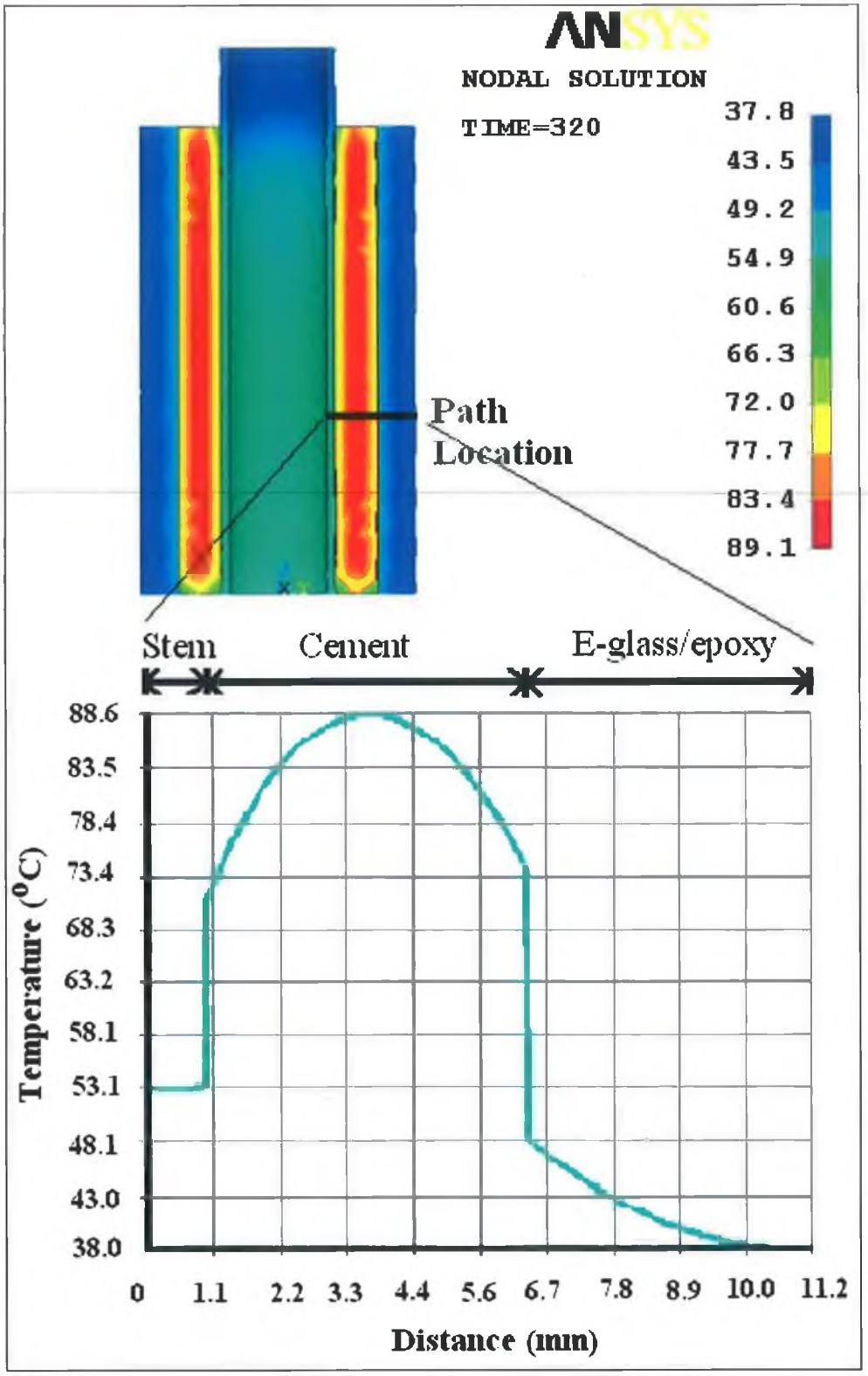

Figure 4.15: Thermal distribution at 320 seconds, the moment of assumed stress locking; (Top) Solid model thermal distribution; (Bottom) Temperature profile along path 25 mm from the base as indicated on solid model result

For the quantification of residual stress, the thermal model need only be run to simulate the first 320 seconds. However to establish confidence in the thermal model, a transient simulation was performed to simulate the first 3,600 seconds (1 hour) of the experimental work. Figure 4.16 compares the finite element result with an experimental result.

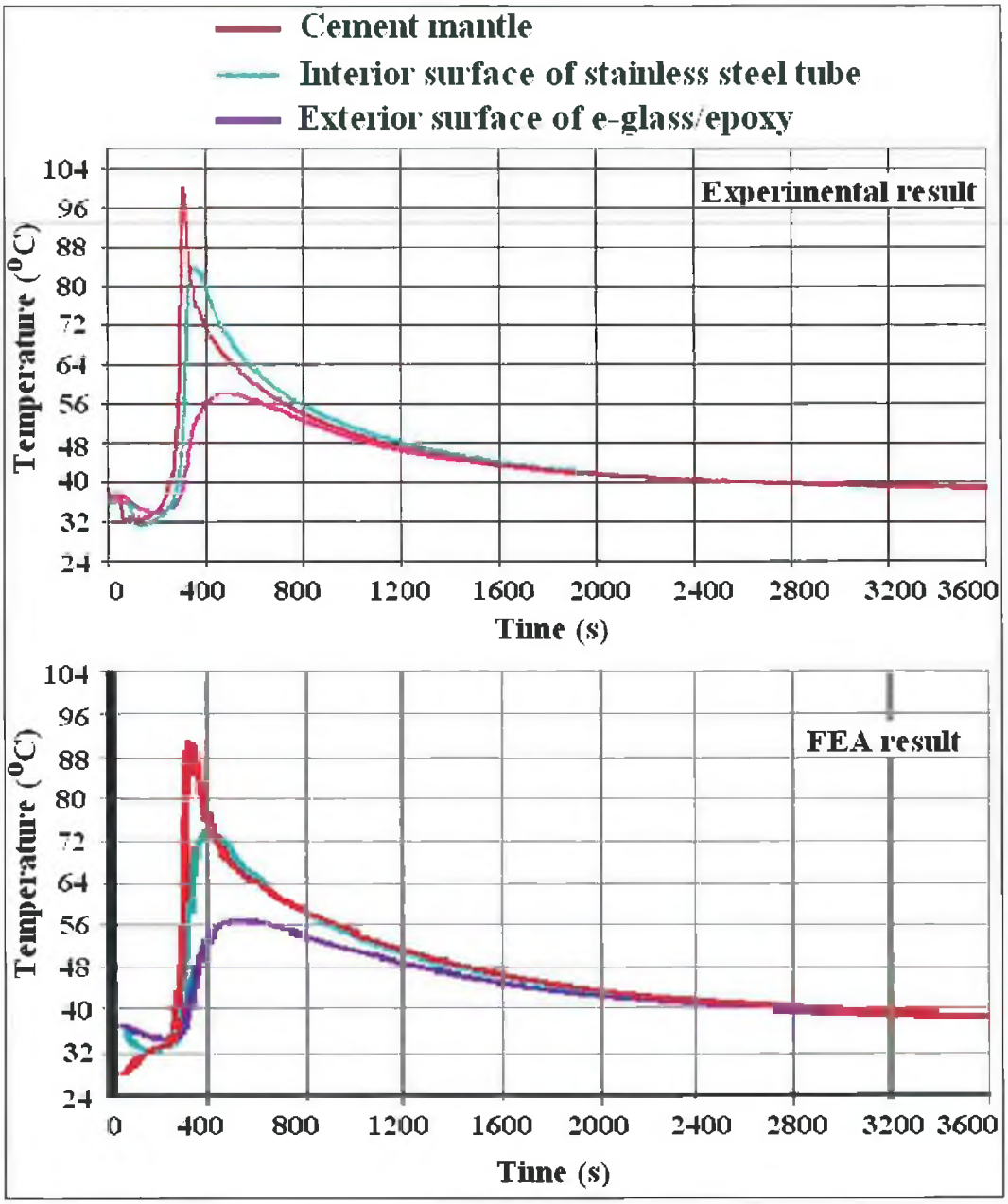

Figure 4.16: Comparison between experimental result (top) and FEA result (bottom) over the first 3,600 seconds (1 hour) after initiation of mixing

4.7.2 Residual Stress Results

Figure 4.15 illustrated the temperature distribution at the moment of assumed stress-locking, i.e. at 320 seconds. This thermal result was applied to the mechanical environment and the residual strains calculated with respect to 37°C. Table 4.12 compares the mean CMW® 1 Gentamicin experimental results for all experiments performed with the instrumented stem that were non-pressurised and the FEA residual strain result.

	Mean Experimental Microstrain (Std. Dev)	**Finite Element Model Microstrain**
E-glass/epoxy axial	-690 (±276)	-659
E-glass/epoxy hoop	-1656 (±315)	-1836
Stainless steel axial	-74 (± 22)	-88
Stainless steel hoop	-82 (± 55)	-74

Table 4.12: Comparison between mean experimental (all experiments performed with the instrumented stem that were non-pressurised) residual strain results versus the residual strains calculated by the finite element model

From Table 4.12 it is evident that the numerically calculated strains compare well with the mean experimental strains. All FEA predicted strains are well within a single standard deviation of the experimental results.

Figure 4.17 (top) illustrates the residual stress result in the Y-direction. For the "cut" faces of the construct (Q-slice through the longitudinal centre-line), it was assumed that this result corresponds with the radial residual stress, due to symmetry of the construction and orientation of the X, Y, and Z planes, as indicated on Figure 4.17. From the same logic, stresses in the X and Z direction were assumed to correspond to the hoop and longitudinal stresses respectively. Figure 4.17 (bottom) illustrates the assumed principal stresses for the path defined on the solid model.

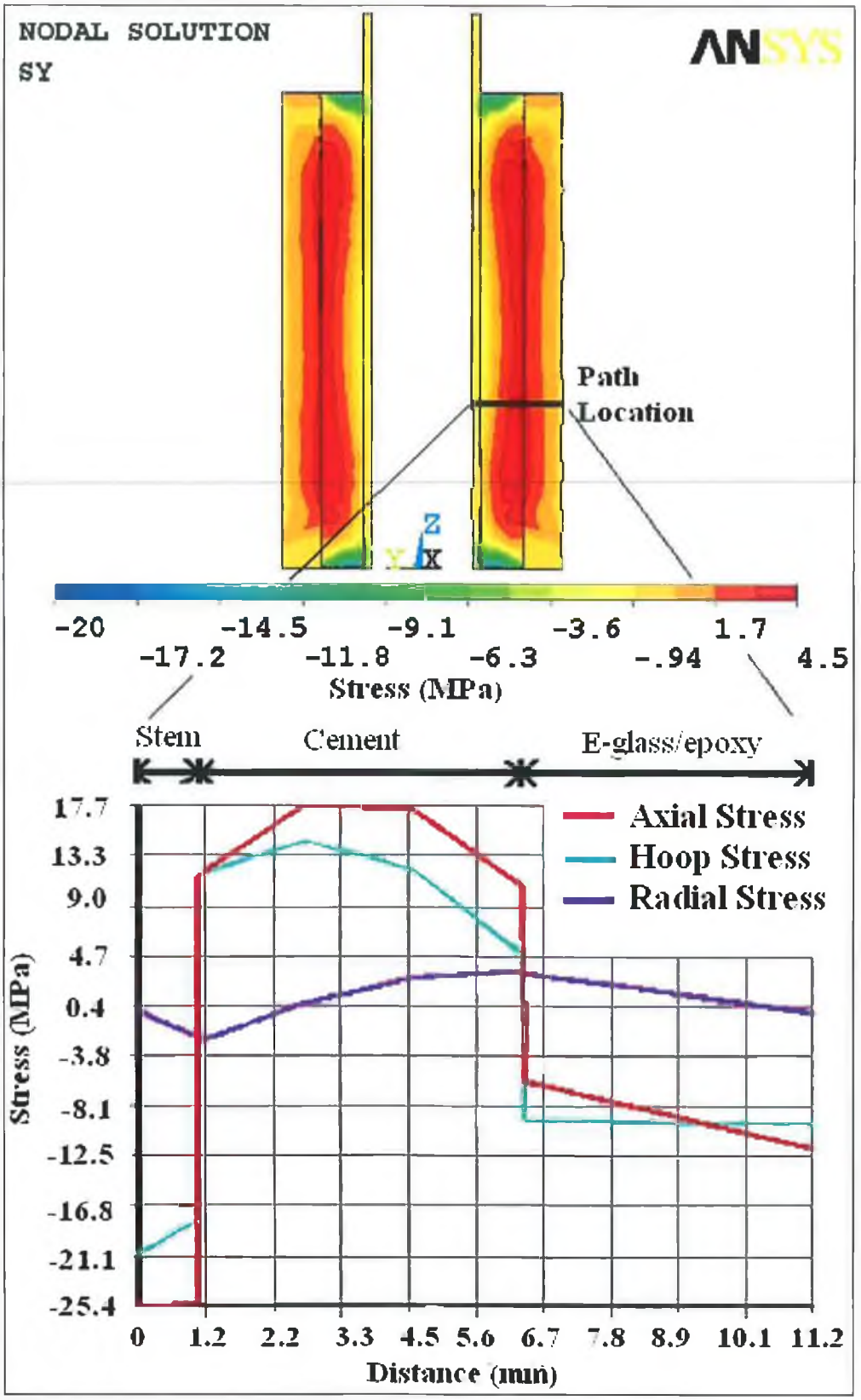

Figure 4.17: (Top) Experimental solid model (Q-slice) residual radial stress (MPa) result; (Bottom) Approximate principal stress distribution for path defined on the solid model

From Figure 4.17, it is evident that of the three assumed principal stresses, longitudinal residual stress had the greatest magnitude. Figure 4.18 illustrates the finite element calculated stresses in the Z direction (assumed to correspond with the longitudinal residual stress).

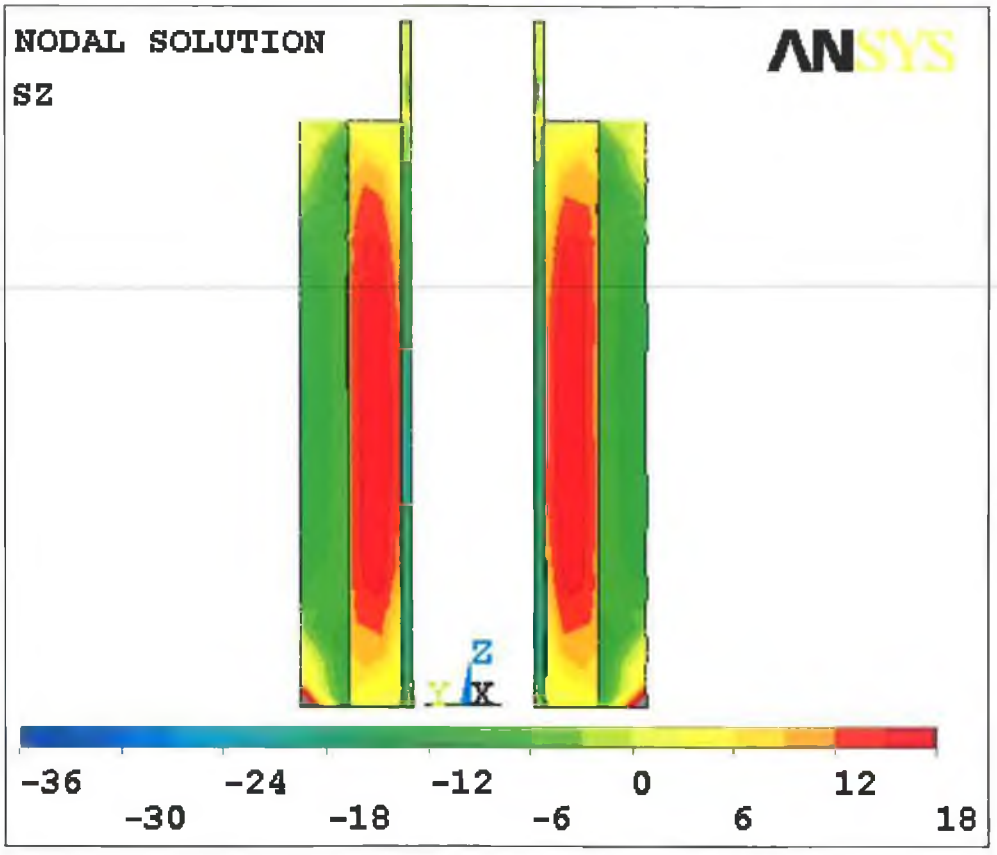

Figure 4.18: Experimental solid model (Q-slice) residual stress (MPa) distribution in the Z direction (assumed longitudinal stresses)

From Figure 4.17, hoop residual stresses had the second greatest magnitude of the principal stresses. Figure 4.19 illustrates the finite element calculated stresses in the X direction (assumed to correspond with the hoop residual stress).

Figure 4.20 illustrates the finite element residual von Mises stress result for the experimental construction.

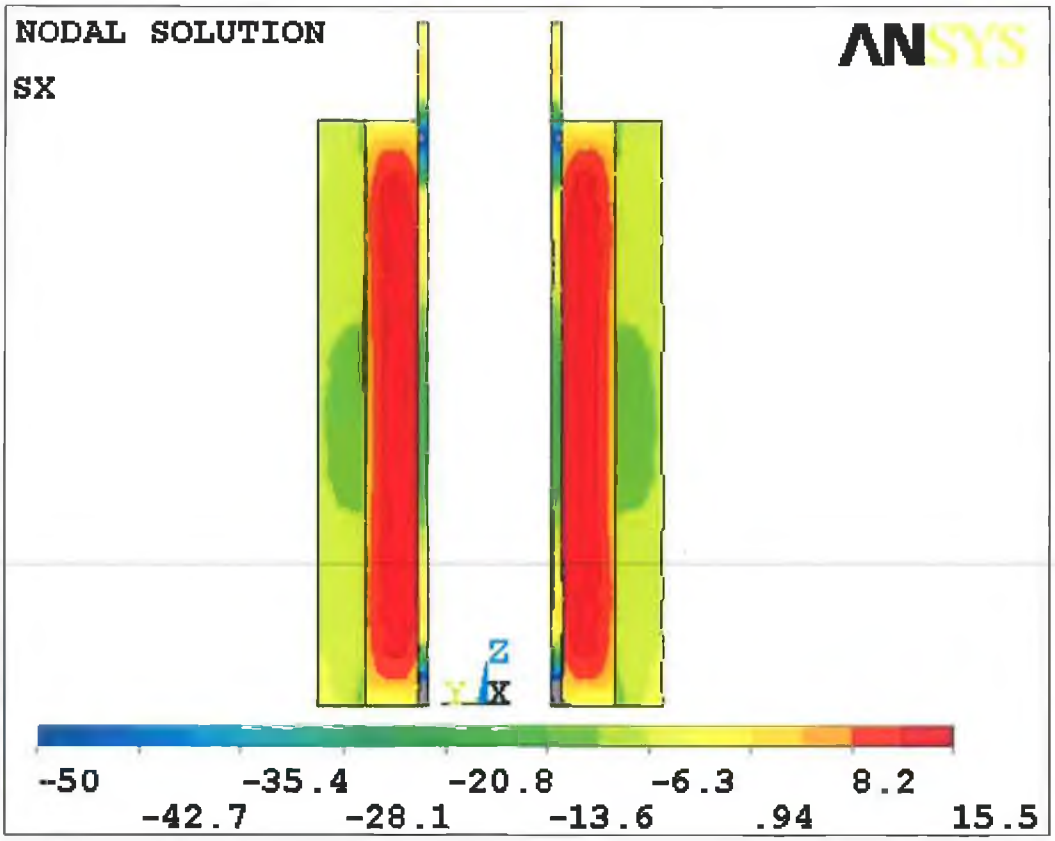

Figure 4.19: Experimental solid model (Q-slice) residual stress (MPa) distribution in the X direction (assumed hoop stresses)

4.8 Discussion

The finite element model of the experimental work published by Orr *et al* [33] calculated hoop stresses up to 15.5 MPa. To validate the finite element model results, a mathematical model derived from thick wall cylinder theory was developed. Both the finite element model and theoretical model results were directly comparable with each other, with an average disparity of 0.3 MPa.

The reported ultimate tensile strength of bone cement varies between 24 to 49 MPa [48]. Therefore the predicted level of residual stress on their own would not be sufficient to produce evidence of fracture damage, as found in the experimental work published by Orr *et al* [33]. However, the calculated magnitude of residual stress, coupled with stress concentrators, such as pores, may be sufficient to concentrate the local stresses to a level where micro-cracks

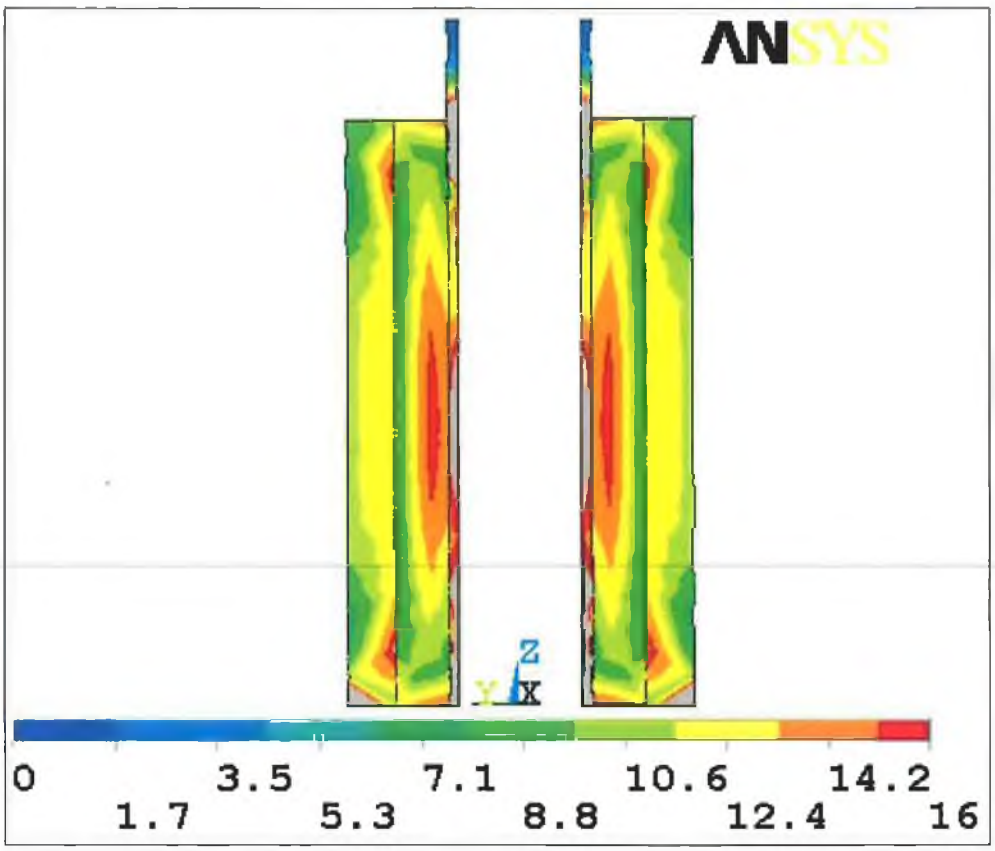

Figure 4.20: Experimental solid model (Q-slice) von Mises stress (MPa) distribution

may form. A number of different authors have calculated sub-ultimate tensile residual stress magnitudes, but concluded that cracking may occur due to stress concentrators [32, 106]. In support of this hypothesis, Orr *et al* [33] did note the formation of micro-cracks at or near the site of pores.

The bone cement coefficient of thermal expansion has a central role in the quantification of residual stress. Only one source from the literature was located that had previously measured the bone cement coefficient of thermal expansion. However that research pertained to Simplex® P bone cement. To quantify the coefficient of thermal expansion for CMW® 1 Gentamicin and SmartSet® HV Gentamicin, dilatometer experiments were performed. From a total of 24 dilatometer experiments performed with CMW® 1 Gentamicin bone cement, it was found that sample age and mixing condition had a negligible effect on the cements coefficient of thermal expansion. Results indicate pressurisation may

have the effect of reducing the coefficient of thermal expansion, however due the large number of factors that affect the bone cements mechanical properties, a larger sample number would be required to confirm this indication. From 16 dilatometer experiments performed with SmartSet® HV Gentamicin, no statistically significant difference was measured between pressurised and non-pressurised samples. On comparison between CMW® 1 Gentamicin and SmartSet® HV Gentamicin, a statistically significant lower coefficient of thermal expansion was measured for SmartSet® HV Gentamicin (mean of 72.6 x $10^{-6}{}^{o}C^{-1}$) compared to CMW® 1 Gentamicin (mean of 89.2 x $10^{-6}{}^{o}C^{-1}$).

One of the objectives of this research is the prediction of residual stresses *in vivo* (Section 1.5). From the literature, a number of different finite element methodologies have been employed to calculate residual stress. Mann *et al* [111] assumed the generation of residual stress from a uniform distributed temperature profile of chosen magnitude. Huiskes and De Wijn [109] and Ahmed *et al* [110] assumed the generation of residual stress from a temperature distribution of chosen magnitude. Huiskes [8] and Swenson *et al* [56] used a predefined exotherm obtained from experimental analyses to define the exotherm for their transient thermal analysis. For this methodology, the bone cement total thermal energy released per unit volume (J/m^3) and the rate of energy release was measured experimentally. This measured exotherm history was then applied to the finite element model to quantify the exothermic reaction. More recently, Lennon and Prendergast [32] and Li *et al* [108] have used a mathematical method developed by Baliga *et al* [55] for the quantification of exotherm rate. This methodology calculates the exothermic rate as a function of local temperature and fraction of monomer polymerised. Despite the ability of the exotherm methodology to include local temperature in the calculation of exotherm rate, a number of points should to be noted. Firstly, Lennon and Prendergast [32] reported 161 seconds (2.7 minutes) spanned between the calculated moment of peak cement temperature and the calculated moment the cement was 97% polymerised. This is interesting as it is generally regarded that the cessation of polymerisation approximately coincides with the attainment of peak cement temperature [8, 105-107]. Based on the DSC measurements from curing CMW® 1 Gentamicin bone cement (Section 4.6.1), the entire exotherm

phase (0–100%) took approximately 150 seconds (2.5 minutes). Secondly, the parameters derived for the theoretical model by Baliga *et al* [55] related to Simplex® P bone cement only and assumed a number of approximations, as the main objective of Baliga *et al's* [55] exotherm model was to propose a new methodology for the numerical modelling of the exothermic reaction [55].

The methodology utilised in this research to model the polymerisation of bone cement was similar to that employed by Huiskes [8] and Swenson *et al* [56] (exotherm measured experimentally and applied to the finite element model). To define the total quantity of thermal energy released per unit volume and the exotherm rate, DSC experiments were performed for CMW® 1 Gentamicin bone cement. The measured exotherm was then applied to the finite element model to simulate the exothermic reaction of polymerising CMW® 1 Gentamicin bone cement. However this methodology has its own set of limitations. From the experimental work documented in Chapter 3, the bone cement slowly increased in temperature from ambient until it reached approximately 40°C, after this point the cement went from this temperature to peak temperature at a typical rate of approximately 30°C/min. While this thermal history was attempted with the DSC experimentation, it proved unfruitful. The condition of isothermal at 30°C for the first 90 seconds and a heating rate of 10°C/min for the remainder of the experiment was the most representative of experimental conditions achieved. While this thermal history does not accurately represent experimental conditions, from the DSC experimentation performed results indicate an ultimate thermal liberation of 126 MJ/m^3 for CMW® 1 Gentamicin. Therefore it is postulated that the difference between the measured exotherm trace and the exotherm trace in the experimental work would not be the total energy released, but a slight variation in the rate of energy released.

Good agreement was found to exist between the finite element model predictions of time and maximum temperature with the average experimental results. A transient simulation was performed to simulate the first 3,600 seconds (1 hour) of the experiment. From a side by side comparison, the finite element and experimental temperature profiles were directly comparable.

Of primary interest was the temperature distribution at the moment of stress-locking. Five points were compared between the finite element calculated temperature and the average experimental temperatures. Over the 5 points considered, a maximum of 4°C difference existed between any of the average experimental temperatures and the corresponding computational model temperature predictions.

At peak temperature, the finite element model was slightly conservative, but yet matched well at the moment of stress-locking. From the residual stress experiments documented in Chapter 3, the bone cement went from 34°C to peak temperature at an average rate of 30°C/min ± 7.2°C/min. However the DSC applied a heating rate of 10°C/min. It is postulated that due to the higher temperature attained under experimental conditions at the moment of peak exotherm, the remaining monomer would polymerise quicker than under the DSC condition. This would enable the bone cement to reach a slightly higher peak temperature in the experimental work compared to the FEA predictions.

A mechanical analysis similar in methodology to that performed for the prediction of residual stress based on the experimental work by Orr *et al* [33] (Section 4.2) was performed to predict the construct residual stresses. The finite element model residual strain predictions at the location of the strain gauges were comparable with the average experimental strain gauge measurements. Converting strain to stress, the finite element model longitudinal residual stress predictions were the most significant of the principal stresses, with a maximum magnitude of approximately 18 MPa. Hoop residual stresses were the next most significant of the principal stresses with a maximum magnitude of approximately 15.5 MPa. Finally radial stresses were the least significant of the principal stresses, with a maximum magnitude of approximately 4.5 MPa. Based the von Mises stress criterion, maximum cement residual stresses of approximately 16.5 MPa were predicted.

The calculated residual stresses are higher than comparable finite element studies reported in the literature. For example Mann *et al* [111] reported longitudinal residual stresses to be the most significant at approximately 6.0 MPa, hoop

residual stresses to be the next most significant at approximately 5.5 MPa and finally radial residual stresses were least significant at approximately -2.5 MPa. Roques *et al* [34] reported maximum residual stresses of 11.85 MPa. Lennon and Prendergast [32] reported residual stress of 1 to 7 MPa, while Huiskes and De Wijn [109] reported residual stresses of approximately 4 MPa. However in all these studies the bone cement stress-locking temperature was significantly lower than those measured in Chapter 3. Therefore higher residual stresses for the current model conform with expectations.

4.9 Chapter Summary

The strain gauge data from the experimental work documented in Chapter 3 quantified the strains experienced by the interior of the representative stem approximately 25 mm from the base and the exterior of the representative femur approximately 30 mm from the base. In this chapter a finite element analysis methodology, independent of the Chapter 3 experimental measurement, was developed to quantify the transient thermal and resultant residual stresses based on the experimental configuration. The finite element thermal and structural results were directly comparable with the experimental results. Longitudinal residual stresses were the most significant of the principal stresses, with a maximum magnitude of approximately 18 MPa. Based on the von Mises criterion, maximum residual stresses of approximately 16.5 MPa were predicted.

Chapter 5

Finite Element Analysis Of *In Vivo* Residual Stresses

5.1 Introduction

From the literature, numerous numerical studies have been performed that calculate the transient thermal distribution of an artificial hip construct throughout bone cement polymerisation. However the majority of these numerical studies were primarily concerned with the cement-bone interface and whether thermal cell necrosis would occur. For this reason, many of the numerical transient thermal analyses in the published literature consider only a small segment of an artificial hip construct. Based on a literature review, all thermal analyses performed for the quantification of residual stresses have been based on simplified geometries, typically cylinders or 3-D models that were based on *in vitro* work. The first objective of this chapter was to apply the same thermal methodology defined and implemented in Chapter 4, to a 3-D anatomical model, to quantify the thermal distribution for the entire artificial femoral construct throughout polymerisation. The second objective of this chapter was to apply to same residual stress methodology defined and implemented in Chapter 4, to quantify the residual stresses based on a 3-D anatomical model.

After a total hip arthroplasty, the patient typically begins rehabilitation 1 to 2 days after surgery [25, 26]. Typical rehabilitation activities include walking,

getting into and out of bed, getting into and of a chair and stair ascent/decent. While bone cement is viscoelastic in nature, Roques [41] has reported that the stress relieving mechanisms from residual stresses appeared to take place at a relatively slow rate. Roques [41] postulated that when the construct is loaded for the first time by the patient, the residual stresses would be only partially relieved. As a result, Roques [41] recommended that residual stresses should be accounted for in the calculation of artificial hip construct stresses, for the early portion of the replacement lifetime. No such research could be located in the published literature. However in a related work, research by Nuno *et al* [38, 112] investigated whether the inclusion of residual stress would have an affect on the cement mantle stress levels, based on a simple finite element model. The authors concluded that the residual stresses would have an effect on the cement mantle stress distribution. However issues pertain with their finite element model and methodology. For example, to represent the residual stresses, a mechanical radial displacement of 5 μm was imposed at the stem-cement interface. To represent an external physiological load, a transverse and axial load of 600 N was applied. A more typical axial load for a hip joint would be approximately 2,000 N [83-86, 146].

The final objective of this chapter was to investigate and quantify the stresses of the artificial hip construct early in the lifetime of the arthroplasty. Walking is one of the first rehabilitation activities performed by the patient. Therefore for the quantification of the construct stresses early in the lifetime of the arthroplasty, the rehabilitation activity of walking was considered. An initial simulation was performed to define the construct stresses considering the forces due to walking only. The results from this simulation were compared with the literature to verify the legitimacy of the model. To define the construct stresses for the rehabilitation activity of walking, both the peak forces due to walking in conjunction with the residual stresses due to bone cement polymerisation were applied to the anatomical finite element model.

5.2 Model Definition

The femur is not symmetric. Neither are the mechanical forces placed upon it during gait. Therefore a 3-D model was required. An attempt was made to develop the 3-D anatomically representative solid model of a reconstructed hip joint from Computer Tomography (CT) or Magnetic Resonance Imaging (MRI) data of a reconstructed joint. With the aid of specialised software, for example Materialise Mimics (Materialise Mimics, Belgium) or 3D Doctor (Able Software Corp, MA, USA), the CT or MRI images may be used to construct and form a 3-D solid model of the stem, cement mantle and femur. Attempts were made to obtain MRI or CT data of a reconstructed femur from a number of different sources. However all attempts were unsuccessful, primarily due to patient-doctor confidentiality laws. To establish the 3-D anatomical model, the femur, stem and bone cement mantle were developed with Pro-Engineer CAD software (PTC, Needham, MA, USA) and assembled together to form the artificial femoral construct.

5.2.1 Femoral Prosthesis Geometry

According to the NJR for England and Wales, the Exeter™ femoral prosthesis by Stryker®-Howmedica-Osteonics (Stryker Corporation, Kalamazoo, MI, USA) was the most popular cemented stem prosthesis in 2003 and 2004 [4, 114]. In 2004 the Exeter™ prosthesis accounted for 44.9% of all cemented hip replacement procedures. According to the Australian National Joint Replacement Registry 2004 annual report, the Exeter™ femoral prosthesis was also the most popular cemented stem brand in Australia, accounting for 38.6% of all cemented primary total hip replacements [5]. Due to its popularity, the Exeter™ stem was selected for the femoral prosthesis of the 3-D anatomical model. Radiographic templates of the Exeter™ V40™ 44 mm No. 2 total hip system were obtained to define the geometry. The templates however only defined the elevation view of the prosthesis. To determine the end-view profile, a physical Exeter™ stem was obtained. From the physical Exeter™ stem, the thickness profile for the stem geometry was estimated. Based on these sources, a 3-D solid model of the

Exeter™ V40™ 44 mm No. 2 total hip system with a 26 mm diameter head was developed with Pro-Engineer version 2001. The developed 3-D CAD model of the Exeter™ stem was not an exact reproduction of the prosthesis. However, its accuracy was sufficient for the finite element purpose intended. Figure 5.1 illustrates the elevation, end-view and auxiliary view of the femoral prosthesis model.

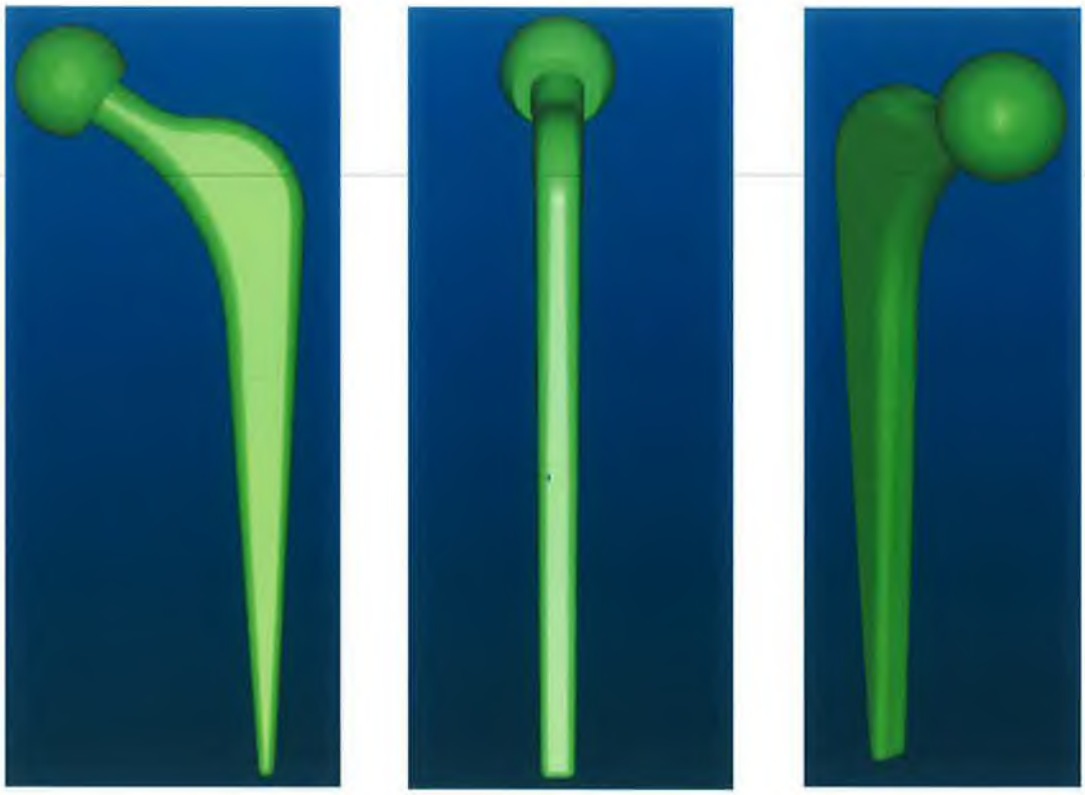

Figure 5.1: 3-D CAD solid model of No.2 44 mm Exeter™ V40™ stem prosthesis with a 26 mm diameter head (Left) Elevation view (Middle) End-view (Right) Auxiliary view

5.2.2 Bone Cement Mantle Geometry

To establish the cement mantle, two geometries are required. The medullary cavity post modification by the surgeon and the femoral prosthesis. The femoral prosthesis has been defined and created in Section 5.2.1. The geometrical definition of the medullary cavity after modification by the surgeon is not

absolute, as every femur is different and the modification of the cavity is a manual process. Therefore variation exists from arthroplasty to arthroplasty.

To define a typical medullary cavity post THA, a number of sources were consulted. Verbal advice was received from surgical staff at Musgrave Park Hospital, Belfast. The surgical staff recommended a 2 to 3 mm thick bone cement mantle for a medium sized femur and a 3 to 5 mm thick bone cement mantle for large sized femur. A surgical final stage femoral taper reamer was obtained and examined to acquire a greater understanding of the reconstructed medullary cavity shape, (Figure 1.3). Finally, longitudinal sectioned image data of reconstructed femora from the literature was examined, (Figure 5.2).

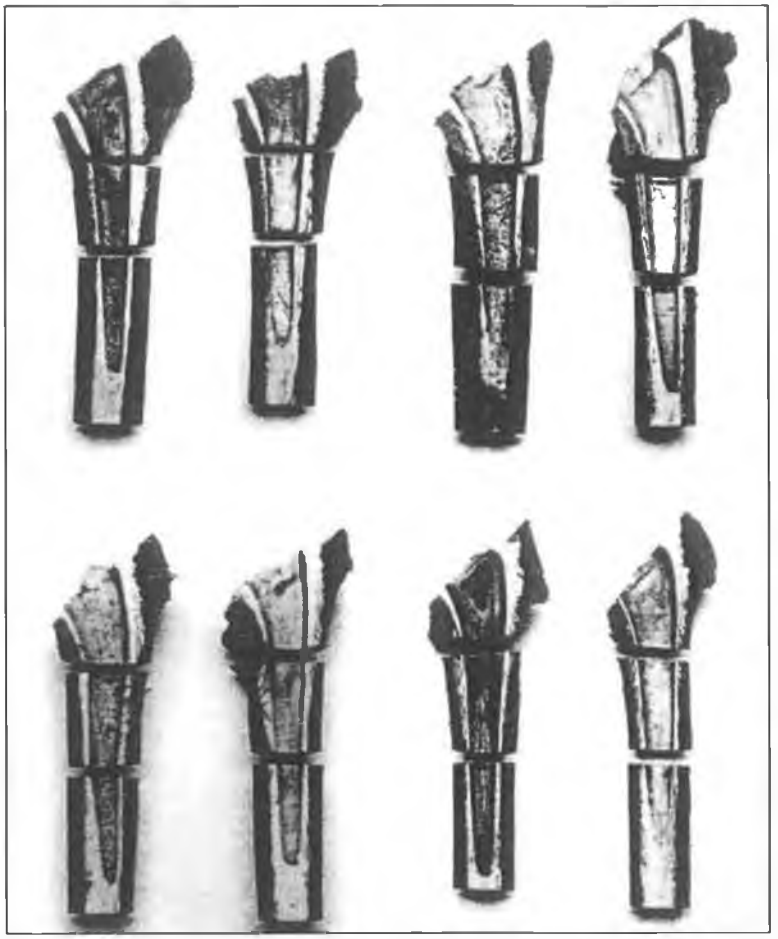

Figure 5.2: Longitudinally sectioned femoral artificial hip joints in cadaver femora. Adapted from Bishop et al [148]

Based on the aforementioned data, a 3-D CAD model of the cement mantle was developed in Pro-Engineer. The Pro-Engineer function *sweep-blend* was the central feature utilised to create a solid bone cement mantle. Figure 5.3 (a) illustrates the created solid bone cement mantle. To produce the cement mantle shell, the Exeter™ stem geometry, developed in Section 5.2.1, was subtracted from the solid bone cement geometry. This was achieved by the Pro-Engineer function *cut-out*. The cement thickness along the majority of the stem was approximately 3 mm. The displacement between the most distal tip of the cement mantle and the most distal tip of the Exeter™ stem was 6.5 mm. The cement mantle was 14 mm thick at the proximal lateral end. Figures 5.3 (b) and (c) illustrate the final bone cement mantle geometry.

(a) (b) (c)

Figure 5.3: 3-D solid model of cement mantle (a) Solid cement mantle before Exeter™ stem volume cut-out (b) Bone cement mantle after Exeter™ volume cut out (c) Auxiliary view of sectioned bone cement mantle

5.2.3 Femur Geometry

It takes a considerable amount of data, time and effort to create an accurate 3-D solid model of a typical femur [149]. In 1996, a group of researchers working in the biomechanics field with a particular interest in biomechanics of the femur, set up the Standardised Femur Project (SFP) [149]. The members of the SFP chose the second-generation, medium, composite left femur, model No. 3103 produced by Pacific Research Labs, (Vashon Island, Washington, USA) to become the Standardised Femur (SF) for their research. The advantages of setting up such an arrangement were twofold. Firstly, it would significantly reduce the amount of time required to create a solid model of the femur, as the femur solid model would be freely available and secondly, due to the fact that each researcher was using the same geometry for their analysis, the SFP greatly enhanced the ability to compare and verify their results. The standardised femur was obtained from the SFP web depository [149] and imported into Pro-Engineer 2001, (Figure 5.4).

(a) (b)

Figure 5.4: Standardised Femur obtained from SFP web depository [149] (a) Anterior-posterior view (b) Medial-lateral view

During a THA, the femoral neck is sectioned to remove the degenerated femoral head. For a cemented THA, the position and angle of this section is not critical [7] and therefore variation exists. Longitudinal image data of reconstructed femora revealed an average section of approximately 50^{o} to the longitudinal femoral shaft centre-line, typically varying between 40 to 60^{o}, (Figure 5.2). Therefore a section of 50^{o} to the femoral longitudinal axis was applied to the standardised femur model. Figure 5.5 illustrates the SF with section applied.

Figure 5.5: Standardised femur with femoral head removed

To create the femoral medullary cavity, the bone cement mantle volume must be subtracted from the solid femur model. Before this may be performed, the stem, cement mantle and femur geometries must be assembled such that the centre of the stem head aligns with the centre of the femoral head [9, 31]. This arrangement is performed during arthroplasty to ensure that the muscle and joint forces remain as closely as possible to the configuration previous to the arthroplasty, thus preventing extra loading of the joint due to ligament or tendon stretching. This arrangement also allows the patient to quickly learn how to operate and control the artificial joint as minimal change has occurred. In

conjunction with aligning the centres of the heads, the stem longitudinal axis should also be aligned with the femoral shaft longitudinal centre axis to ensure an even cement mantle.

5.2.4 Model Assembly

Pro-Assembly 2001 (the component assembly package of Pro-Engineer 2001) was utilised to assemble the stem, cement mantle and femur geometries. The centre of the head of the Exeter™ stem was assembled such that it aligned with the centre of the femoral head. However this alignment caused the axial centre line of the stem shaft not to align with the axial centre line of the femoral shaft, as illustrated in Figure 5.6 (a). To achieve alignment with both shaft centre-lines and head pivot points, the size of the femur geometry was reduced by 13%. The femur was selected to be reduced in size, as opposed to increasing the Exeter™ stem size, as no two femora are identical while the Exeter™ geometry is absolute. Figure 5.6 (b) illustrates the final assembly of the Exeter™ stem and reduced femur.

The distal end of the femur was sectioned 20 mm below the distal end of femoral stem to reduce the model size, as the full length of the femur was not required. The final anatomical geometry was 194 mm from the most distal tip of the femur to the most proximal tip of the stem. Figure 5.7 illustrates the 3-D anatomical model definition.

Element

In line with previous 3-D models, the anatomical model was exported from Pro-Engineer into ANSYS. Also in line with previous modelling, and for the reasons specified in Section 4.4, the 10-node tetrahedral element SOLID87 was selected for the thermal environment simulation, while the element SOLID92 was selected for the mechanical environment simulations, for the reasons specified in Section 4.2.1.

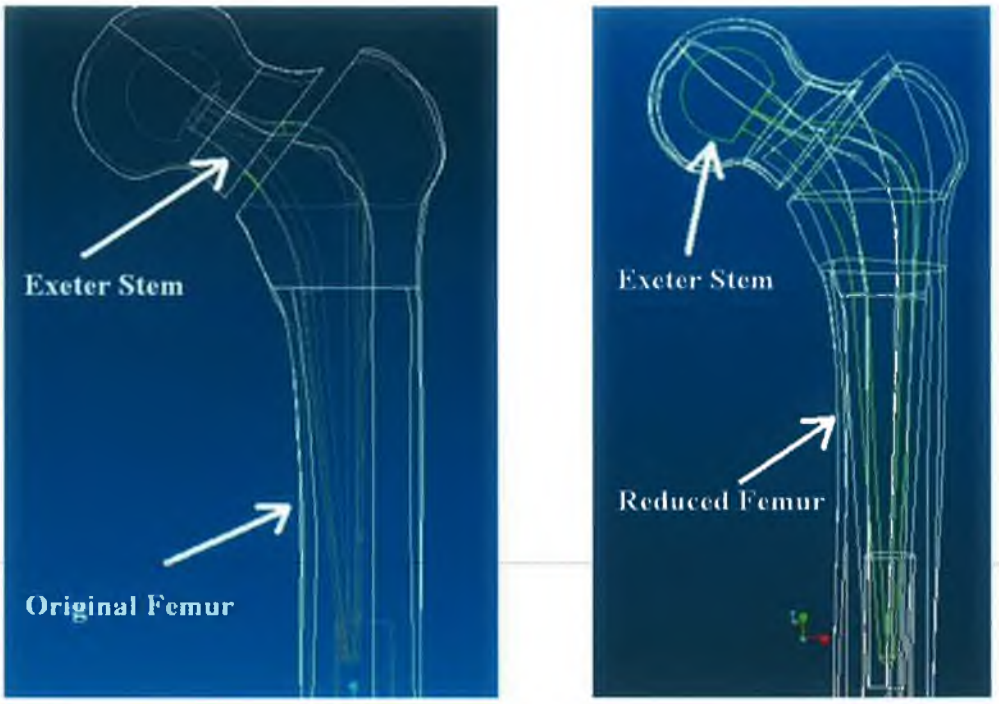

(a) (b)

Figure 5.6: Assembly of Exeter™ stem with femur (a) Assembly with original standardised femur, note shaft misalignment (b) Assembly with reduced femur. Note alignment with both shaft centre-lines and head pivot points.

Mesh

All geometries were meshed with the ANSYS v10.0 "Meshtool". As mentioned previously, due to licence constraints a maximum of 32,000 nodes was permitted. The "smartsize" meshing feature was not utilised, as this feature refined the mesh at locations that were not of primary importance to this study. The mesh density was controlled by setting the maximum element size for each volume and meshing each volume separately. Free meshing was employed. The mesh density at the most distal tip of the stem and the coinciding region of the bone cement mantle were refined to increase the mesh density at these locations. Post meshing the stem geometry contained approximately 9,000 nodes, the cement mantle geometry contained approximately 8,500 nodes and the femur geometry contained approximately 8,500 nodes. Appendix K contains image data of the mesh applied to each geometry. Figure 5.8 illustrates the meshed anatomical model.

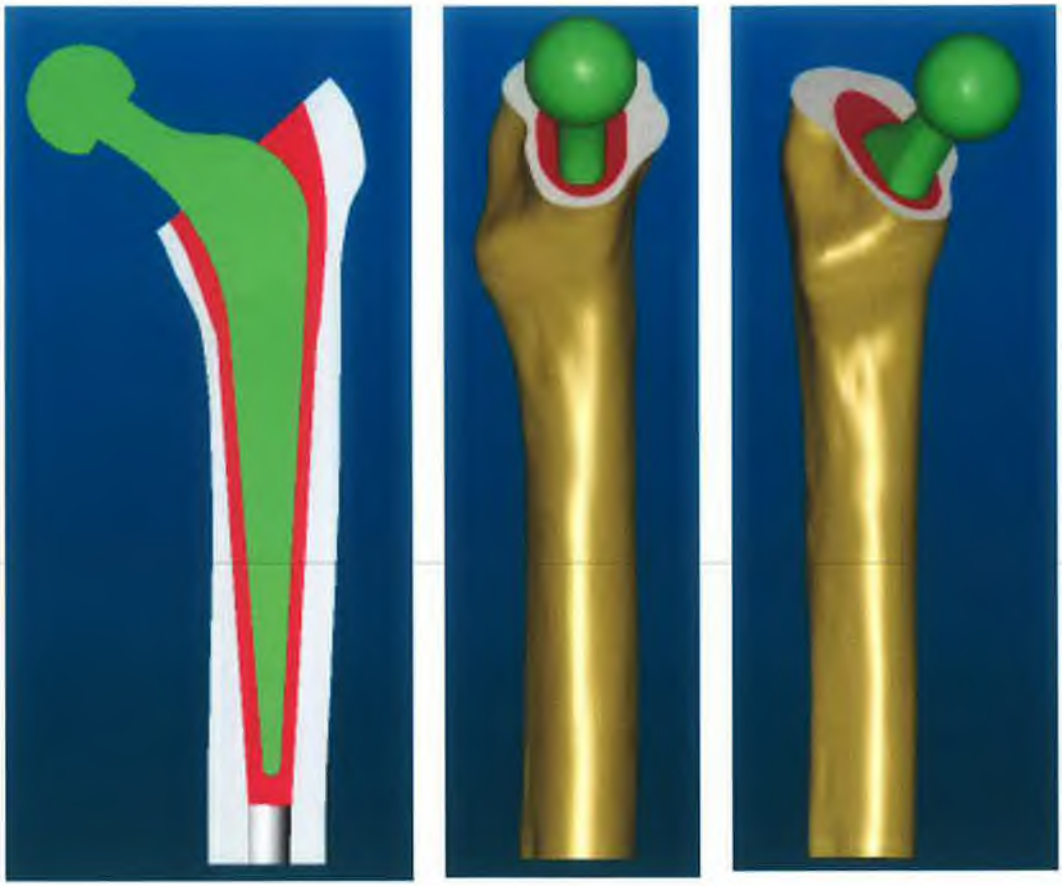

(a) (b) (c)

Figure 5.7: 3-D CAD anatomical model (a) Sectioned anterior-posterior view (b) Medial-lateral view (c) Auxiliary view

Contact

Similar to previous simulations, to account for the stem-cement and cement-femur interface conditions, flexible-to-flexible, surface-to-surface contact elements TARGET170 and CONTA174 were applied to the model. To mesh the surfaces, the ANSYS v10.0 "Contact Wizard" was utilised. Post meshing, the model contained approximately 6,000 contact nodes.

5.3 Material Properties

5.3.1 Femoral Prosthesis Material Properties

The Exeter™ prosthesis is made from 316L stainless steel [113]. Table 5.1

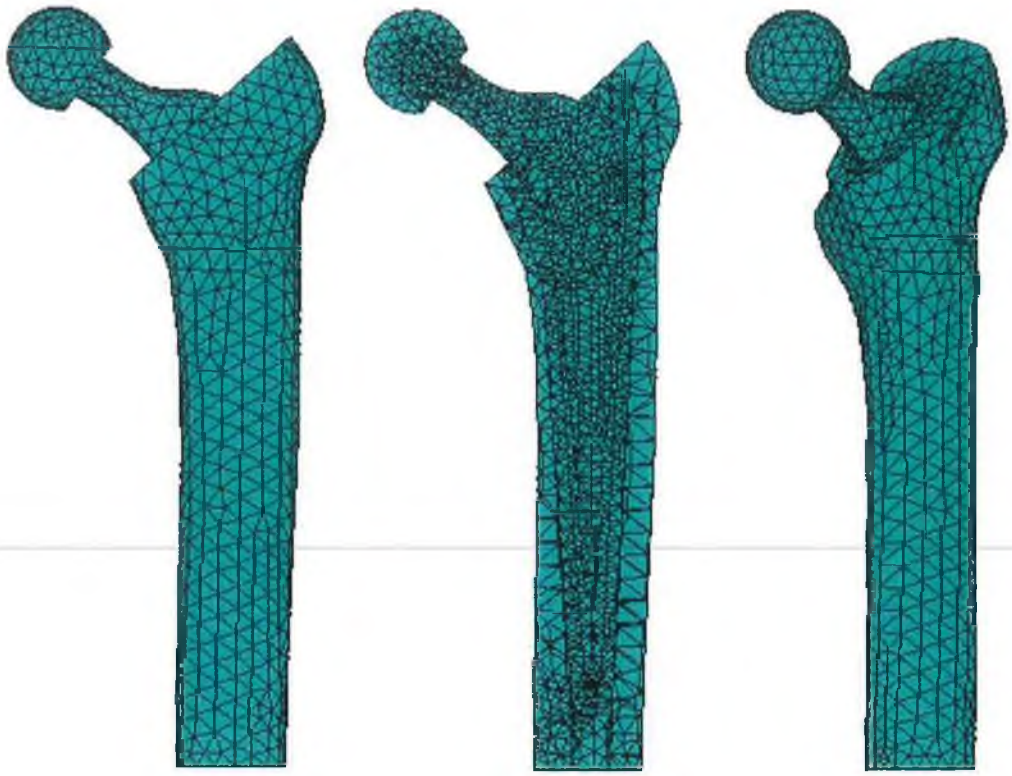

(a) *(b)* *(c)*

Figure 5.8: Anatomical model post meshing (a) Elevation view of meshed anatomical model (b) Elevation view of sectioned anatomical model to reveal internal mesh (c) Auxiliary view of anatomical model

summarises the mechanical and thermal properties assumed for the Exeter™ prosthesis. The Exeter™ prosthesis was assumed to be linearly isotropic and homogeneous. All material properties were assumed to be independent of temperature for the temperature range considered.

Young's modulus (GPa)	**Poisson's ratio**	**Coefficient of thermal expansion (10^{-6} °C^{-1})**	**Density (kg/m^3)**	**Specific heat capacity (J/kgK)**	**Conductivity (Wm/K)**
193 [122]	0.28 [132]	16 [122]	8000 [122, 132]	500 [122]	16.3 [122]

Table 5.1: Mechanical and thermal properties applied to Exeter™ prosthesis

5.3.2 Bone Cement Material Properties

Table 5.2 summarises the mechanical and thermal properties assumed for the bone cement. Section 4.5.3 contains a rationale for the bone cement mechanical and thermal properties assumed. The bone cement mantle was assumed to be linearly isotropic and homogeneous. All material properties were assumed to be independent of temperature for the temperature range considered.

Young's modulus (GPa)	Poisson's ratio	Coefficient of thermal expansion (10^{-6} °C^{-1})	Density (kg/m^3)	Specific heat capacity (J/kgK)	Conductivity (Wm/K)
2.6 [110]	0.43 [33]	92*	1190 [32, 33, 57]	1450 [32]	0.17 [57, 135]

Table 5.2: Mechanical and thermal properties applied to bone cement mantle

* Experimentally measured, see Section 4.5.1

5.3.3 Femoral Bone Material Properties

The mechanical properties for bone are dependent on a large number of variables including gender, age, lifestyle and heretical characteristics [1, 150, 151]. Therefore the published mechanical properties for femoral bone vary significantly in the literature [151, 152]. Wirtz *et al* [152] reported bone density to be the best variable with which to correlate bone mechanical properties. Figure 5.9 demonstrates findings by Writz *et al* for femoral cortical bone.

In conjunction with bone's variability, bone is also anisotropic and non-homogeneous in nature [150, 152, 153]. However according to research by Huiskes and Chao [153], both cortical and cancellous bone behave in a linear elastic fashion by approximation in quasi-static loading, despite being anisotropic and non-homogeneous in nature. Huiskes [154] demonstrated excellent agreement between theoretical and experimental results for the femur, when cortical bone material was assumed to exhibit linear elastic, transverse isotropic

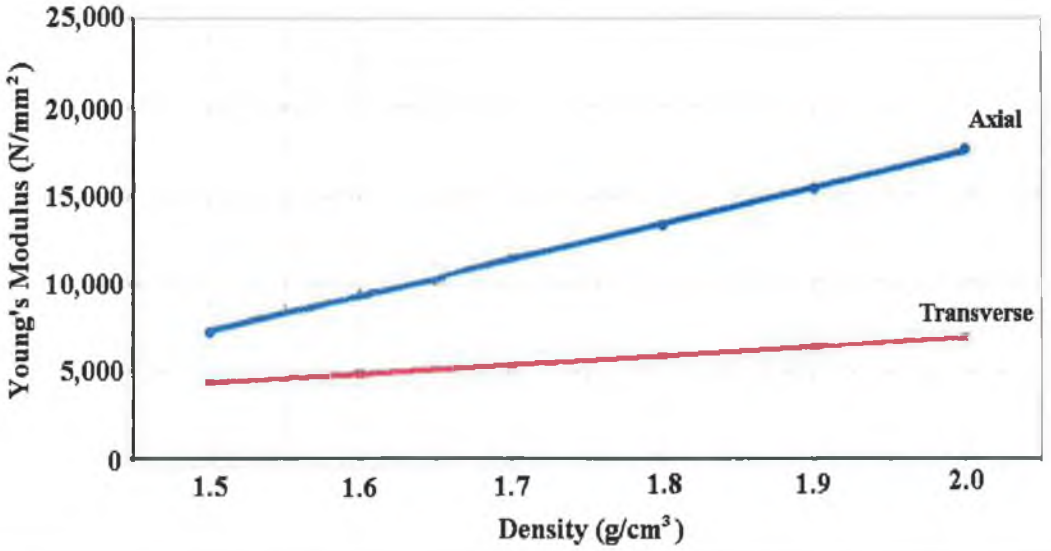

Figure 5.9: Young's modulus versus femoral cortical bone density. Adapted from Wirtz et al [152].

and homogeneous behaviour. Huiskes [154] however, did state that some local inaccuracies due to non-homogeneity should be expected. Research by both Taylor *et al* [155] and Couteau *et al* [156] reported the orthotropic elastic constants of femoral bone, (Table 5.3).

	Couteau *et al* [156]	**Taylor *et al* [155]**
E_{Radial} (GPa)	11.6	17.9
E_{Hoop} (GPa)	12.2	18.8
E_{Axial} (GPa)	19.9	22.8
$G_{Radial-Hoop}$ (GPa)	4.0	5.7
$G_{Radial-Axial}$ (GPa)	5.0	6.5
$G_{Hoop-Axial}$ (GPa)	5.4	7.1
Density (kg/m^3)		1932

Table 5.3: Summary of femur mechanical properties as reported by Couteau et al [156] and Taylor et al [155]

From Table 5.3 it is evident that the mechanical properties in the hoop and axial directions are similar. This provides further evidence that femoral bone may be

modelled as being transversely isotropic, as suggested by Huiskes [154]. Thus, the femur assumed linear elastic, transverse isotropic and homogeneous behaviour. Due to the spread in published femoral bone mechanical properties, instead of taking the femoral mechanical properties from one specific source, typical values found in the literature were assumed. Table 5.4 summarises the assumed mechanical and thermal properties for the femoral bone. All material properties were assumed to be independent of temperature for the temperature range considered.

	Axial	**Transverse**
Young's modulus (GPa)	15.0	9.0
Shear Modulus (GPa)	4.5	4.0
Poisson's ratio	0.37	0.29
Coefficient of thermal expansion ($10^{-6}\,^{o}C^{-1}$)	0.1 [110]	0.1 [110]
Density (Kg/m^3)	1900	1900
Specific heat capacity (J/kgK)	1300 [57, 108, 135, 139]	1300 [57, 108, 135, 139]
Conductivity (Wm/k)	0.4 [57, 135, 139]	0.4 [57, 135, 139]

Table 5.4: Mechanical and thermal properties assumed for the femoral bone

5.4 Boundary Conditions And Loading

Four finite element simulations were performed, namely;

1. A transient thermal analysis to quantify the anatomical model temperature profile at the assumed moment of cement stress-locking.
2. A mechanical analysis to quantify the residual stresses.
3. A mechanical analysis to quantify the peak stresses on the construct due to the physical activity of walking. To implement this, the peak

mechanical load from walking, including the most significant muscle groups were applied to the anatomical model.

4. A mechanical analysis to quantify the construct stresses for the rehabilitation activity of walking. That is, the residual stresses (point 2) in conjunction with the peak stresses from walking (point 3).

5.4.1 Transient Thermal Analysis

Exotherm History

The bone cement exothermic reaction history quantifies the total thermal energy released and the rate of energy release during polymerisation. In line with the finite element methodology employed in Chapter 4, the measured exotherm result for CMW® 1 Gentamicin bone cement, as defined in Figure 4.11, was applied as a body load to the bone cement volume by the ANSYS function HGEN (Heat GENeration). The *tabular input* method in ANSYS was utilised to apply the heat generation rate. A tabular input (data point) was taken every 5 seconds. Ramped conditions were assumed between data points. Exotherm history limitations as considered in the modelling of the experimental work, (Section 4.6.1) also apply to the current model.

Convection And Conduction

A coefficient of convection of 10 W/m^2K was assumed and applied to all areas that were in direct contact with air, i.e. proximal end of femoral prosthesis, the proximal surface of the bone cement mantle, and the proximal sectioned surface of the femur. An ambient air temperature of 20°C was assumed for all convection loads applied. For the remaining exterior surfaces of the femur, i.e. all exterior surfaces except the sectioned proximal surface in direction contact with air, it was assumed the femur was in direct contact with body tissue (fascia, muscle, fat etc). It is postulated that these tissues would have a high specific heat capacity and high thermal conductivity. In conjunction with this, these tissues would have a blood supply. From the aforementioned deductions, it is postulated that for the

exterior surfaces of the femur, a temperature of approximately 37°C would apply throughout polymerisation. Therefore a constant temperature of 37°C was applied to all the exterior surfaces of the femur, except for the proximal sectioned area that assumed thermal convection as previously discussed.

Interface Conditions

For the finite element model of the experimental work described in Chapter 4, (Section 4.6.1), the stem-cement interface assumed a conductivity of 0.14 W/mK, to account for possible debris and air that may be entrapped at the stem-cement interface at a microscopic level. However, for the Exeter™ stem, its external surfaces are smooth and highly polished. Also it is extensively cleaned and sterilised to prevent infection. Due to the aforementioned reasons, it was postulated that the thermal interface conductivity would be negligible compared to the bone cement conductivity. Therefore for the anatomical model, the stem-cement interface was modelled assuming thermal bonded conditions. This is in line with previous work involving similar thermal analyses [8, 32, 142].

For the finite element model of the experimental work described in Chapter 4, the e-glass/epoxy-cement interface assumed a conductivity of 0.08 W/mK, to account for possible debris and air that may be entrapped at the interface at a microscopic level. *In vivo* however, the aforementioned conditions would not occur. It is postulated that the cement-femur interface thermal conductivity would be negligible compared to the bone cement conductivity. Therefore, for the anatomical model the cement-femur interface was modelled assuming thermal bonded conditions. This is in line with previous researchers who have performed similar thermal analyses [8, 32, 142]. The MPC contact algorithm was selected to solve both interface conditions.

Initial Conditions

The femur was assumed to have an initial temperature of 37°C. The Exeter™ prosthesis assumed an initial temperature of 20°C. From the experimental work performed in Chapter 3, the bone cement was measured to be approximately

27°C when it first contacted the representative femoral construct after mixing. In line with this measurement, the bone cement was assumed to have an initial temperature of 27°C.

From the experimental work performed in Chapter 3, the bone cement did not come into contact with the representative stem and femur until approximately 70 seconds after the initiation of mixing. It is hypothesised that in the operating theatre, 120 seconds would be more representative of this time span, due to the more complex nature of a THA. Thus all initial temperatures remained constant until 120 seconds after the initiation of cement mixing. A maximum time step of 5 seconds was applied to the transient time stepping algorithm.

5.4.2 Residual Stress Analysis

At the cement-bone interface, the bone cement protrudes into the cancellous bone structure while in a viscous state. After stress-locking, this forms a mechanical lock between the bone cement mantle and the cancellous bone structure, provided the cement penetrated sufficiently into the cancellous bone structure [23, 157]. It has been established that with the correct surgical technique, bone cement does penetrate sufficiently into the cancellous bone to produce a reliable bond between the bone cement mantle and the femoral cancellous bone. Evidence of this mechanical lock between the bone cement mantle and the cancellous bone may be found in post-mortem findings. Maloney *et al* [158] retrieved 11 cemented THR's at autopsy, ranging from 0.5 to 210 months post implantation. From examining sections of the assembly, no intervening tissue was found at the cement-bone interface for the vast majority of sections examined. Similarly, Jasty *et al* [159] revealed only small regions of fibrous tissue between the femoral bone and the bone cement mantle, never more that a few millimetres long. Therefore from these observations, it was assumed that the bone cement mantle was perfectly bonded to the femur. This assumption is in line with previous residual stress analyses in literature [32, 38, 112]. The MPC contact algorithm was selected to model the bonded cement-femur interface condition, as per the finite element analysis methodology employed in Chapter 4.

As mentioned previously, the external surface of the Exeter™ prosthesis is smooth and highly polished. In line with the modelling of the experimental work documented in Chapter 4, the cement-Exeter™ prosthesis interface assumed debonded conditions with a coefficient of friction of 0.32. Section 4.6.2 gives a rationale for this assumption. No data pertaining to differences between static and dynamic coefficients of friction could be located in the literature. Therefore a static to dynamic ratio of 1 was assumed. The Augmented-Lagrange contact algorithm was selected, to model the debonded stem-cement interface condition, due to its ability to model stick (shear stress is less than friction times normal stress), slip (shear stress is greater than friction times normal stress), and open conditions (normal stress = 0).

From the experimental work documented in Chapter 3, the first measurement of residual strain occurred approximately 7 seconds before the attainment of peak cement temperature, (Section 3.3.2). In line with this result and the finite element methodology employed in Chapter 4, stress-locking was assumed to occur 7 second before the attainment of peak cement temperature. Section 4.6.2 outlines the background to this assumption.

5.4.3 Physiological Load Analysis

The patient typically undergoes rehabilitation 1 to 2 days after arthroplasty [25, 26]. Rehabilitation activities typically include walking, getting into and out of a chair, and getting into and out of a bed. As patients with an artificial hip replacement spend a significant portion of their time walking [30], this physical activity was selected for the quantification of the stresses in the artificial hip construct for early portion of the lifetime of the implant. To infer confidence in the method, the stress due to physiological loads alone i.e. no inclusion of residual stress was initially considered.

Heller *et al* [83] developed a model of the human lower extremity for the activity of walking. This model was validated against *in vivo* data from 4 patients with an artificial hip joint. The average weight of these patients was 836 N (mass of

approximately 85 kg). While the model matched well with experimental data, it was complex, with over 30 different lines of muscle action, as illustrated in Figure 5.10 (a). The authors in a later work developed a simplified musculo-skeletal load profile for the hip joint for walking, by grouping functionally similar hip muscles with minimal alteration to the joint forces [84]. The simplified model reduced the hip joint loading to three forces, namely the contact force acting on the femoral head, a musculo-skeletal force applied to the greater trochanter and a musculo-skeletal force applied to the vastus lateralis. Figure 5.10 (b) illustrates the simplified hip joint model.

Figure 5.10: Comparison of the complex model (a) and most simplified model (b) of the hip musculature developed by Heller et al [84]. Image adapted from Heller et al [84].

The peak resultant force for walking, based on the simplified model defined by Heller *et al* [84] was applied to the anatomical model. The peak load occurred at approximately 20% through the gait cycle. The coordinate system defined by Bergmann *et al* [160] and used by Heller *et al* [84] was applied to the anatomical

model. In this system, the centre of the coordinate system is located at the centre of the femoral head. For the left femur, as in the anatomical model, the positive x-axis is orientated from lateral to medial, the positive y-axis from posterior to anterior and finally the positive z-axis from distal to proximal. Table 5.5 summarises the forces reported by Heller *et al* [84] based on the simplified model and the forces applied to the anatomically model, based on a typical patient of 836 N.

	F_x (N)	F_y (N)	F_z (N)
Centre of femoral head	-519	-381	-2,570
Greater trochanter	541	127	675
Vastus lateralis	-7.5	155	-777

Table 5.5: Forces applied to the anatomical finite element model, representative of peak load from walking

To prevent point stress concentrations, the loads applied to the finite element model were distributed across a number of nodes. Figure 5.11 illustrates the location of the applied loads on the anatomical model. Note that the loading for the centre of the femoral head was applied on the proximal surface to ensure the applied forces acted through the centre of the stem head and were not biased posteriorly or anteriorly.

In line with the anatomical model residual stress initial conditions, the cement-femur interface was assumed to have bonded conditions, while the stem-cement interface was assumed to have debonded conditions, with a coefficient of friction of 0.32. The MPC algorithm was utilised to model the bonded cement-femur interface condition, while the Augmented-Lagrange contact algorithm was utilised to model the stem-cement interface. Section 5.4.2 details the rationale for these interface conditions.

Figure 5.11: Posterior-anterior view of anatomical model with loads applied. Note triad at bottom right denoting X, Y, and Z directions; (Left) Complete model with loads applied. Note loads were applied over 2 to 3 nodes; (Right) Nodal view of proximal portion of construct with loads applied

5.4.4 Rehabilitation Analysis

To quantify the construct stresses for the rehabilitation activity of walking, the boundary conditions and loads, as defined in Section 5.4.2, for the residual stresses in conjunction with the boundary conditions and loads as defined in Section 5.4.3 for physiological activity of walking were applied to the anatomical model, to form a new simulation.

5.5 Results

5.5.1 Transient Thermal Results

Figure 5.12 illustrates the transient thermal simulation result over the first 600 seconds.

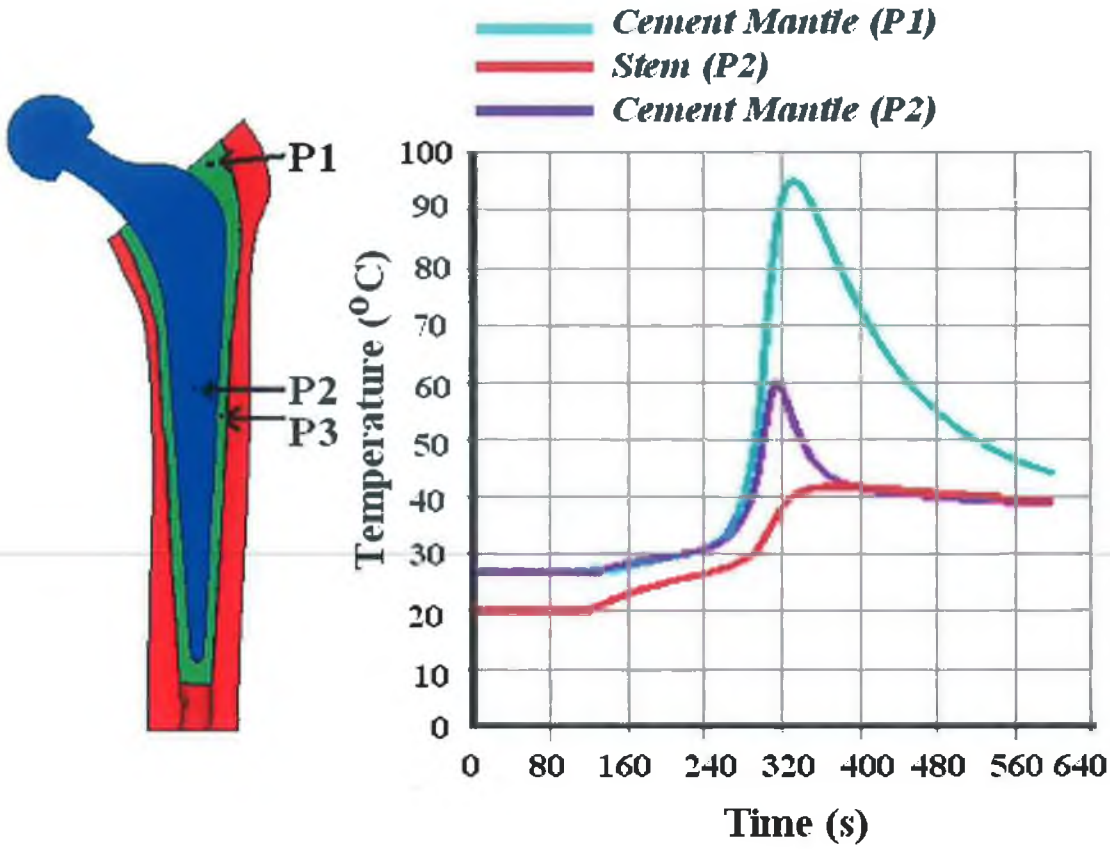

Figure 5.12: Anatomical model transient thermal result over first 600 seconds (10 minutes)

Time 0 seconds coincides with the initiation of bone cement mixing. Over the first 120 seconds, it was assumed that the bone cement and stem had not been added to the medullary cavity and therefore the temperatures remained unchanged. After 120 seconds, it was assumed that both the stem and cement had been added to the medullary cavity, and thermal transfer initiates. After 240 seconds the bone cement begins to significantly exotherm, (Figure 4.11). The increase in cement temperature up until this time (240 seconds) was primarily due to thermal conduction.

From Figure 5.12 it is evident that different portions of the cement mantle reached different peak temperatures. Also from Figure 5.12 it is evident that all the bone cement did not reach peak temperature at the same time. For the cement along the shaft portion of the stem, where the cement mantle was typically 3 mm thick, the peak temperature was typically 59°C and occurred at 315 seconds. For

the cement at the proximal lateral location (in the region of P1 on Figure 5.12), the peak temperature was typically 95°C and occurred at 333 seconds. As the majority of the cement mantle was approximately 3 mm thick and reached peak temperature at 315 seconds, model peak temperature was assumed to occur at 315 seconds. Figure 5.13 illustrates the temperature profile at 315 seconds after the initiation of bone cement mixing.

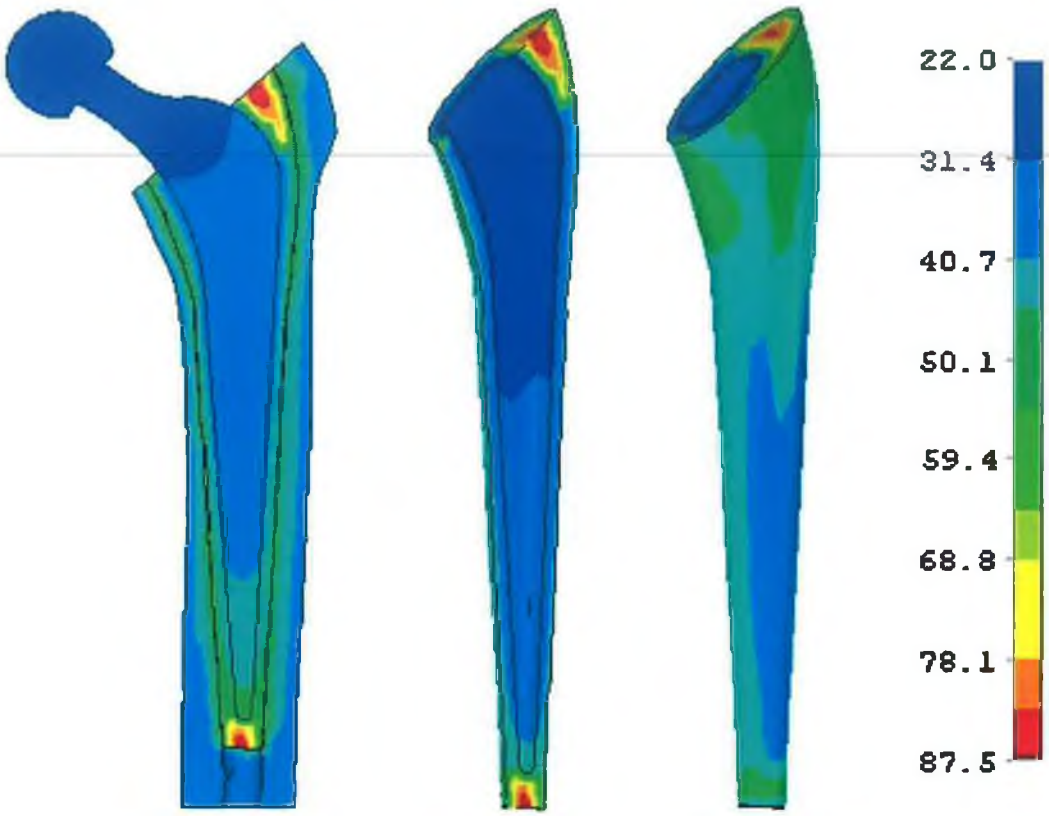

Figure 5.13: Thermal distribution (°C) at 315 seconds after initiation of bone cement mixing. This thermal distribution represents the moment of peak temperature for the majority of the cement mantle.

From the experimental work, the average first registration of residual strain occurred at approximately 7 seconds before the attainment of peak cement temperature. As outlined in Section 4.6.2, for the calculation of residual stress, stress-locking was assumed to occur 7 seconds before the attainment of peak temperature. *In vivo* it is unlikely that the entire cement mantle would have sufficiently solidified to sustain a stress at exactly the same time. However it has

been postulated in the literature [32] and is the authors opinion, that the time span between different regions for stress-locking is small, and the effect of this assumption would not significantly affect the residual stress levels. Figure 5.14 illustrates the anatomical model thermal distribution at the moment of assumed stress-locking, i.e. 308 seconds.

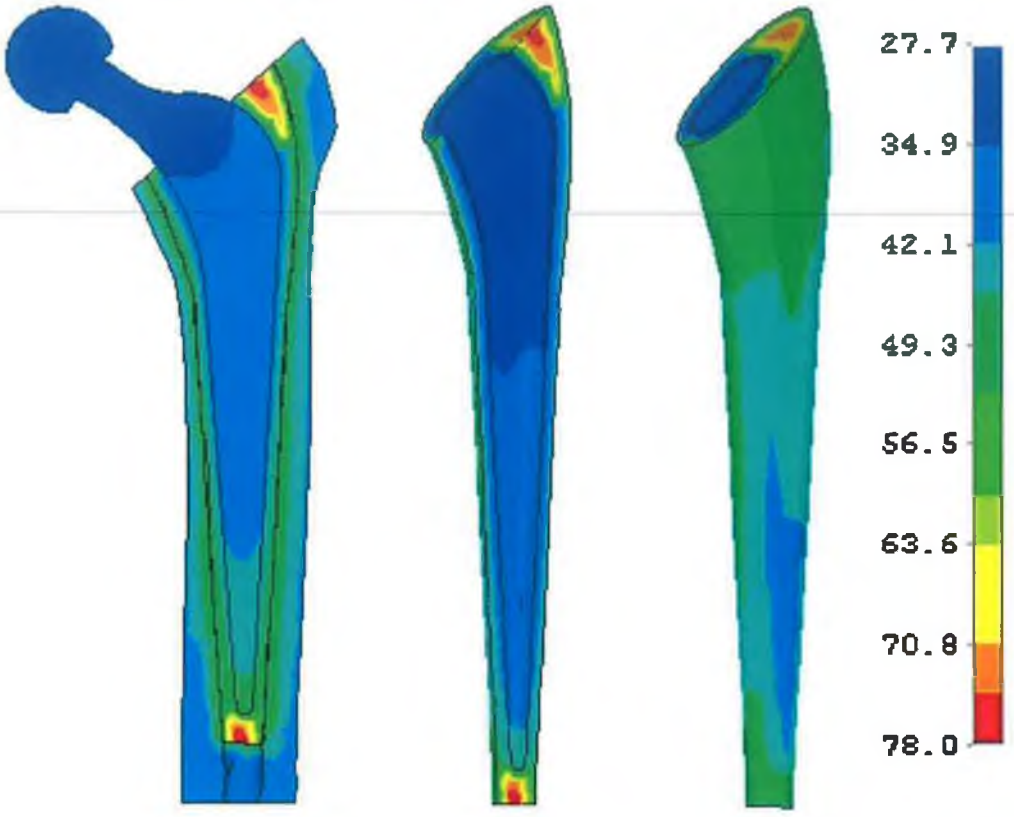

Figure 5.14: Thermal distribution (°C) at 308 seconds after initiation of cement mixing. This thermal distribution represents the moment of assumed bone cement stress-locking.

Figure 5.15 illustrates the temperature profile at 308 seconds after the initiation of cement mixing, for the path indicated on the left diagram of Figure 5.15.

5.5.2 Residual Stress Results

Figures 5.14 and 5.15 illustrated the temperature distribution at the assumed

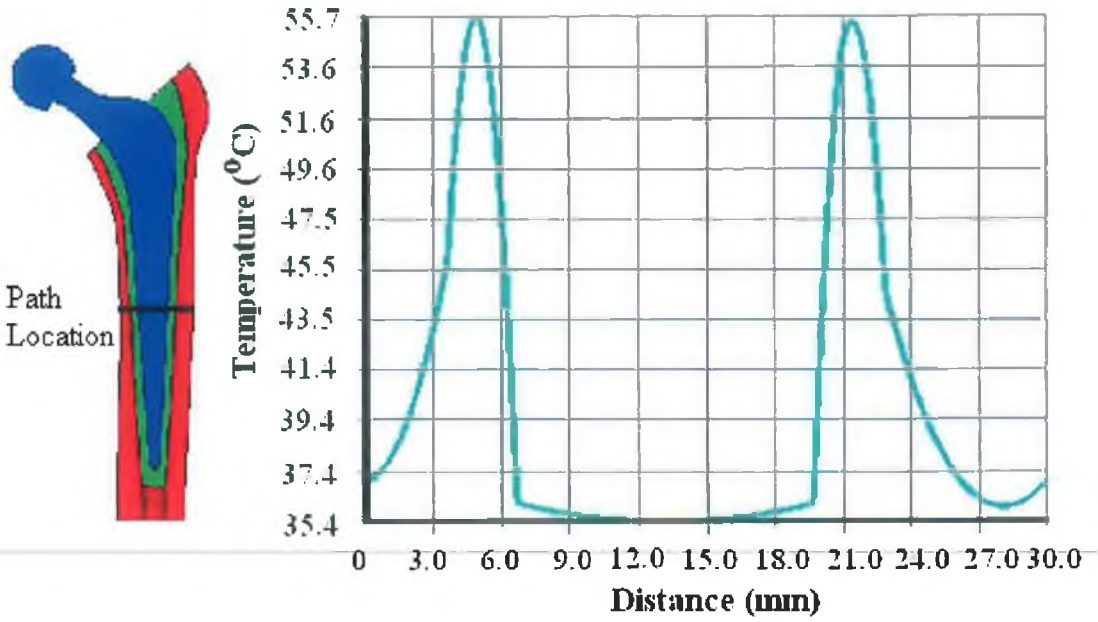

Figure 5.15: Temperature profile (°C) along the path as indicated on left solid model at the moment of assumed stress-locking.

moment of stress-locking, i.e. 308 seconds after the initiation of mixing. This thermal profile was applied to the mechanical environment and the residual stresses calculated with respect to 37°C.

A peak von Mises residual stress of approximately 25 MPa was predicted to occur at the most distal tip of the cement mantle at the cement-femur interface. Figure 5.16 illustrates the peak bone cement mantle von Mises residual stress distribution.

While the peak calculated von Mises residual stress was approximately 25 MPa, from Figure 5.16 it is evident that the majority of the bone cement mantle was at a residual stress significantly below 25 MPa. To examine the bone cement mantle distribution of residual stress quantitatively, the von Mises stress for each node in the cement mantle was grouped into stress ranges. Figure 5.17 illustrates the percentage volume of the bone cement mantle within each stress range. The average von Mises residual stress for the bone cement mantle volume was 5.25 MPa, with a standard deviation of 2.8 MPa.

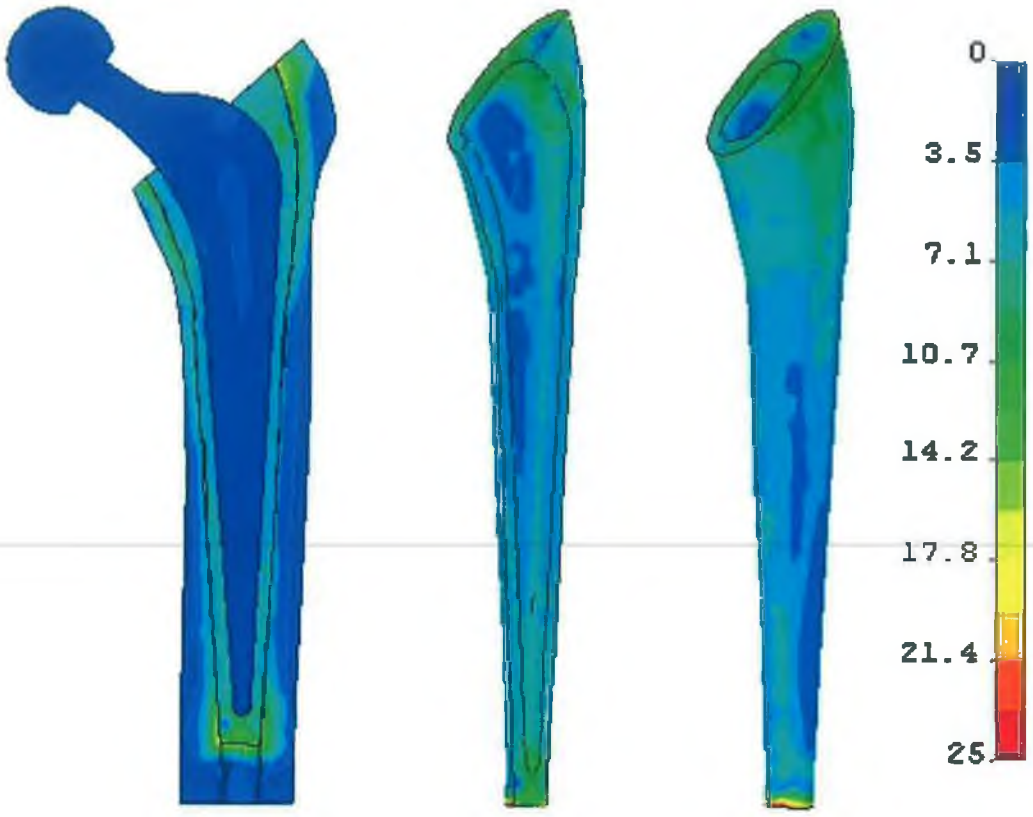

Figure 5.16: Peak bone cement mantle von Mises residual stress distribution (MPa)

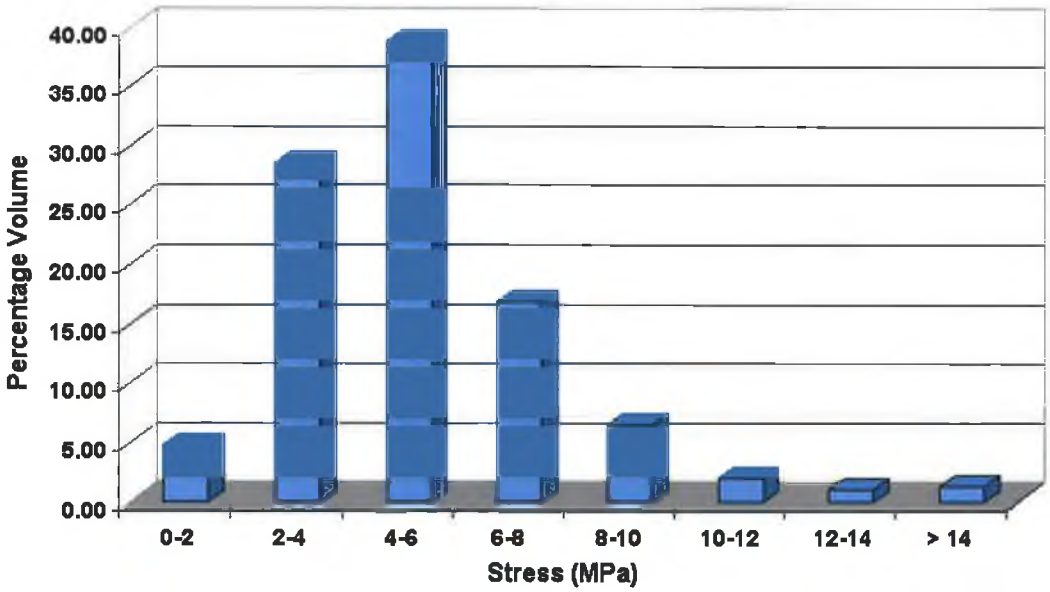

Figure 5.17: Bone cement mantle residual stress distribution over a stress range of 0 to 14 MPa

Note that 95.5% of the bone cement mantle had a residual stress below 10 MPa, and 84.2% of the cement mantle had a residual stress between 2 to 8 MPa. Figure 5.18 illustrates the portions of the cement mantle with a von Mises stress greater than 10 MPa.

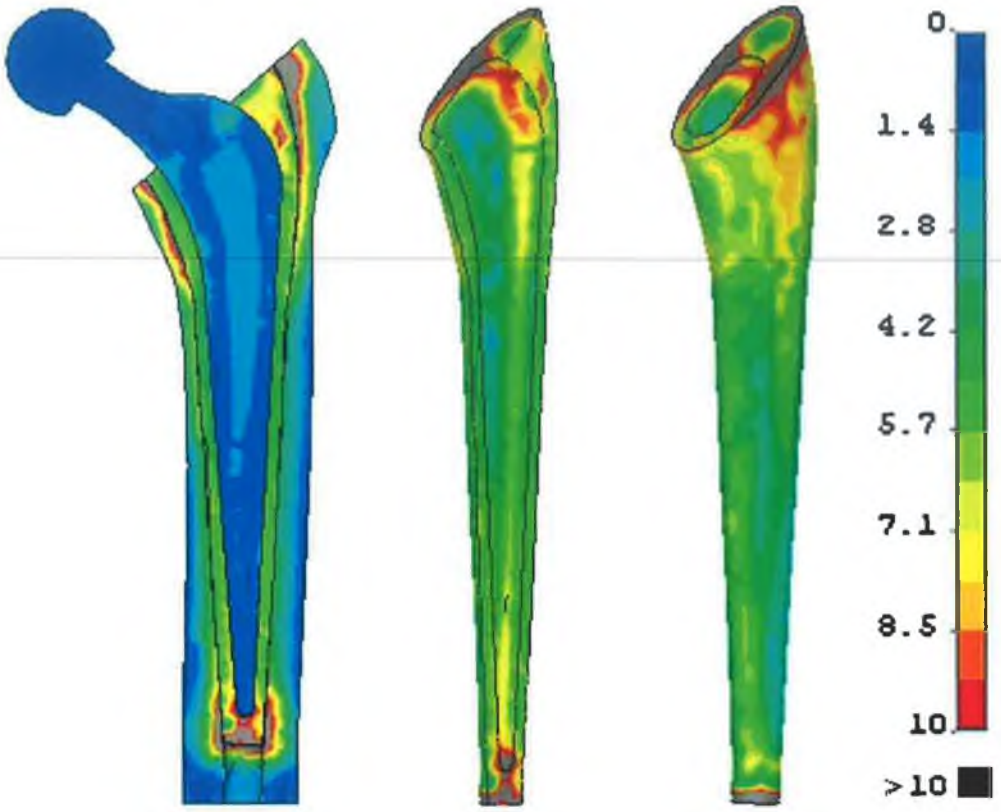

Figure 5.18: Bone cement mantle von Mises residual stress (MPa), with regions of the mantle under highest stress indicated by grey

In an attempt to quantify the individual longitudinal, hoop and radial stresses, a path was defined approximately in line with both the coordinate system and the ANSYS vector plot of the principal stresses. The path location is illustrated on the solid model in Figure 5.19. Onto this path, the stresses in the X, Y and Z directions were defined, approximately coinciding with the radial, hoop and longitudinal stresses respectively. Note however that the stresses plotted in Figure 5.19 are only approximate principal stresses, as the path defined may not be exactly in line with the true principal stress directions. For the same path, the ANSYS predicted principal stresses were also calculated. Minimal differences

existed between Figure 5.19 and the ANSYS plot of principal stresses. Appendix L contains a plot of the principal stresses for the same path defined in Figure 5.19.

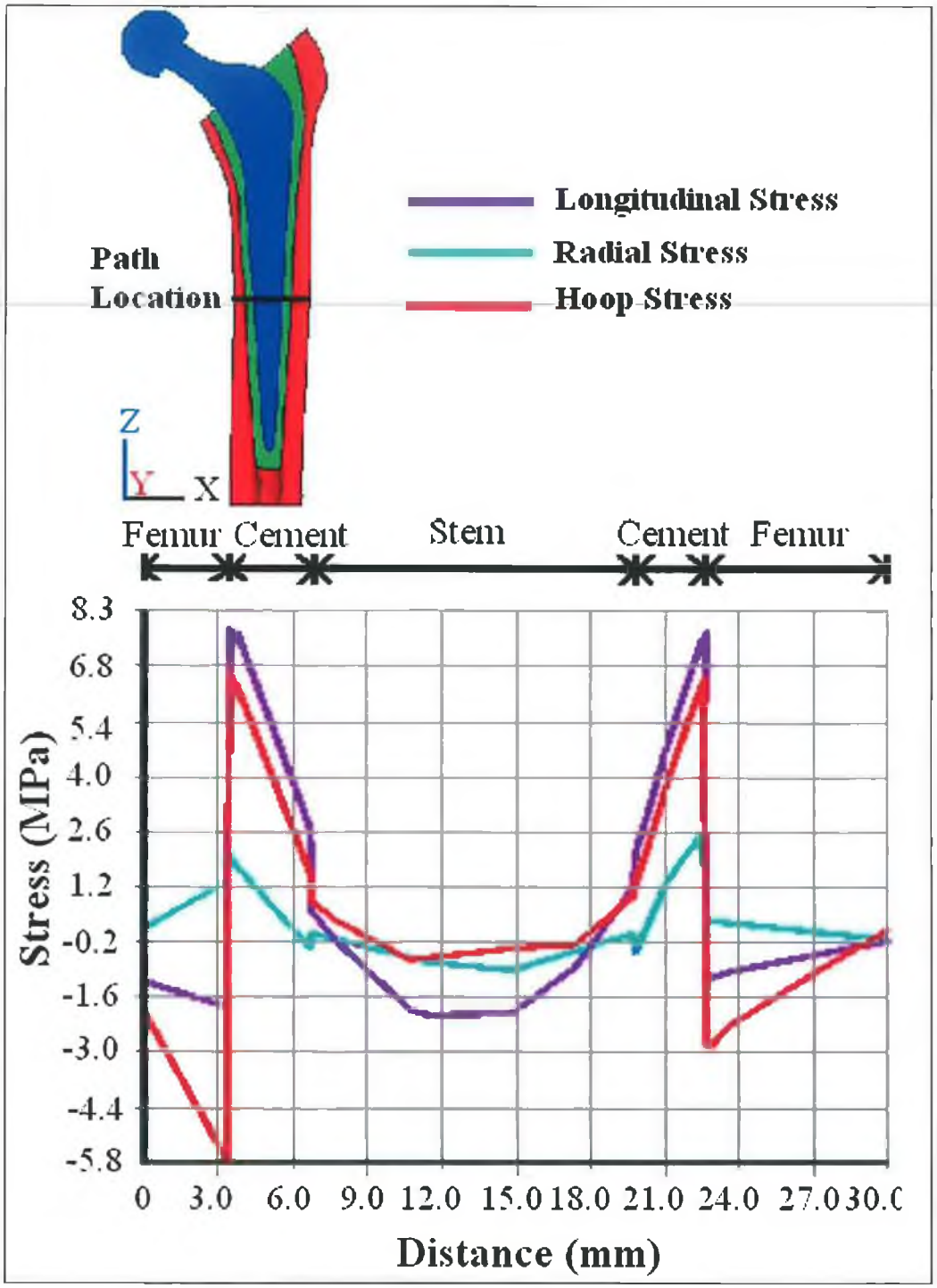

Figure 5.19: Approximate principal residual stresses for the path defined on solid model

For the path defined in Figure 5.19, longitudinal residual stresses were the most significant of the principal stresses at approximately 8 MPa. Hoop residual stress were the next most significant at approximately 6.5 MPa, while radial stresses were the least significant at approximately 2.5 MPa. For all the principal stresses, the peak stress occurred at the cement-femur interface.

5.5.3 Physiological Load Results

Based on the peak physiological load from walking, results revealed the peak von Mises stress to occur in the Exeter™ prosthesis at the middle to distal longitudinal portion on the medial side, (Figure 5.20). The peak von Mises magnitude was 250 MPa, however the majority of the stem volume was at a stress substantially less than 250 MPa.

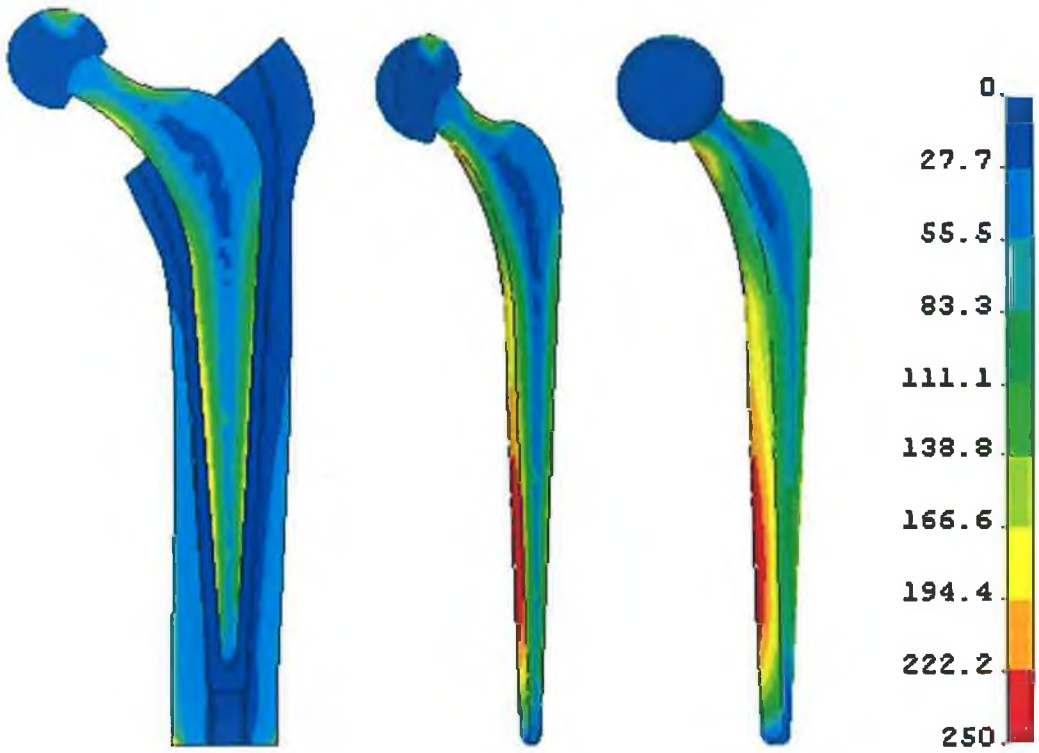

Figure 5.20: Von Mises stress (MPa) distribution for the artificial hip construct due to the peak physiological load from walking

From Figure 5.20 it is evident that the stresses of the bone cement mantle were substantially less than those of the Exeter™ stem. The peak bone cement von Mises stress was 27 MPa and occurred at the distal end of the cement mantle, where the most distal tip of the Exeter™ stem met the bone cement mantle, (Figure 5.21).

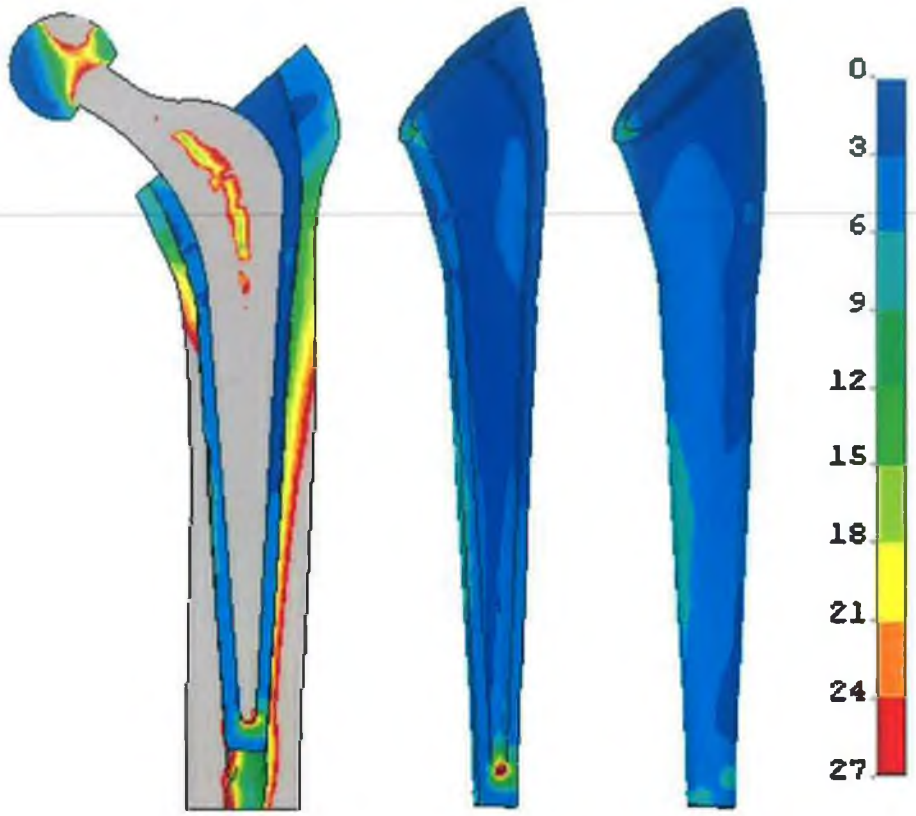

Figure 5.21: Von Mises stress (MPa) distribution for the bone cement mantle due to the peak physiological load from walking

From Figure 5.21 it is evident that the majority of the cement mantle is at a stress substantially below 27 MPa. To examine the bone cement mantle distribution of stress quantitatively, the von Mises stress of each node in the cement mantle was divided into stress ranges and the percentage volume of the bone cement volume within each stress range was calculated. Figure 5.22 illustrates the stress distribution result. The mean von Mises stress for the bone cement mantle volume was 3.21 MPa, with a standard deviation of 2.3 MPa.

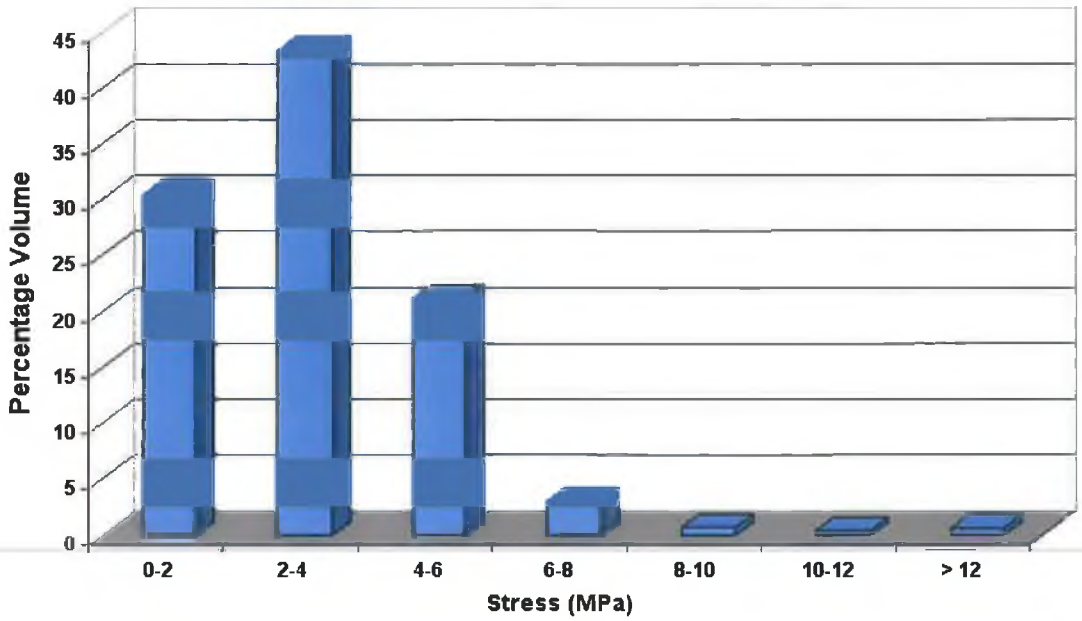

Figure 5.22: Bone cement mantle stress percentage volume distribution over a von Mises stress range of 0 to 12 MPa, due to the peak load from walking

As illustrated in Figure 5.22, the majority of the cement mantle (98%) had a von Mises stress less than 8 MPa, with 95% of the cement mantle with a von Mises stress less than 6 MPa. Figure 5.23 illustrates the stress distribution over 0-8 MPa, with the portions of the cement mantle greater than 8 MPa shaded in grey.

In an attempt to quantify the longitudinal, hoop and radial stresses, a path was defined approximately in line with both the coordinate system and the ANSYS vector plot of principal stresses. Onto this path, the stresses in the X, Y and Z direction were mapped, approximately coinciding with the radial, hoop and longitudinal stresses respectively, (Figure 5.24). Note however that the principal stresses calculated are approximate, as the path defined may not be exactly in line with the true principal stress directions. For the same path, the ANSYS predicted principal stresses were also calculated. Minimal difference existed between Figure 5.24 and the ANSYS plot of principal stresses. Appendix L contains a plot of the principal stresses for the same path defined in Figure 5.24.

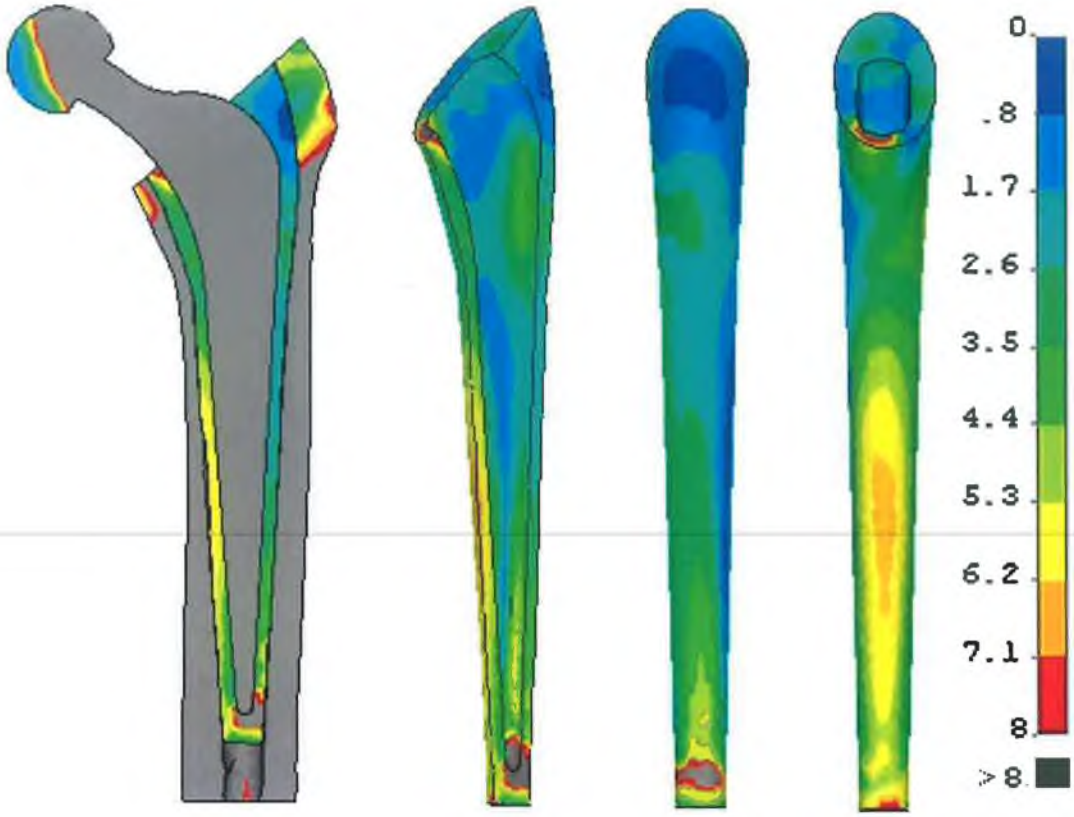

Figure 5.23: Von Mises stress (MPa) due to peak walking load, with regions of the mantle under highest stress indicated by grey

From Figure 5.24, it is evident that the longitudinal stress was the most significance of the principal stresses. Radial and hoop stresses appear to be of negligible magnitude for the path location considered.

5.5.4 Rehabilitation Stress Results

To approximately quantify the peak stresses in the artificial hip construct during the patient rehabilitation activity of walking, the residual stresses due to bone cement polymerisation in conjunction with the peak physiological load from walking was applied to the anatomical model. Figure 5.25 illustrates the maximum von Mises stresses calculated for the artificial hip replacement for the rehabilitation activity of walking. The peak von Mises stress was 250 MPa and occurred in the femoral prosthesis, at the middle to distal longitudinal portion on

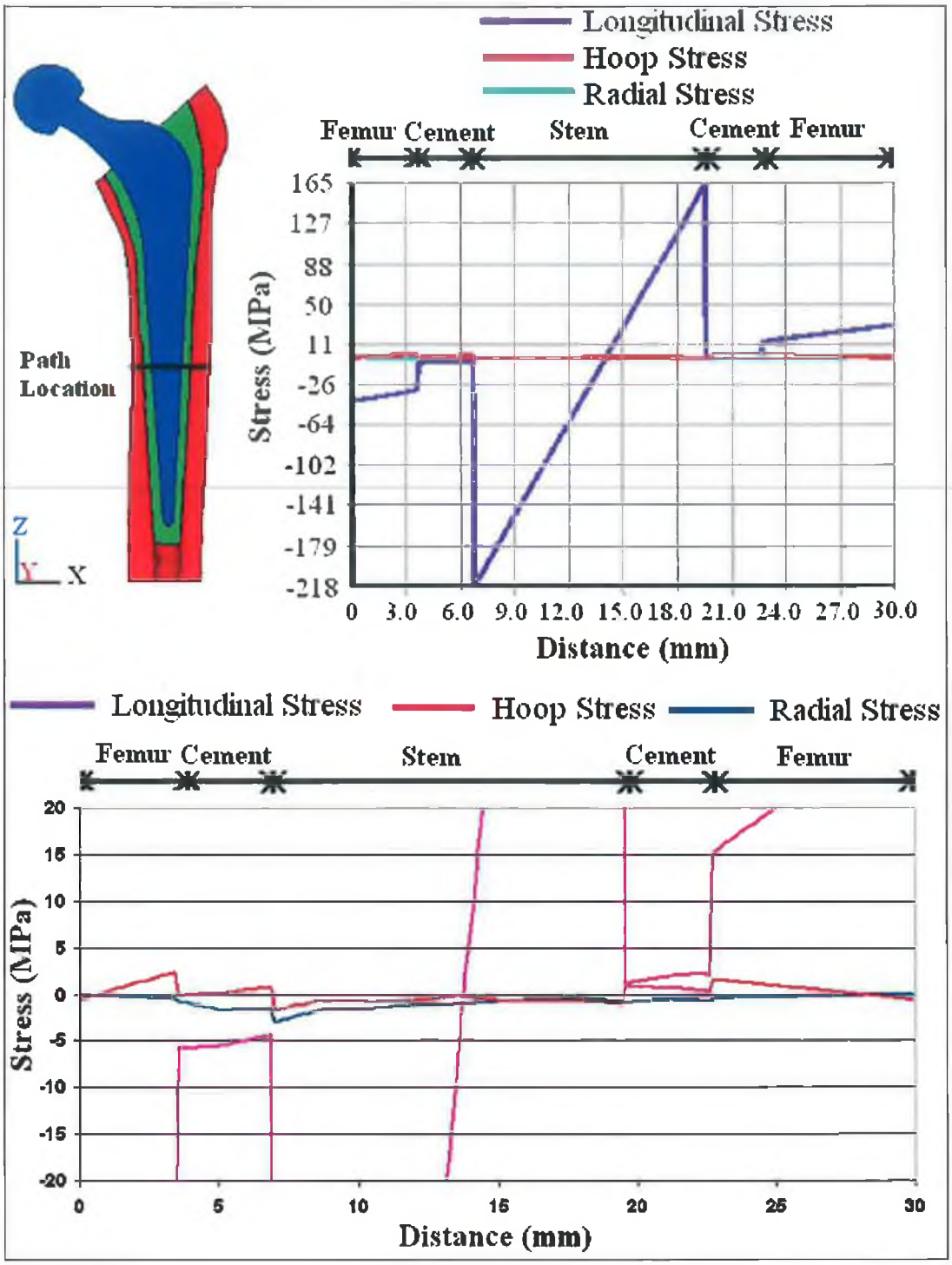

Figure 5.24: Approximate longitudinal, hoop and radial stresses due to the peak load from walking; (Top) Path location and principal stresses along defined path; (Bottom) Magnified view of defined path principal stresses

the medial side, (Figure 5.25). Note the location and magnitude of the peak stress is similar to that for the application of physiological walking forces only.

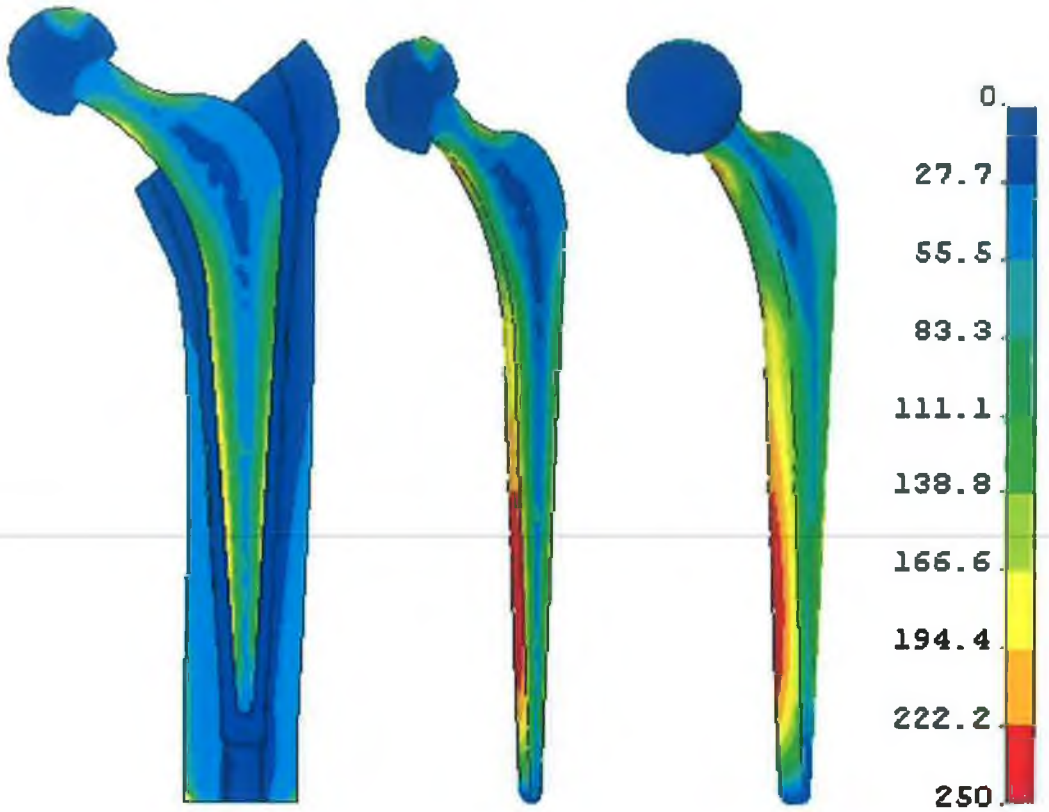

Figure 5.25: Von Mises stress (MPa) for the rehabilitation activity of walking on the artificial hip construct

With respect to the bone cement mantle, a peak von Mises stress of 40 MPa was predicted to occur. The peak stress occurred at the distal end of the cement mantle, where the stems most distal tip met the bone cement mantle, (Figure 5.26). The location of the peak bone cement mantle stress is similar to that for the application of physiological walking forces only.

Similar to previous findings, the majority of the cement mantle was at a stress substantially below the peak stress. The average von Mises residual stress for the bone cement mantle volume was 6.9 MPa, with a standard deviation of 3.6 MPa. Figure 5.27 illustrates the percentage volume of the bone cement volume within defined stress ranges up to 14 MPa.

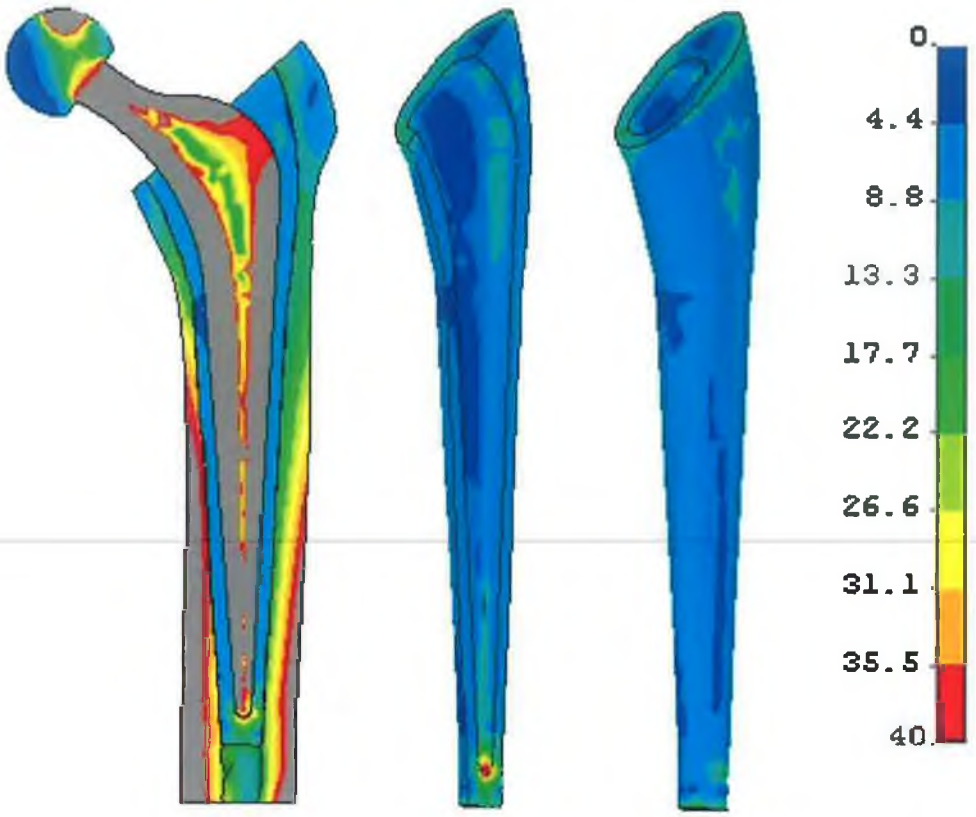

Figure 5.26: Peak bone cement mantle von Mises stress (MPa) for the rehabilitation activity of walking

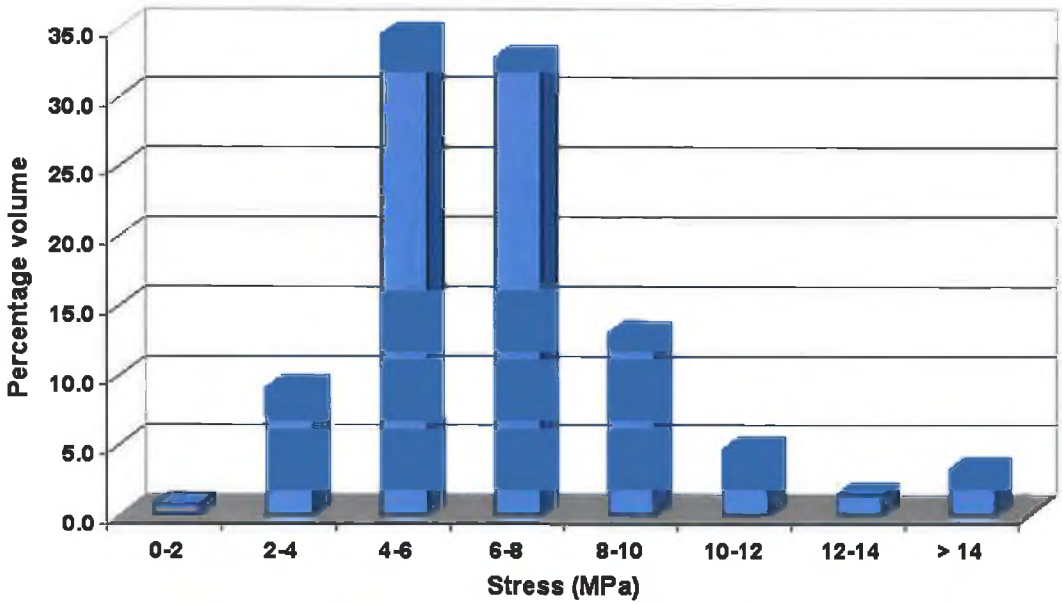

Figure 5.27: Bone cement mantle stress percentage volume distribution over a von Mises stress range of 0 to 14 MPa for the rehabilitation activity of walking

The peak bone cement von Mises stress was 40 MPa, however 97% of the bone cement mantle had a von Mises stress less than 14 MPa, with 90% of the cement mantle between 2 to 10 MPa. Figure 5.28 illustrates the portions of the cement mantle with a von Mises stress greater than 14 MPa.

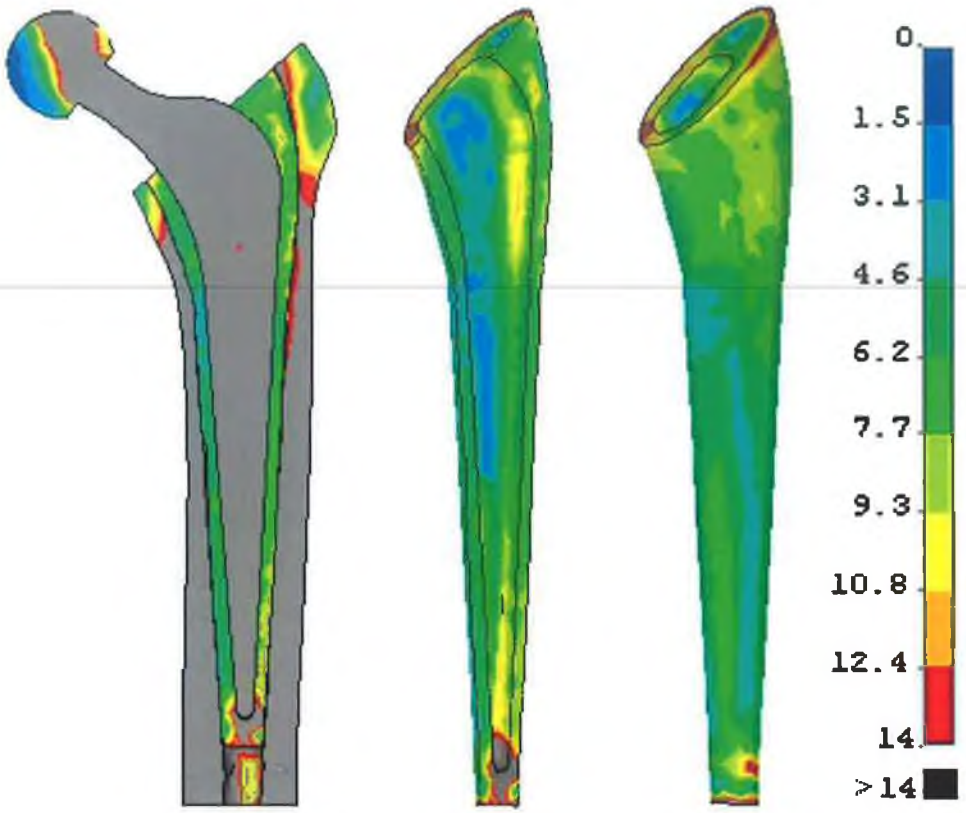

Figure 5.28: Bone cement von Mises stress (MPa) for the rehabilitation activity of walking, with regions of the mantle under highest stress indicated by grey

The reported ultimate tensile stress of bone cement varies between 24 to 49 MPa [48]. Due to the presence of stress concentrators (pores, debris etc), the lower end of this failure stress band is postulated to be sufficient to induce fracture damage. Figure 5.29 illustrates the stress distribution over 0 to 24 MPa, with the portion of the cement mantle greater than 24 MPa shaded in grey.

In an attempt to quantify the longitudinal, hoop and radial principal stresses, a path was defined approximately in line with both the coordinate system and the ANSYS vector plot of the principal stresses. Onto this path, the stresses in the X,

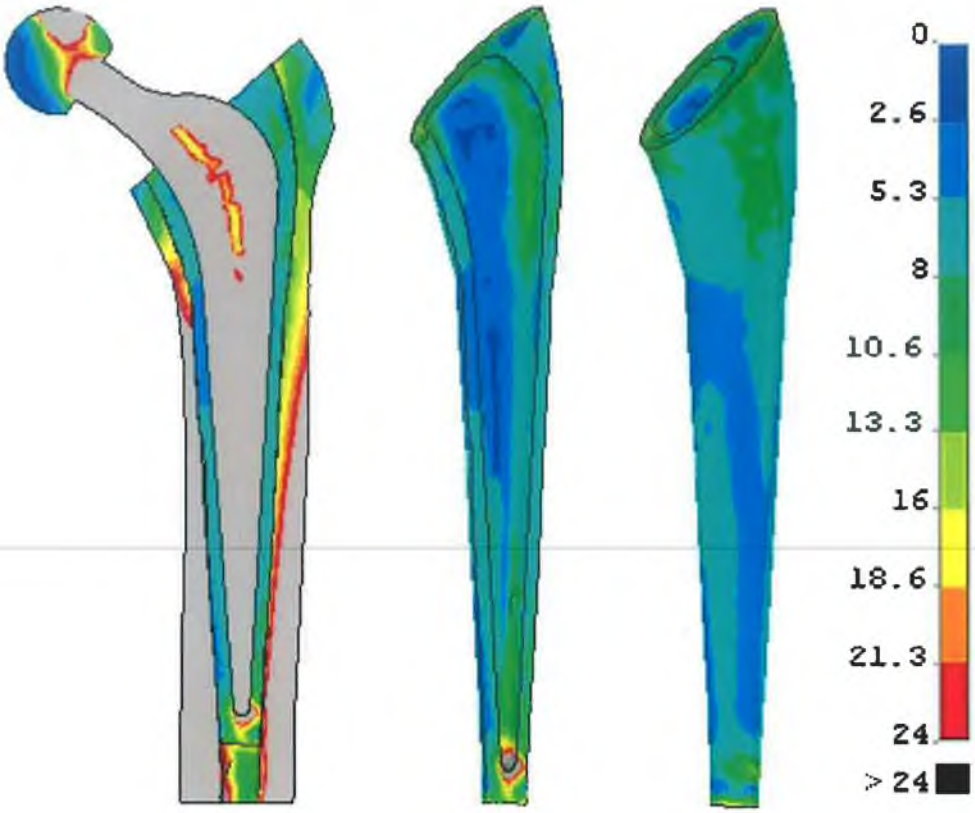

Figure 5.29: Bone cement von Mises stresses (MPa) for the rehabilitation activity of walking, with regions of the mantle with a von Mises stress greater than 24 MPa indicated by grey

Y and Z directions were defined, approximately coinciding with the radial, hoop and longitudinal stresses respectively. Figure 5.30 illustrates the assumed principal stresses along the path. Note that these principal stresses are approximate, as the path may not be exactly aligned with the true principal stress directions. For the same path, the ANSYS predicted principal stresses were also calculated and compared. Minimal difference existed between Figure 5.30 and the ANSYS plot of principal stresses. Appendix L contains a plot of the principal stresses for the same path defined in Figure 5.30.

For the path location defined in Figure 5.30, the bone cement radial stresses were approximately 2.5 MPa, the hoop stresses were approximately 7 MPa and the longitudinal stress were approximately 2.5 MPa medially and 10 MPa laterally. For all the principal stresses, the peak stress occurred at the cement-femur interface.

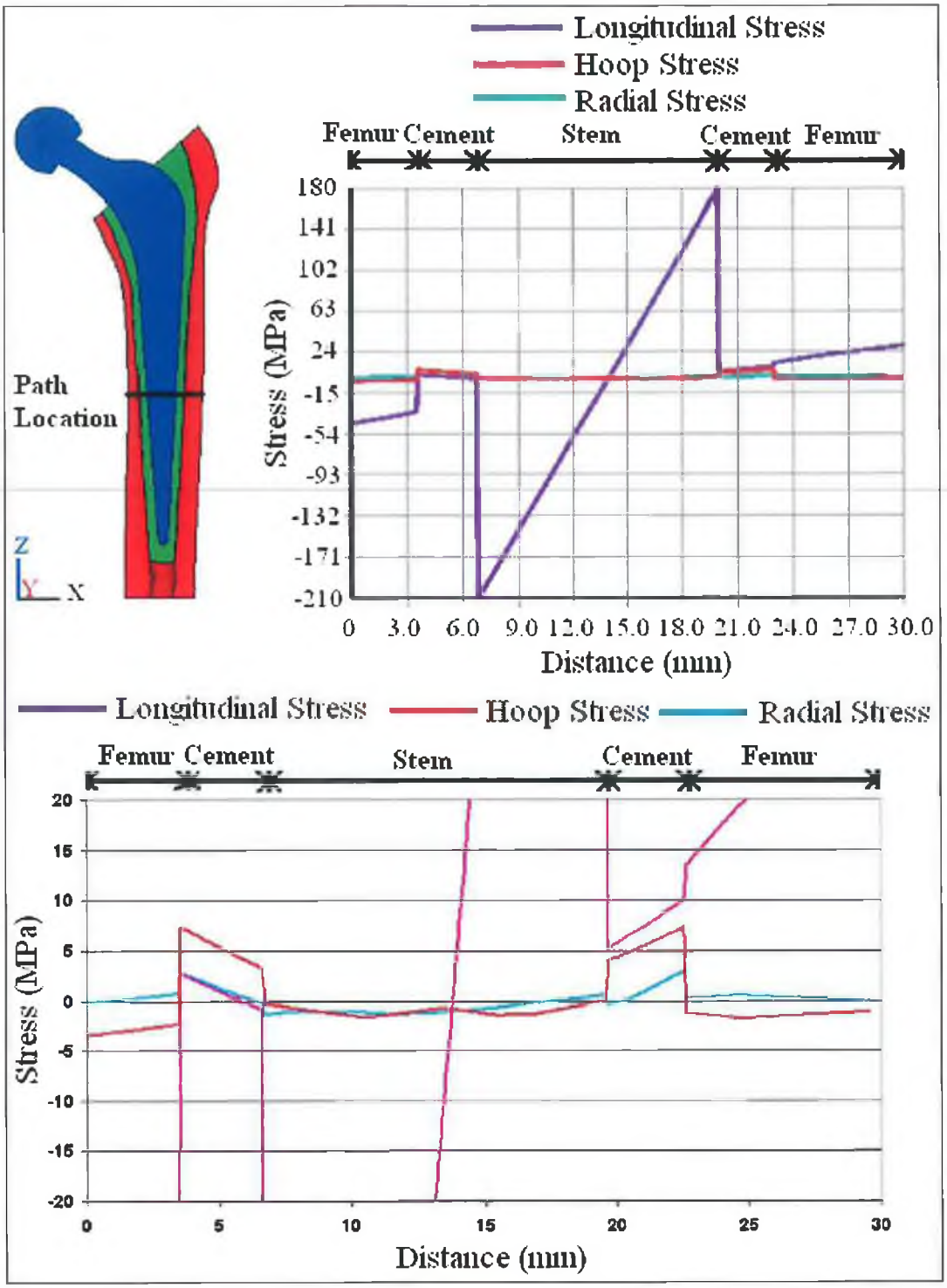

Figure 5.30: Approximate longitudinal, hoop and radial stresses for the rehabilitation activity of walking; (Top) Path location and principal stresses along defined path; (Bottom) Magnified view of principal stresses

5.6 Discussion

5.6.1 Transient Thermal Analysis

Results from the transient thermal analysis revealed that different regions of the cement mantle reached different peak temperatures. For example, along the shaft portion of the prosthesis where the cement mantle was typically 3 mm thick, the peak temperature was typically 59°C, while for the cement at the proximal lateral and distal portion of the cement mantle, where the mantle was relatively thick (greater than 5 mm), the peak temperature was typically 95°C. The different peak temperatures were primarily due the non-uniform cement mantle thickness. Numerous thermal analyses in the literature also have reported non-uniform peak temperature results [56, 57, 66, 142].

The peak temperature of 59°C, where the cement mantle was typically 3 mm thick, matches well with similar reports in the literature. Roques *et al* [34] measured a peak cement temperature of approximately 58°C based on a 2 mm thick cement mantle about a stainless steel tube 1 mm thick. Hansen [142] reported a peak temperature of 53°C based on a finite element model with an approximately 3 mm thick cement mantle. Starke *et al* [66] reported a peak temperature of approximately 50°C based on a finite element model with a 2.5 mm thick cement mantle.

At the proximal lateral and distal locations of the cement mantle, where the mantle was relatively thick (greater than 5 mm), the cement reached a much greater peak temperature of approximately 95°C. This finding also matches well with similar reports in the literature. Swenson *et al* [56] calculated a peak temperature of 98°C based on a 10 mm thick cement mantle. Li *et al* [108] calculated a peak temperature of 87°C based on a 5 mm thick cement mantle. Ahmed *et al* [65] measured a peak temperature of approximately 110°C based on an 8 mm thick cement mantle. The average peak temperature from the experimental work documented in Chapter 3, based on a 5.4 mm thick cement mantle of CMW® 1 Gentamicin cement was 95.6°C.

The cement-femur interface has been the focus point of many *in vivo*, *in vitro* and computational research projects to investigate if thermal cell necrosis occurs. Based on the developed anatomical model, the femoral bone tissue in direct contact with the bone cement reached a peak temperature of 54°C both at the proximal-lateral and distal locations of the bone cement mantle where the cement reached a peak temperature of approximately 95°C. For the majority of the cement mantle, where the cement was approximately 3 mm thick, the peak bone tissue temperature was approximately 48°C. This result matches well with the literature. In a recent finite element study, Hansen [142] predicted a peak cement-femur interface temperature of 48°C, based on a 3 mm thick cement mantle. Toksvig-Larsen *et al* [61] measured the cement-femur interface temperature *in vivo* during 41 arthroplasties. The average cement-femur interface temperature was 40°C, ranging between 29 to 56°C with a standard deviation of 6°C. Huiskes [8] reported *in vivo* studies by Labitzke *et al* [62] and Biehl *et al* [63] that reported the *in vivo* femur-cement interface to be 45°C and 47°C respectively.

For the cement-femur interface, a higher peak temperature was predicted compared to the stem-cement interface. This is in line with numerous thermal analyses in the published literature [32, 56, 67, 108] and is due to the higher initial temperature of the femur, its lower heat capacity and lower thermal conductivity compared to the stem prosthesis. For the stem material in direct contact with the bone cement, at the proximal-lateral region, the peak temperature was approximately 39°C. For the middle stem shaft portion longitudinally, the peak temperature was approximately 43°C. Finally at the most distal tip of the Exeter™ stem, the peak temperature was 51°C. It is difficult to compare these magnitudes with sources in the literature, as relatively few authors have reported the stem-cement interface temperature. However, based on an axisymmetric model with a 5 mm thick cement mantle, Swenson *et al* [56] reported a prosthesis-cement interface temperature of approximately 50°C and Li *et al* [108] reported a stem-cement interface temperature of 57°C based on a 5 mm thick cement mantle about an aluminium cylinder to represent the femoral prosthesis.

The transient thermal analysis also predicted that the entire bone cement mantle would not reach peak temperature simultaneously. For the majority of the cement mantle along the shaft portion of the stem where the cement was approximately 3 mm thick, the cement reached its peak temperature at approximately 315 seconds, while for the cement at the thicker regions, the proximal lateral section of the mantle for example, reached its peak temperature approximately 18 seconds later. This observation is in line with a number of sources in the literature. Thermal FEA by Lennon and Prendergast [32] reported a 38 second interval between the first and last element reaching peak temperature. Starke *et al* [66] reported a 20 seconds interval between peak temperatures, while research by Li *et al* [108] and Baliga *et al* [55] also noted this observation.

5.6.2 Residual Stress Analysis

Residual stress results predicted a peak von Mises stress of 25 MPa to occur at the cement-femur interface, at the most distal tip of the cement mantle. Typical cement mantle stresses however were much lower, with 95.5% of the cement mantle volume at a von Mises residual stresses below 10 MPa. Only the proximal-lateral and distal regions of the cement mantle exceed a stress of 10 MPa. These regions coincide with the locations of highest temperature at the moment of stress-locking and therefore the occurrence of peak residual stresses at these locations fit current residual stress understanding. The average von Mises residual stress for the bone cement mantle volume was 5.25 MPa, with a standard deviation of 2.8 MPa.

Approximate principal stresses were quantified for the middle longitudinal region of the construct. Longitudinal residual stresses were the most significant at approximately 8 MPa. Hoop residual stresses were the next most significant at approximately 6.5 MPa. While radial stresses were the least significant of the principal stresses and were substantially below both the longitudinal and hoop stresses at 2.5 MPa.

It is not possible to directly compare the anatomical model predicted residual stress magnitude and distribution with the literature, as all previous residual stress analyses, both experimental and computational, have been based on simplified geometries, typically regular straight cylinders. Possibly the most similar residual stress analysis in the published literature was research by Lennon and Prendergast [32]. While their finite element model was 3-D, it was essentially 2-D in character, as the model consisted of a medial and lateral bone cement strip of unknown thickness to represent the cement mantle, (Figure 2.20). As such, the hoop stresses were not accounted for in their model. Lennon and Prendergast [32] reported the maximum principal stresses to be between 4 to 7 MPa, from a peak stress-locking temperature of 53°C. Assuming longitudinal stress was their maximum principal stress, 7 MPa compares well with our typical longitudinal stress of 8 MPa.

Comparing the residual stress magnitudes between the middle longitudinal portion of the anatomical model, with the experimental model documented in Chapter 4, it is evident that both models predicted longitudinal stresses to be the most significant, closely followed by hoop stresses, with radial stresses being the least significant. The anatomical model predicted residual stresses approximately half the magnitude compared to those of the experimental model. This was to be expected as the stress-locking temperature for the experimental model was approximately 89°C, while the stress-locking temperature for the anatomical model was approximately 56°C. Based on the anatomical model, the peak residual stresses occurred at the femur-cement interface, while for the experimental model the peak residual stresses occurred at the centre of the cement mantle. It is postulated that this change in peak residual stress location is due to the greater Young's modulus of femoral bone in the hoop direction (approximately 9 GPa) compared to that of the e-glass/epoxy (approximately 3 GPa). Therefore, for the experimental model, the e-glass/epoxy was relatively yielding and the peak residual stress coincided with the location of peak temperature. For the anatomical model, the femoral bone is much more stiff and prevents the cement mantle from shrinking about the stem, therefore shifting the peak residual stress from the middle of the cement mantle to the femur-cement interface.

The reported ultimate tensile strength of bone cement varies between 24 to 49 MPa [48]. Experimental results have revealed the presence of microcracks in bone cement at or near the site of a stress concentrator before any functional loading [33]. It is postulated that due to the presence of stress concentrators, the lower end of this failure stress band would be sufficient to induce fracture damage. It is therefore postulated that the regions of the bone cement mantle under peak residual stress would incur fracture damage before any functional loading. However, this would occur for a relatively small volume of the cement mantle and considering the average cement mantle residual stress was 5.25 MPa, the artificial hip construct would function as expected with no obvious sign(s) of damage apparent to the patient or the medical staff. In the long term however, for the small region that incurred fracture damage, the presence of fractures would accelerate fatigue damage and this localised failure in turn may increase the stresses for the remaining undamaged cement mantle.

5.6.3 Physiological Stress Analysis

Based on the peak load for the physical activity of walking, the maximum von Mises stress was approximately 250 MPa, and occurred in the femoral prosthesis at the middle to distal portion of the shaft longitudinally on the medial side. This result matches well with the literature. El-Shiehk [161] calculated the stresses for a cemented total hip replacement under physiological loading. In line with our research, the author reported the maximum von Mises stress of the construct to occur in the femoral prosthesis at approximately the middle of the shaft longitudinally, on the medial side. However El-Shiehk reported a lower maximum von Mises stress of approximately 175 MPa. This lower stress may be attributed to the substantially thicker stem modelled by El-Shiehk compared to the Exeter™ stem. Brockhurst and Svensson [9] and Svensson *et al* [162] also reported the peak stress to occur in the femoral prosthesis at approximately the middle of the shaft longitudinally, on the medial side. The authors reported a peak compression principal stress of 131 MPa. The lower stress in this case may be attributed to the lower loads applied to their model in conjunction with a thicker stem utilised, in comparison with the Exeter™ stem.

McNamara [163] predicted the stresses for an adapted standard femur with a stem implanted utilising finite element techniques. McNamara predicted Von Mises stresses of approximately 25 to 45 MPa for the cortical bone region of the femoral shaft, with the highest stresses located at the exterior surface of the femur. This result compares well with the physiological load model. For the consideration of the same femoral region, von Mises stresses of 25 to 45 MPa were also predicted, with the highest stresses at the exterior surface of the femur.

For the bone cement mantle, the peak von Mises stress was 27 MPa and occurred at the distal end of the cement mantle, where the distal tip of the Exeter™ prosthesis met the bone cement mantle. Similar to the residual stresses previously discussed, the majority of the bone cement mantle volume had a stress substantially less than the peak stress. The average von Mises stress for the bone cement mantle volume was 3.2 MPa, with a standard deviation of 2.3 MPa. 95% of the bone cement volume had a von Mises stress less than 6 MPa. These results compare well with the literature. Lennon and Prendergast [146] calculated the stresses for the bone cement mantle based on a 3-D finite element model under physiological load conditions with a debonded stem-cement interface with a coefficient of friction of 0.32. Lennon and Prendergast [146] reported a peak stress of 38 MPa to occur at the distal end of the cement mantle, where the most distal tip of the stem met with the bone cement mantle. The larger peak stress calculated by Lennon and Prendergast [146] may be attributed to the greater physiological force applied to their model. The authors also reported that the majority (approximately 95%) of the cement mantle volume remained at a stress below 6 MPa stress. El-Shiehk reported a peak von Mises stress of 18 MPa for the bone cement mantle, with the majority of the cement mantle below 4 MPa, for physiological load conditions. The lower peak stress reported by El-Shiehk, however, may be attributed to the bonded stem-cement condition assumed. Lennon and Prendergast [146] reported a significant reduction in cement mantle stress are inferred if bonded conditions are assumed.

Approximate principal stresses were predicted for the middle longitudinal region of the construct. Longitudinal stress was the most significant at approximately

-5.5 MPa medially and approximately 3 MPa laterally. Both hoop and radial stress had negligible magnitudes of approximately 1 MPa. Unlike the residual stresses, which had the peak stress at the cement-femur interface, all stresses were relatively uniform across the cement mantle.

It is postulated that the region of the bone cement mantle under peak stress would incur fracture damage. However, as the affected volume is relatively small, and as the average stress was 3.2 MPa, it is postulated that the artificial hip construct would function as expected with no obvious sign(s) of damage.

5.6.4 Rehabilitation Stress Analysis

From the literature, residual stresses have been mostly ignored in the calculation of the artificial hip joint construct stresses under loaded physiological conditions due to the assumption that the viscoelastic properties of bone cement would reduce the residual stresses to negligible levels before the patient first loads the artificial joint. Indeed many viscoelastic analyses in the literature support this assumption, (Section 2.2.6). However, most of these viscoelastic experiments were performed at relatively high stresses, much higher than those typically resultant from residual stresses. Bone cement creeps at a much faster rate at higher stresses compared to lower stresses [91] and therefore these viscoelastic measurements may not be applicable to residual stress relaxation. To the best of the authors knowledge, only research by Roques *et al* [34, 41] has monitored stress relaxation from residual stresses. These authors measured negligible stress relaxation over the first 2 hours from the initiation of cement mixing. From such, these authors postulated that when the construct is loaded for the first time by the patient, the residual stresses would be only partially relieved. As a result Roques [41] recommended that residual stresses should be accounted for in the calculation of artificial hip construct stresses, for the early portion of the replacement lifetime. Previous research by Nuno *et al* [38, 112] similarly recommended the inclusion of residual stresses in the calculation of artificial hip construct stresses.

In Chapter 3, 23 residual stress experiments were performed with CMW® 1 Gentamicin bone cement to quantify the residual stress levels based on a number of different initial conditions. For all experiments, the transient residual strains were measured for at least 3 hours. A number of these residual stress experiments were allowed to run for an extended period of time to investigate the stress relaxation properties of CMW® 1 Gentamicin bone cement from residual stresses. Appendix M contains the experimental results. While variation exists in the stress relaxation rates, typically the stress relaxation rates were low and indicate that the majority of the residual stresses would be present in the construction during patient rehabilitation, 24 to 48 hours after surgery. From this, for the quantification of the construct stresses during rehabilitation, the residual stresses as predicted in Section 5.5.2 were assumed to be present during rehabilitation.

For the rehabilitation activity of walking, the peak von Mises stress of the artificial hip construct occurred in the femoral prosthesis at the middle to distal region longitudinally, on the medial side and was of 250 MPa magnitude. This peak construct stress result was identical with the peak stress result for the consideration of walking forces only, and indicates that bone cement residual stresses have negligible impact on the peak femoral prosthesis stress levels. For the bone cement mantle, the peak rehabilitation von Mises stress was 40 MPa and occurred at the distal end of the cement mantle, where the stem distal tip ended. The peak stress location in the bone cement mantle coincided with the peak stress location for the consideration of walking forces only. However the inclusion of residual stress has increased the peak stress due to walking by 48%.

As mentioned previously, the peak von Mises stress under the considered condition of rehabilitation was 40 MPa. A stress of this magnitude, coupled with stress concentrators would almost certainly induce fracture damage to the cement mantle. However the volume of the cement mantle at a sufficiently high stress to induce fracture damage was relatively small. Therefore it is postulated that during rehabilitation, the artificial hip construct would function as expected with no obvious sign(s) of damage apparent to the patient or the medical staff. The localised damage in the short time would have negligible immediate consequences due to the small volume affected. However in the long term, the

presence of these fractures would accelerate fatigue damage. This in turn may increase the stresses for the remaining undamaged cement mantle and accelerate the occurrence of aseptic loosening due to fatigue failure.

For the physiological activity of walking, 95% of the bone cement mantle remained below 6 MPa, while for the rehabilitation activity of walking 95% of the cement mantle remained below 12 MPa. Comparing the averages, for the physiological scenario the average stress was 3.2 MPa ± 2.3 MPa, while for the rehabilitation scenario the average stress was 6.9 MPa ± 3.6 MPa. This comparison clearly demonstrates the significance of residual stresses and reveals residual stresses should be included to accurately establish the cement mantle stress magnitude and distribution for the early portion of the artificial hip replacement lifetime. This research also suggests an extended period of time in bed for the patient post arthroplasty may significantly reduce early cement mantle damage during rehabilitation and therefore extend the lifetime of the THR in the long term.

5.7 Chapter Summary

The finite element methodology defined and implemented in Chapter 4 was applied to a 3-D anatomical model based on the Exeter™ femoral prosthesis. Chapter 5 findings may be enumerated as follows;

1. The transient thermal analysis predicted different regions of the cement mantle reached different peak temperatures. For example, along the shaft portion of the prosthesis where the cement mantle was typically 3 mm thick, the peak predicted temperature was typically 59°C, while for the cement at the proximal lateral and distal portion of the cement mantle, where the mantle was relatively thick (greater than 5 mm), the peak predicted temperature was typically 95°C.

2. The transient thermal analysis also predicted that all regions of the bone cement mantle would not reach peak temperature simultaneously. Where

the cement was approximately 3 mm thick, the cement reached its peak temperature 18 seconds before the proximal lateral and distal portions of the cement mantle, where the mantle was relatively thick.

3. For the consideration of residual stress on its own, von Mises stresses up to 25 MPa were predicted. However the average cement mantle residual von Mises stress was significantly lower at 5.3 MPa.

4. For the consideration of walking stress on its own, von Mises stresses up to 27 MPa were predicted. However the average von Mises stress was significantly lower at 3.2 MPa.

5. For the rehabilitation activity of walking, that is, both residual and walking stresses, results revealed von Mises stresses up to 40 MPa, with an average bone cement von Mises stress of 6.9 MPa.

Results demonstrate that for the early portion of the replacement lifetime, residual stresses are significant and should be included to establish the cement mantle stress distribution and magnitude. This research also suggests that an extended period of time in bed for the patient post arthroplasty, may significantly reduced cement mantle damage during rehabilitation.

Chapter 6

Conclusions And Future Work

6.1 Thesis Contribution

To the best of the author's knowledge, this research represents the following novel contributions;

- The prediction of bone cement mantle residual stresses for a cemented femoral hip replacement based on a 3D *in vivo* finite element model. In conjunction with this the cement mantle stresses from the rehabilitation activity of walking (residual stress in conjunction with the peak load from walking) were also predicted.

- An experimental investigation of the hypothesis that bone cement mantle pressurisation may have a significant effect on the residual stress levels.

- An experimental investigation of the hypothesis that different commercial bone cement brands may produce significantly different residual stress levels.

- An experimental investigation of whether vacuum mixing bone cement has an effect on the residual stress magnitudes.

- The experimental measurement of the linear coefficient of thermal expansion for CMW® 1 Gentamicin and SmartSet® HV Gentamicin bone cements.

- The experimental measurement of bone cement residual stress relaxation for a period of time in excess of 2 hours.

6.2 Conclusions

- This research reveals that bone cement residual stresses are significant, and should be included in calculations to establish the cement mantle stress magnitude and distribution for the early portion of the replacement lifetime.

- For the rehabilitation activity of walking, bone cement mantle von Mises stresses up to 40 MPa were predicted. From this it is postulated that stresses are sufficiently high to produce fracture damage to the bone cement mantle due to this rehabilitation activity. The extent of damage is dependent upon the degree of stress concentration. However it is postulated that a relatively small volume of the cement mantle would incur fracture damage during rehabilitation, as the average von Mises cement mantle stress was 6.9 MPa. This research suggests, and the author recommends, an extended period of rest in bed for the patient post arthroplasty. The extended rest period may significantly reduce residual stresses (due to the bone cements viscoelastic nature) and therefore the extent of cement mantle damage when the patient loads the artificial hip construct for the first time.

- Bone cement mantle von Mises residual stresses up to 25 MPa were predicted based on the *in vivo* model. From this it is postulated that residual stresses on there own are sufficiently high to produce fracture damage in the bone cement mantle before any functional loading. The

extent of damage is dependent on the degree of stress concentration. However it is postulated that a relatively small volume of the cement mantle would incur fracture damage, as the average cement mantle von Mises stress was 5.3 MPa.

- Bone cement von Mises stresses up to 27 MPa were predicted *in vivo* due to the activity of walking. It is postulated that a relatively small volume of the cement mantle would incur fracture damage, as the average cement mantle von Mises stress was 3.2 MPa.

- Pressurisation of the bone cement mantle during polymerisation significantly alters the residual stress levels. A large reduction in the residual strains in the representative femur, with a slight increase in residual strains for the representative stem was measured. Experimental results indicate that a significant reduction in residual stresses *in vivo* may be achieved by cement mantle pressurisation.

- CMW® 1 Gentamicin and SmartSet® HV Gentamicin bone cements both produced similar residual stress levels, based on experimental residual strain measurements.

- Results indicate that mixing bone cement under vacuum conditions does not alter residual stress levels compared with cement mixed under atmospheric conditions. Previous research [33, 74, 98] has established a clear relationship between pore reduction mixing methods and increased cement shrinkage. As no increase in cement residual strain was recorded between non-vacuum mixed cement and cement prepared under vacuum conditions, this result indicates that the dominant shrinkage mechanism after the cement has achieved its properties as a solid is thermal shrinkage.

- SmartSet® HV Gentamicin has a lower coefficient of thermal expansion (mean of 72.6 x $10^{-6}{}^{o}C^{-1}$) compared to CMW® 1 Gentamicin (mean of 89.2 x $10^{-6}{}^{o}C^{-1}$), based on dilatometer experiments.

- The first measurement of residual strain occurred approximately 7 seconds before the attainment of peak cement temperature. Stress-locking must have occurred some time shortly previous to this point before residual strains could have been registered. From this it is postulated that bone cement stress-locks between 7 to 14 seconds before the attainment of peak cement temperature.

- Pressurisation of the polymerising bone cement mantle has a negligible effect on cement mantle temperatures.

- CMW® 1 Gentamicin and SmartSet® HV Gentamicin bone cements produce equally high peak cement temperatures despite notable difference between their polymerisation transient temperature profiles.

- CMW® 1 Gentamicin bone cement liberates approximately 126 MJ/m^3 of thermal energy during polymerisation, based on DSC measurements.

- Finite element analysis of the experimental work predicted von Mises residual stresses up to 16.5 MPa. Of the principal stresses, longitudinal residual stresses were the most significant, with a predicted magnitude of approximately 18 MPa. Hoop stress were the second most significant of the principal stresses with a maximum magnitude of approximately 15.5 MPa. Finally radial stresses were the least significant of the principal stresses, with a maximum magnitude of approximately 4.5 MPa.

- A finite element methodology has been successfully employed to predict transient thermal results throughout bone cement polymerisation and for the quantification of resultant residual stresses.

6.3 *Future Work*

- Results from the experimental investigation of pressurisation affects on the residual stresses revealed a significant reduction in the residual strains for the representative femur and a slight increase in residual strains for the representative stem. A hypothesis was proposed for the explanation of these results, (Section 3.5). The hypothesis suggests a reduction for both the stem and femur residual stresses *in vivo*. Further experimentation to gain a greater understanding of the pressurisation affects and the verification of the proposed hypothesis is proposed.

- A number of residual stress experiments were allowed to run for an extended period of time to investigate residual stress relaxation rates, due to the viscoelastic nature of bone cement (Appendix M). A more in depth experimental analysis is proposed to measure the residual stress relaxation rates over significant periods of time (10 days for example) and the development of a theoretical formulation to predict residual stress relaxation is proposed.

- Different brands of bone cement encompass different thermal profiles [43-46]. From Section 4.5.1, experimental measurement reveals that CMW® 1 Gentamicin and SmartSet® HV Gentamicin have different coefficients of thermal expansion. It is hypothesised from these observations that different brands of bone cement may produce significantly different residual stress levels. In the present study, the residual strains between two brands of bone cement, namely CMW® 1 Gentamicin and SmartSet® HV Gentamicin were compared with each other. An investigation of a more comprehensive range of bone cement brands is proposed, to determine if some brands of cement produce significantly lower residual stresses compared to others.

- The bone cement coefficient of thermal expansion is a central property in the quantification of residual stress. The coefficient of thermal expansion utilised in this research has been based on previously mixed and

solidified cement. It is postulated that the coefficient of thermal expansion for previously solidified cement may not be the same as the cement that is cooling from polymerisation. Experimentation to measure the coefficient of thermal contraction for cooling bone cement from polymerisation is proposed.

- Results from this research indicate that bone cement mixed under the application of vacuum may slightly reduce peak polymerisation temperatures. Additional experimentation is proposed to investigate this indication.

References

[1] Seeley, R., Stephens, T. and Tate, P., (2000), *Anatomy and Physiology (6th ed)*, McGraw-Hill, New York, pp.167-266.

[2] Bowling, A., (2001), *Measuring Disease (2nd ed)*, Open University Press, Buckingham, pp.225-247.

[3] Scales, J.T., (1967), "Arthroplasty of the hip using foreign materials: A History", *Proceedings of the Institution of Mechanical Engineering*, Vol.181 pp.63-84.

[4] National Joint Registry for England and Wales -2nd Annual Report [online], http://www.njrcentre.org.uk/, (Accessed 30-01-2006)

[5] Australian Orthopaedic Association; National Joint Replacement Registry; Annual Report 2004, [online], http://www.aoa.org.au/, (Accessed 10-10-2005)

[6] Malchau, H., Herberts, P. and Ahnfelt, L., (1993), "Prognosis of total hip replacement in Sweden. Follow-up of 92,675 operations performed 1978-1990", *Acta orthopaedica Scandinavica*, Vol.64 (5), pp.497-506.

[7] Ghista, D.N., (1981), *Biomechanics of medical devices*, Marcel Dekker Inc, New York, pp.325-371.

[8] Huiskes, R., (1980), "Some fundamental aspects of human joint replacement. Analyses of stresses and heat conduction in bone-prosthesis structures", *Acta Orthopaedica Scandinavica - Supplementum*, Vol.185 pp.1-208.

[9] Brockhurst, P.J. and Svensson, N.L., (1977), "Design of total hip prosthesis: the femoral stem", *Medical Progress Through Technology*, Vol.5 (2), pp.73-102.

[10] Kuhn, K.D., (2000), *Bone Cements: Up to date comparison of physical and chemical properties of commercial materials*, Springer-Verlag, Berlin, pp.1-115.

[11] Biomet Europe, Sweden, [online], http://www.bonecement.com/index.php?id=16935&no_cache=1, (Accessed 28-06-2006)

[12] Arthritis Foundation of Ireland, [online], http://www.arthritis-foundation.com/old/index.html, (Accessed 10-5-2005)

[13] Sedel, L. and Cabanela, M.E., (1998), *Hip Surgery: Materials and Developments*, Mosby, St. Louis, pp.91-103.

[14] Chen, W., Zang, F., Chang, S., Hui, K. and Lineaweaver, W., (2006), "Microsurgical fibular flap for treatment of avascular necrosis of the femoral head", *(In Press)*.

[15] Tortora, G.R. and Grabowski, S.R., (1996), *Principles of anatomy and physiology* HaperCollins Publishers Inc, New York, pp.219-224.

[16] Hip and Pelvis, USA, [online], http://www.hipandpelvis.com/patient_education/totalhip/intro.html, (Accessed 30-12-2006)

[17] Colwell, C. and Ritter, M., (1995), "Cementing techniques for primary total hip arthroplasty", *Operative techniques in orthopaedics*, Vol.5 (4), pp.316-324.

[18] Dunne, N.J., Orr, J.F. and Beverland, D.E., (2004), "Assessment of cement introduction and pressurization techniques", *Proceedings of the Institution of Mechanical Engineers. Part H, Journal of Engineering in Medicine*, Vol.218 (1), pp.11-25.

[19] Benjamin, J.B., Gie, G.A., Lee, A.J., Ling, R.S. and Volz, R.G., (1987), "Cementing technique and the effects of bleeding", *The Journal of Bone and Joint Surgery. British volume*, Vol.69 (4), pp.620-624.

[20] ElMaraghy, A.W., Humeniuk, B., Anderson, G.I., Schemitsch, E.H. and Richards, R.R., (1999), "Femoral bone blood flow after reaming and intramedullary canal preparation: a canine study using laser Doppler flowmetry", *The Journal of Arthroplasty*, Vol.14 (2), pp.220-226.

[21] Reading, A.D., McCaskie, A.W., Barnes, M.R. and Gregg, P.J., (2000), "A comparison of 2 modern femoral cementing techniques: analysis by cement-bone interface pressure measurements, computerized image analysis, and static mechanical testing", *Journal of Arthroplasty*, Vol.15 (4), pp.479-487.

[22] Krause, W.R., Krug, W. and Miller, J., (1982), "Strength of the cement-bone interface", *Clinical orthopaedics and related research* (163), pp.290-299.

[23] Mann, K.A., Ayers, D.C., Werner, F.W., Nicoletta, R.J. and Fortino, M.D., (1997), "Tensile strength of the cement-bone interface depends on the amount of bone interdigitated with PMMA cement", *Journal of Biomechanical Engineering*, Vol.30 (4), pp.339-346.

[24] Halawa, M., Lee, A.J., Ling, R.S. and Vangala, S.S., (1978), "The shear strength of trabecular bone from the femur, and some factors affecting the shear strength of the cement-bone interface", *Archives of Orthopaedic and Trauma Surgery*, Vol.92 (1), pp.19-30.

[25] Virtual Hospital - University of Iowa, [online], http://www.vh.org/adult/patient/orthopaedics/hipreplace/#6, (Accessed 30-12-2005)

[26] Arthritis Insight, USA, [online], http://arthritisinsight.com/medical/surgery/thr.html, (Accessed 15-01-2006)

[27] Krause, W. and Mathis, R.S., (1988), "Fatigue properties of acrylic bone cements: review of the literature", *Journal of Biomedical Materials Research*, Vol.22 (A1 Suppl), pp.37-53.

[28] Topoleski, L.D., Ducheyne, P. and Cuckler, J.M., (1990), "A fractographic analysis of in vivo poly(methyl methacrylate) bone cement failure mechanisms", *Journal of Biomedical Materials Research*, Vol.24 (2), pp.135-154.

[29] McCormack, B.A. and Prendergast, P.J., (1999), "Microdamage accumulation in the cement layer of hip replacements under flexural loading", *Journal of Biomechanics*, Vol.32 (5), pp.467-475.

[30] Morlock, M., Schneider, E., Bluhm, A., Vollmer, M., Bergmann, G., Muller, V. and Honl, M., (2001), "Duration and frequency of every day activities in total hip patients", *Journal of Biomechanics*, Vol.34 (7), pp.873-881.

[31] Huiskes, R., (1993), "Mechanical failure in total hip arthroplasty with cement", *Current Orthopaedics*, Vol.7 pp.239-247.

[32] Lennon, A.B. and Prendergast, P.J., (2002), "Residual stress due to curing can initiate damage in porous bone cement: experimental and theoretical evidence", *Journal of Biomechanical Engineering*, Vol.35 (3), pp.311-321.

[33] Orr, J.F., Dunne, N.J. and Quinn, J.C., (2003), "Shrinkage stresses in bone cement", *Biomaterials*, Vol.24 (17), pp.2933-2940.

[34] Roques, A., Browne, M., Taylor, A., New, A. and Baker, D., (2004), "Quantitative measurement of the stresses induced during polymerisation of bone cement", *Biomaterials*, Vol.25 (18), pp.4415-4424.

[35] Lennon, A.B., McCormack, B.A. and Prendergast, P.J., (2003), "The relationship between cement fatigue damage and implant surface finish in proximal femoral prostheses", *Medical Engineering & Physics*, Vol.25 (10), pp.833-841.

[36] Jasty, M., Maloney, W.J., Bragdon, C.R., O'Connor, D.O., Haire, T. and Harris, W.H., (1991), "The initiation of failure in cemented femoral components of hip arthroplasties", *Journal of Bone and Joint Surgery. British Volume*, Vol.73 (4), pp.551-558.

[37] Benham, P.P., Crawford, R.J. and Armstrong, C.G., (1987), *Mechanics of engineering materials*, Addison Wesley Longman Ltd., Harlow, England,

[38] Nuno, N. and Amabili, M., (2002), "Modelling debonded stem-cement interface for hip implants: effect of residual stresses", *Clinical Biomechanics (Bristol, Avon)*, Vol.17 (1), pp.41-48.

[39] Holm, N.J., (1980), "The formation of stress by acrylic bone cements during fixation of the acetabular prosthesis", *Acta orthopaedica Scandinavica*, Vol.51 pp.719-726.

[40] De Wijn, J.R., Driessens, F.C. and Slooff, T.J., (1975), "Dimensional behaviour of curing bone cement masses", *Journal of Biomedical Materials Research*, Vol.6 pp.99-103.

[41] Roques, A., (2003), "Novel approaches to the structural integrity assessment of acrylic bone cement as part of the bone/cement/stem construct" Ph.D. Thesis, University of Southampton, Southampton, UK.

[42] Dunne, N.J. and Orr, J.F., (2001), "Influence of mixing techniques on the physical properties of acrylic bone cement", *Biomaterials*, Vol.22 (13), pp.1819-1826.

[43] Dunne, N.J. and Orr, J.F., (2001), "Thermal characteristics of curing acrylic bone cement", *ITBM-RBM*, Vol.22 pp.88-97.

[44] Dunne, N.J. and Orr, J.F., (2002), "Curing characteristics of acrylic bone cement", *Journal of Materials Science. Materials in Medicine*, Vol.13 (1), pp.17-22.

[45] Dunne, N.J., (1996), "Evaluation of static and dynamic properties of polymethyl methacrylate bone cements and their effects on implant fixation" Ph.D. Thesis, The Queen's University Belfast, Belfast, UK.

[46] Rahman, M.M., Olabi, A.G. and Hashmi, M.S.J. (2004) Thermal properties of curing acrylic bone cement mixed at different vacuum level. In: 12th International Conference of Experimental Mechanics, Politecnico di Bari, Italy

[47] Harper, E.J. and Bonfield, W., (2000), "Tensile characteristics of ten commercial acrylic bone cements", *Journal of Biomedical Materials Research*, Vol.53 (5), pp.605-616.

[48] Lewis, G., (1997), "Properties of acrylic bone cement: state of the art review", *Journal of Biomedical Materials Research*, Vol.38 (2), pp.155-182.

[49] Haas, S.S., Brauer, G.M. and Dickson, G., (1975), "A characterization of polymethylmethacrylate bone cement", *Journal of Bone and Joint Surgery. American Volume*, Vol.57 (3), pp.380-391.

[50] Ginebra, M.P., Albuixech, L., Fernandez-Barragan, E., Aparicio, C., Gil, F.J., San, R.J., Vazquez, B. and Planell, J.A., (2002), "Mechanical performance of acrylic bone cements containing different radiopacifying agents", *Biomaterials*, Vol.23 (8), pp.1873-1882.

[51] Jefferiss, C.D., Lee, A.J. and Ling, R.S., (1975), "Thermal aspects of self-curing polymethylmethacrylate", *Journal of Bone and Joint Surgery. British Volume*, Vol.57 (4), pp.511-518.

[52] Meyer, P.R., Jr., Lautenschlager, E.P. and Moore, B.K., (1973), "On the setting properties of acrylic bone cement", *The Journal of Bone and Joint Surgery. American volume*, Vol.55 (1), pp.149-156.

[53] DiPisa, J.A., Sih, G.S. and Berman, A.T., (1976), "The temperature problem at the bone-acrylic cement interface of the total hip

replacement", *Clinical orthopaedics and related research* (121), pp.95-98.

[54] Park, J.B., (1983), "Acrylic bone cement: in vitro and in vivo property-structure relationship--a selective review", *Annals of Biomedical Engineering*, Vol.11 (3-4), pp.297-312.

[55] Baliga, B.R., Rose, P.L. and Ahmed, A.M., (1992), "Thermal modeling of polymerizing polymethylmethacrylate, considering temperature-dependent heat generation", *Journal of Biomechanical Engineering*, Vol.114 (2), pp.251-259.

[56] Swenson, L.W., Jr., Schurman, D.J. and Piziali, R., (1981), "Finite element temperature analysis of a total hip replacement and measurement of PMMA curing temperatures", *Journal of Biomedical Materials Research*, Vol.15 (1), pp.83-96.

[57] Mazzullo, S., Paolini, M. and Verdi, C., (1991), "Numerical simulation of thermal bone necrosis during cementation of femoral prostheses", *Journal of Mathematical Biology*, Vol.29 (5), pp.475-494.

[58] Nzihou, A., Attias, L., Sharrack, P. and Ricard, A., (1998), "A rheological, thermal and mechanical study of bone cement - from a suspension to a solid biomaterial", *Powder Technology*, Vol.99 pp.60-69.

[59] Yang, J.M., Shyu, J.S. and Chen, H.L., (1998), "Additive modification of the polymerization and properties of an acrylic bone cement", *Polymer engineering and science*, Vol.38 (3), pp.530-533.

[60] Yang, J.M., Shyu, J.S. and Chen, H.L., (1997), "Polymerization of acrylic bone cement investigated by differential scanning calorimetry: Effects of heating rate and TCP content", *Polymer engineering and science*, Vol.37 (7), pp.1182-1187.

[61] Toksvig-Larsen, S., Franzen, H. and Ryd, L., (1991), "Cement interface temperature in hip arthroplasty", *Acta orthopaedica Scandinavica*, Vol.62 (2), pp.102-105.

[62] Labitzke, R. and Paulus, M., (1974), "[Intraoperative measuring of temperature in the surgery of hip during the polymerisation of the bone cement palacos (author's transl)]", *Archiv Für Orthopädische und Unfall-Chirurgie*, Vol.79 (4), pp.341-346.

[63] Biehl, G., Harms, J. and Hanser, U., (1974), "[Experimental studies on heat development in bone during polymerization of bone cement. Intraoperative measurement of temperature in normal blood circulation and in bloodlessness]", *Archiv Für Orthopädische und Unfall-Chirurgie*, Vol.78 (1), pp.62-69.

[64] Ohnsorge, J. and Goebel, G., (1969), "[Surface temperatures of the hardening bone cement Palacos during fixation of metal endoprotheses in the femoral bone marrow space. Experimental study]", *Arch Orthop Unfallchir*, Vol.67 (2), pp.89-100.

[65] Ahmed, A.M., Pak, W., Burke, D.L. and Miller, J., (1982), "Transient and residual stresses and displacements in self-curing bone cement - Part I: characterization of relevant volumetric behavior of bone cement", *Journal of Biomechanical Engineering*, Vol.104 (1), pp.21-27.

[66] Starke, G.R., Birnie, C. and Van den Blink, P.A. (1997) Numerical Modelling of cement polymerisation and thermal bone necrosis. In: Third International Symposium of Computer Methods in Biomechanics and Biomedical Engineering (Middleton, J. et al., eds.), London, pp. 163-172

[67] Li, C., Schmid, S. and Mason, J., (2003), "Effects of pre-cooling and pre-heating procedures on cement polymerization and thermal osteonecrosis in cemented hip replacements", *Medical Engineering and Physics*, Vol.25 (7), pp.559-564.

[68] Scheuermann, H., (1976), *Bestimmung des monomergehaltes von knochenzementen und bestimmung der monomerfreisetzung an wassrigen*, Ingenieruarbeit Fachhochschule Fresenius, Wiesbaden, Germany,

[69] James, S.P., Jasty, M., Davies, J., Piehler, H. and Harris, W.H., (1992), "A fractographic investigation of PMMA bone cement focusing on the relationship between porosity reduction and increased fatigue life", *Journal of Biomedical Materials Research*, Vol.26 (5), pp.651-662.

[70] Demarest, V.A., Lautenschlager, E.P. and Wixson, R.L. (1983) Vacuum mixing of acrylic bone cement. In: Proceedings of the ninth annual meeting of the Society for Biomaterials, Birmingham, Alabama, pp. 37.

[71] Wixson, R.L., Lautenschlager, E.P. and Novak, M.A., (1987), "Vacuum mixing of acrylic bone cement", *Journal of Arthroplasty*, Vol.2 (2), pp.141-149.

[72] McCaskie, A.W., Barnes, M.R., Lin, E., Harper, W.M. and Gregg, P.J., (1997), "Cement pressurisation during hip replacement", *The Journal of Bone and Joint Surgery. British volume*, Vol.79 (3), pp.379-384.

[73] Bourne, R.B., Aitken, G.K.F., J. B. and Andraca, P.R. (1985) Femoral cement pressurisation in vitro: the effect of intermedullary plugs. In: 31st Annual Meeting Of The Orthopaedic Research Society, Nevada, pp. 224.

[74] Hamilton, H.W., Cooper, D.F. and Fels, M., (1988), "Shrinkage of centrifuged cement", *Orthopaedic Review*, Vol.17 (1), pp.48-54.

[75] Vaughan, M., (1995), "Characterization and structural aspects of acrylic bone cement" M.S. thesis, University of Memphis.

[76] Trieu, H.H., Paxson, R.D., Carroll, M.E. and Bert, J.M. (1994) A comparative study of bone cement preparation using a new centrifugation mixing technique. In: 20th Annual Meeting of the Society for Biomaterials, Boston, MA

[77] Lewis, G. and Austin, G.E., (1994), "Mechanical properties of vacuum-mixed acrylic bone cement", *Journal of Applied Biomaterials*, Vol.5 (4), pp.307-314.

[78] Tanzi, M.C., Sket, I., Gatti, A.M. and Monari, E., (1991), "Physical characterization of acrylic bone cement cured with new accelerator systems", *Clinical Materials*, Vol.8 (1-2), pp.131-136.

[79] Krause, W. and Hofmann, A., (1989), "Antibiotic impregnated acrylic bone cements: A comparative study of the mechanical properties", *Journal of bioactive and compatible polymers*, Vol.4 pp.345-361.

[80] Kindt-Larsen, T., Smith, D.B. and Jensen, J.S., (1995), "Innovations in acrylic bone cement and application equipment", *Journal of Applied Biomaterials*, Vol.6 (1), pp.75-83.

[81] Krause, W., Mathis, R.S. and Grimes, L.W., (1988), "Fatigue properties of acrylic bone cement: S-N, P-N, and P-S-N data", *Journal of Biomedical Materials Research*, Vol.22 (3 Suppl), pp.221-244.

[82] Davies, J.P., O'Connor, D.O., Greer, J.A. and Harris, W.H., (1987), "Comparison of the mechanical properties of Simplex P, Zimmer

Regular, and LVC bone cements", *Journal of Biomedical Materials Research*, Vol.21 (6), pp.719-730.

[83] Heller, M.O., Bergmann, G., Deuretzbacher, G., Durselen, L., Pohl, M., Claes, L., Haas, N.P. and Duda, G.N., (2001), "Musculo-skeletal loading conditions at the hip during walking and stair climbing", *Journal of Biomechanics*, Vol.34 (7), pp.883-893.

[84] Heller, M.O., Bergmann, G., Kassi, J.P., Claes, L., Haas, N.P. and Duda, G.N., (2005), "Determination of muscle loading at the hip joint for use in pre-clinical testing", *Journal of Biomechanics*, Vol.38 (5), pp.1155-1163.

[85] Bergmann, G., Deuretzbacher, G., Heller, M., Graichen, F., Rohlmann, A., Strauss, J. and Duda, G.N., (2001), "Hip contact forces and gait patterns from routine activities", *Journal of Biomechanics*, Vol.34 (7), pp.859-871.

[86] Bergmann, G., Graichen, F. and Rohlmann, A., (1995), "Is staircase walking a risk for the fixation of hip implants?" *Journal of Biomechanics*, Vol.28 (5), pp.535-553.

[87] McCormack, B.A., Prendergast, P.J. and Gallagher, D.G., (1996), "An experimental study of damage accumulation in cemented hip prostheses", *Clinical Biomechanics (Bristol, Avon)*, Vol.11 (4), pp.214-219.

[88] Lautenschlager, E.P., Wixson, R.L., Novak, M.A. and Bakir, N. (1986) Fatigue and fracture toughness of Simplex-P. In: 32nd Annual Orthopaedic Research Society, New Orleans Louisiana, pp. 118.

[89] Murphy, B.P. and Prendergast, P.J., (2000), "On the magnitude and variability of the fatigue strength of acrylic bone cement", *International Journal of Fatigue*, Vol.22 pp.855-864.

[90] Eden, O.R., Lee, A.J. and Hooper, R.M., (2002), "Stress relaxation modelling of polymethylmethacrylate bone cement", *Proceedings of the Institution of Mechanical Engineers. Part H, Journal of Engineering in Medicine*, Vol.216 (3), pp.195-199.

[91] Norman, T.L., Kish, V., Blaha, J.D., Gruen, T.A. and Hustosky, K., (1995), "Creep characteristics of hand- and vacuum-mixed acrylic bone cement at elevated stress levels", *Journal of Biomedical Materials Research*, Vol.29 (4), pp.495-501.

[92] Chwirut, D.J., (1984), "Long-term compressive creep deformation and damage in acrylic bone cements", *Journal of Biomedical Materials Research*, Vol.18 (1), pp.25-37.

[93] Lee, A.J., Ling, R.S., Gheduzzi, S., Simon, J.P. and Renfro, R.J., (2002), "Factors affecting the mechanical and viscoelastic properties of acrylic bone cement", *Journal of Materials Science. Materials in Medicine*, Vol.13 (8), pp.723-733.

[94] Liu, C., Green, S.M., Watkins, N.D., Gregg, P.J. and McCaskie, A.W., (2002), "Creep behavior comparison of CMW1 and palacos R-40 clinical bone cements", *Journal of Materials Science. Materials in Medicine*, Vol.13 (11), pp.1021-1028.

[95] Liu, C.Z., Green, S.M., Watkins, N.D., Baker, D. and McCaskie, A.W., (2005), "Dynamic creep and mechanical characteristics of SmartSet GHV bone cement", *Journal of Materials Science. Materials in Medicine*, Vol.16 (2), pp.153-160.

[96] Charnley, J., (1970), *Acrylic cement in orthopaedic surgery* E. and S. Livingstone, , Edinburgh and London, pp.1-550

[97] Debrunner, H.U., Wettstein, A. and Hofer, P., (1976), *The polymerization of self-curing acrylic cements and problems due to the cement anchorage of joint prostheses: Advances in Artificial Hip and Knee Joint Technology*, Springer-Verlang, Berlin,

[98] Gilbert, J.L., Hasenwinkel, J.M., Wixson, R.L. and Lautenschlager, E.P., (2000), "A theoretical and experimental analysis of polymerization shrinkage of bone cement: A potential major source of porosity", *Journal of Biomedical Materials Research*, Vol.52 (1), pp.210-218.

[99] Silikas, N., Al-Kheraif, A. and Watts, D.C., (2005), "Influence of P/L ratio and peroxide/amine concentrations on shrinkage-strain kinetics during setting of PMMA/MMA biomaterial formulations", *Biomaterials*, Vol.26 (2), pp.197-204.

[100] Loshaek, S. and T.G., F., (1953), "Cross-linked polymers: Factors influencing the efficiency of cross-linking in copolymers of methyl methacrylate and glycol dimethacrylates", *Journal of the American Chemical Society*, Vol.75 pp.3544-3550.

[101] Dunne, N.J., Orr, J.F., Mushipe, M.T. and Eveleigh, R.J., (2003), "The relationship between porosity and fatigue characteristics of bone cements", *Biomaterials*, Vol.24 (2), pp.239-245.

[102] Lidgren, L., Drar, H. and Moller, J., (1984), "Strength of polymethylmethacrylate increased by vacuum mixing", *Acta orthopaedica Scandinavica*, Vol.55 (5), pp.536-541.

[103] Rimnac, C.M., Wright, T.M. and McGill, D.L., (1986), "The effect of centrifugation on the fracture properties of acrylic bone cements", *Journal of Bone and Joint Surgery. American Volume*, Vol.68 (2), pp.281-287.

[104] Wang, J.S., Toksvig-Larsen, S., Muller-Wille, P. and Franzen, H., (1996), "Is there any difference between vacuum mixing systems in reducing bone cement porosity?" *Journal of Biomedical Materials Research*, Vol.33 (2), pp.115-119.

[105] Whelan, M.P., Kenny, R.P., Cavalli, C., Lennon, A.B. and Prendergast, P.J. (2000) Application of optical fibre Bragg grating sensors to the study of PMMA curing. In: Proceedings of the 12th Conference of the European Society of Biomechanics (Prendergast, P.J. et al., eds.), Dublin, Ireland, pp. 252.

[106] Stachiewicz, J.W., Miller, J. and Burke, D.L. (1976) Hoop stress generated by shrinkage of polymethyl-methacrylate as a source of prosthetic loosening. In: Digest of the 11th International Conference on Medical and Biological Engineering, Ottawa, pp. 532-533.

[107] Lennon, A.B., Prendergast, P.J., Whelan, M.P., Kenny, R.P. and Cavalli, C. (2000) Modelling of temperature history and residual stress generation due to curing in polymethylmethacrylate. In: Proceedings of the 12th Conference of the European Society of Biomechanics (Prendergast, P.J. et al., eds.), Dublin, Ireland, pp. 253.

[108] Li, C., Wang, Y. and Mason, J., (2004), "The effects of curing history on residual stresses in bone cement during hip arthroplasty", *Journal of Biomedical Materials Research. Part B, Applied Biomaterials*, Vol.70 (1), pp.30-36.

[109] Huiskes, R. and De Wijn, J.R. (1979) Locked-in acrylic cement stresses, caused by thermal shrinkage after fixation of intramedullary joint

prostheses. In: Second Conference of the European Society of Biomechanics, Strasbourg, France

[110] Ahmed, A.M., Nair, R., Burke, D.L. and Miller, J., (1982), "Transient and residual stresses and displacements in self-curing bone cement - Part II: thermoelastic analysis of the stem fixation system", *Journal of Biomechanical Engineering*, Vol.104 (1), pp.28-37.

[111] Mann, K.A., Bartel, D.L., Wright, T.M. and Ingraffea, A.R., (1991), "Mechanical characteristics of the stem-cement interface", *Journal of Orthopaedic Research*, Vol.9 (6), pp.798-808.

[112] Nuno, N. and Avanzolini, G., (2002), "Residual stresses at the stem-cement interface of an idealized cemented hip stem", *Journal of Biomechanics*, Vol.35 (6), pp.849-852.

[113] Stryker Corporation, MI, USA, [online], http://www.stryker.com/jointreplacements/sites/primarystems/exeter.php, (Accessed 17-01-2006)

[114] National Joint Registry for England and Wales; 1st Annual Report, [online], http://www.njrcentre.org.uk/, (Accessed 05-04-2006)

[115] Sawbones Inc, USA, [online], https://secure.sawbones.com/products/bio/testblocks/default.asp, (Accessed 01-04-2006)

[116] DePuy Inc, USA, [online], http://www.jnjgateway.com/home.jhtml?loc=USENG&page=viewContent&contentId=fc0de00100000249&parentId=fc0de00100000249, (Accessed 17-01-2006)

[117] DePuy Inc, USA, [online], http://www.jnjgateway.com/home.jhtml?loc=USENG&page=viewContent&contentId=09008b98807c0741&parentId=09008b98807c0741, (Accessed 17-01-2006)

[118] DePuy Inc, USA, [online], http://www.jnjgateway.com/home.jhtml?loc=USENG&page=viewContent&contentId=09008b9880768228&parentId=09008b9880768228, (Accessed 17-01-2006)

[119] Window, A.L., (1992), *Strain gauge technology (2nd Ed.)*, Elsevier science publishers Ltd., Essex, England, pp.2-276.

[120] Engineering, O., (1998), *Force-related measurements* (Transactions in measurement and control, Volume 3), The curtis publishing company, Indianapolis, Indiana, pp.1-85.

[121] Vishay Intertechnology, Inc., USA, [online], http://www.vishay.com/brands/measurements_group/strain_gages/mm.htm, (Accessed 23-01-2006)

[122] Harvey, P.D., (1992), *Engineering properties of steel*, American society for metal, Ohio, pp.292-298.

[123] Goodfellow Cambridge Ltd., UK, [online], http://www.goodfellow.com/csp/active/STATIC/A/E-glass-Epoxy.HTML, (Accessed 23-01-2006)

[124] Adams, L.F., (1981), *Engineering measurement and instrumentation*, Arrowsmith Ltd., Bristol, England, pp.319-351.

[125] National Instruments Inc, USA, [online], http://sine.ni.com/nips/cds/view/p/lang/en/nid/1867, (Accessed 24-01-2006)

[126] Lidgren, L., Bodelind, B. and Moller, J., (1987), "Bone cement improved by vacuum mixing and chilling", *Acta orthopaedica Scandinavica*, Vol.58 (1), pp.27-32.

[127] Moaveni, S., (1999), *Finite element analysis: Theory and application with ANSYS*, Prentice-Hall, New Jersey, pp.1-45.

[128] Sherline Products, Inc, CA, USA, [online], http://www.sherline.com/dimen.htm, (Accessed 22-03-2006)

[129] Newman Tools, Inc., Canada, [online], http://www.newmantools.com/tech/taper.htm, (Accessed 22-03-2006)

[130] ANSYS, Inc., (2004), *ANSYS 8.1 Help Documentation*, PA, USA,

[131] Ramos, A. and Simoes, J.A., (2006), "Tetrahedral versus hexahedral finite elements in numerical modelling of the proximal femur", *Medical Engineering and Physics*.

[132] Efunda, Inc., USA, [online], http://www.efunda.com/materials/alloys/stainless_steels/show_stainless.cfm?ID=AISI_Type_316L&prop=all&Page_Title=AISI%20Type%20316L, (Accessed 26-03-2006)

[133] Matweb, division of Automation Creations, Inc., USA

[online],
http://www.matweb.com/search/SpecificMaterial.asp?bassnum=O1700,
(Accessed 25-03-2006)

[134] Matweb, division of Automation Creations, Inc., USA, [online], http://www.matweb.com/search/SpecificMaterial.asp?bassnum=CGF004, (Accessed 25-03-2006)

[135] Fukushima, H., Hashimoto, Y., Yoshiya, S., Kurosaka, M., Matsuda, M., Kawamura, S. and Iwatsubo, T., (2002), "Conduction analysis of cement interface temperature in total knee arthroplasty", *Kobe Journal of Medical Sciences*, Vol.48 (1-2), pp.63-72.

[136] Callister, W.D., (1997), *Materials science and engineering: an introduction (4th ed)*, John Wiley and Sons, Inc., New York, USA, pp.510-550.

[137] Amstutz, H.C. and Guren, T.A. (1973) Clinical application of polymethyl methacrylate for total joint replacement. In: Current Practice in Orthopaedic Surgery (Ahstrom, J.P. and Mosby, C.V., eds.), St. Louis, USA

[138] Lewis, G., Janna, S. and Bhattaram, A., (2005), "Influence of the method of blending an antibiotic powder with an acrylic bone cement powder on physical, mechanical, and thermal properties of the cured cement", *Biomaterials*, Vol.26 (20), pp.4317-4325.

[139] Stanczyk, M., (2005), "Study on modelling of PMMA bone cement polymerisation", *Journal of Biomechanical Engineering*, Vol.38 (7), pp.1397-1403.

[140] Forbes, M.J., (1977), "Polymethylmethacrylate: Heat generation pertaining to the total hip joint operation" Undergraduate honours thesis, McGill Univerisity.

[141] Holman, J.P., (1981), *Heat transfer*, McGraw Hill, New York, pp.265-292.

[142] Hansen, E., (2003), "Modelling heat transfer in a bone-cement-prosthesis system", *Journal of Biomechanical Engineering*, Vol.36 (6), pp.787-795.

[143] Kalpakjian, S., (1995), *Manufacturing engineering and technology (3rd edition)*, Addison-Wesley Publishing Company Inc., NY, USA, pp.955.

[144] Goldring, S.R., Jasty, M., Roelke, M.S., Rourke, C.M., Bringhurst, F.R. and Harris, W.H., (1986), "Formation of a synovial-like membrane at the bone-cement interface. Its role in bone resorption and implant loosening after total hip replacement", *Arthritis and Rheumatism*, Vol.29 (7), pp.836-842.

[145] Fornasier, V.L. and Cameron, H.U., (1976), "The femoral stem/cement interface in total hip replacement", *Clinical orthopaedics and related research* (116), pp.248-252.

[146] Lennon, A.B. and Prendergast, P.J., (2001), "Evaluation of cement stresses in finite element analyses of cemented orthopaedic implants", *Journal of Biomechanical Engineering*, Vol.123 (6), pp.623-628.

[147] Nuno, N., Amabili, M., Groppetti, R. and Rossi, A., (2002), "Static coefficient of friction between Ti-6Al-4V and PMMA for cemented hip and knee implants", *Journal of Biomedical Materials Research*, Vol.59 (1), pp.191-200.

[148] Bishop, N.E., Ferguson, S. and Tepic, S., (1996), "Porosity reduction in bone cement at the cement-stem interface", *The Journal of Bone and Joint Surgery. British volume*, Vol.78 (3), pp.349-356.

[149] B. Greer, whole_femur.igs, The ISB Finite Element Repository, Instituti Rizzoli,, [online], http://www.cineca.it/hosted/LTM/back2net/ISB_mesh, (Accessed 01-09-2005)

[150] Fung, Y.C., (1993), *Biomechanics: Mechanical properties of living tissues (2nd ed)*, Springer-Verlag, New York, pp.500-531.

[151] Bayraktar, H.H., Morgan, E.F., Niebur, G.L., Morris, G.E., Wong, E.K. and Keaveny, T.M., (2004), "Comparison of the elastic and yield properties of human femoral trabecular and cortical bone tissue", *Journal of Biomechanics*, Vol.37 (1), pp.27-35.

[152] Wirtz, D.C., Schiffers, N., Pandorf, T., Radermacher, K., Weichert, D. and Forst, R., (2000), "Critical evaluation of known bone material properties to realize anisotropic FE-simulation of the proximal femur", *Journal of Biomechanics*, Vol.33 (10), pp.1325-1330.

[153] Huiskes, R. and Chao, E.Y., (1983), "A survey of finite element analysis in orthopedic biomechanics: the first decade", *Journal of Biomechanics*, Vol.16 (6), pp.385-409.

[154] Huiskes, R., (1982), "On the modelling of long bones in structural analyses", *Journal of Biomechanics*, Vol.15 (1), pp.65-69.

[155] Taylor, W.R., Roland, E., Ploeg, H., Hertig, D., Klabunde, R., Warner, M.D., Hobatho, M.C., Rakotomanana, L. and Clift, S.E., (2002), "Determination of orthotropic bone elastic constants using FEA and modal analysis", *Journal of Biomechanics*, Vol.35 (6), pp.767-773.

[156] Couteau, B., Hobatho, M.C., Darmana, R., Brignola, J.C. and Arlaud, J.Y., (1998), "Finite element modelling of the vibrational behaviour of the human femur using CT-based individualized geometrical and material properties", *Journal of Biomechanics*, Vol.31 (4), pp.383-386.

[157] Fagan, M.J. and Lee, A.J.C., (1986), "Material selection in the design of the femoral component of cemented total hip replacement", *Clinical Materials*, Vol.1 pp.151-167.

[158] Maloney, W.J., Jasty, M., Burke, D.W., O'Connor, D.O., Zalenski, E.B., Bragdon, C. and Harris, W.H., (1989), "Biomechanical and histologic investigation of cemented total hip arthroplasties. A study of autopsy-retrieved femurs after in vivo cycling", *Clinical orthopaedics and related research* (249), pp.129-140.

[159] Jasty, M., Maloney, W.J., Bragdon, C.R., Haire, T. and Harris, W.H., (1990), "Histomorphological studies of the long-term skeletal responses to well fixed cemented femoral components", *The Journal of Bone and Joint Surgery. American volume*, Vol.72 (8), pp.1220-1229.

[160] Bergmann, G., Graichen, F. and Rohlmann, A., (1993), "Hip joint loading during walking and running, measured in two patients", *Journal of Biomechanics*, Vol.26 (8), pp.969-990.

[161] El-Shiekh, H., (2002), "Finite element simulation of hip joint replacement under static and dynamic loading" Ph.D Thesis, Dublin City University, Dublin.

[162] Svensson, N.L., Valliappan, S. and Woods, R.D., (1977), "Stress analysis of human femur with implanted charnley prosthesis", *Journal of Biomechanics*, Vol.10 pp.581-588.

[163] McNamara, B.P., (1995), "Damage stimulated bone remodelling: An assessment" Ph.D Thesis, University of Dublin Trinity College, Dublin.

[164] Buckwalter, J.A., Einhorm, E.A. and Simon, S.R., (2000), *Orthopaedic Basic Science: Biology and Biomechanics of the Musculoskeletal System*, American Academy of Orthopaedic Surgeons, Illinois, pp.730-844.

[165] Nordin, M. and Frankel, V.H., (1989), *Basic Biomechanics of the musculoskeletal system*, Lippincott Williams and Wilkins, Philadelphia, pp.135-153.

[166] Hall, S.R., (1999), *Basic Biomechanics*, McGraw Hill, Singapore, pp.234-247.

[167] Gray's Anatomy, USA, [online], http://bartleby.com/107/18.html, (Accessed 30-06 2004)

[168] Hearn, E.J., (1997), *Mechanics of materials 1 (3rd ed)*, Butterworth-Heinmann, Oxford, UK, pp.215-252.

Appendix A

Hip Anatomy

The hip joint is a ball and socket or spheroid joint [15]. Ball and socket joints are termed *triaxial* because they permit movement in three planes, abduction-adduction, flexion-extension and rotation. The ball of the joint, which forms approximately two-thirds of a sphere, is called the *head of femur* or *femoral head.* The socket of the joint consists of a cuplike depression within the hipbone and is called the *acetabulum,* (Figure A.1).

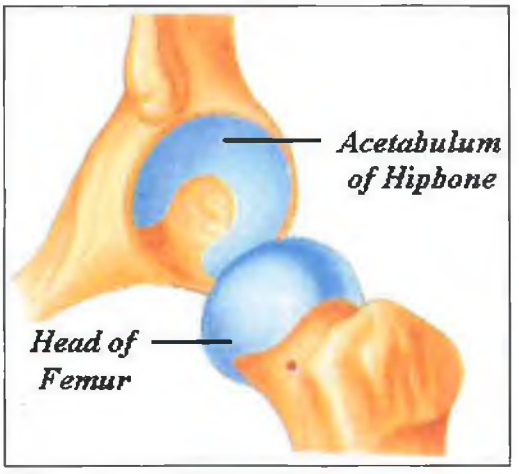

Figure A.1: The hip joint. Adapted from Tortora and Grabowski [15].

In a healthy joint, the femoral head resides in the acetabulum of the hipbone. The femoral head is captured by the acetabular socket, leading the joint to be highly constrained [164]. This constraint imparted by the hip architecture, results in the joint being inherently stable and well suited to bear and perform under load. Also this feature minimises the need for ligaments and other tissue constraints to maintain the stability of the hip under articulation.

Both mating surfaces of the hip joint are covered with *hyaline* or *articular* cartilage [165]. Articular cartilage performs two main functions. Firstly it distributes the joint load over a wide area, thus decreasing the stresses and strains upon the joint. Secondly it provides a smooth surface for the articular surfaces, thus reducing the coefficient of friction. To further reduce friction, the hip joint also receives *synovial fluid* from the synovial membrane about the joint. This combination of both articular cartilage and synovial fluid results in a very low coefficient of friction, approximately 0.008 [7].

Anatomy Of The Pelvic Girdle

The *pelvic girdle* consists of the right and left *hipbone* or *coxae* and the *sacrum* to form a ring of bone called the *pelvis*. The pelvis performs many functions including support and attachments for the lower limbs. The hipbone in turn is made of three bones all fused together, the *llium*, *pubis* and *ischium*, (Figure A.2).

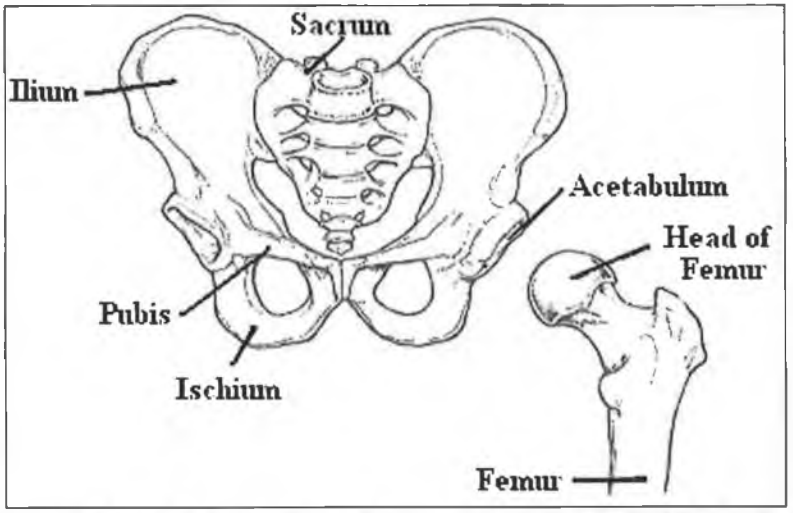

Figure A.2: Pelvic girdle and femur. Adapted from Hall [166].

Anatomy Of The Femur

The *thighbone* or *femur* is the longest, strongest and heaviest bone in the human body [15]. The proximal end of the femur consists of the femoral head that articulates with the acetabulum. The lower end of the femur forms a double

knuckle or *condyle* that articulates with the tibia, forming the knee joint. The femoral head contains a pit or depression called *fovea capitis*. This forms the site where the ligament *ligamentum capitis* connects or joins the femoral head to the acetabulum of the hipbone. Just below the femoral head is a constriction called the *femoral neck* or *collum femoris*. The femoral neck connects the femoral head to the *body of femur* or *femoral shaft*. In an adult, the femoral neck forms an angle of approximately 125° with the shaft of the femur, dependent on age and sex [167]. Below the femoral neck lies the trochanteric region. The trochanteric region consists of the *greater trochanter* and *lesser trochanter* and serves as the points of attachment for some of the buttock and thigh muscles. Between the trochanters on the front (anterior) side lies the *intertrochanteric line*, while on the rear (posterior) side lays the *intertrochanteric crest,* (Figure A.3).

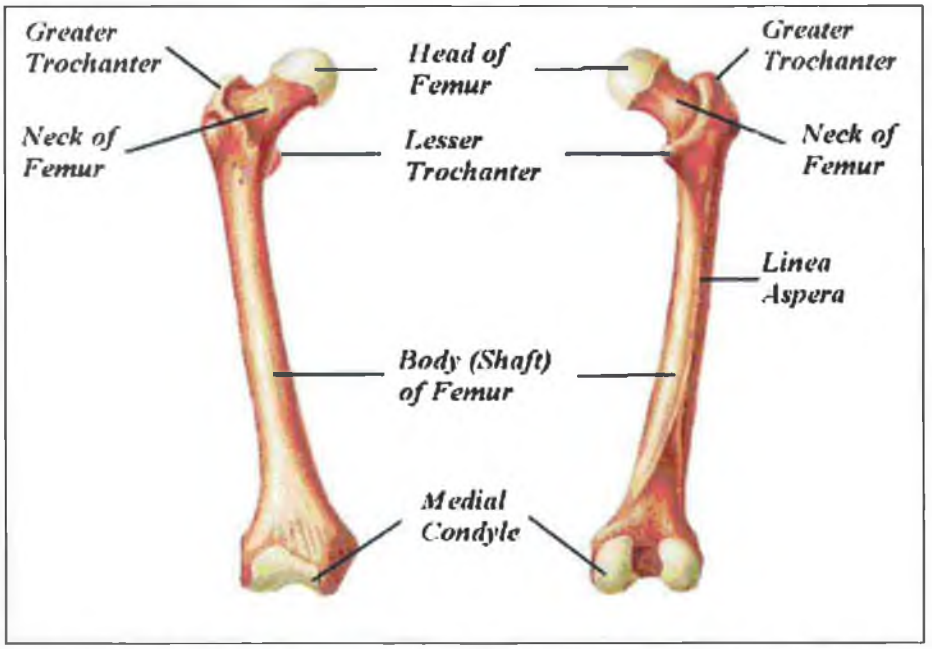

Figure A.3: Anatomy of the femur. Adapted from Seeley et al [1].

The interior of the femur consists of a cylindrical cavity called the *medullary cavity* [1]. The medullary cavity is filled with a soft tissue called *bone marrow*. Bone marrow is primarily used for blood formation and mineral storage. When compared with bone, bone marrow adds negligible mechanical strength to the system.

Appendix B

Anatomical Directional Terminology

Anatomical directional terms describe parts of the body relative to each other. All directional terms are in relation to a person in the anatomic position. The anatomic position refers to a person standing erect (upright) with their face directed forward, their upper limbs hanging to their sides and the palms of their hands facing forward. Directional terms with respect to a femoral hip replacement are illustrated in Figures B.1 and B.2.

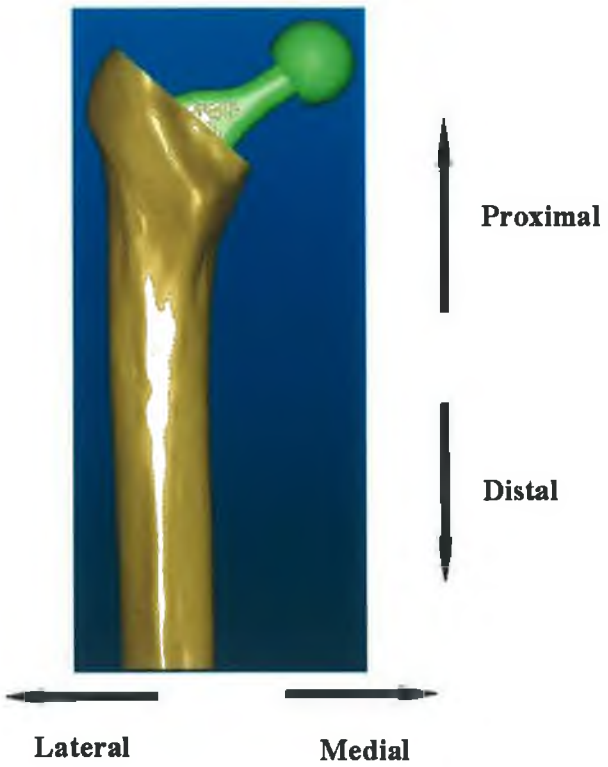

Figure B.1: Directional terminology with respect to a left femur with an artificial hip implanted

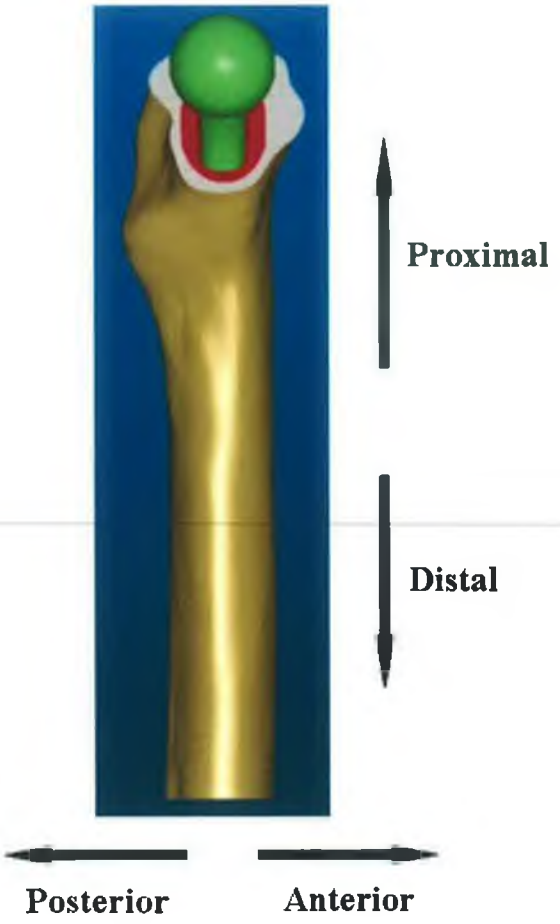

Figure B.2: Directional terminology with respect to a left femur with an artificial hip implanted

Table B.1 summarises the anatomical directional terminology.

Term	Definition
Proximal	Closer to the point of attachment to the body than another
Distal	Further from the point of attachment to the body than another
Anterior	Toward the front of the body
Posterior	Toward the back of the body
Lateral	Away from the midline of the body
Medial	Toward the midline of the body

Table B.1: Definitions of anatomical directional terms

Appendix C

Electrical Resistance Strain-Gauge Principles

Electrically conductive materials have a resistance-strain relationship, as given by Equation C.1 [124].

$$R = \frac{\rho L}{A} \tag{C.1}$$

Where "R" denotes *resistance*, "ρ" denotes *resistivity*, "L" denotes *length* and "A" denotes *cross sectional area*. Thus consider the case where the wire is extended;

$$L \rightarrow L + \Delta L \tag{C.2}$$

By Poisson's ratio effect, there will also be a reduction in the cross sectional area, thus;

$$A \rightarrow A - \Delta A \tag{C.3}$$

From this it can be seen that both effects contribute to an increase in the resistance of the conductor. Therefore, tensile forces increase the strain gauge resistance while compression forces reduce the strain gauge resistance.

The strain gauges sensitivity or the amount of resistance gauge per change in length is called the "Gauge Factor" and is a dimensionless relationship expressed mathematically as;

$$G.F = \frac{\Delta R}{R}\frac{\Delta L}{L} \tag{C.4}$$

Where "G.F" denotes *gauge factor*, "ΔR" denotes *change in resistance*, and ΔL denotes *change in length.*

Wheatstone Bridge Circuit Principles

A strain gauge is a passive resistor which requires a power source. The Wheatstone bridge circuit is the most common method to power the "resistor" and convert the small change of resistance of the strain gauge(s) into a voltage suitable of acquisition [119]. Figure C.1 illustrates the circuit diagram of a Wheatstone bridge circuit.

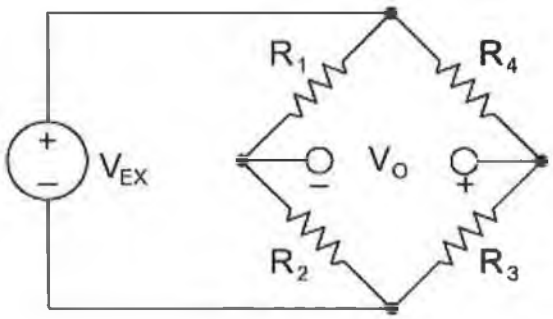

Figure C.1: Schematic of Wheatstone bridge circuit

From viewing the circuit, it is apparent that when R1/R2 = R4/R3, V_{out} will be 0 V. The circuit is termed "balanced". A change in resistance of R4 will unbalance the bridge and produce a voltage at V_{out}. If a similar change in both magnitude and polarity occurs in an adjacent arm of the bridge, R1 for example, the bridge will remained balanced at 0 V. Equation C.5 defines the output voltage induced by a strain [119].

$$V_{out} = \frac{(G.F)(\varepsilon)(N)(V_{in})}{4} \tag{C.5}$$

Where "N" is the number of active arms of the bridge and "ε" denotes *strain*. One active strain gauge is referred to as a quarter bridge circuit, two active strain gauges are referred to as a half bridge circuit, while 4 active strain gauges are referred to as a full bridge circuit. For a full Wheatstone bridge, normally two are wired to measure compression and the remaining two to measure tension. The output will be proportional to the sum of all the strains measured separately [120].

Appendix D

Data Acquisition

National Instruments supply with the NI4351 data acquisition card, Labview code recommended for the measurement of temperature. The supplied code utilises the full temperature hardware circuitry embedded in the NI4351 card for optimum accuracy. This code was adapted such that the new Labview programme would print on the screen the individual temperatures and also log all temperature data to an excel file. This programme was further adapted such that the programme would also measure, display and log the strain gauge data. Figure D.1 illustrates the user interface of the adapted Labview programme.

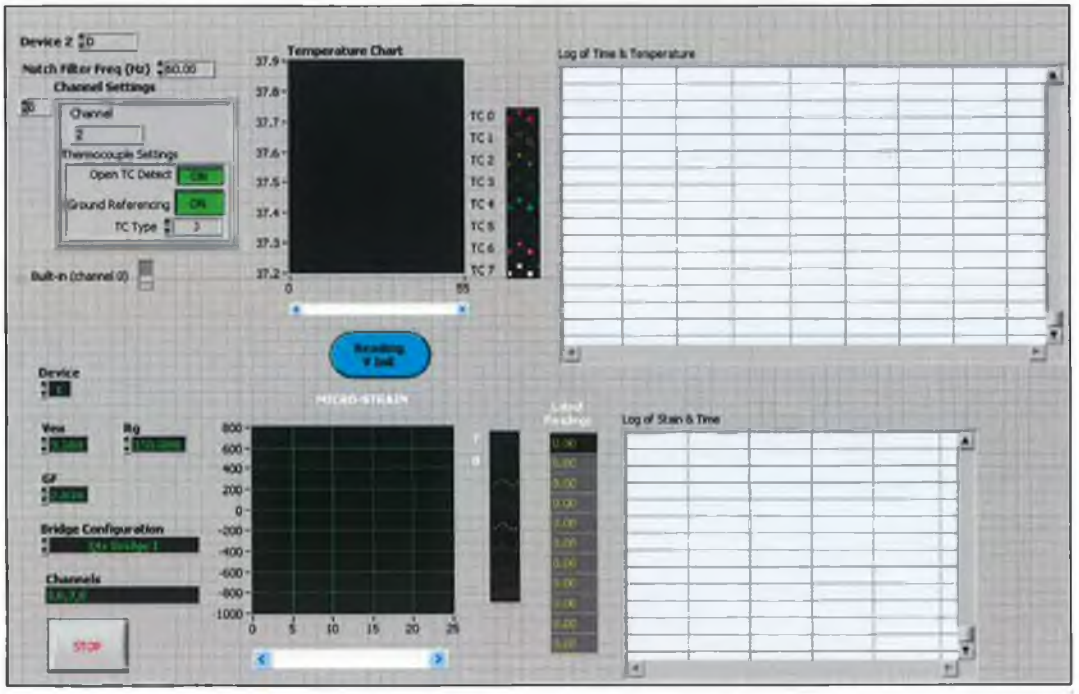

Figure D.1: Graphical user interface of adapted Labview programme used for the acquisition and logging of thermocouple and strain gauge data

Figures D.2 to D.5 illustrate the labview code used for the data acquisition programme.

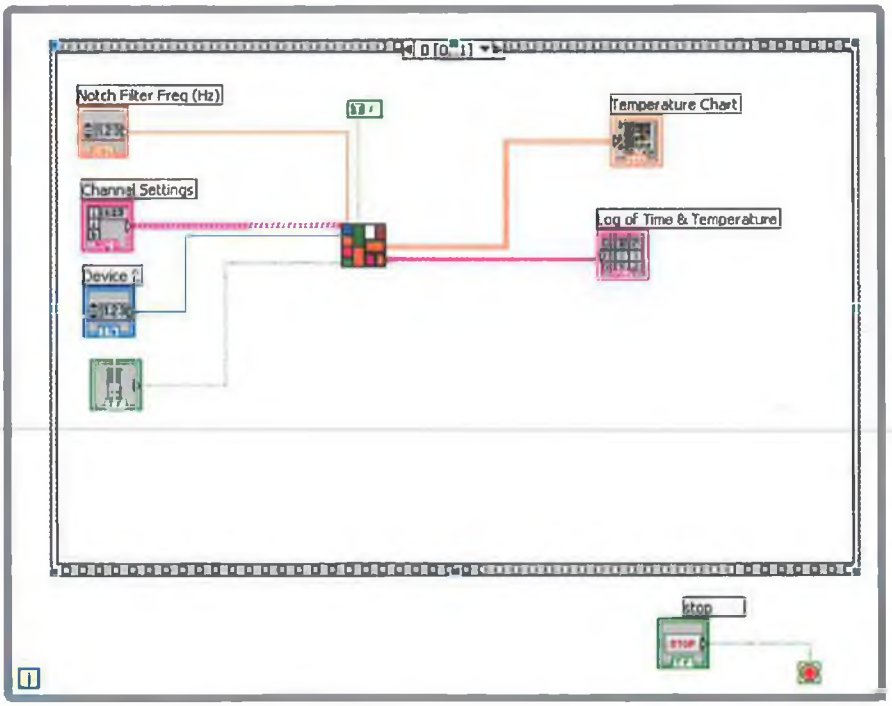

Figure D.2: Temperature measurement subroutine

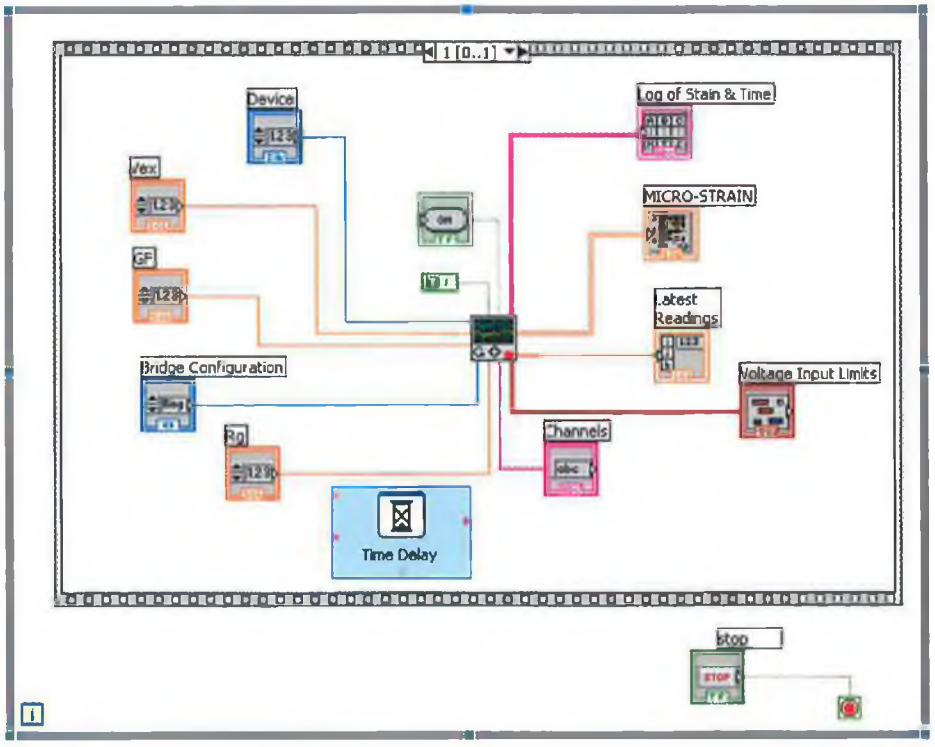

Figure D.3: Strain gauge measurement subroutine

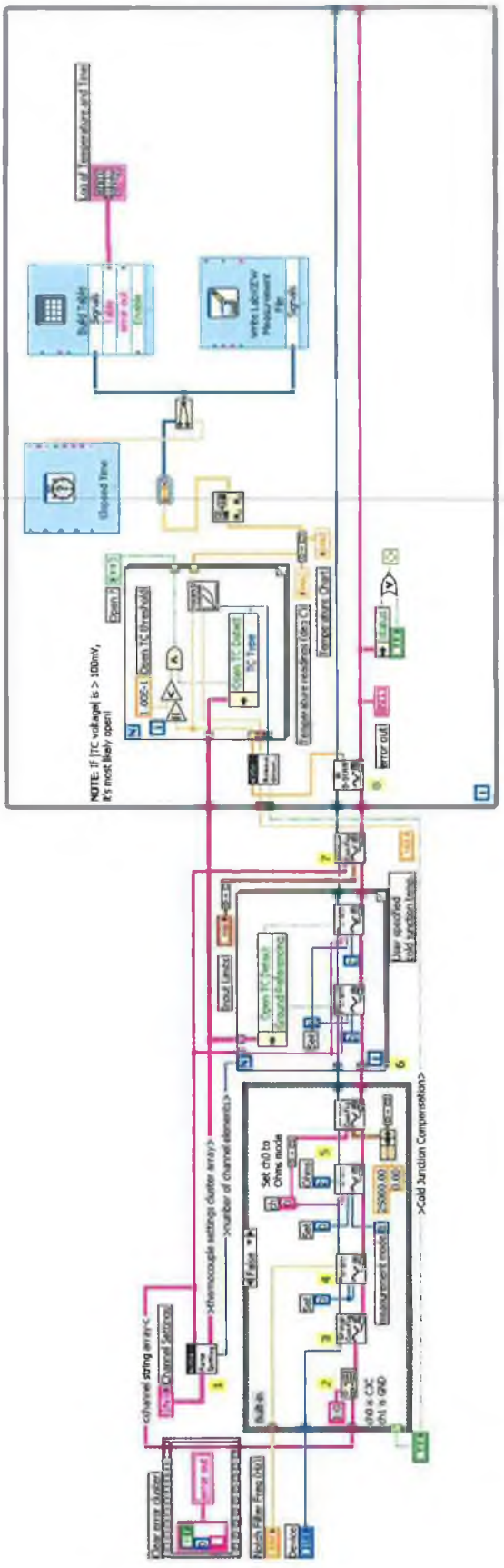

Figure D.4: Temperature measurement subroutine code

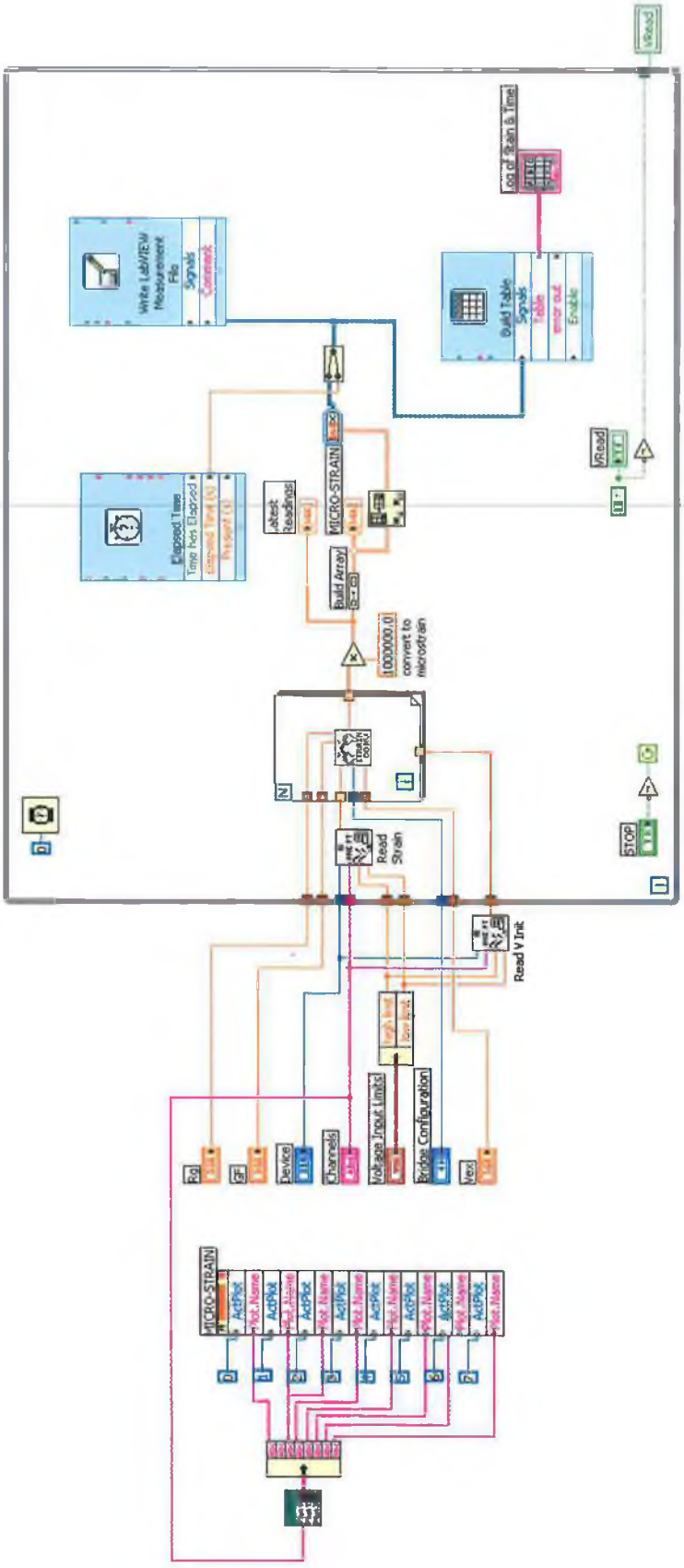

Figure D.5: Strain gauge measurement subroutine code

Appendix E

CMW® 1 Gentamicin Transient Thermal Results

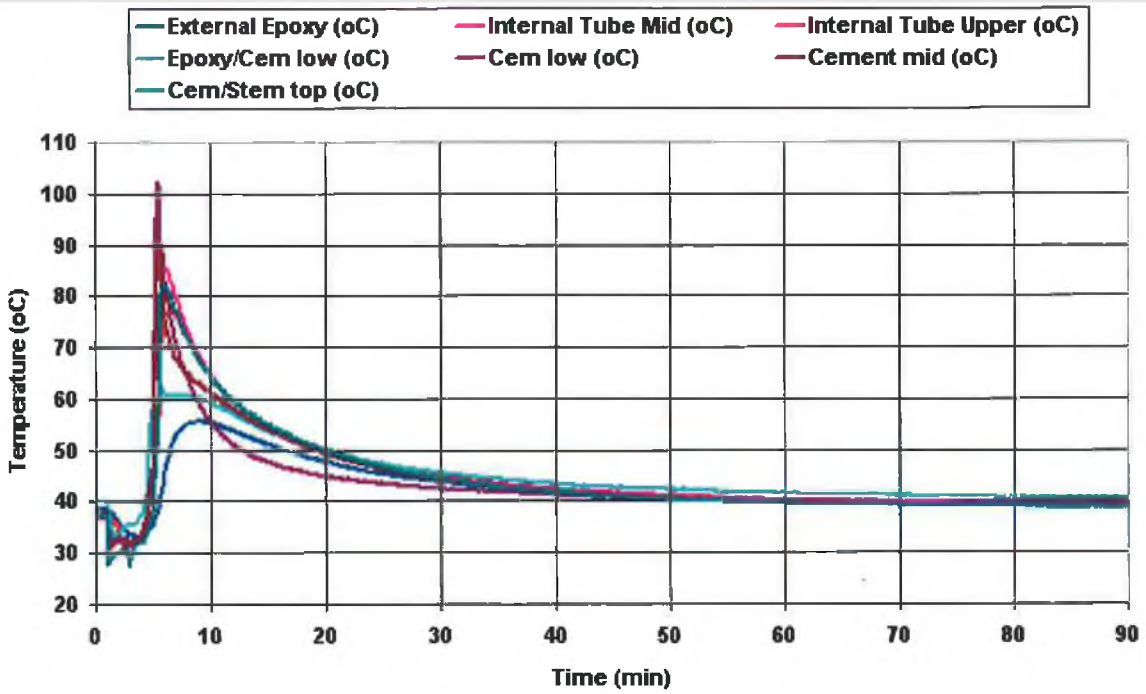

Figure E.1: Thermal history for polymerising CMW® 1 Gentamicin bone cement over the first 1.5 hours. Data taken from experiment number 3 (CMW® 1 Gentamicin, non-vacuumed, non-pressurised).

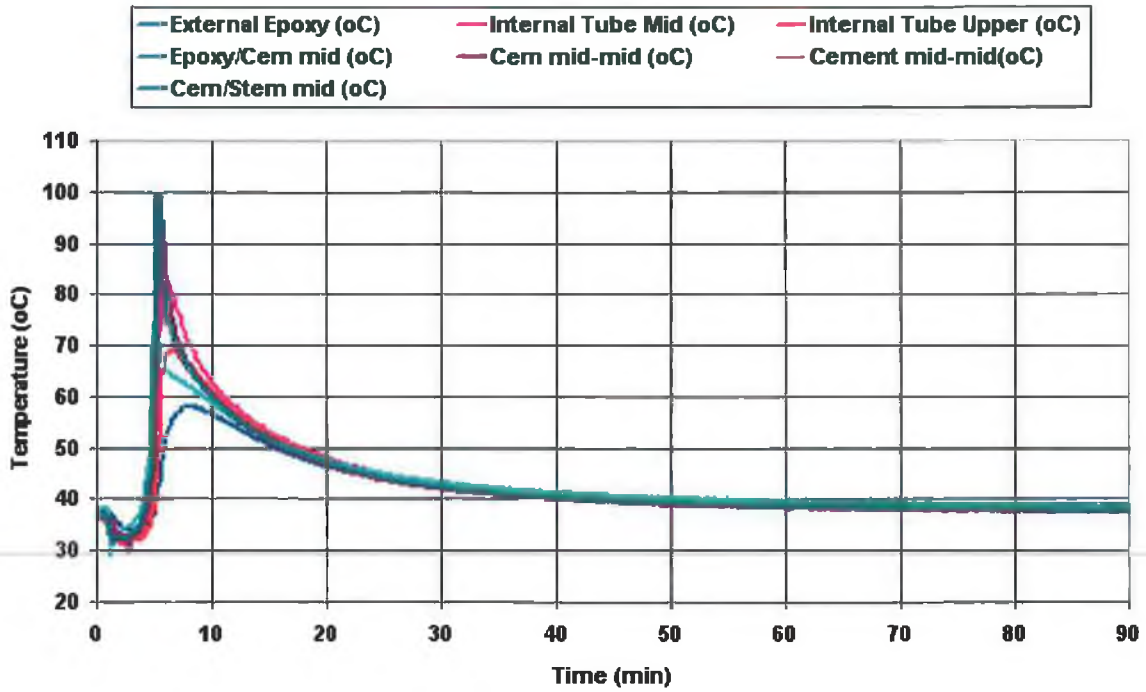

Figure E.2: Thermal history for polymerising CMW® 1 Gentamicin bone cement over the first 1.5 hours. Data taken from experiment number 19 (CMW® 1 Gentamicin, non-vacuumed, pressurised).

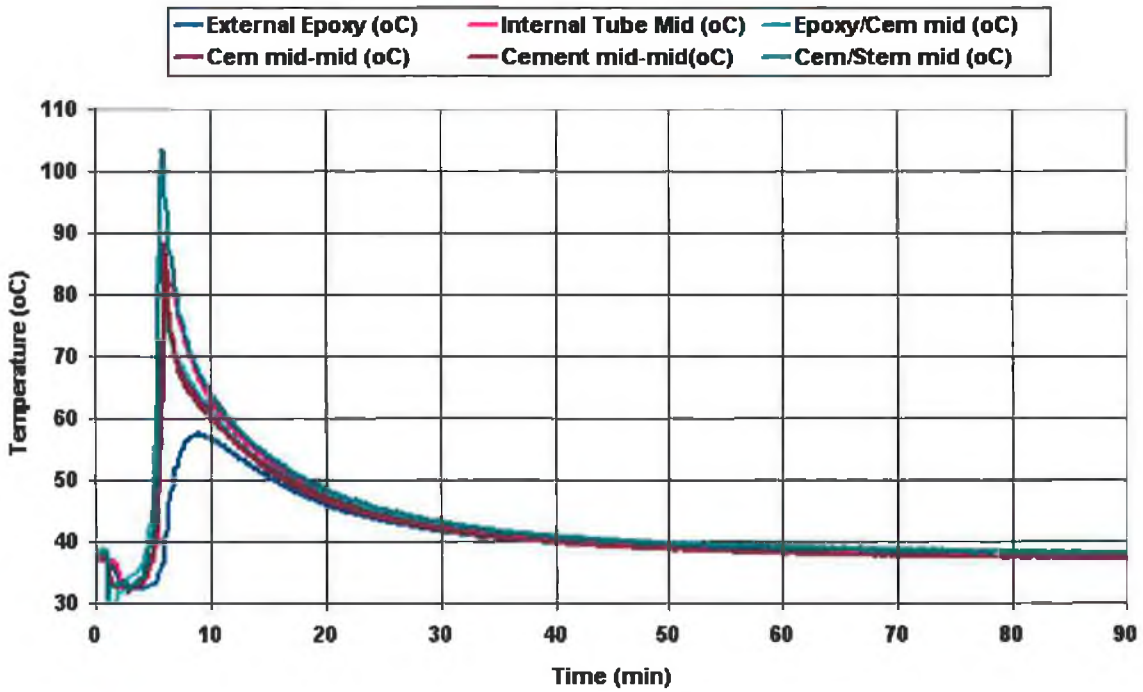

Figure E.3: Thermal history for polymerising CMW® 1 Gentamicin bone cement over the first 1.5 hours. Data taken from experiment number 20 (CMW® 1 Gentamicin, non-vacuumed, pressurised).

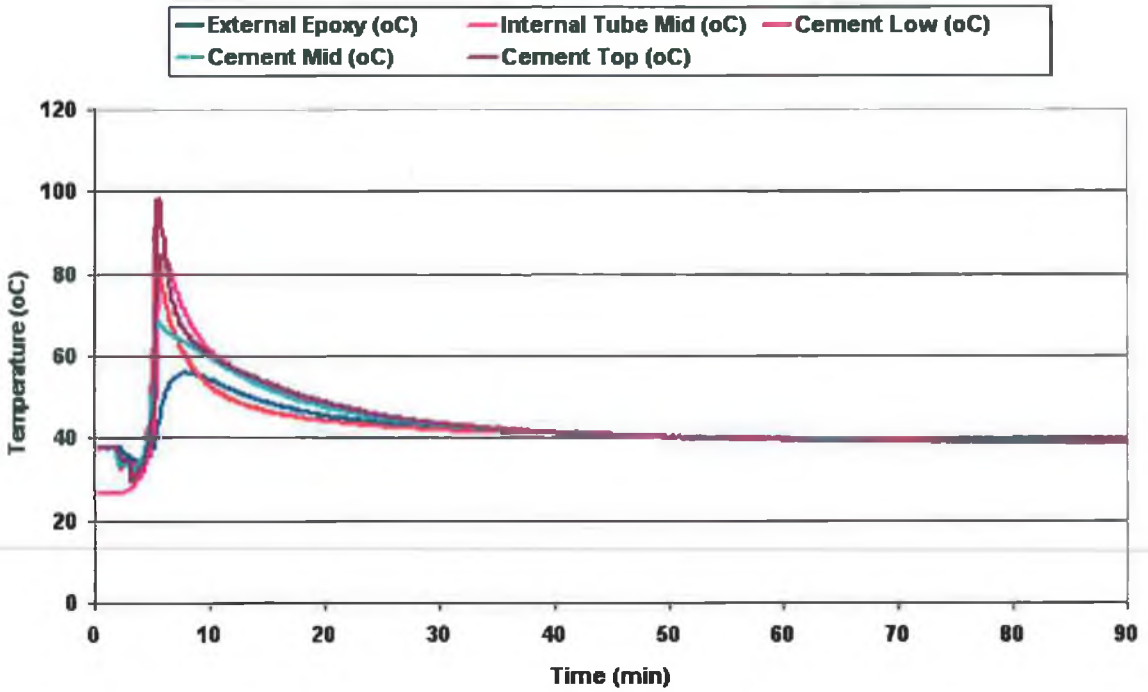

Figure E.4: Thermal history for polymerising CMW® 1 Gentamicin bone cement over the first 1.5 hours. Data taken from experiment number 22 (CMW® 1 Gentamicin, vacuumed, non-pressurised).

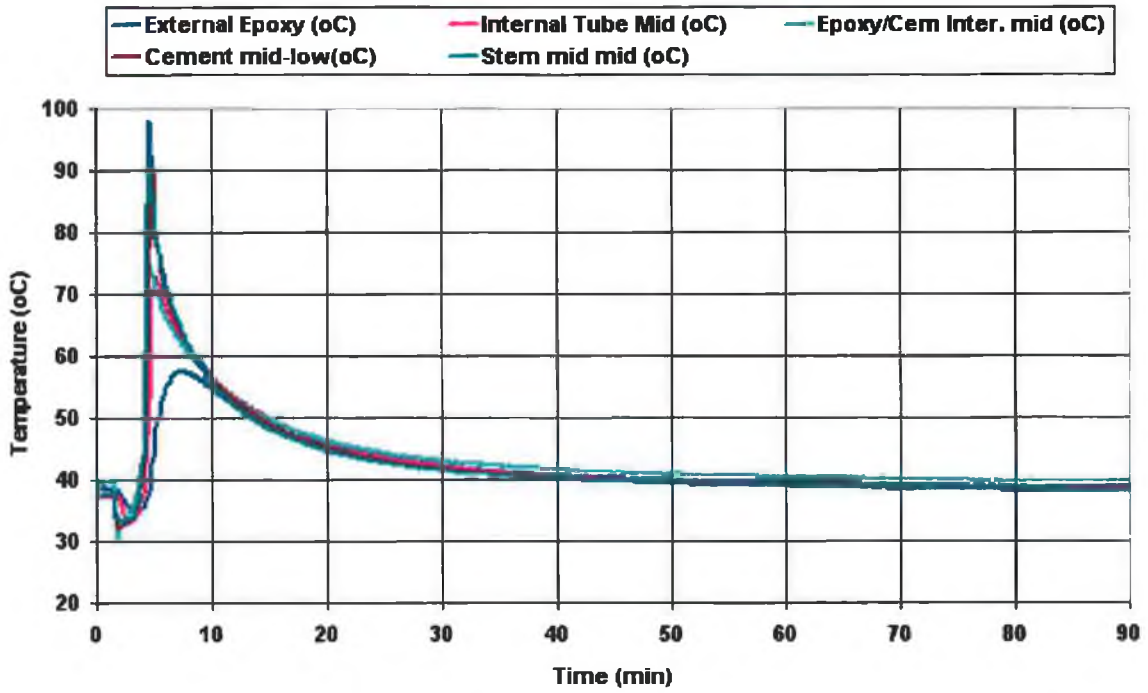

Figure E.5: Thermal history for polymerising CMW® 1 Gentamicin bone cement over the first 1.5 hours. Data taken from experiment number 27 (CMW® 1 Gentamicin, vacuumed, pressurised).

Appendix F

SmartSet® Gentamicin Transient Thermal Results

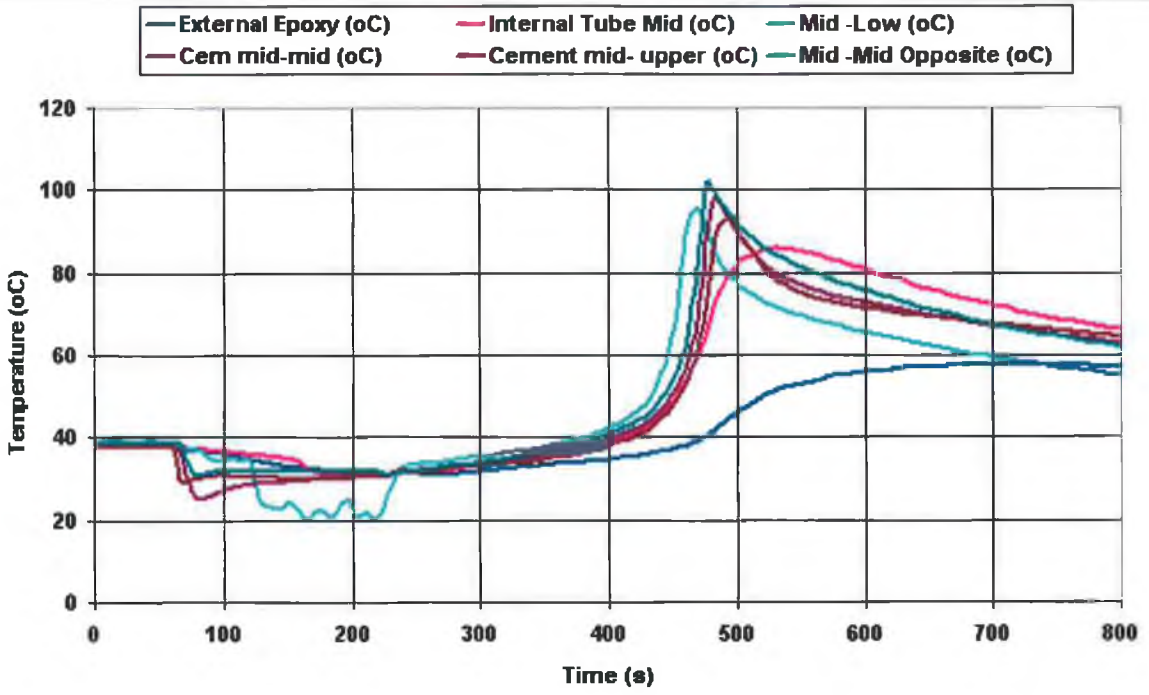

Figure F.1: Thermal history for polymerising SmartSet® Gentamicin bone cement over the first 800 seconds. Data taken from experiment number 7 (SmartSet® Gentamicin, non-vacuumed, non-pressurised).

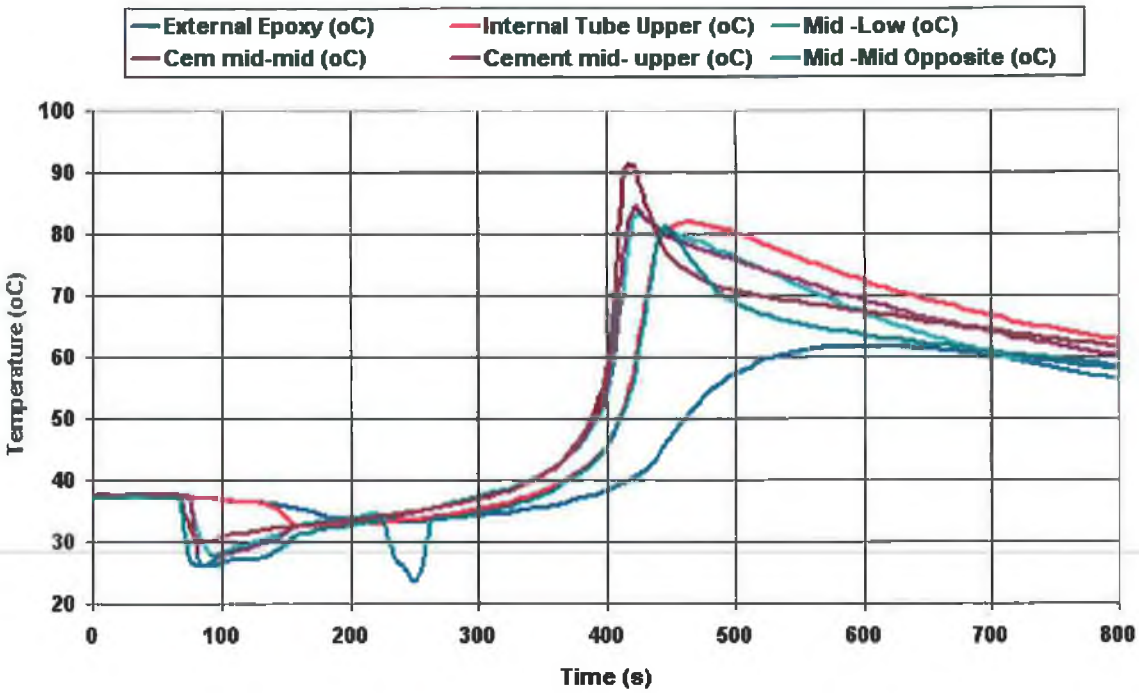

Figure F.2: Thermal history for polymerising SmartSet® Gentamicin bone cement over the first 800 seconds. Data taken from experiment number 8 (SmartSet® Gentamicin, non-vacuumed, non-pressurised).

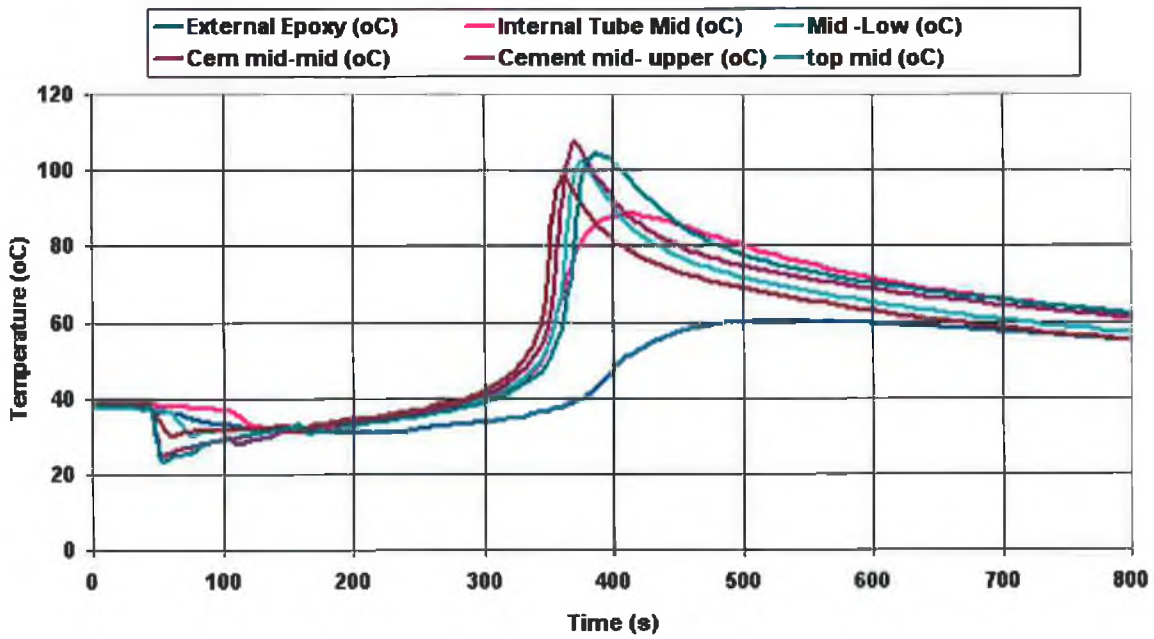

Figure F.3: Thermal history for polymerising SmartSet® Gentamicin bone cement over the first 800 seconds. Data taken from experiment number 10 (SmartSet® Gentamicin, non-vacuumed, non-pressurised).

Appendix G

Instrumented Femur Transient Strain Results

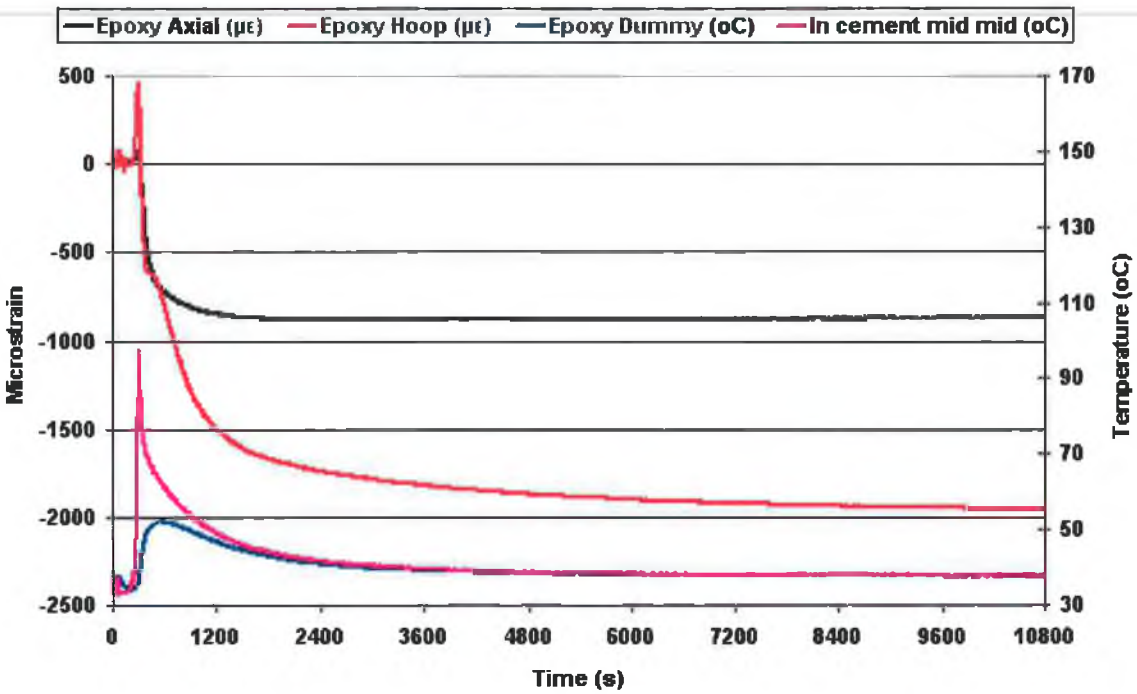

Figure G.1: Instrumented femur strain result with associated temperatures over the first 10,800 seconds (3 hours). Data taken from experiment number 1 (CMW® 1 Gentamicin, non-vacuumed, non-pressurised).

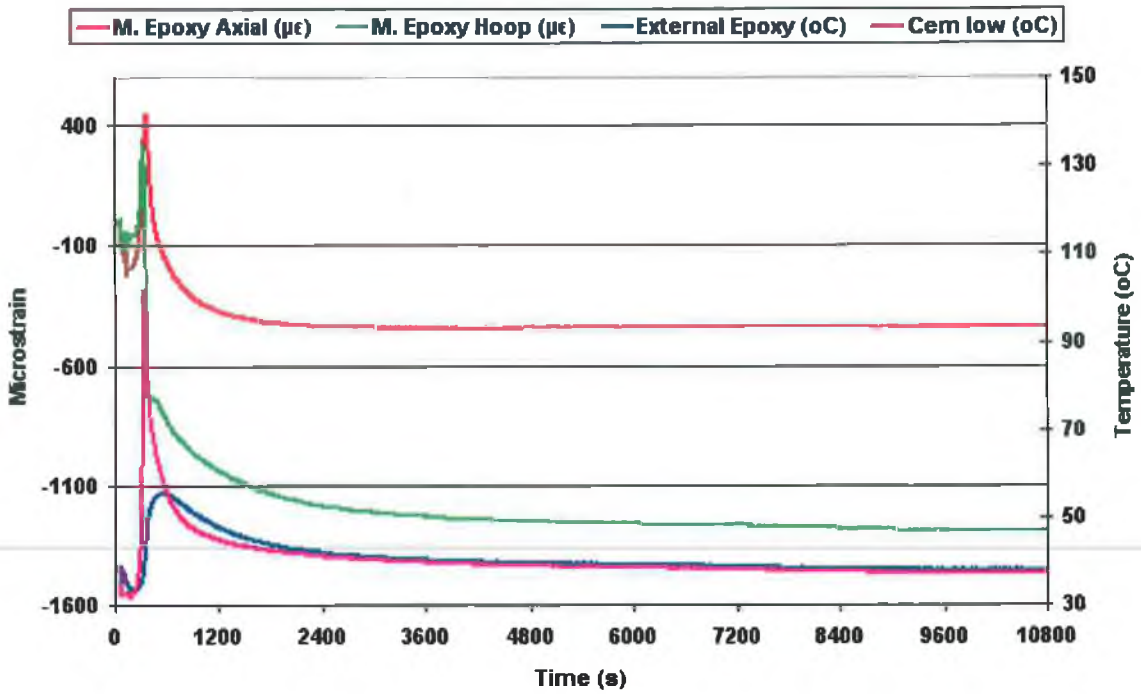

Figure G.2: Instrumented femur strain result with associated temperatures over the first 10,800 seconds (3 hours). Data taken from experiment number 3 (CMW® 1 Gentamicin, non-vacuumed, non-pressurised).

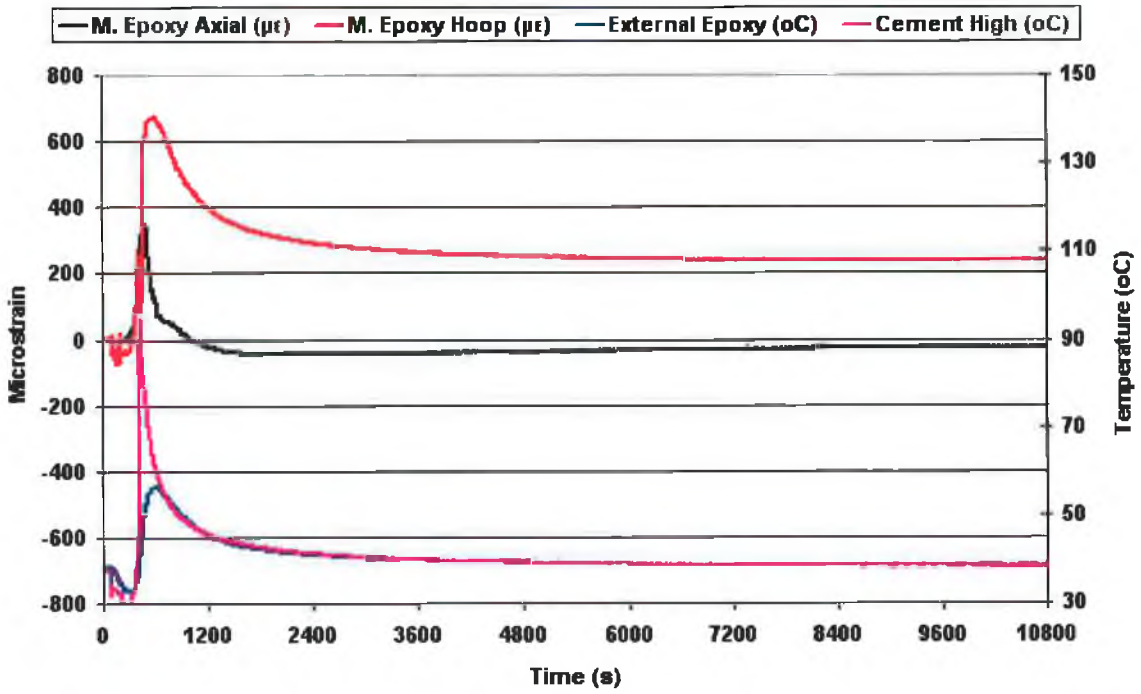

Figure G.3: Instrumented femur strain result with associated temperatures over the first 10,800 seconds (3 hours). Data taken from experiment number 15 (CMW® 1 Gentamicin, non-vacuumed, pressurised).

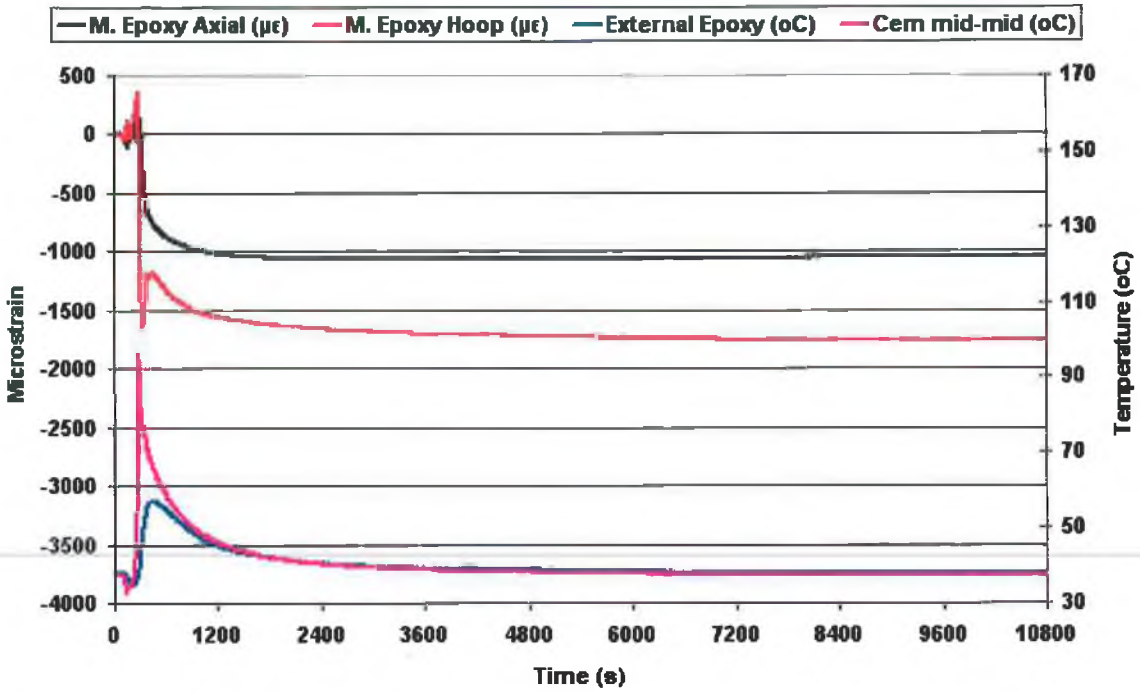

Figure G.4: Instrumented femur strain result with associated temperatures over the first 10,800 seconds (3 hours). Data taken from experiment number 23 (CMW® 1 Gentamicin, vacuumed, non-pressurised).

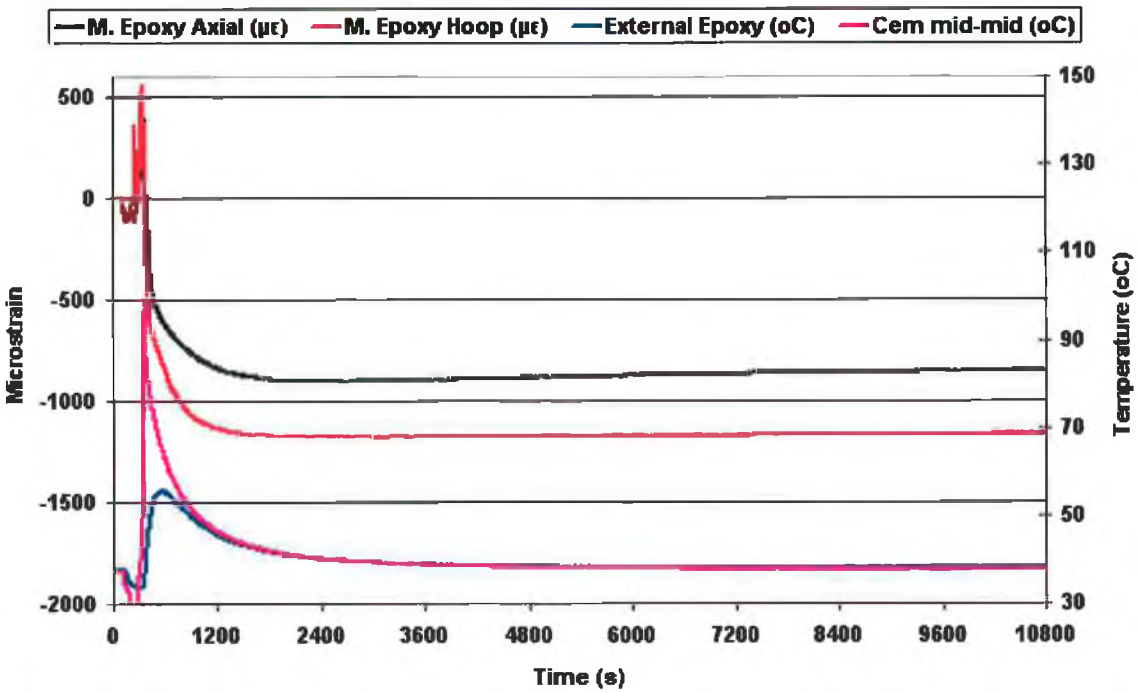

Figure G.5: Instrumented femur strain result with associated temperatures over the first 10,800 seconds (3 hours). Data taken from experiment number 26 (CMW® 1 Gentamicin, vacuumed, pressurised).

Appendix H

Instrumented Stem Transient Strain Results

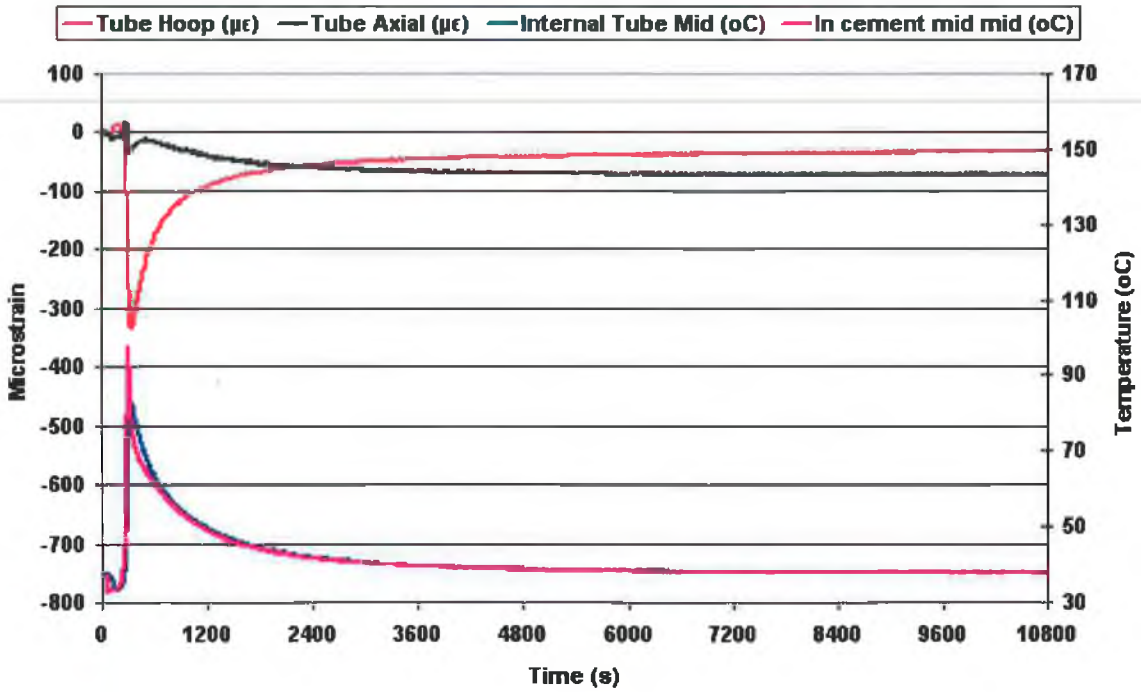

Figure H.1: Instrumented stem strain result with associated temperatures over the first 10,800 seconds (3 hours). Data taken from experiment number 1 (CMW® 1 Gentamicin, non-vacuumed, non-pressurised).

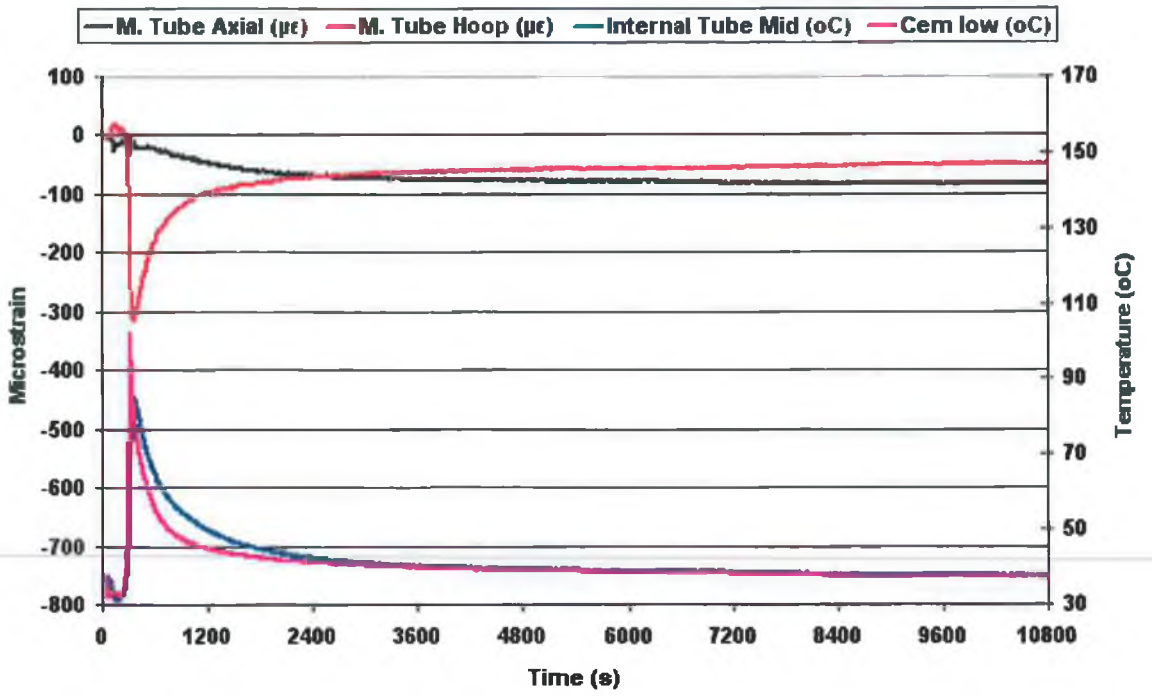

Figure H.2: Instrumented stem strain result with associated temperatures over the first 10,800 seconds (3 hours). Data taken from experiment number 3 (CMW® 1 Gentamicin, non-vacuumed, non-pressurised).

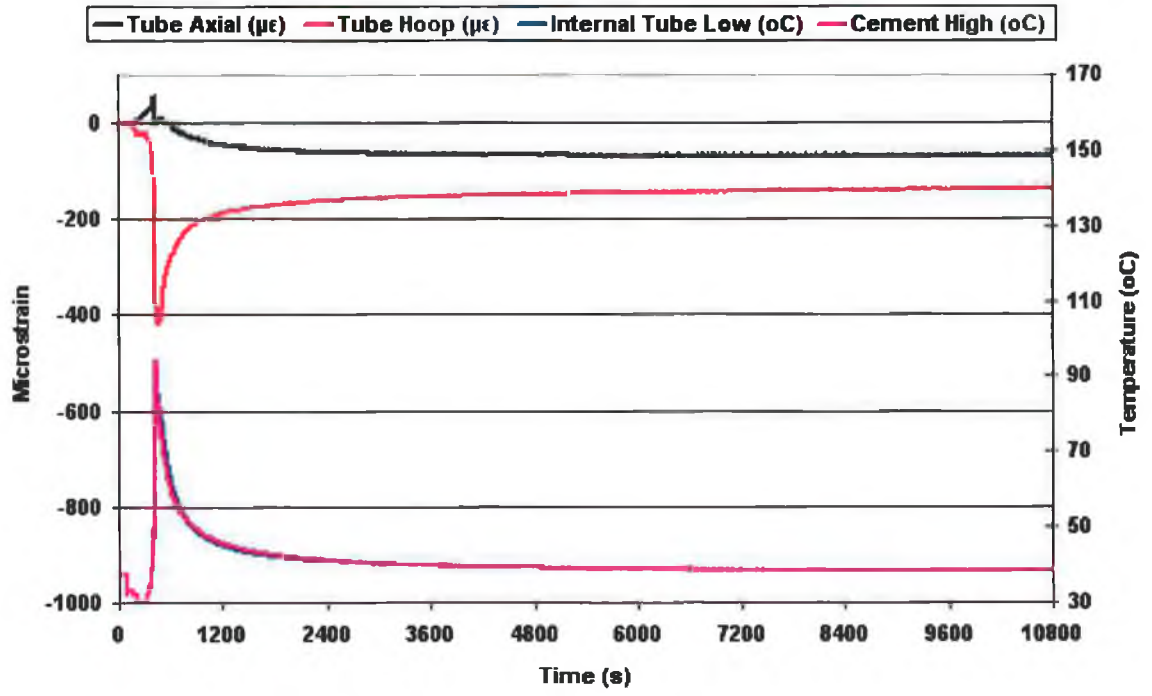

Figure H.3: Instrumented stem strain result with associated temperatures over the first 10,800 seconds (3 hours). Data taken from experiment number 15 (CMW® 1 Gentamicin, non-vacuumed, pressurised).

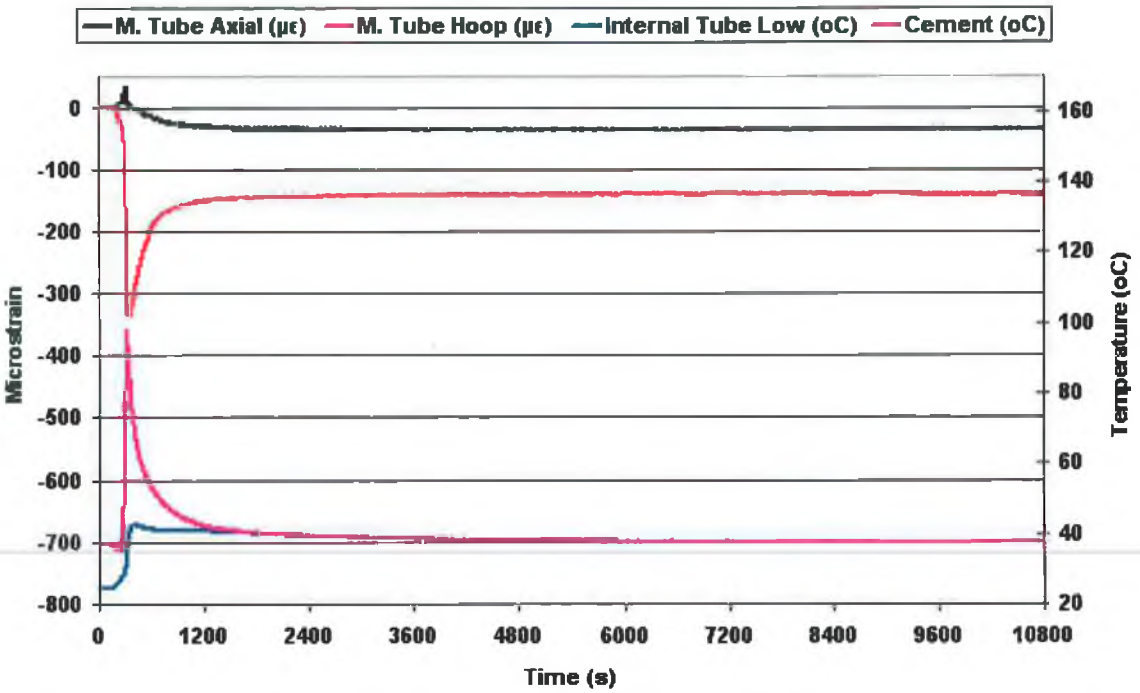

Figure H.4: Instrumented stem strain result with associated temperatures over the first 10,800 seconds (3 hours). Data taken from experiment number 21 (CMW® 1 Gentamicin, vacuumed, non-pressurised).

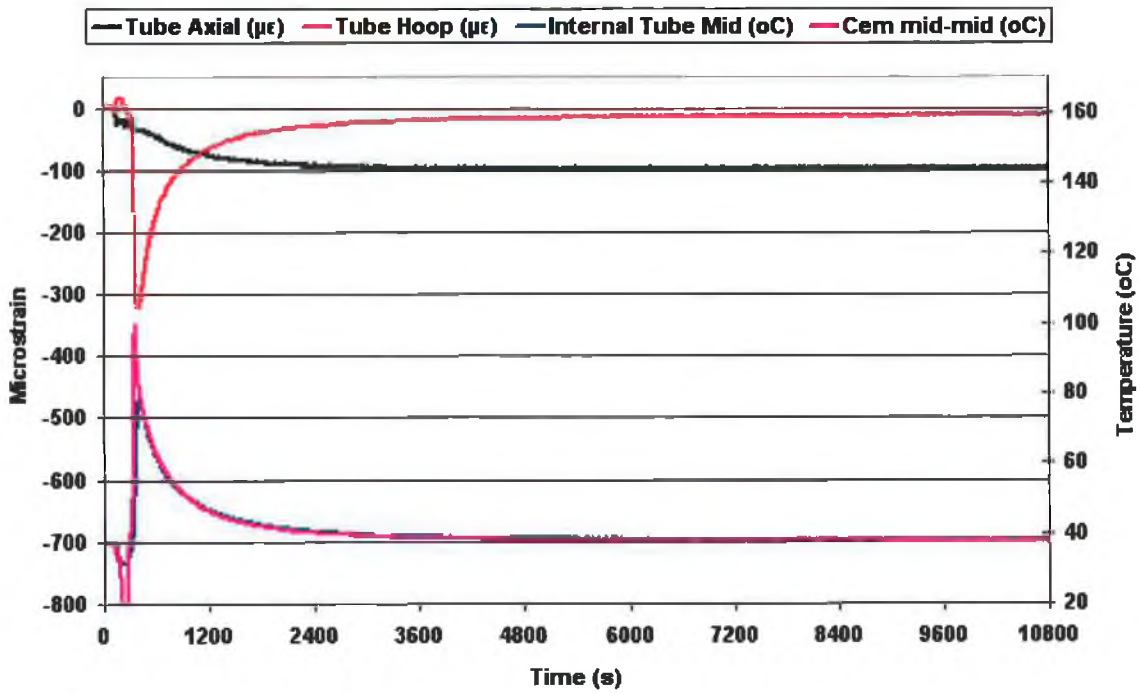

Figure H.5: Instrumented stem strain result with associated temperatures over the first 10,800 seconds (3 hours). Data taken from experiment number 26 (CMW® 1 Gentamicin, vacuumed, pressurised).

Appendix I

Theoretical Model

Consider a compound cylinder as illustrated in Figure I.1. A shrink fit exists between the two cylinders, i.e. the inner diameter of the outer cylinder is slightly less (in the order of micrometers) than the outer diameter of the inner cylinder. Based on the experimental work, this shrink fit is created by the thermal expansion of the Morse taper from ambient temperature to body temperature coupled with the thermal contraction of the bone cement from the preset elevated temperature (60 to 120°C) to body temperature. By the creation of this interference at the mating surface, a system of hoop and radial stresses are set up in both cylinders.

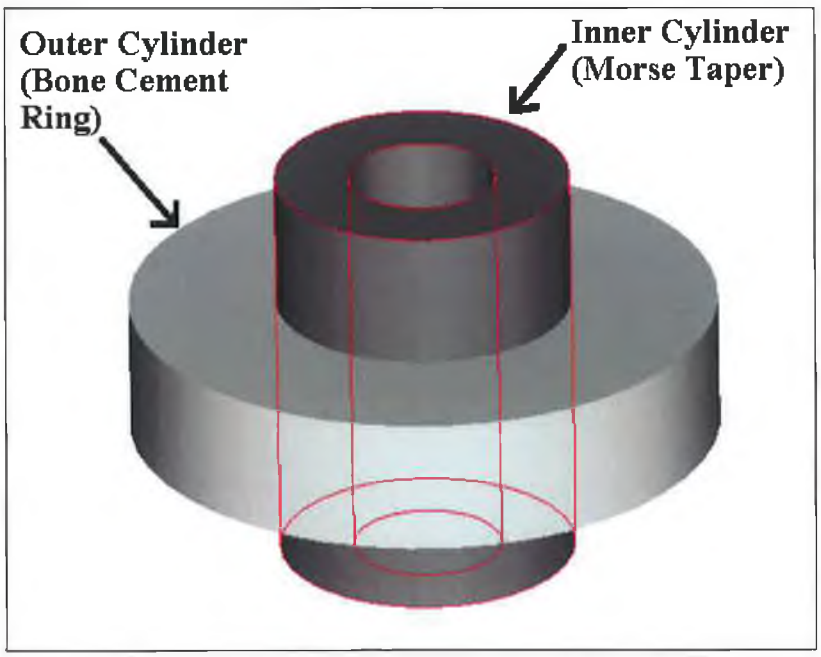

Figure I.1: Compound cylinder

From the experimental methodology, the bone cement samples were gently placed about the Morse taper with no external loads applied to either cylinder [33]. Therefore plane stress conditions were assumed to aid the derivation.

Assuming both cylinders are within their elastic range and plane stress conditions prevail, thick wall cylinder theory may be used to describe the stresses, equations I.1 to I.4 [37, 168].

$$\sigma_{rm} = A - \frac{B}{r^2} \tag{I.1}$$

$$\sigma_{\theta m} = A + \frac{B}{r^2} \tag{I.2}$$

$$\sigma_{rc} = C - \frac{D}{r^2} \tag{I.3}$$

$$\sigma_{\theta c} = C + \frac{D}{r^2} \tag{I.4}$$

Where the subscripts "m" and "c" are used to denote *Morse taper* and *bone cement* respectively. To solve for the constants A, B, C and D, 4 equations from initial conditions are required.

There was no internal pressure acting on the inside of the Morse taper. Therefore at $r = r_i$;

$$0 = A - \frac{B}{r_i^2} \tag{I.5}$$

There was no external pressure acting on the outside of the bone cement ring. Therefore at $r = r_o$;

$$0 = C - \frac{D}{r_0^2} \tag{I.6}$$

At the mating surface r_m, the radial stresses for the Morse taper and bone cement sample must be equal. Therefore at $r = r_m$;

$$A - \frac{B}{r_m^2} = C - \frac{D}{r_m^2} \tag{I.7}$$

At the mating surface r_m, the radial interference Δ, is given by the sum of the Morse taper displacement inwards δ_m and the bone cement displacement outwards, δ_c as shown in Figure I.2.

$$\Delta = -\delta_m + \delta_c \tag{I.8}$$

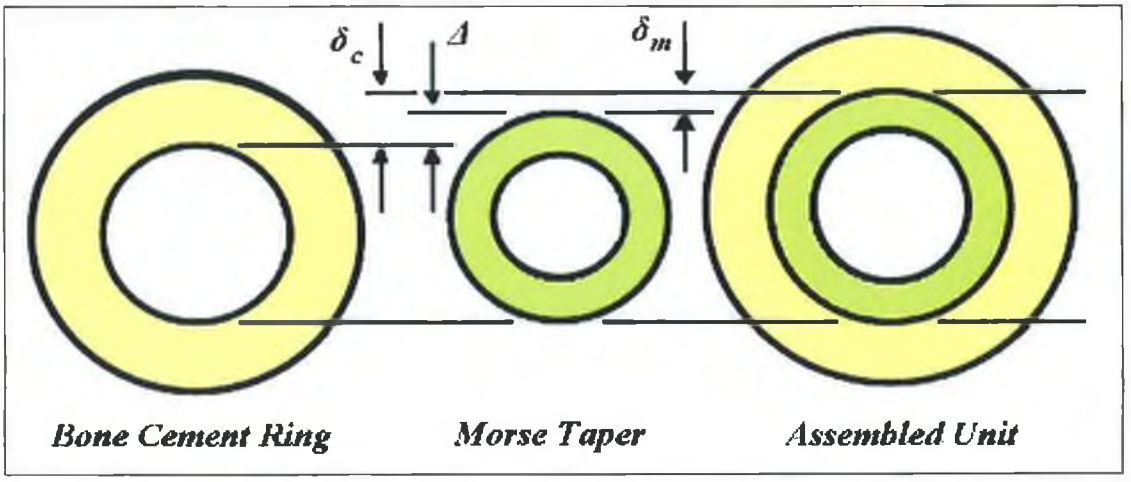

Figure I.2: Graphical description of interference

From the definition of strain;

$$\delta l = \varepsilon . l_o \tag{I.9}$$

$$\Rightarrow \Delta = r_m(\varepsilon_c - \varepsilon_m) \tag{I.10}$$

From the plane stress assumption;

$$\varepsilon_\theta = \frac{\sigma_\theta}{E} - \frac{\nu\sigma_r}{E} \tag{I.11}$$

$$\Rightarrow \Delta = r_m\left(\frac{\sigma_{\theta c}}{E_c} - \upsilon_c\frac{\sigma_{rc}}{E_c} - \frac{\sigma_{\theta m}}{E_m} + \upsilon_m\frac{\sigma_{rm}}{E_m}\right) \tag{I.12}$$

Substituting Equations I.1 through I.4 into Equation I.12;

$$\Delta = r_m\left(\frac{C+\frac{D}{r^2}}{E_c} - \upsilon_c\frac{C-\frac{D}{r^2}}{E_c} - \frac{A+\frac{B}{r^2}}{E_m} + \upsilon_m\frac{A-\frac{B}{r^2}}{E_m}\right) \tag{I.13}$$

From linear thermal expansion theory;

$$\delta l = \alpha\left(T_f - T_i\right) l_o \tag{I.14}$$

Where "δl" represents *change in length* due to a temperature difference, "α" represents the *coefficient of thermal expansion*, "l_o" represents *original length* and "T_f" and "T_i" represent final and initial temperature respectively. When the Morse taper is heated, it radially expands about its revolute axis. Likewise the bone cement ring would radially contract when cooled. Therefore interference is given by how much the bone cement ring would contract going from peak temperature to body temperature (negative displacement) minus how much the Morse taper expands. Therefore the radial interference Δ, of Equation I.15 is the sum of both negative expressions.

From Equations I.8 and I.14;

$$\Delta = -\alpha_m\left(T_f - T_i\right) r_m + \alpha_c\left(T_f - T_i\right) r_m \tag{I.15}$$

Combining Equations I.13 and I.15;

$$-\alpha_m (T_f - T_i) r_m + \alpha_c (T_f - T_i) r_m = r_m \left(\frac{C + \frac{D}{r^2}}{E_c} - \upsilon_c \frac{C - \frac{D}{r^2}}{E_c} - \frac{A + \frac{B}{r^2}}{E_m} + \upsilon_m \frac{A - \frac{B}{r^2}}{E_m} \right) \quad \text{(I.16)}$$

To solve for the 4 unknown constants A, B, C and D simultaneous equations may be used with equations I.5, I.6, I.7 and I.16. In turn the radial and hoop stresses in the cement mantle may be calculated by equations I.3 and I.4 respectively, while the radial and hoop stresses in the Morse taper may be calculated by equations I.1 and I.2 respectively.

Quantification Of Residual Stresses

The objective of this section was to apply the theoretical model developed to quantify the residual stresses induced for the experimental work by Orr *et al* [33].

Model Definition

The cement rings had an outer radius of 15 mm and an inner radius of 7.5 mm. The Morse taper used in the experimental work was solid. However the theoretical model prescribes the Morse taper to have some finite inner radius. To minimise the effects associated with this assumption, a hole of radius 10 μm was assumed. As the outside diameter of the Morse taper is vastly greater (750 times) than that of the hole and as the Young's modulus of the Morse taper is approximately 90 times greater than that of the bone cement, it is postulated that this assumption would impose negligible effects for the calculation of residual stress. Material properties identical to those assumed for the FE model were assumed for the theoretical model. See Section 4.2.2 for material properties assumed.

Boundary Conditions And Loading

An even initial and final temperature distribution for both components was applied, as per experimental work [33]. The cement samples were set to a predefined temperature of 60, 80, 100 or 120°C, while the stem for each

simulation was always assigned an initial temperature of 20°C. Both materials were assigned a final temperature of 37°C.

Computation

A Matlab v.5.3 (The MathWorks Inc., MA, USA) script was wrote to:

1. Solve the simulations equations and therefore define the constants A to D
2. Compute the von Mises, hoop and radial stresses at points of interest e.g. at r_m and print these results to screen
3. Compute the von Mises, hoop and radial stresses for $0.00001 \leq r \leq 0.015$ meters
4. Plot the von Mises, hoop and radial stresses over the range considered.

The following is the Matlab code developed to calculate the residual stresses based on an assembly temperature of 100°C. To generate the results for the 60°C, 80°C, and 120°C, the variable "peak_temp" as given in line 12 of the code is assigned the value of 60, 80, or 120 respectively.

```
% Programme to calculate hoop, radial and von Mises stresses
% in both the bone cement and morse taper.
% Plane stress conditions are assumed.
% Peak bone cement temperature given by variable "peak temp", line 12.
% By John Hingston

% *************** INITIAL CONDITIONS ***************

amb_temp = 20;          %Ambient temperature
body_temp = 37;         %Body temperature
peak_temp = 100;        %Peak cement temperature

pi = 0;                 %Internal Pressure
po = 0;                 %External Pressure

ri = 0.00001;           %Inner Radius
rm = 0.0075;            %Mating Radius
ro = 0.015;             %Outer Radius

Ebc = 2.11e9;           %Bone cement Young's modulus
vbc = 0.455;            %Bone cement poisons ratio
alpha_bc = 8.0e-5;      Bone cement coefficient of thermal expansion

Emt = 1.93e11;          %Morse taper Young's modulus
vmt = 0.28;             %Morse taper  poisons ratio
alpha_mt = 1.6e-5;      %Morse taper  coefficient of thermal expansion

% ****************  CALCULATION OF RADIAL INTERFERENCE  **************

% Radial Interference = Outer cylinder outwards - Inner cylinder inwards
delta = alpha_bc*rm*(peak_temp - body_temp) - alpha_mt*rm*(amb_temp - body_temp)

%  ***************     CALCULATION  OF  THICK  WALL  CYLINDER  THEORY  CONSTANTS
*************
```

```
X = [1 -1/(ri^2) 0 0;
     0 0 1 -1/(ro^2);
     1 -1/(rm^2) -1 (1/(rm^2));
     -(1-vmt)/Emt -(1+vmt)/((rm^2)*Emt) (1-vbc)/Ebc (1+vbc)/((rm^2)*Ebc)];

Z = [-pi; -po; 0; delta/rm];

Y = inv(X)*Z;

A = Y(1,1);
B = Y(2,1);
C = Y(3,1);
D = Y(4,1);


% ************* RESULTS AT POINTS OF INTEREST ****************

%Results at ri
Hoop_st_MT_ri = A + (B/ri^2);
Radial_st_MT_ri = A - (B/ri^2);

%Results at rm
Hoop_st_MT_rm = A + (B/rm^2);
Radial_st_MT_rm = A - (B/rm^2);
Hoop_st_BC_rm = C + (D/rm^2)
Radial_st_BC_rm = C - D/rm^2

%Results at ro
Hoop_st_BC_ro = C + (D/ro^2);
Radial_st_BC_ro = C - D/ro^2;


% ************* RESULTS FOR GRAPH ****************

mt = 0.00001:0.00001:0.0075;
bc = 0.0075:0.0001:0.015;
Hoop_st_MT = A + (B./(mt.*mt));
Radial_st_MT = A - (B./(mt.*mt));
Hoop_st_BC = C + (D./(bc.*bc));
Radial_st_BC = C - D./(bc.*bc);


% *************** CALCULATION OF VON MISES STRESS *****************


Sigma_z = 0;   % Assume plane stress conditions

%Morse Taper Section
Von_Mises_mt = sqrt(((Hoop_st_MT - Radial_st_MT).*(Hoop_st_MT - Radial_st_MT) +
(Radial_st_MT - Sigma_z).*(Radial_st_MT - Sigma_z) +(Sigma_z -
Hoop_st_MT).*(Sigma_z - Hoop_st_MT))/2);
Von_Mises_bc = sqrt(((Hoop_st_BC - Radial_st_BC).*(Hoop_st_BC - Radial_st_BC) +
(Radial_st_BC - Sigma_z).*(Radial_st_BC - Sigma_z) +(Sigma_z -
Hoop_st_BC).*(Sigma_z - Hoop_st_BC))/2);
Von_Mises = sqrt((Hoop_st_BC_rm - Radial_st_BC_rm)^2 + (Radial_st_BC_rm -
Sigma_z)^2 +(Sigma_z - Hoop_st_BC_rm)^2)/2)


% *************** PLOT RESULTS *********************

Figure
plot (mt, Hoop_st_MT, 'r--')
hold on
plot (bc, Hoop_st_BC, 'r--')
hold on
plot (mt, Radial_st_MT, 'b-.')
hold on
plot (bc, Radial_st_BC, 'b-.')
plot (mt, Von_Mises_mt, 'g-')
plot (bc, Von_Mises_bc, 'g-')

xlabel (' Radius (m) ')
ylabel (' Stress (Pa)')
title  ('                  Von Mises = Green Solid Line,  Hoop = Red Dashed Line,
Radial = Blue Dash-Dot Line  ')
```

Results

Figure I.3 reveals the von Mises, hoop and radial stress magnitude and distribution for the Morse taper and bone cement from an assembly temperature of 100°C. The stress distributions for the 60°C, 80°C and 120°C peak cement temperature were of similar format.

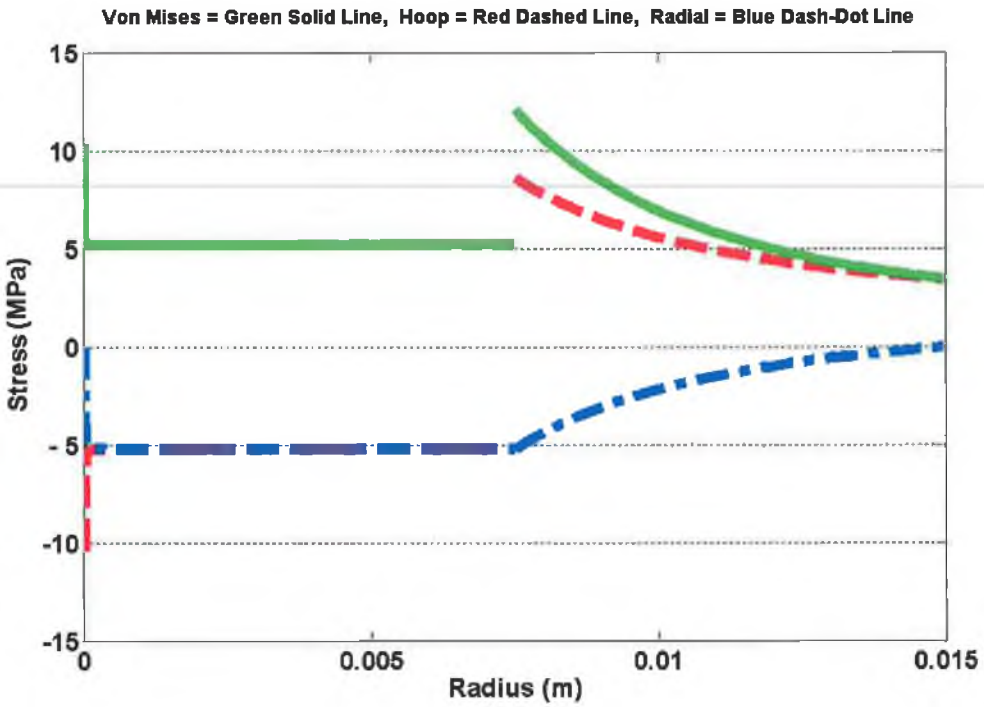

Figure I.3: Von Mises, hoop and radial stress distributions within Morse taper and bone cement ring, based on cement assembly temperature of 100 °C

From Figure I.3 it is evident that the peak principal stresses occur at the Morse taper-cement interface. This result is in agreement with the published experimental findings of Orr *et al* [33]. Figure I.4 summarises the peak residual stresses calculated from the theoretical model over the "stress-locking" temperature range considered.

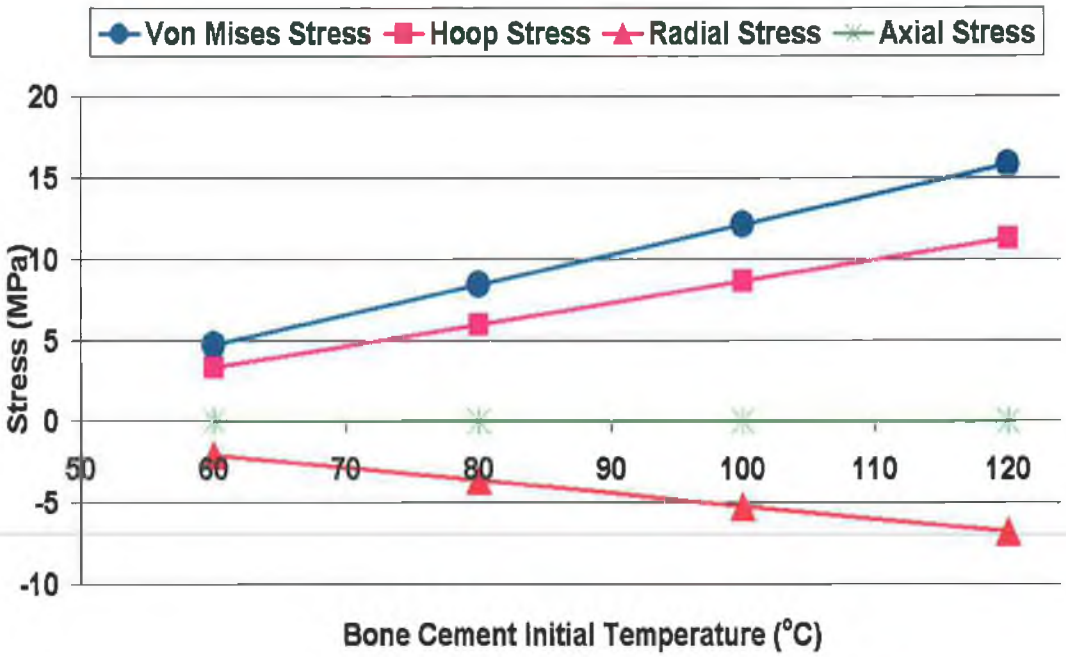

Figure I.4: Residual stresses versus peak cement temperature, calculated by theoretical model

Appendix J

Coefficient Of Thermal Convection

Equation J.1 relates the approximate free thermal convection coefficient for a vertical cylinder, surrounded by air at atmospheric pressure, at a moderate temperature under laminar air flow conditions [141].

$$h = 1.42\left(\frac{\Delta T}{L}\right)^{1/4} \tag{J.1}$$

Where "h" represents the *convection coefficient* with units of W/m^2-K, and "L" represents the *length* of the cylinder. The "ΔT" term relates to the *temperature difference* between the cylinder and ambient air temperature. From the experimental work, it is known that the representative cylinders undergo a change in temperature with respect to time due to the exotherm of the cement. As Equation J.1 is an approximation of free thermal coefficient and due to the many factors that affect the convection coefficient [141], the middle temperature value was assumed for the determination of ΔT.

Coefficient Of Convection For Exterior Of Representative Femur

Mean representative femur peak temperature = 57°C

ΔT = (57-37)/2 = 10°C

L = 0.05 m (Not 60 mm to account for the instrumented femur holder)

Based on Equation J.1, a convection coefficient of 5.1 W/m^2K was calculated. This coefficient of convection was applied to the exterior surfaces of the representative femur.

Coefficient Of Convection For Interior Of 316L Tube

Mean representative stem peak temperature = 81°C

$\Delta T = (81-37)/2 = 22°C$

L = 0.07 m

Based on Equation J.1, a convection coefficient of 6.0 W/m^2K was calculated for the interior surfaces of the representative stem. However there may not be free convection of air as the lower end of the cylinder was sealed. Also, the strain gauge and thermocouple wires running along the inside of the tube would interfere with the free flow of air. To account for these conditions, a 50% reduction to the calculated value of thermal convection was applied. This yielded a coefficient of thermal convection of 3 W/m^2K for the inside of the stainless steel tube.

Appendix K

Anatomical Model Mesh

Post meshing the stem contained approximately 9,000 nodes. Figure K.1 illustrates the mesh applied to the stem geometry.

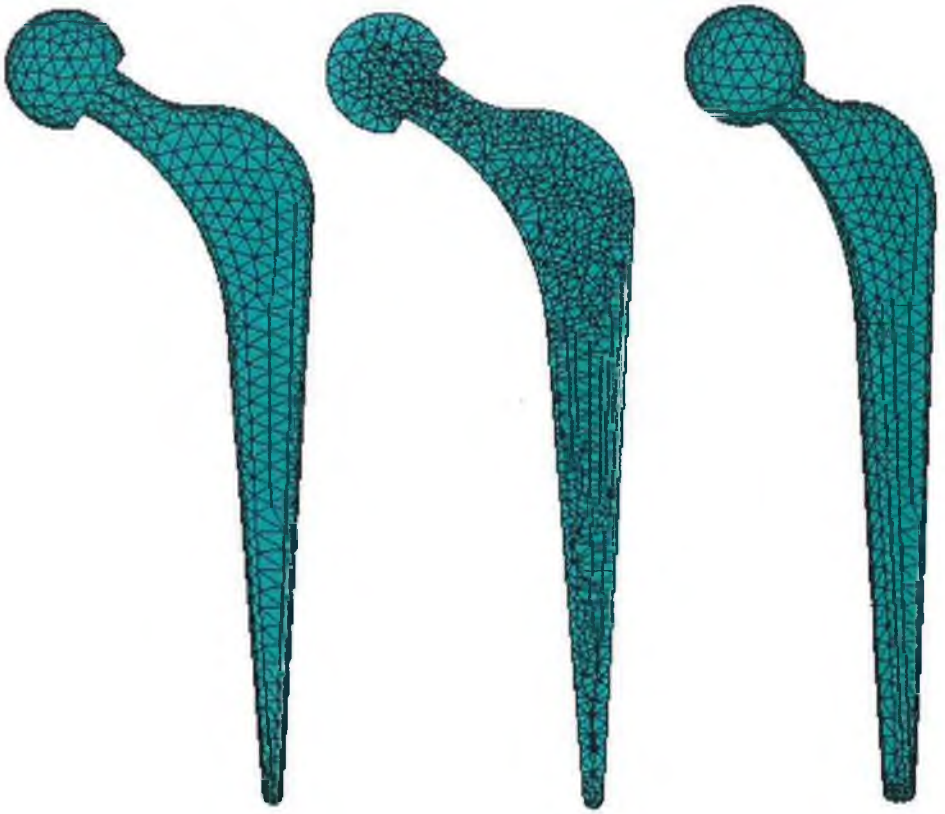

Figure K.1: (Left) Elevation view of meshed Exeter™ stem; (Middle) Elevation view of sectioned Exeter™ stem to reveal internal mesh; (Right) Auxiliary view of meshed Exeter™ stem

Post meshing the cement mantle contained approximately 8,500 nodes. Figure K.2 illustrates the mesh applied to the bone cement mantle geometry.

Figure K.2: (Left) Elevation view of meshed cement mantle; (Middle) Elevation view of sectioned cement mantle to reveal internal mesh; (Right) Auxiliary view of meshed bone cement mantle

Post meshing the femur contained approximately 8,500 nodes. Figure K.3 illustrates the mesh applied to the femur geometry.

Figure K.3: (Left) Elevation view of meshed femur; (Middle) Elevation view of sectioned femur to reveal internal mesh; (Right) Auxiliary view of meshed femur

Appendix L

Anatomical Model Principal Stress Results

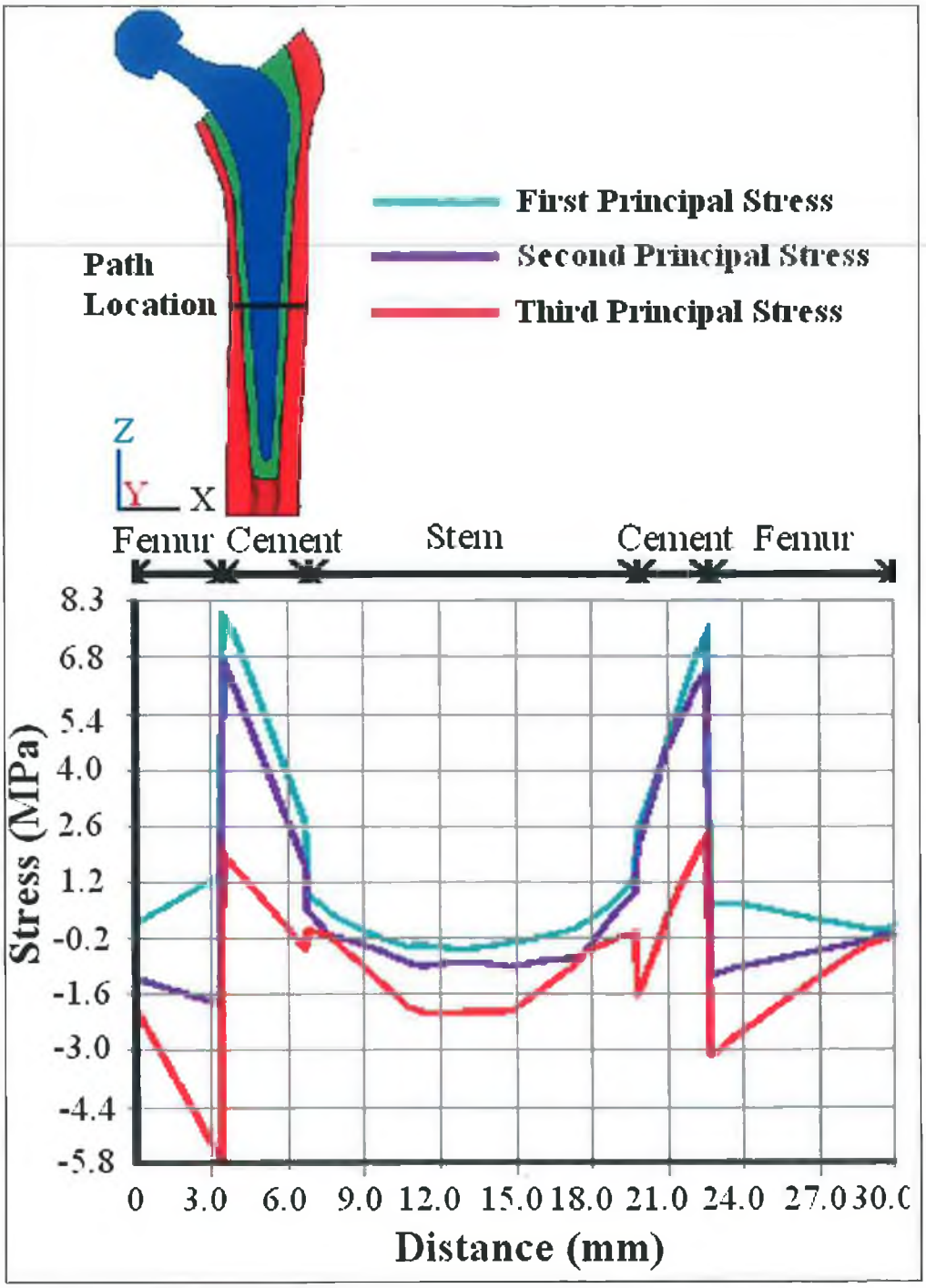

Figure L.1: Anatomical model principal residual stresses for path defined

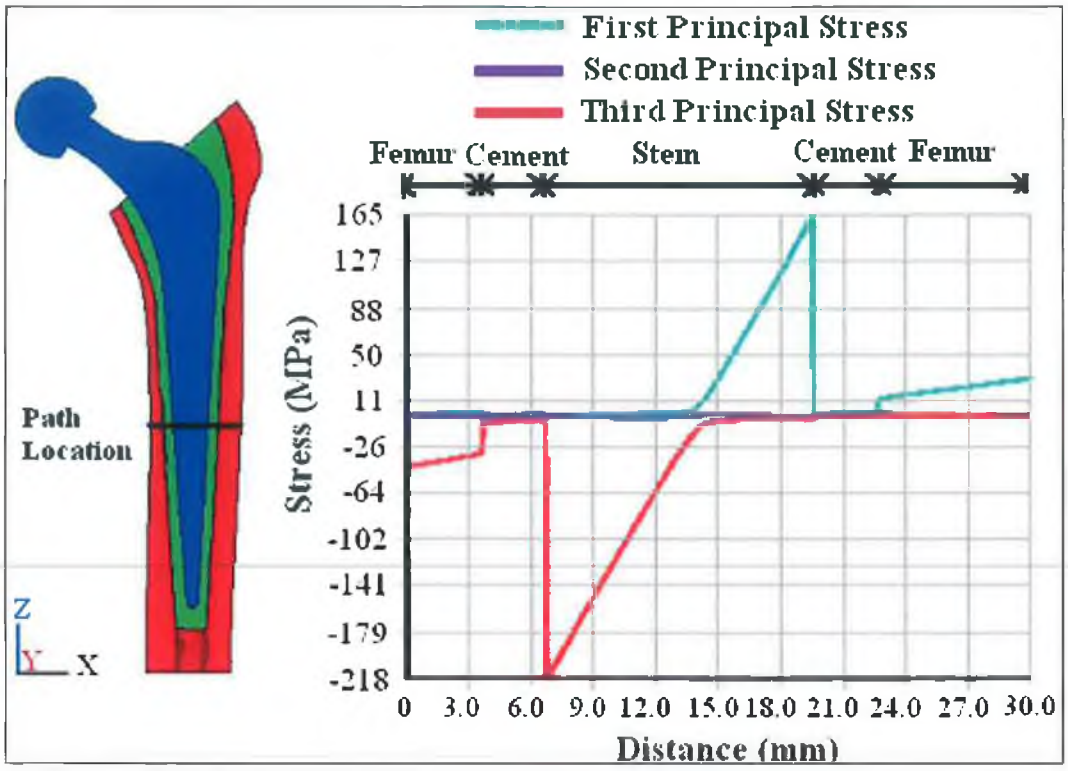

Figure L.2: Principal stresses due to the peak load from walking for path defined on solid model

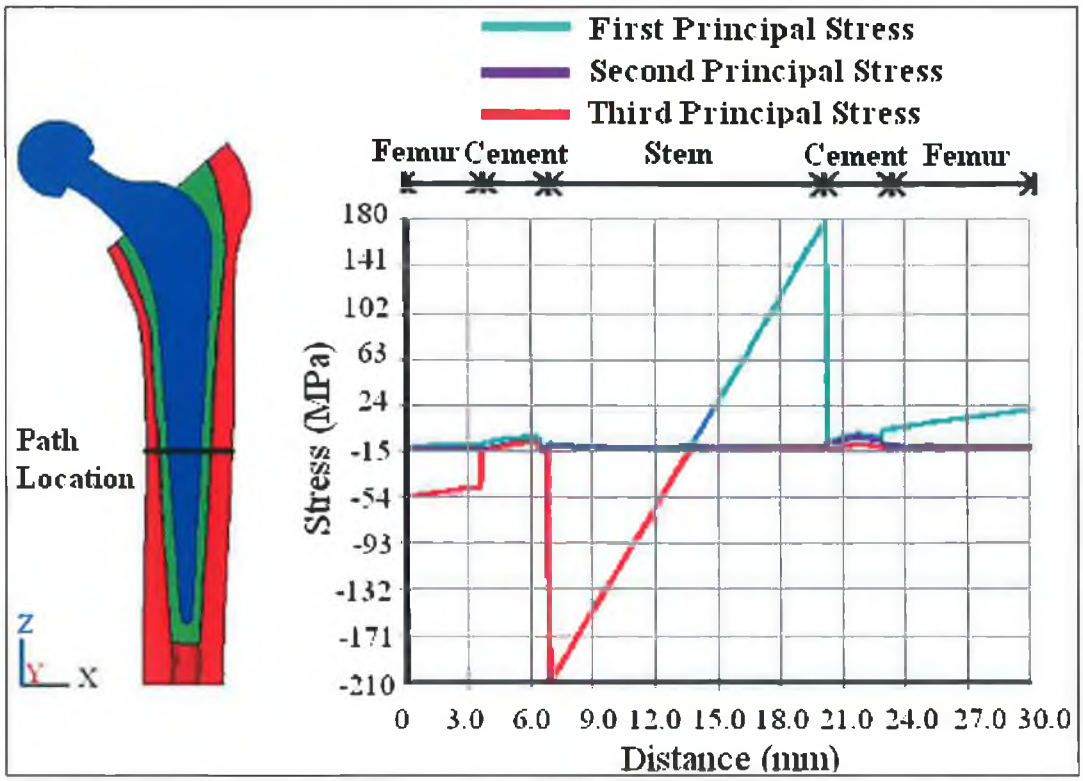

Figure L.3: Principal stresses for the rehabilitation scenario for the path defined on solid model

Appendix M

Residual Stress Relaxation

In Chapter 3, 24 residual stress experiments were performed with CMW® 1 Gentamicin bone cement to quantify the residual stress levels based on a number of different initial conditions. All the experimental data reported in Chapter 3 was taken 3 hours after the initiation of bone cement mixing. A number of these residual stress experiments were allowed to run for an extended period of time to investigate the residual stress relaxation rate for CMW® 1 Gentamicin bone cement. Figure M.1 illustrates a typical result.

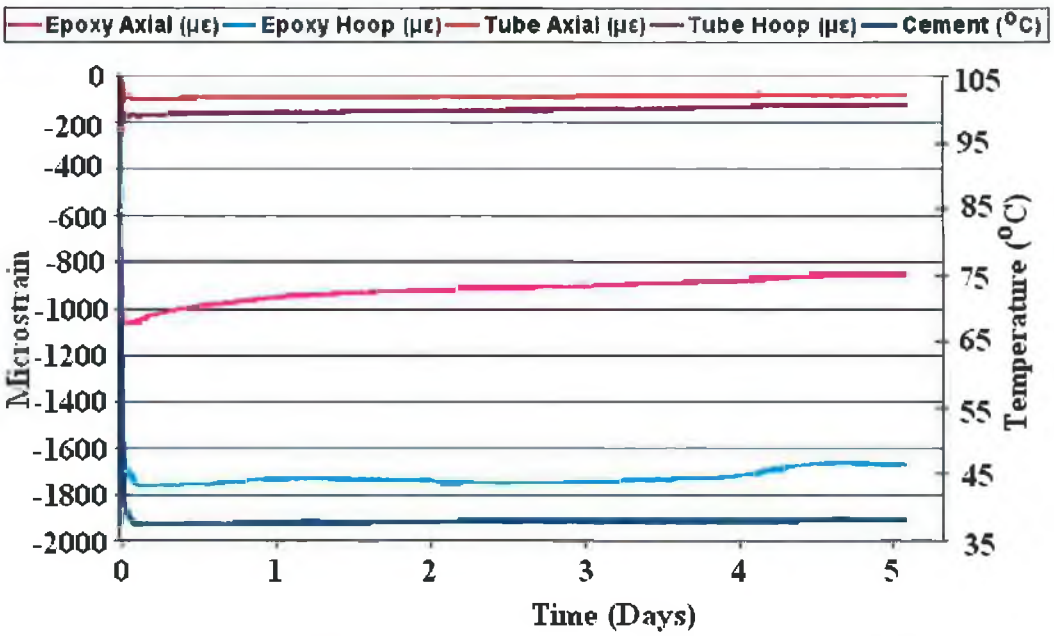

Figure M.1: CMW® 1 Gentamicin residual stress relaxation over 5.1 days. Data taken from a vacuum mixed non-pressurised experiment

From Figure M.1 it is evident that a slight fluctuation occurred for the e-glass/epoxy (representative femur) hoop microstrain. This strain fluctuation approximately coincided with a slight temperature fluctuation in the oven. Therefore it is hypothesised that apparent strains are the primary source for this fluctuation. Table M.1 summarises the strain relaxation measured for the representative femur in the axial direction.

Experiment Number	Duration of experiment (Days)	E-glass/epoxy - Axial (με)		Reduction (%)	Reduction per day (%)
		At 3hrs	At end of experiment		
No.1	1.02	-874	-831	5	4.8
No.2	3.63	-711	-593	17	4.6
No.3	3.93	-437	-328	25	6.4
No.4	1.92	-450	-409	9	4.6
No.5	0.78	-774	-730	6	7.2
No.17	0.68	-490	-470	4	6.0
No.18	0.86	-382	-329	14	16.1
No.22	2	-974	-906	7	3.5
No.23	5.09	-1045	-854	18	3.6
No.24	0.98	-890	-714	20	20.2
No.28	2.07	-795	-743	7	3.2
No.29	2.71	-705	-675	4	1.6
Mean					**7**

Table M.1: Measured residual strain levels for the representative femur in the axial direction

Table M.2 summarises the strain relaxation measured for the representative stem in the axial direction. Table M.3 summarises the strain relaxation measured for the representative stem in the hoop direction. It is worth noting, with the exclusion of experiment numbers 5, 17 and 18, the average percentage reduction was 9%. It is unknown why experiments 5, 17 and 18 reduced in stress much faster compared to the remainder of the experimental data.

Experiment Number	Duration of experiment (Days)	Steel tube - Axial (με)		Reduction (%)	Reduction per day (%)
		At 3hrs	At end of experiment		
No.1	1.02	-72	-64	11.1	10.9
No.2	3.63	-97	-85	12.5	3.5
No.3	3.93	-84	-68	18.9	4.8
No.4	1.92	-71	-59	16.2	8.4
No.5	0.78	-56	-51	9.2	11.8
No.6	2.67	-133	-121	9.0	3.4
No.15	10.86	-67	-47	29.9	2.7
No.16	2.25	-41	-31	24.4	10.8
No.17	0.68	-128	-118	8.0	11.7
No.18	0.86	-120	-114	5.0	5.8
No.22	2	-72	-58	19.4	9.7
No.23	5.09	-102	-84	17.8	3.5
No.25	2.9	-64	-48	25.0	8.6
Mean					**7**

Table M.2: Measured residual strain levels for the representative stem in the axial direction

Experiment Number	Duration of experiment (Days)	Steel tube - Hoop (με)		Reduction (%)	Reduction per day (%)
		At 3hrs	At end of experiment		
No.2	3.63	-52	-35	32.1	8.9
No.3	3.93	-49	-27	44.4	11.3
No.4	1.92	-57	-42	25.1	13.1
No.5	0.78	-65	-44	32.5	41.6
No.6	2.67	-73	-44	39.7	14.9
No.15	10.86	-135	-56	58.5	5.4
No.16	2.25	-138	-109	21.0	9.3
No.17	0.68	-57	-37	35.7	52.6
No.18	0.86	-47	-30	36.2	42.1
No.23	5.09	-174	-123	29.2	5.7
No.24	0.98	-112	-100	10.7	10.9
No.25	2.9	-113	-95	15.9	5.5
Mean					**18**

Table M.3: Measured residual strain levels for the representative stem in the hoop direction